

*Quantum Information Approaches
to Holographic Dualities*

Dissertation

zur Erlangung des Grades eines

Dr. rer. nat.

am

Fachbereich Physik

der

Freien Universität Berlin

vorgelegt von

Alexander Jahn

Berlin, Oktober 2020

Eigenständigkeitserklärung

Ich erkläre gegenüber der Freien Universität Berlin, dass ich die vorliegende Dissertation selbstständig und ohne Benutzung anderer als der angegebenen Quellen und Hilfsmittel angefertigt habe. Die vorliegende Arbeit ist frei von Plagiaten. Alle Ausführungen, die wörtlich oder inhaltlich aus anderen Schriften entnommen sind, habe ich als solche kenntlich gemacht. Diese Dissertation wurde in gleicher oder ähnlicher Form noch in keinem früheren Promotionsverfahren eingereicht.

Mit einer Prüfung meiner Arbeit durch ein Plagiatsprüfungsprogramm erkläre ich mich einverstanden.

Alexander Jahn, Berlin, den 11. Oktober 2020.

Erstgutachter

Prof. Dr. Jens Eisert

Zweitgutachter

Prof. Dr. Matthias Staudacher

Datum der Disputation

26. Februar 2021

Zusammenfassung

Die AdS/CFT-Korrespondenz, eine erstaunliche Dualität zwischen bestimmten Gravitationstheorien in anti-de Sitter (AdS) Raumzeit und Quantenfeldtheorien mit konformer Symmetrie (CFT), hat die Entwicklung der theoretischen Physik der letzten zwei Jahrzehnte entscheidend geprägt. Jüngst wurden viele Verbindungen zwischen AdS/CFT und der Quanteninformationstheorie entdeckt, welche insbesondere duale gravitative Beschreibungen von verschiedenen Verschränkungsmaßen ermöglichen. Um diese Realisierungen von AdS/CFT und des zugrundeliegenden holografischen Prinzips zu verstehen, bedarf es einer Kombination von Werkzeugen der Hochenergiephysik und der Quanteninformationsphysik.

In dieser kumulativen Dissertation wird der Zusammenfluss von diesen beiden Feldern aus zwei verschiedenen Richtungen betrachtet: Erstens durch Berechnungen in der dualen Gravitationstheorie und zweitens durch einen Tensornetzwerk-Ansatz zur Beschreibung der Quantensysteme, von denen eine gravitative Beschreibung vermutet wird.

Im ersten Ansatz wird die gravitationstheoretische Seite der AdS/CFT-Korrespondenz genutzt, um Verschränkungsentropien komplizierter 2+1-dimensionaler angeregter konformer Feldtheorien zu berechnen. Dies zeigt die Möglichkeiten des holografischen Ansatzes auf, Zugang zu bislang mit praktischen Methoden nicht beschreibbaren Systemen zu erhalten und führt neue numerische Methoden ein, die für diesen Ansatz benötigt werden.

Die zweite Richtung beinhaltet Tensornetzwerke, ein höchst erfolgreicher Ansatz zur Berechnung von ein- und zweidimensionalen Quantensystemen. Effizient berechenbare Klassen von Tensornetzwerken werden auf ihre Fähigkeit hin untersucht, die Eigenschaften einfacher holografischer Systeme darzustellen, wobei sowohl hyperbolische Geometrien als auch kritische Randzustände erfolgreich reproduziert werden. Außerdem werden die allgemeinen Eigenschaften von holografischen Tensornetzwerken auf regulär-hyperbolischen Tesselierungen untersucht, was zu neuen Verbindungen mit Modellen führt, welche bislang nicht im Zusammenhang mit Holografie betrachtet wurden.

Dieses Zusammenspiel verschiedener Ansätze der Quanteninformationsholografie bezeugt die reichen Eigenschaften dieses neuen Gebiets und legt nahe, dass noch ein weites Feld physikalischer Phänomene durch die uns nun zur Verfügung stehenden Werkzeuge erschlossen werden kann.

Abstract

The AdS/CFT correspondence, a remarkable duality between certain gravitational theories in anti-de Sitter (AdS) spacetime and quantum field theories with conformal symmetry (CFT), has had a profound effect on the development of theoretical physics in the past two decades. Recently, many connections of AdS/CFT to quantum information theory have been found, in particular by providing gravitationally dual descriptions of various entanglement measures. Understanding these manifestations of AdS/CFT — or more generally, the conjectured holographic principle encompassing it — requires the combination of tools from both high-energy theory and quantum information physics.

In this cumulative thesis, the convergence between these two fields is approached from two fronts: First, by calculations within the dual gravitational theory, and second, using a tensor network ansatz to describe the quantum states suspected to possess such a gravitational description.

In the first approach, using the gravitational side of AdS/CFT, entanglement entropies of complicated 2+1-dimensional excited CFTs are computed, thus showing how the holographic approach provides access to systems previously out of reach of practical methods, while introducing new numerical methods that this approach necessitates.

The second approach is given by tensor networks, a highly successful ansatz for computing properties of one- and two-dimensional quantum systems. Efficiently computable classes of tensor networks are tested in their ability to represent simple holographic systems, successfully reproducing both hyperbolic geometrical features as well as critical boundary states. In addition, the general properties of tensor networks on regular hyperbolic tessellations are considered, leading to new connections to models not previously considered in the context of holography.

This interplay of different approaches to quantum information holography showcases the richness of this new field and suggests that a wide range of physical phenomena is accessible via the new tools now at our disposal.

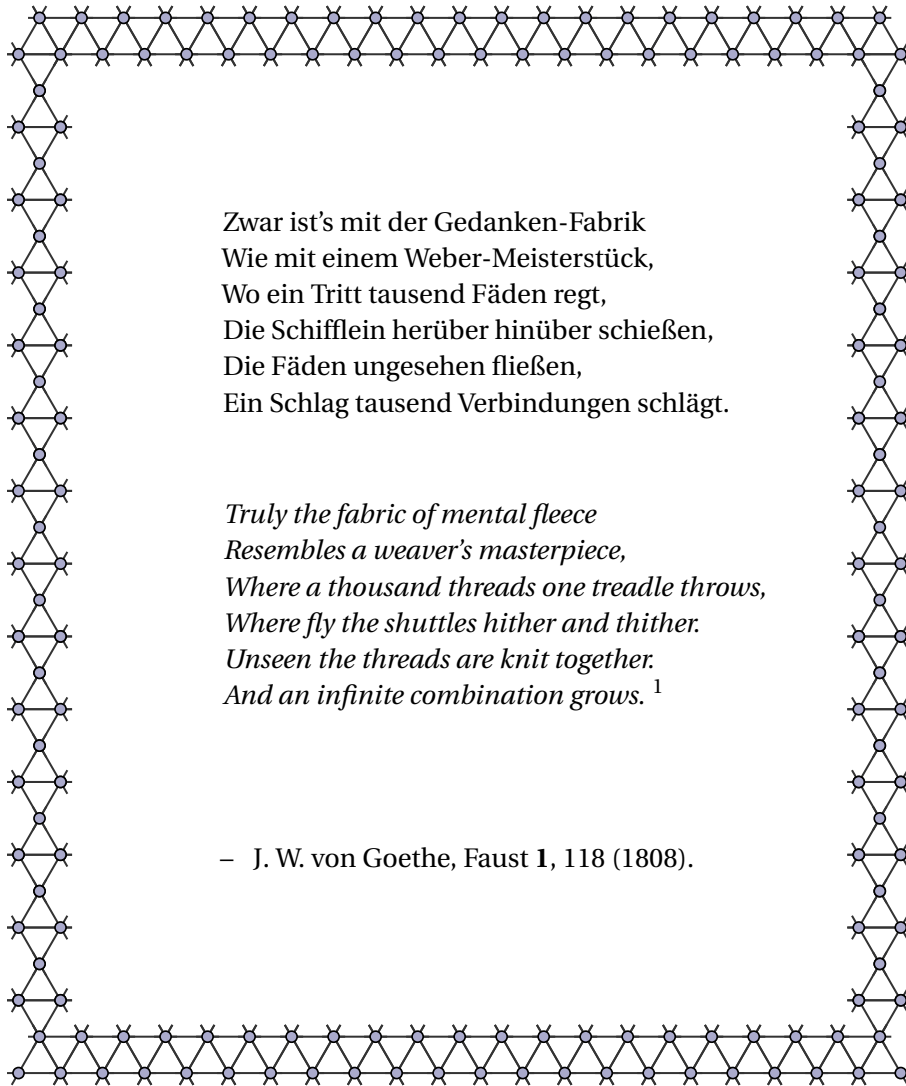
List of publications

This cumulative dissertation is comprised of the following four journal publications of which Alexander Jahn is the first author.

- A. Jahn and T. Takayanagi,
“Holographic Entanglement Entropy of Local Quenches in AdS_4/CFT_3 : A Finite-Element Approach,”
J. Phys. A **51** (2018) Iss. 1, 015401.
arXiv:1705.04705 [hep-th] DOI: 10.1088/1751-8121/aa8afa
- A. Jahn, M. Gluza, F. Pastawski, and J. Eisert,
“Holography and criticality in matchgate tensor networks,”
Science Advances **5**, eaaw0092 (2019).
arXiv:1711.03109 [quant-ph] DOI: 10.1126/sciadv.aaw0092
- A. Jahn, M. Gluza, F. Pastawski, and J. Eisert,
“Majorana dimers and holographic quantum error-correcting codes,”
Phys. Rev. Research. **1** (2019), Iss. 3, 033079.
arXiv:1905.03268 [hep-th] DOI: 10.1103/PhysRevResearch.1.033079
- A. Jahn, Z. Zimborás, and J. Eisert,
“Central charges of aperiodic holographic tensor network models,”
Phys. Rev. A **102** (2020), 042407.
arXiv:1911.03485 [hep-th] DOI: 10.1103/PhysRevA.102.042407

The following publications and preprints with listed authorship were also produced in the course of doctoral research.

- A. Bhattacharyya, A. Jahn, T. Takayanagi, and K. Umemoto,
“Entanglement of Purification in Many Body Systems and Symmetry Breaking,”
Phys. Rev. Lett. **122** (2019) Iss. 20, 201601.
arXiv:1902.02369 [hep-th] DOI: 10.1103/PhysRevLett.122.201601
- A. Jahn, Z. Zimborás, and J. Eisert,
“Tensor network models of $AdS/qCFT$.”
arXiv:2004.04173 [quant-ph]
- H. A. Camargo, L. Hackl, M. P. Heller, A. Jahn, T. Takayanagi, and B. Windt,
“Entanglement and Complexity of Purification in (1+1)-dimensional free Conformal Field Theories.”
arXiv:2009.11881 [hep-th]
- B. Windt, A. Jahn, J. Eisert, and L. Hackl,
“Local optimization on pure Gaussian state manifolds.”
arXiv:2009.11884 [quant-ph]



Zwar ist's mit der Gedanken-Fabrik
Wie mit einem Weber-Meisterstück,
Wo ein Tritt tausend Fäden regt,
Die Schifflin herüber hinüber schießen,
Die Fäden ungesehen fließen,
Ein Schlag tausend Verbindungen schlägt.

*Truly the fabric of mental fleece
Resembles a weaver's masterpiece,
Where a thousand threads one treadle throws,
Where fly the shuttles hither and thither.
Unseen the threads are knit together.
And an infinite combination grows.*¹

– J. W. von Goethe, *Faust I*, 118 (1808).

¹From the 1870 translation by Bayard Taylor.

Contents

1	Introduction	1
2	Foundations	3
2.1	Holography from strings	3
2.1.1	String theory	4
2.1.2	The AdS/CFT proposal	6
2.2	Tensor networks	12
2.3	Quantum error correction	17
2.4	Holography in quantum information	20
2.4.1	Holographic entanglement entropy	20
2.4.2	Holographic tensor networks	21
2.4.3	Holographic quantum error correction	22
2.4.4	Gravity and entanglement	24
3	Roads to holography	27
3.1	Gravitational approaches	27
3.2	Tensor network approaches	28
3.3	Publication overview	31
4	Publications	34
4.1	Holographic Entanglement Entropy of Local Quenches in $\text{AdS}_4/\text{CFT}_3$: A Finite-Element Approach	35
4.2	Holography and criticality in matchgate tensor networks	66
4.3	Majorana dimers and holographic quantum error-correcting codes	94
4.4	Central charges of aperiodic holographic tensor network models	133
5	Concluding remarks	151

Chapter 1

Introduction

It is the unfortunate reality of theoretical physics, among other disciplines, that some problems are hard. While often glossed over in secondary education, it is in the early stages of undergraduate physics that a student usually begins to realize that some problems — such as determining the analytical form of certain integrals — cannot be resolved, even by tenured professors. After having spent a few years in the realm of university physics, it gradually becomes clear to the student that indeed most physical problems of interest are not directly solvable, and that the true mettle of a physicist consists in cleverly contriving indirect approaches to tackling the chosen system. While the experimental physicist's approach usually involves an intricate measurement apparatus whose function is several degrees removed from the most straightforward but infeasible setup, the theoretical physicist has to resort to similarly intricate constructions on the analytical or numerical side.

Fortunately, while few exactly solvable systems are at the theoretical physicist's disposal (most somehow related to harmonic oscillators), great ingenuity has been applied to extending knowledge of these exact solutions onto new problems. Of great help is the continuing discovery of *dualities*, direct relationships between seemingly different physical theories. Once the precise framework of a duality is understood, it often allows the transfer of known results on one side to produce solutions on the other. A famous example is the *Jordan-Wigner transformation*, which provides a correspondence between a system composed of spins and one composed of fermions. Despite the different physical behavior of these two types of quantum-mechanical objects, e.g. under exchange of two of them, they are related by a deep mathematical connection that simplifies many practical computations. The duality upon which the work in this thesis is founded is a recent one in the timescales of physics: Discovered twenty-three years ago, the *anti-de Sitter/conformal field theory correspondence*, or simply *AdS/CFT*, has led us to fascinating new connections between old theories, producing a concrete realization of the previously proposed *holographic principle*. Similar to the holography that allows for the creation of three-dimensional images on a two-dimensional surface,

the holographic principle is a proposal that certain higher-dimensional physical theories involving gravity may be effectively lower-dimensional. While highly counter-intuitive, AdS/CFT confirmed this intuition for a special type of gravitational system involving a negative cosmological constant, or equivalently, global negative spacetime curvature. Perhaps surprisingly, the usefulness of AdS/CFT for practical applications arises mostly from using results on the higher-dimensional gravitational side — usually the “easy” side of the duality — and applying it to the lower-dimensional side containing a complicated quantum theory.

For all its achievements, the AdS/CFT correspondence remains a conjecture, largely because the theories it relates are not themselves fully (i.e., non-perturbatively) understood. Furthermore, AdS/CFT is deeply embedded into the framework of string theory, whose mighty mathematical apparatus complicates the application of its results onto more pedestrian branches of physics. Fortunately, the burgeoning field of quantum information theory has recently produced many new paths to understanding facets of holography in great generality, beyond many of the constraints of the original AdS/CFT setup. In this work, some of these paths will be explored in detail, all deeply related to the perhaps most quantum of physical phenomena, entanglement. In particular, we will make great use of the language of tensor networks to illuminate the quantum information side of holography, a language that encompasses a range of physical setups from simple quantum-mechanical systems to — as it is hoped — aspects of quantum gravity.

The many theoretical concepts underlying these endeavors are introduced in Chapter 2, preparing the reader for the chapters that follow. It also contains short summary boxes that sketch topics of relevance that are mentioned throughout the sections. References to introductory books and articles for further reading are listed at the end of each section. Chapter 3 then motivates the central themes of this thesis and provides an overview of the publications that comprise its cumulative part. These are then included in Chapter 4 in their original publication format in the order in which they were published. The final Chapter 5 closes with an outlook on future developments as well as acknowledgements.

Chapter 2

Foundations

2.1 Holography from strings

The origins of the holographic principle can be traced back to the 1970s, when physicists began to consider black holes from a new vantage point: Based on the work of Stephen W. Hawking and Jacob D. Bekenstein, it was realized that black holes are thermodynamical objects with a well-defined temperature and entropy [1, 2]. For a black hole with a given mass M , these are given by¹

$$T_{\text{H}} = \frac{\hbar c^3}{8\pi k_{\text{B}} G M}, \quad S_{\text{BH}} = \frac{4GM^2}{\hbar c} = \frac{c^3 A_{\text{hor}}}{4\hbar G}, \quad (2.1.1)$$

commonly called the *Hawking temperature* and *Bekenstein-Hawking entropy* of a black hole, respectively. When expressed in terms of the area A_{hor} of the event horizon, the latter equation, more succinctly written in natural units as $S_{\text{BH}} = A_{\text{hor}}/4G$, contains a surprising insight: Rather than growing with its volume, as a conventional thermodynamical system, a black hole's entropy grows with its surface area! This has led to the suggestion that the information of a black hole's microstates are *holographically* encoded on its horizon. The "resolution" of this encoding is on the order of the Planck scale, as we can see by writing the denominator of (2.1.1) in terms of the Planck length l_{P} as $4\hbar G/c^3 = 4l_{\text{P}}^2$. From this observation, Leonard Susskind and Gerardus 't Hooft declared that a consistent theory of quantum gravity would have to obey a *holographic principle*: The dynamics of gravity in 3+1-dimensional spacetime in such a theory would have to be reducible to an effective 2+1-dimensional description [3, 4]. While the entropy scaling in terms of area rather than volume appeared in gravitational settings other than black holes [5], the holographic principle was fundamentally vague: It neither specified *which* theory of quantum gravity would produce such a holographic mapping between systems in different dimensions, nor *how* this mapping would be implemented.

¹During the remainder of this thesis, *natural units* with $\hbar = c = 1$ will be used. Newton's constant G will be kept explicit, as it acts as a useful scale in AdS/CFT.

For this reason, the conjecture of the *AdS/CFT correspondence*, a specific holographic duality between a $d+1$ -dimensional gravitational theory and a d -dimensional quantum field theory by Juan M. Maldacena in 1997 [6] was met with a tremendous amount of research activity. It fundamentally changed the field of string theory, from which it was derived, and had repercussions in a wide range of research areas beyond the high-energy theory community.

The basic setup of AdS/CFT, along with the necessary string-theoretic concepts it is built upon, will be reviewed in the next sections.

2.1.1 String theory

The development of quantum field theory in the second half of the 20th century led to a consistent and precise description of high-energy processes occurring in nature. With the *Standard Model* of particle physics, quantum field theory unified electromagnetic, weak and strong interactions into one formulation. Quantum field theory, however, is an inherently effective theory. The fields of the Standard Model require *renormalization*: Their naive formulation leads to diverging physical quantities, requiring the introduction of a regulating energy or length scale (similar to the lattice scale in solid state models) and leading to physical observables such as coupling “constants” depending on the energy at which the system is probed. This implies that as higher and higher energies are considered, the behavior of the theory changes; a quantum field theory valid at lower energies may need to be replaced by a more complicated one at higher energies, e.g. by introducing new intermediate particles. While the Standard Model with its finite parameters describes the three aforementioned forces in a manner that can in principle be extended to arbitrarily high energies, this is not true for the fourth fundamental force: Gravity. A quantum field theory of gravity which replaces the metric of spacetime by a dynamical quantum field (with excitations known as *gravitons*) can be easily constructed at low energies. However, at high energies the process of renormalization requires the introduction of increasingly many parameters to cancel out divergences, making the theory useless for actual predictions. This suggests that a naive field quantization of gravity is only an effective theory for a more fundamental theory of *quantum gravity* appearing at exceedingly high energies.

One candidate for such a theory is given by string theory. Rather than the fundamental point-like particles appearing in quantum field theory, this approach proposes the quantization of one-dimensional objects called strings. Similar to how the trajectories of point particles correspond to worldlines in spacetime, a string traces out a two-dimensional *worldsheet* $X^\mu(\tau, \sigma)$ parametrized by two coordinates τ and σ . Note that the D -vector X^μ can describe a point in a *target spacetime* of arbitrary dimension $D > 2$. Extending the action of a point particle in special relativity to a two-dimensional object,

one arrives at the *Nambu-Goto* action²

$$S_{\text{NG}} = \frac{-1}{2\pi\sqrt{l_s}} \int d\tau d\sigma \sqrt{\left(\frac{\partial X^\mu}{\partial \tau} \frac{\partial X_\mu}{\partial \sigma}\right)^2 - \left(\frac{\partial X^\mu}{\partial \tau} \frac{\partial X_\mu}{\partial \tau}\right) \left(\frac{\partial X^\mu}{\partial \sigma} \frac{\partial X_\mu}{\partial \sigma}\right)}, \quad (2.1.2)$$

where $X_\mu = \eta_{\mu\nu} X^\nu$ (with the Minkowski metric $\eta_{\mu\nu}$) and the constant l_s is known as the *string length* (often replaced by a coefficient $\alpha' = l_s^2$).

Solutions to the action (2.1.2) can be either *open* or *closed* strings; in the former case, this means that the string endpoints need to be associated with Dirichlet or Neumann boundary conditions. It was later realized that in the first case, the dynamics of the endpoints are related to higher-dimensional objects known as *Dirichlet-branes* or *D-branes* for short.

The spectrum of possible excitations on strings can be identified with particles of mass M . For the purely bosonic action (2.1.2), the vacuum state of both open and closed strings leads to unphysical *tachyons* with $M^2 < 0$. The first excited states, however, become massless if the target space dimension is chosen as $D = 26$. These states can be identified with gauge bosons for open strings and gravitons for closed strings. In addition, closed string excitations contain scalar *dilatons* and an antisymmetric tensor field.

Interactions in string theory are considerably more constrained than in regular quantum field theory, where coupling constants are often free parameters to be determined by experiment. In contrast, interactions of strings follow directly from geometrical considerations: For example, by pinching together two points of a closed string it is split into two new ones. Similarly, open strings can turn into closed ones through the joining of endpoints. The effective string coupling g_s is determined by the vacuum expectation value of the dilaton field.

While twenty-six dimensions could be reduced to our familiar four by compactification of the remaining dimensions to small scales, leading to new effective lower-dimensional fields, the problem of a tachyonic ground state is not easily circumvented. However, after extending the bosonic action to a *supersymmetric* one containing both bosonic and fermionic degrees of freedom (see Summary 1), the tachyonic states can be removed through the *GSO projection* [8]. This projection removes states of even fermionic parity, including the unphysical vacuum. In the case of supersymmetric string theory, the critical number of dimensions necessary to produce massless states is reduced to ten. Different projections led to different ten-dimensional superstring theories. For closed superstrings, due to different possible choices of worldsheet (anti-)periodicity of the left- and right-moving modes, two consistent models known as *type IIA* and *type IIB* superstring theory emerge. In addition, by separately placing bosonic and supersymmetric modes in the left- and right-moving sector, another consistent solution known

²Named after Yoichiro Nambu and Tetsuo Goto, though no formal publication of theirs exists. In practice, a reformulation in terms of the equivalent *Polyakov action* [7] is more conveniently used.

Summary I: Supersymmetry

Classifying quantum field theories by their symmetries has driven much of the development of the Standard Model over the late 20th century. While bosons and fermions in the Standard Model are intimately related by gauge symmetries, it is possible to extend its field content to allow for a direct symmetry between bosonic and fermionic fields, called *supersymmetry*. Following Noether's theorem, supersymmetry implies the existence of *supercharges* Q . These act as operators on fields that change their spin by $1/2$, turning bosonic fields into fermionic ones and vice-versa. The number \mathcal{N} of possible distinct supercharges is subject to physical constraints. Models of *extended supersymmetry* with $\mathcal{N} > 1$ preserve chiral symmetry and are thus incompatible with the Standard Model. In $3+1$ dimensions, a theory with spins $s \leq 1$ can have $\mathcal{N} = 4$ at most. A particular example of such a theory is $\mathcal{N} = 4$ *super-Yang-Mills* theory, which also possesses conformal symmetry. Supersymmetries with $\mathcal{N} > 8$ imply fields with spin $s > 2$.

as *heterotic* string theory is recovered.³ Finally, another possibility is given by *type I* superstring theory, which contains both open and closed *unoriented* strings. This web of consistent string theories was later found to be connected by dualities that map from one theory to another. Furthermore, it was speculated that these theories might be related to a unique eleven-dimensional theory called *M theory*. [9]

For the purposes of the AdS/CFT correspondence, we are mostly interested in type IIB superstring theory. In the low-energy limit, only the lowest string excitations are relevant, leading to an effective quantum field theory known as type IIB *supergravity*. In addition to the graviton, this theory contains a number of additional fields that preserve supersymmetry. Interestingly, this theory allows for non-perturbative (solitonic) objects known as D-branes [10] that fill out some of the ten dimensions. Beyond containing endpoints of open strings, as mentioned earlier, D-branes can themselves carry masses and charges and perturb the metric around them. These two perspectives on D-branes are essential for the construction that led to AdS/CFT.

For more information on string theory, please refer to the several textbooks on the subject both at the introductory (undergraduate) [11, 12] and advanced level [13, 14].

2.1.2 The AdS/CFT proposal

The original AdS/CFT setup [6] is based on type IIB superstring theory in $D=10$ space-time dimensions. This theory supports non-perturbative D-brane solutions. We consider a stack of N parallel D3-branes filling out three of the nine spatial dimensions. This setup has the following parameters: The string coupling g_s , the string length l_s , the

³Due to different possible symmetries of this construction, there are actually two heterotic string theories: $SO(32)$ and $E_8 \times E_8$.

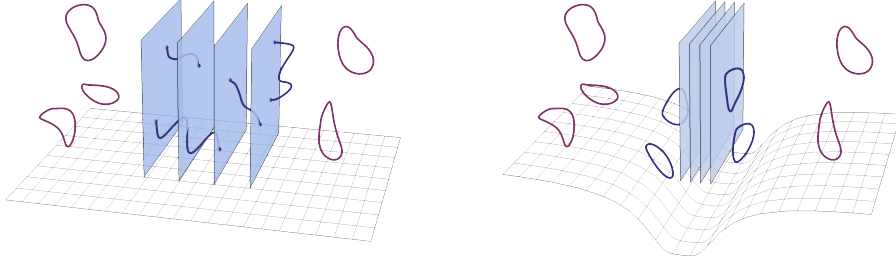


Figure 2.1: Visualization of two perspectives on the AdS/CFT setup. LEFT: At small coupling Ng_s , open strings between N D-branes form an effective $U(N)$ gauge theory in the low-energy limit, with decoupled closed strings described by IIB supergravity in a flat $\mathbb{R}^{9,1}$ background. RIGHT: At large Ng_s , the D-branes deform the spacetime background filled with closed strings. At low energies, strings near to and far away from the D-branes decouple; both are approximated by IIB supergravity, with the metric described by $\text{AdS}_5 \times S^5$ and flat $\mathbb{R}^{9,1}$, respectively.

distance d between the branes and their number N .

As mentioned in the previous section, D-branes serve as endpoints of open strings and carry fields. We consider the low-energy limit of vanishing string length $l_s \rightarrow 0$, i.e., we “zoom out” to scales where all excitations (of order $1/l_s$) beyond the ground state become negligible. To keep the mass of string modes between different branes constant, $U = d/l_s^2$ is fixed (so that $d \rightarrow 0$, as well). Considering the open strings as small perturbations (in Ng_s) of the branes, one finds an effective $U(N)$ Yang-Mills theory with coupling constant $g_{\text{YM}}^2 = 2\pi g_s$ in the low-energy limit. Specifically, this theory has $\mathcal{N} = 4$ supercharges (half of the original type IIB theory, broken by the D-branes) and is known as $\mathcal{N} = 4$ super-Yang-Mills (SYM) theory. The limit $l_s \rightarrow 0$ also removes interactions between the open strings on the branes and the closed strings in the type IIB background, so that the $U(N)$ theory decouples. The remaining closed strings can be treated by the low-energy limit of type IIB strings, given by type IIB supergravity.

Alternatively, we can look at the branes as a massive perturbation of the background of the closed strings in the type IIB string theory. The metric around N D3-branes is given by [15]

$$ds^2 = \frac{dx^2}{\sqrt{1 + 4\pi N g_s (l_s/r)^4}} + \sqrt{1 + 4\pi N g_s (l_s/r)^4} (dr^2 + r^2 d\Omega_5^2), \quad (2.1.3)$$

where x are the spacetime coordinates along the branes and r is the radial coordinate away from the D-branes. At large r , this metric simply describes flat 10-dimensional space. However, at small r we can rewrite it as

$$ds^2 = \frac{r^2}{\alpha^2} dx^2 + \frac{\alpha^2}{r^2} dr^2 + \alpha^2 d\Omega_5^2, \quad (2.1.4)$$

Summary 2: Anti-de Sitter spacetime

A particularly symmetric class of D -dimensional spacetimes are those with constant *scalar curvature* R at all points. For vanishing R , we have the flat Minkowski spacetime $\mathbb{R}^{D-1,1}$. The cases $R > 0$ and $R < 0$ are known as *de Sitter* (dS) and *anti-de Sitter* (AdS) spacetimes, respectively. The latter case can be expressed in different metrics; most commonly used are *global coordinates* $(\tau, \rho, \Omega_1, \dots, \Omega_{D-2})$ with

$$ds^2 = -\left(1 + \frac{\rho^2}{\alpha^2}\right) d\tau^2 + \frac{\alpha^2}{\alpha^2 + \rho^2} d\rho^2 + \rho^2 d\Omega_{D-2}^2, \quad (2.1.5)$$

and *Poincaré coordinates* $(t, r, x_1, \dots, x_{D-2})$ with

$$ds^2 = \frac{r^2}{\alpha^2} (-dt^2 + d\vec{x}^2) + \frac{\alpha^2}{r^2} dr^2. \quad (2.1.6)$$

The *AdS radius* α determines the scalar curvature $R = -D(D-1)/\alpha^2$. Characteristic of AdS spacetime is a horizon at spatial infinity ($\rho \rightarrow \infty$ or $r \rightarrow 0$) that no timelike geodesics can reach. The metric at this horizon is given by flat $D-1$ -dimensional Minkowski spacetime $\mathbb{R}^{D-2,1}$. AdS spacetime has $SO(D-1,2)$ symmetry, the same symmetry as a $D-1$ -dimensional conformal field theory (CFT), an important cornerstone of the AdS/CFT correspondence.

where we defined $\alpha = (4\pi N g_s)^{1/4} l_s$. The metric (2.1.4) describes 4+1-dimensional *anti-de Sitter* (AdS) spacetime in the *Poincaré coordinates* (x, r) in addition to the angular coordinates Ω_5 of the 5-sphere S^5 . This combination is denoted as $\text{AdS}_5 \times S^5$. The AdS radius α is also the radius of the 5-sphere in this setup. AdS spacetime has constant negative curvature of the same magnitude as the positive curvature of S^5 . As explained in Summary 2, the branes at $r = 0$ form a horizon that is infinitely spatially separated from the remaining spacetime.

We again consider the low-energy limit of this setup: As $l_s \rightarrow 0$, the closed strings at both large and small r are described by type IIB supergravity while decoupling from one another. At large r , the spacetime background is flat and we find the same supergravity theory as in the previous setup where we considered the open string dynamics between branes. However, at small r we find a theory of supergravity on an AdS background, rather than the $U(N)$ theory resulting from the previous analysis using open strings. Assuming that both descriptions of the D-brane setup are equally valid across the whole range of couplings $N g_s$, it appears that both theories should be equivalent, as well. This leads to the following duality:

$$\mathcal{N} = 4 \text{ } SU(N) \text{ SYM theory on } \mathbb{R}^{3,1} \quad \equiv \quad \text{Type IIB superstring theory on } \text{AdS}_5 \times S^5.$$

Note that we changed the gauge group from $U(N)$ to $SU(N)$, as a set of $U(1)$ modes on the boundary is non-dynamical [16]. The coupling constants are related via $g_{\text{YM}}^2 = 2\pi g_s$

Summary 3: Conformal field theory

As stated by the Coleman-Mandula theorem [18], it is generally not possible to combine internal symmetries of quantum fields with spacetime symmetries in any nontrivial way. One exception to this theorem is supersymmetry, based on a graded Lie algebra beyond the scope of Coleman-Mandula, which directly relates bosonic and fermionic fields (see Summary 1). [19] As the theorem is based on the properties of the S -matrix describing scattering between asymptotic particles, it also breaks down in theories without a length scale. This includes scale-invariant and *conformally* invariant models. Conformal transformations $g_{\mu\nu}(x) \rightarrow \Omega^2(x)g_{\mu\nu}(x)$ (with positive $\Omega^2(x)$) preserve local angles but not lengths. This greatly restricts the physical properties of a conformal field theory (CFT). Correlations generally depend polynomially on distances, with the form of two- and three-point functions fixed by symmetry. Extending D -dimensional Poincaré symmetries (translations, rotations and Lorentz transformations) with conformal symmetry leads to the *conformal group* $SO(D, 2)$. While higher-dimensional CFTs are hard to study analytically, in $1+1$ dimensions many examples (such as the critical *Ising model* [20]) are exactly solvable. Further requiring supersymmetry leads to *superconformal* theories, a class that also includes $\mathcal{N} = 4$ super-Yang-Mills (see Summary 1).

and $2Ng_{\text{YM}}^2 = (\alpha/l_s)^4$. This leads to a remarkable property. The effective coupling constant in the SYM theory is given by

$$\lambda = Ng_{\text{YM}}^2 = \frac{\alpha^4}{2l_s^4}. \quad (2.1.7)$$

As we are working in the $l_s \ll \alpha$ limit, λ is large and the SYM theory is thus *strongly* coupled. However, if we are also taking the $N \rightarrow \infty$ limit, the string coupling $g_s = \lambda/(2\pi N)$ is *weak* and the type IIB superstring theory can be studied perturbatively.⁴ This duality between supersymmetric gauge theory and supergravity (or gauge/gravity duality, for short) is thus often called a strong/weak duality. The name *AdS/CFT correspondence* comes from a particular property of the $SU(N)$ SYM theory: It possesses *conformal* invariance (see Summary 3) and is thus belongs to the class of *conformal field theories* (CFTs).

The range of applicability of the AdS/CFT correspondence appears to be much larger than the specific example just given: Rather than a relationship between supergravity in $4+1$ -dimensional AdS_5 and a $3+1$ -dimensional CFT_4 ($\mathcal{N} = 4$ SYM), similar $\text{AdS}_{D+1}/\text{CFT}_D$ dualities can be constructed for different D .⁵ This is consistent with the symmetries of

⁴The large N limit at fixed λ is usually called the '*t Hooft limit*', after an earlier observation that Yang-Mills theory in this limit has a perturbation series similar to that of a quantized string. [17]

⁵Other examples for $D = 1, 2, 3$ and 6 were already proposed in Maldacena's original paper [6] using different D-brane setups and compactifications.

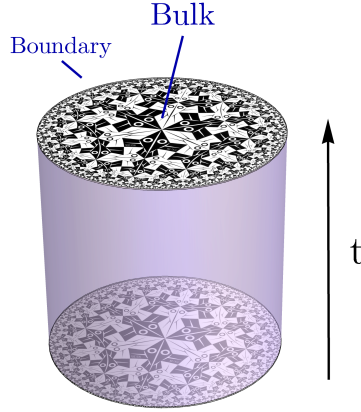


Figure 2.2: Bulk/boundary relation in the AdS/CFT correspondence: The bulk AdS_{D+1} spacetime (shaded cylinder) has a flat asymptotic boundary at spatial infinity. Each time-slice $t = \text{const}$ is a hyperbolic space with negative curvature.

both theories: The spacetime symmetries of AdS_{D+1} are given by $SO(D, 2)$, as it can be embedded onto a hyperbola in flat $\mathbb{R}^{D,2}$ spacetime. This exactly matches the spacetime and conformal symmetries of a CFT_D , which taken together also form $SO(D, 2)$. The observation that the algebra of AdS_{D+1} symmetry generators turns into the D -dimensional conformal algebra at the asymptotic boundary of AdS_{D+1} spacetime was already observed in the $D = 2$ case long before the AdS/CFT correspondence. [21] Supersymmetry on the field theory side corresponds to the additional compact dimensions of matching symmetry on the gravity side: For the $\text{AdS}_5/\text{CFT}_4$ case, the $\mathcal{N} = 4$ supersymmetry corresponds to an $SU(4)$ symmetry that again matches the $SO(6) \sim SO(4)$ symmetry of S^5 . This relationship between supersymmetry and additional compact dimensions suggests the existence of some non-supersymmetric duality between gravity in AdS_{D+1} and CFT_D . Similarly, one may speculate about the validity of AdS/CFT at small 't Hooft coupling λ , where a weakly coupled CFT in the above construction appears to be related to a strongly interacting — i.e., non-perturbative — theory of quantum gravity. While examples in both directions have been constructed, the general validity of AdS/CFT remains unknown. This is intimately tied to the problem that in a strong/weak duality, one of the two sides of the duality will always be hard to treat analytically. For this reason, a fundamental motivation for the focus of this thesis is the construction of simpler models than can be more directly studied with analytical and numerical tools.

Beyond being a duality between theories, AdS/CFT can also be formulated more concretely as a *dictionary* between degrees of freedom on both sides. First, note that the flat background spacetime of the gauge theory side is associated with the location of the D-brane stack, which lies at the asymptotic boundary $r = 0$ of the AdS spacetime (2.1.4). As explained in Summary 2, this is a natural identification, as AdS_{D+1} spacetime indeed has a flat $\mathbb{R}^{D-1,1}$ horizon at spatial infinity. It is customary to refer to the AdS_{D+1} space-

time as the *bulk* and to the asymptotic $\mathbb{R}^{D-1,1}$ as the *boundary*. The relation between the two is visualized in Fig. 2.2. The bulk/boundary mapping effected by AdS/CFT generally relates fields ϕ in the AdS background to operators \mathcal{O} in the boundary conformal field theory. The dynamics on both sides are equivalent; in the language of partition functions,

$$Z_{\text{bulk}}[\phi] = Z_{\text{boundary}}[\mathcal{O}]. \quad (2.1.8)$$

This relationship was first proposed by Edward Witten [22]. Concretely, consider a CFT operator \mathcal{O} with scaling dimension Δ , i.e., with two-point correlations

$$\langle \mathcal{O}(x)\mathcal{O}(y) \rangle_{\text{CFT}} \propto \frac{1}{|x-y|^{2\Delta}}, \quad (2.1.9)$$

between two boundary points x and y . Assume that the AdS/CFT dictionary relates \mathcal{O} to a dual field ϕ with boundary values ϕ^0 . The bulk configuration of ϕ is determined as a boundary value problem from a given ϕ^0 , so that the bulk action can be expressed purely in terms of ϕ^0 .⁶ The bulk action then follows from a simple coupling between \mathcal{O} and ϕ^0 as

$$Z_{\text{bulk}}[\phi] \equiv Z_{\text{bulk}}[\phi^0] = \left\langle \exp \int d^D x \phi^0 \mathcal{O} \right\rangle_{\text{CFT}}. \quad (2.1.10)$$

The boundary operator \mathcal{O}_k thus acts as a source term for the boundary bulk field ϕ_k^0 . Conversely, for expectation values on the boundary, ϕ_k^0 acts as a source term for the operator \mathcal{O}_k . Remarkably, (2.1.10) leads to a direct relationship between the mass m of a massive bulk field and the scaling dimension Δ of its dual operator, given by [22]

$$\Delta = \frac{1}{2} \left(D + \sqrt{D^2 + 4m^2} \right). \quad (2.1.11)$$

AdS/CFT thus implies a concrete relationship between asymptotic bulk fields and boundary operators in a conformal field theory.⁷

While the AdS/CFT correspondence is still a conjecture, many specific examples of the AdS/CFT dictionary with applications from high-energy to condensed matter physics have been found, with its impact on quantum information theory being a particular focus of this thesis. With now more than fifteen thousand citations, Juan Maldacena's original paper has led to a vast amount of research whose end is nowhere in sight.

Beyond technical papers, a number of introductory texts to AdS/CFT have been written, from formal textbooks [23, 24, 25] to notes that are freely available online [26, 27, 28, 29, 30], occasionally by the same authors. Due to the breadth of current AdS/CFT research, each of the citation listed has its own target audience, with numerous more specialized introductions available.

⁶As the fields ϕ are technically divergent at the boundary, one generally defines $\phi^0 = \lim_{r \rightarrow 0} (r^\Delta \phi)$, where r is the radial AdS coordinate from (2.1.4) and Δ the scaling dimension of its dual field. The dependence of the bulk fields ϕ on the boundary fields ϕ^0 can be written in a diagrammatic expansion known as *Witten diagrams*.

⁷Note that the *operator/state correspondence* allows each CFT state to be characterized by a single, local operator, as scale invariance allows us to effectively project the path integral evolution of any state onto a point. Specifying CFT states and operators is thus equivalent.

2.2 Tensor networks

Hilbert spaces are large. While most problems in classical mechanics can be reduced to a small parameter space that is approachable with efficient analytical and numerical techniques, the state spaces of quantum mechanics rarely offer such a relief. Beyond perturbative methods that can describe problems close to one of the few analytically solvable, usually *non-interacting* ones, only approximate numerical techniques are available. To see how the size of Hilbert spaces becomes a fundamental problem in this approach, consider a simple system of N quantum mechanical degrees of freedom each corresponding to an M -level system (e.g. spins for $M = 2$). To describe a single quantum state ψ in this system, we use a basis representation

$$|\psi\rangle = \sum_{k_1, k_2, \dots, k_N=1}^M T_{k_1, k_2, \dots, k_N} |k_1, k_2, \dots, k_N\rangle, \quad (2.2.1)$$

where each basis state can be expressed as a direct product of local state vectors

$$|k_1, k_2, \dots, k_N\rangle \equiv |k_1\rangle \otimes |k_2\rangle \otimes \dots \otimes |k_N\rangle. \quad (2.2.2)$$

The state (2.1.1) is thus expressed by the M^N amplitudes $T_{k_1, \dots, k_N} \in \mathbb{C}$. We can view T as a complex-valued rank N tensor. The dimension of each index, often called the *bond dimension* χ , is given by $\chi = M$. A fundamental problem of any numerical method to tackle a quantum-mechanical problem — e.g., finding the ground state of a Hamiltonian — is that describing a quantum state and optimizing over its components takes an exponential amount of memory. A spin chain of only fifty sites already requires $2^{50} \approx 1.126 \cdot 10^{15}$ complex numbers to store, which in the C++ type `complex<double>` corresponds to around 18 petabytes of data, slightly less than the 30 petabytes that the entire LHC experiment produces every year.⁸ When performing classical algorithms on such a gigantic state vector, even operations scaling linearly in the number of components require extreme computational resources.

A naturally occurring question is thus: Do we really *need* to be able to describe the full Hilbert space in most practical problems? If we already know certain physical properties that our quantum states have to fulfill, can we simply ignore the part of the Hilbert space that contains states irrelevant to our problem? One of the properties for which the answer appears to be yes is *area-law entanglement*. [31] Entanglement in many-body systems is often quantified by the *entanglement entropy* S_A , defined for a subdivision of the entire physical space into a subsystem A and its complement A^C . Specifically, for a total system specified by a density matrix ρ ,

$$S_A = -\text{tr}(\rho_A \log \rho_A), \quad \rho_A = \text{tr}_{A^C}(\rho), \quad (2.2.3)$$

where ρ_A is the *reduced density matrix* on the subsystem A . We say that a system's entanglement entropy follows an area law if S_A scales with the size of the boundary ∂A

⁸See <https://home.cern/resources/faqs/facts-and-figures-about-lhc>.

of A ; in particular, for an area law in $d = 1$ dimensions S_A is constant. Entanglement area laws are characteristic of ground states of Hamiltonians that are *local*, i.e. contain only coupling terms over a distance that does not grow with the total system size, and *gapped*, meaning that even in the continuum limit a separation between the ground state and the first excitation exists. As this energy gap ΔE induces an energy scale, this condition excludes scale-invariant (and by extension, conformally invariant) quantum systems.

Having identified a class of interesting states with characteristic properties, how do we restrict the Hilbert space to states than conform to these? For the case of area-law states, we clearly need a state description that encodes the (potential) entanglement entropy between subsystems, so we can discard states with large long-range entanglement. This description is afforded by *tensor networks*.

A tensor network is an ansatz for the state amplitudes T_{k_1, k_2, \dots, k_N} in (2.2.1) in terms of a *contraction* of tensors. For example, for $N = 3$ we may write

$$T_{k_1, k_2, k_3} = \sum_{j_1, j_2, j_3=1}^{\chi_j} U_{k_1, j_3, j_1} V_{k_2, j_1, j_2} W_{k_3, j_2, j_3}, \quad (2.2.4)$$

where U, V, W are rank 3 tensors and χ_j is the bond dimension (number of possible values) of the j indices. Note that this form of contraction is simply a sum over pairs of indices, and a rank r tensor an r -dimensional collection of complex numbers; there are no notions of co- and contravariance here that the words *tensor* and *contraction* imply in the context of relativistic theories. As the name suggests, tensor networks can be represented as a graph, with nodes and edges representing tensors and their indices, respectively. For example, we can represent the rank 3 tensor U as

$$U_{k, j_1, j_2} = \begin{array}{c} U \\ \bullet \\ \left. \begin{array}{l} \text{--- } j_1 \quad \text{--- } j_2 \\ | \\ k \end{array} \right\} \end{array} . \quad (2.2.5)$$

The full contraction (2.2.4) is represented graphically as

$$T_{k_1, k_2, k_3} = \begin{array}{c} \text{---} U \quad V \quad W \text{---} \\ \left. \begin{array}{l} \text{---} \bullet \quad \bullet \quad \bullet \\ | \quad | \quad | \\ k_1 \quad k_2 \quad k_3 \end{array} \right\} \end{array} , \quad (2.2.6)$$

where the contracted indices j_1, j_2, j_3 correspond to connected edges between nodes (tensors) without being labeled explicitly. The uncontracted edges are often referred to as *open legs* or *free indices*. Equivalently, a tensor of rank r is often called an r -leg tensor. The tensor labels on each node are often suppressed in larger networks for clarity.

The ansatz (2.2.4) is not a smart one: Assuming a bond dimensions χ_k for the k indices, we have expressed χ_k^3 coefficients on the left-hand side through $3\chi_k\chi_j^2$ on the

right-hand side. Unless $\chi_k > \sqrt{3}\chi_j$, the tensor network does not reduce the number of coefficients required to describe a state. However, this changes dramatically when looking at larger tensor networks. The generalization of (2.2.4)/(2.2.6) to N sites, known as a *matrix product state* (MPS)⁹, consists of a chain of N 3-leg tensors each contracted with two neighbors (excepting possible non-periodic boundary conditions). Such a tensor network describes χ_k^N coefficients by $N\chi_k\chi_j^2$ ones, thus allowing for a representation exponentially smaller in N . Of course, this means that unless χ_j is chosen to depend exponentially on N , only a subset of the full N -site Hilbert space can be reached by the MPS. Fortunately, this ansatz is sufficient to describe ground states of one-dimensional local Hamiltonians as long as they are gapped [32, 33, 34], or more generally, exhibit an exponential decay of correlations [35]. This condition leads to an area law, which is indeed reproduced with the MPS ansatz: Entanglement entropies S_A of connected subsystems A are constant in the subsystem size $|A|$.

Which tensor network geometries are needed to reproduce more complicated entanglement? To answer this question, it is necessary to understand how boundary subsystems and tensor network subregions are related. When computing a reduced density matrix ρ_A from whose spectrum entanglement entropies (and their generalization, *Rényi entropies* [36]) are gleaned, we decompose our system in two parts: A and its complement A^C . If no entanglement between both parts exist, the total state vector can be written as a tensor product of two parts in each subsystem,

$$|\psi\rangle = |\psi\rangle_A \otimes |\psi\rangle_{A^C}, \quad (2.2.7)$$

so that $\rho_A = |\psi\rangle_{A^C} \langle\psi|_{A^C}$ is pure, leading to $S_A = 0$. For a generic entangled state, we need the more general form known as the *Schmidt decomposition*

$$|\phi\rangle = \sum_k \lambda_k |\psi_k\rangle_A \otimes |\psi_k\rangle_{A^C}, \quad (2.2.8)$$

where the $|\psi_k\rangle_A$ and $|\psi_k\rangle_{A^C}$ each form an orthogonal set of state vectors on A and A^C , respectively. The number of terms in the Schmidt decomposition increases with the amount of entanglement between both subsystems: If the Schmidt values λ_k are normalized so that $\sum_k |\lambda_k|^2 = 1$, we find an entanglement entropy

$$S_A = -\sum_k |\lambda_k|^2 \log |\lambda_k|^2. \quad (2.2.9)$$

For a single term with $\lambda_1 = 1$, we recover (2.2.7) and $S_A = 0$. Given an MPS, the Schmidt decomposition for any connected subsystem A is exactly the contraction of the block of tensors associated with A with the remaining tensors, that is, the contraction over two legs (one at each endpoint of A). Thus (2.2.8) can contain at most χ_j^2 terms, where χ_j is again the bond dimension of all internal contracted legs. S_A becomes maximal

⁹The terminology becomes clear when rewriting each three-leg tensor U_{k_n, j_{n-1}, j_n} in the chain as a matrix $(U_{k_n})_{j_{n-1}, j_n}$, as the tensor contraction can then be written as $\text{tr}[U_{k_1} U_{k_2} \dots U_{k_N}]$.

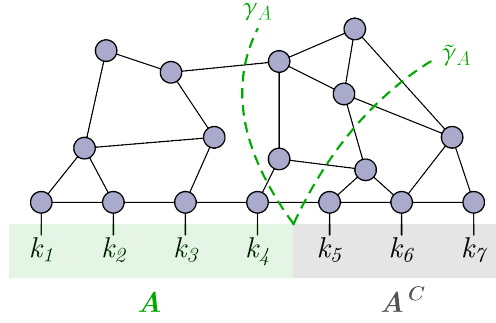


Figure 2.3: Cuts γ_A and $\tilde{\gamma}_A$ through a tensor network, with their endpoints on the boundary between the subsystem A and its complement A^C . γ_A is the minimal cut, passing through the fewest legs between tensors.

if all Schmidt values are identical, i.e., $|\lambda_k|^2 = 1/\chi_j^2$. Thus the entanglement entropy is generally bounded as

$$S_A \leq 2 \log \chi_j . \quad (2.2.10)$$

This equation can be generalized to tensor networks of arbitrary geometry: Any cut through the network ending on the boundary ∂A between A and A^C can be associated with a decomposition (2.2.8). As shown in Fig. 2.3, such a cut effectively associates two smaller tensor networks to each subsystem A and A^C . The contraction between them over the chosen cut entangles both boundary regions, with the total entanglement entropy bounded by the length of the cut. This bound is tightest for the *minimal cut* γ_A over the fewest legs. Again assuming constant bond dimension χ_j on all internal legs, we thus arrive at the well-known bound

$$S_A \leq |\gamma_A| \log \chi_j , \quad (2.2.11)$$

where $|\gamma_A|$ is the length of γ_A counted as the number of cut legs ($|\gamma_A| = 2$ for the example in Fig. 2.3). In order to describe states with more entanglement than a simple area law, it is thus necessary to increase either the bond dimension χ_j or the lengths $|\gamma_A|$ of minimal cuts through the tensor network, i.e., consider geometries more complicated than the geometry of the physical sites themselves.

A particularly interesting class of states with entanglement not following an area law is afforded by *critical* or *gapless states*, which naturally follow from systems with conformal invariance: In a system without characteristic length scale l , there also cannot exist a characteristic energy ϵ , such as $\epsilon = \hbar c/l$. In 1+1-dimensional conformal field theory, for example, the entanglement entropy of a subsystem A of length $\ell = |A|$ generally follows a logarithmic scaling [37, 38, 39]

$$S_A = \frac{c}{3} \log \frac{\ell}{a} , \quad (2.2.12)$$

where c is the central charge and a is a lattice regulator. Note that in the continuum

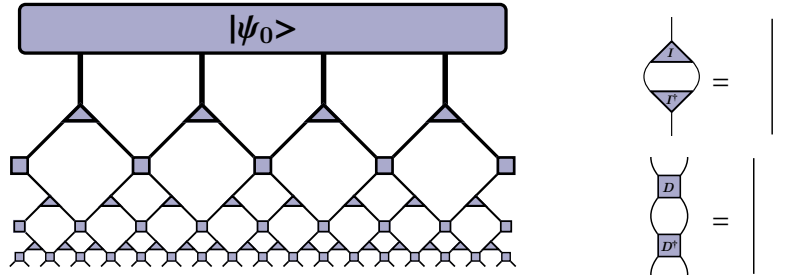


Figure 2.4: A MERA tensor network composed of isometries (triangles) and disentanglers (squares). LEFT: The full network acting on an initial coarse-grained state vector $|\psi_0\rangle$. RIGHT: Identities of the isometries and disentanglers for contractions of each tensor with its Hermitian conjugate over two legs.

limit $a \rightarrow 0$, S_A is infinite; entanglement on all scales provides contributions that diverge as infinitely small scales are included.

To reproduce states with an entanglement following (2.2.12), an MPS would require a bond dimension that scales linearly in ℓ/a and would thus fail at reproducing entanglement of sufficiently large subsystems. A more effective approach is to replace the MPS by a tensor network whose geometry automatically reproduces a relation $|\gamma_A| \propto \log \ell/a$. Such a tensor network indeed exists and is known as the *multi-scale entanglement renormalization ansatz* (MERA), first introduced by Guifr  Vidal [40]. As visualized in Fig. 2.4, it consists of two types of tensors, unitary *disentanglers* and directional *isometries*, arranged in a tree-like structure. Due to special properties of each of these two tensor types, evaluating local observables is significantly more efficient than an evaluation of the entire tensor network would be in principle. The tree-like structure ensures that a shortest cut associated with a boundary region A generally protrudes deeper into the “bulk” geometry as $|A|$ is increased, leading to the desired entanglement entropy bounds.

The MERA also has a further interesting property: It can be interpreted as an *entanglement renormalization* [41] that transforms a coarse-grained state to a fine-grained one (or vice-versa), as shown in Fig. 2.4 for a coarse-grained state $|\psi_0\rangle$. Each layer in the MERA network thus has an associated length or energy scale at which it produces entanglement in the output state.

As we will see later, these properties of the MERA are reminiscent of AdS/CFT, of which it was proposed as an early toy model [42]. The usefulness of tensor networks in understanding and modeling properties of AdS/CFT is the main motivation of a large part of the work presented in this thesis, extending beyond the tensor network approaches presented in this introduction.

Reviews for a broader introduction to tensor network methods include Refs. [43, 44, 45].

2.3 Quantum error correction

Information is susceptible to errors. Even in a purely classical system, both the storage and transmission of information — digital or analog — is affected by corruption of the physical medium carrying the information. In case of information storage, this includes corruption of bits on hard drives or SSDs, while in the case of transmission, noise in the conducting material can affect the signal from which the data is later read. As it is impossible to preclude errors completely, error correction becomes necessary. This means that information is encoded such that recovery of the logical data is still possible after small errors have occurred. The simplest way of achieving such resilience is by simply storing or transmitting multiple copies of the original data in what is called a *repetition code*. For example, one may transfer the bit sequences 000 and 111 in place of the logical bits 0 and 1. If one of the bits becomes corrupted, the remaining two still allow the reconstruction of the original logical bit (e.g. 1 from 101). Classical codes are often categorized by the notation $[n, k, d]$, which denotes an encoding of k logical bits in n physical ones, with a *Hamming distance* d . The latter is the minimal number of physical single-bit errors required to map one logical state (sequence of bits) to another. If we think of all possible physical bitstrings for a given code block as nodes in a graph, and of single-bit errors as edges connecting them, d becomes the minimal graph distance between the bitstrings corresponding to logical states, showcasing the notion of code distance. In the given notation, an n -fold repetition code for a single logical bit is denoted as an $[n, 1, n]$ code, as n physical bits need to be flipped in order to change the bitstring $00 \dots 0$ to $11 \dots 1$ and vice-versa.

Classical codes in practical use are much more complicated than simple repetition codes, but rely on the same concept of spreading out the information of logical bits over larger bitstrings. For example, the popular class of *Reed-Solomon codes* interprets k logical values as coefficients in a polynomial function whose result is mapped onto $n > k$ physical ones [46], leading to an $[n, k, n - k + 1]$ code.

The appearance of errors and methods for their correction are fundamentally different for quantum systems. When interacting with an environment, isolated quantum systems exhibit *decoherence*, i.e., the breakdown of quantum superposition and in turn, entanglement. As entanglement is a necessary resource for any quantum computation,¹⁰ its breakdown must be avoided if computational power beyond classical limits is desired.

Methods of *quantum error correction* are thus required to store and manipulate quantum information with a certain resilience to coupling with an environment. The most useful approach in classical error correction, the duplication of information, is impossible for quantum systems due to the *no-cloning theorem*: No unitary operator, and thus no physical time evolution, can duplicate an arbitrary quantum state [48, 49]. Quantum error correction thus requires other approaches. The most popular and relevant for

¹⁰Though necessary, more entanglement does not automatically make a quantum system more useful for computations. [47]

this thesis is the use of *stabilizer codes*, first introduced by Daniel Gottesman in his own PhD thesis [50], extending earlier approaches to the problem by Peter Shor and Andrew Steane [51, 52]. The idea of stabilizer codes is to encode quantum information in ground states of Hamiltonians

$$H_{\mathcal{S}} = - \sum_{i=1}^m S_i \quad (2.3.1)$$

that are given by the sum of orthogonal operators S_i , called the *generators* of the *stabilizer* $\mathcal{S} = \{S_1, S_2, \dots, S_m\}$. The generators are chosen to commute with one another and act as “parity checks” on different parts of the Hilbert space, i.e., have eigenvalues ± 1 . The space of ground states of $H_{\mathcal{S}}$, given an n -qubit system, is thus 2^{n-m} -dimensional and contains all states that are in the $+1$ -eigenspace of each generator. For qubits, it is convenient to choose stabilizer generators that are direct products of the Pauli operators $\sigma_x, \sigma_y, \sigma_z$ and the identity $\mathbb{1}$, as well as using them as a basis set for operators that represent local errors. This ensures that any product of such errors either commutes or anticommutes with each generator. The errors thus flip the eigenvalue of one or more of the generators, leading to a measured pattern or *syndrome* from which the type of error can be deduced and reversed.

Stabilizer codes are generally denoted as $[[n, k, d]]$ codes, in a generalization of the notation for classical codes introduced above. Here n and k again denote the number of physical and logical sites, respectively, usually qubits. The code distance d , however, has a slightly more nuanced meaning than the classical Hamming distance. Consider, for example, a single logical qubit encoded in a basis of states $\bar{0}$ and $\bar{1}$ (read as “logical zero” and “logical one”):

$$|\bar{\psi}\rangle = \alpha |\bar{0}\rangle + \beta |\bar{1}\rangle, \quad (2.3.2)$$

where $|\alpha|^2 + |\beta|^2 = 1$. The quantum analogon of classical bit flip errors is a basis flip $\bar{0} \leftrightarrow \bar{1}$, expressed by an operator \mathcal{O}_b that interchanges the basis as

$$\mathcal{O}_b |\bar{\psi}\rangle = \beta |\bar{0}\rangle + \alpha |\bar{1}\rangle. \quad (2.3.3)$$

Clearly this operator fulfills the condition $\mathcal{O}_b^2 = \mathbb{1}$, which followed directly from our expression of errors in terms of products of Pauli operators. However, there exists another type of error which fulfills this condition as well; these *phase flip* errors, expressed by an operator \mathcal{O}_p act on a logical qubit basis as

$$\mathcal{O}_p |\bar{\psi}\rangle = \alpha |\bar{0}\rangle - \beta |\bar{1}\rangle. \quad (2.3.4)$$

Note that this type of error maps the $\bar{0}$ basis state onto itself, but adds a phase $e^{-i\pi}$ to $\bar{1}$. This implies that when calculating the error distance d , we have to count the minimal number of fundamental error operations (local Pauli operators) that not only map logical basis states to other eigenstates of the stabilizer Hamiltonian, but also include errors that produce basis-dependent phases. Note that in a classical system, an operation of arbitrary complexity that maps each bit string to itself produces no effective error, a simplification that no longer applies for code states in a quantum superposition.

Summary 4: The 5-qubit code

The $[[5, 1, 3]]$ quantum error correcting code [54, 55] is built from the stabilizer

$$\mathcal{S}_5 = \{\sigma_x \sigma_z \sigma_z \sigma_x \mathbb{1}, \mathbb{1} \sigma_x \sigma_z \sigma_z \sigma_x, \sigma_x \mathbb{1} \sigma_x \sigma_z \sigma_z, \sigma_z \sigma_x \mathbb{1} \sigma_x \sigma_z\}. \quad (2.3.6)$$

Note that all generators are cyclic permutations of one another, and that multiplying all of them yields a fifth generator $\sigma_z \sigma_z \sigma_x \mathbb{1} \sigma_x$ that is precisely the missing permutation. This code is optimal in a variety of ways: It saturates the quantum Hamming bound [56] as well as the *quantum Singleton bound* [50], which follows from conditions on reconstructability after erasures [57] and is given by

$$n \geq 2(d-1) + k, \quad (2.3.7)$$

for an arbitrary $[[n, k, d]]$ code. The two local eigenstates $\bar{0}$ and $\bar{1}$ of the 5-qubit code can be distinguished by the total parity $\sigma_z^{\otimes 5}$, which thus acts as the logical parity operator $\bar{\sigma}_z$. Similarly, $\bar{\sigma}_x = \sigma_x^{\otimes 5}$ and $\bar{\sigma}_y = \sigma_y^{\otimes 5}$ act as the remaining logical Pauli operators. Conveniently, a *Jordan-Wigner transformation* maps $\bar{0}$ and $\bar{1}$ to fermionic states that are Gaussian, i.e., can be expressed as ground states of a Hamiltonian that is only quadratic in fermionic operators.

As in classical codes, to increase d one generally needs to increase n , the number of physical sites, as well. This is quantified by the *quantum Hamming bound* [53], which can be derived from the following argument: The full n -qubit Hilbert space can contain 2^n orthogonal states, 2^k of which are logical states. If the code distance is d , then $\lfloor \frac{d-1}{2} \rfloor$ errors can be corrected, i.e., lead to distinct orthogonal states.¹¹ There are $3n$ possible local errors, one for each physical qubit and Pauli operator, and $3^m \binom{n}{m}$ possibilities of applying exactly m non-trivial errors. As all errors applied to the logical states must be distinct and contained in the physical Hilbert space, we arrive at the following bound for an $[[n, k, d]]$ code:

$$\sum_{m=0}^{\lfloor \frac{d-1}{2} \rfloor} 3^m \binom{n}{m} \leq \frac{2^n}{2^k}. \quad (2.3.5)$$

For a single logical qubit, the quantum Hamming bound leads to the requirement of $n \geq 5$ physical sites. Indeed, a $[[5, 1, 3]]$ code that can correct an arbitrary Pauli-type error on one logical qubit exists, often simply called the “5-qubit code”. This code, which will be highly relevant throughout this work, is explained in more detail in Summary 4.

A widely used class of stabilizer codes are *Calderbank-Shor-Steane (CSS) codes* [58, 52], built from a combination of two classical codes. Each is mapped onto stabilizer generators containing, up to local identities, only σ_x or only σ_z operators, respectively, which makes it easier to realize such codes in practice; indeed, they were the first

¹¹Note that we can *detect* $d-1$ errors, but may not be able to identify the original logical state.

quantum codes to be realized experimentally [59]. Recently, *topological codes* [60] like the *surface code* [61] and the *color code* [62] have enjoyed large popularity for potential quantum error correction in large systems of qubits (see e.g. Ref. [63]). In addition, an experimental realization of the 9-qubit *Bacon-Shor code*, a *subsystem code* that extends stabilizer codes by a notion of gauge transformations [64], has recently been achieved in trapped ions [65]. However, as the codes considered in the context of holography are usually simple stabilizer codes, no more details on the fascinating subject of experimental realizations of quantum error correction will be given here.

As the general reference for all things quantum information, the book by Michael A. Nielsen and Isaac L. Chuang [66] contains a broad introduction to quantum error correction, as does chapter 7 of the lecture notes by John Preskill [67]. The previously mentioned PhD thesis by Daniel Gottesman [50] provides a more extensive introduction to the field of quantum error correction. For a more recent overview of the field, consult Refs. [68, 69].

2.4 Holography in quantum information

In recent years, viewing the AdS/CFT correspondence through the lens of quantum information theory has led to surprising connections between both fields. These “holographic” descriptions of quantum information concepts deepen our understanding of holography itself, but also offer potential approaches to problems that were not originally thought to be associated with AdS/CFT.

2.4.1 Holographic entanglement entropy

Probably the first connection between AdS/CFT and quantum information was introduced by Shinsei Ryu and Tadashi Takayanagi, when they considered the following question: What is the dual AdS_{d+1} bulk description of the entanglement entropy S_A of a boundary subsystem A in a holographic CFT_d? The answer is provided by a startling generalization of the black hole entropy formula (2.1.1) which relates the black hole entropy to its horizon area. It turns out that the bulk quantity dual to S_A is the area of a $d-1$ -dimensional minimal surface γ_A homologous to A , i.e., with $\partial A = \partial\gamma_A$ (see Fig. 2.5, left). This is quantified by the *Ryu-Takayanagi (RT) formula* [70]

$$S_A = \frac{|\gamma_A|}{4G}, \quad (2.4.1)$$

where $|\gamma_A|$ is the area of γ_A and G is the gravitational constant in the $d+1$ -dimensional bulk spacetime. Note that this formula has no dependence on the actual holographic model, e.g., the degree of supersymmetry and the bulk structure. Given an excited CFT with a dual bulk geometry other than “pure”, undeformed AdS, the shape and area of γ_A change, reflecting entanglement produced or destroyed by the excitation. For example, consider a thermal CFT, whose bulk dual is given by an AdS black hole geometry (see Fig. 2.5, right). The horizon deforms the minimal surface towards the AdS boundary,

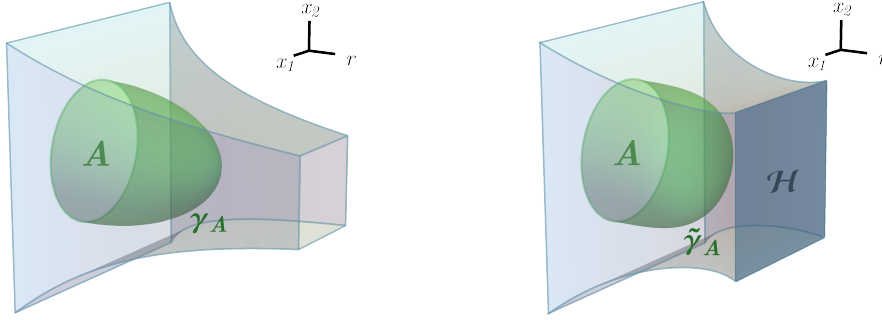


Figure 2.5: LEFT: Minimal surface γ_A homologous to a boundary region A in an AdS time-slice (blue-shaded throat region). RIGHT: Deformed minimal surface $\tilde{\gamma}_A$ in an AdS geometry with black hole horizon \mathcal{H} .

increasing its area and thus reproducing the thermal entanglement associated with a finite-temperature CFT [70]. If we start growing the subsystem A until it encompasses the entire boundary, the minimal surface starts wrapping around the black hole horizon, as this horizon is itself extremal. In that limit, (2.4.1) becomes the Bekenstein-Hawking formula (2.1.1) for the classical entropy S , showing the intimate connection between both formulae.

Strictly speaking, the definition of γ_A is only properly coordinate-independent if we restrict the boundary system to the time-slice of a static spacetime geometry. For more general space-like boundary regions A , we have to consider a space-like bulk surface γ_A that is *extremal*: It is minimal with regard to space-like variations and maximal with regard to time-like ones. This generalized form of the RT formula is often called the *Hubeny-Rangamani-Takayanagi (HRT) formula* [71].

While originally a conjecture within AdS/CFT, the RT formula was proven first for 1+1-dimensional CFTs [72, 73] and shortly afterwards for the more general case [74]. It was soon understood that (2.4.1) only holds in the AdS/CFT limit of large G (classical bulk gravity) and $N \rightarrow \infty$, where N is the rank of the gauge group $SU(N)$ of the boundary CFT, and that quantum corrections lead to additional terms constant in G and N that can be interpreted as entanglement between bulk regions [75].

For an introduction to holographic entanglement entropy, the extended version of S. Ryu and T. Takayanagi's original paper [76] is a good starting point. There also exists a book on the topic [77], a shortened version of which is available online [78].

2.4.2 Holographic tensor networks

The form of the Ryu-Takayanagi formula (2.4.1) bears a striking resemblance to the entanglement entropy bound (2.2.11) in generic tensor networks, both involving a minimal surface through a geometry that extends the direct geometry of the boundary state. This leads to a straightforward question: Can the time-slice of an AdS spacetime,

which we consider in the RT formula, be expressed as a tensor network? The first proposal in this direction was made by Brian Swingle, who suggested the MERA tensor network for this particular interpretation [42]. This identification is tempting, because the MERA implements entanglement renormalization between discretized quantum systems at different scales. Similarly, we expect a timeslice in the AdS metric (2.1.6) at fixed radius r from the AdS boundary to describe an increasingly fine-grained system as r is decreased. Furthermore, the gapless states produced by the MERA resemble those expected in the conformal boundary theories of AdS/CFT, though being ground states of much simpler critical Hamiltonians that usually feature neither supersymmetry nor non-Abelian gauge symmetries. While the MERA produces boundary states with conformal symmetries, its tensor network geometry does not exactly match an AdS time-slice — the hyperbolic *Poincaré disk* — and leads to inconsistencies when treated as such [79]. Alternatively, the MERA geometry was interpreted both as a time-like surface in positively curved de Sitter (dS) spacetime [80] and as a path integral discretization of an AdS light-like surface [81]. In either case, using the MERA as a discrete realization of AdS/CFT requires abandoning the simple time-slice picture in which the RT formula was derived, leading to a setting whose relationship to holography is not yet fully understood.

In principle, the indices of any tensor network can be separated into two sets between which it acts as a linear map on states. Clearly, labeling these two sets “bulk” and “boundary” and expecting the map to show any holographic features is pointless for most setups. Invoking the RT formula, we at minimum desire an ansatz that gives the correct entanglement entropy scaling for minimal cuts through the network. Choosing a tensor network whose geometry discretizes the Poincaré disk is not generally sufficient; we also need the entanglement entropy bound (2.2.11) to saturate for *any* choice of subsystem. The right choice of tensors is thus crucial. Surprisingly, choosing random tensors already reproduces many of the expected properties, such as polynomially decaying correlation functions, as long as the bond dimension is large [82, 83]. Rather than a mapping between individual states, such a construction considers averages of random bulk configurations, leading to a bulk partition that is in fact equivalent to the classical Ising model. Unfortunately, many of the observed holographic results break down at finite bond dimension, and even in the infinite limit, the Rényi entropies $S_A^{(n)} = \frac{1}{1-n} \log(\text{tr} \rho_A^n)$ do not reproduce the expected behavior for CFTs.

Which other choices of tensors are possible? Conditions to constrain suitable tensors, as we will see in the next section, are found by considering quantum information quantities beyond simple entanglement measures.

While a broad introduction to tensor network holography remains to be written, the initial proposal by Brian Swingle [42] contains many of the key ideas that various implementations over the past decade have been based on.

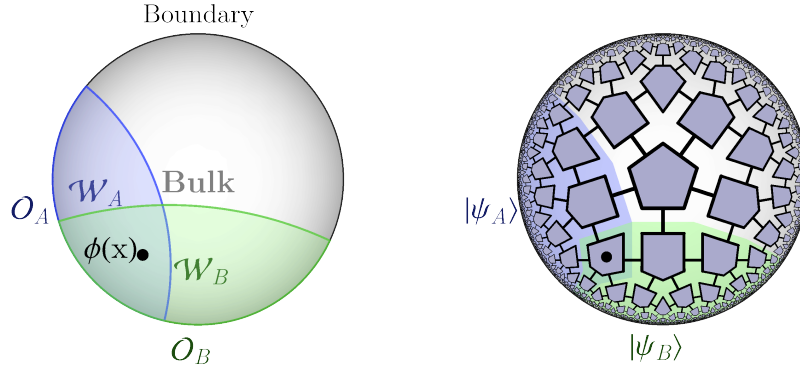


Figure 2.6: LEFT: Causal wedges \mathcal{W}_A and \mathcal{W}_B in an AdS timeslice (Poincaré disk), corresponding to two regions in which a bulk field $\phi(x)$ can be reconstructed as two operators \mathcal{O}_A and \mathcal{O}_B with support on boundary regions A and B . RIGHT: The discrete form of causal wedges in the hyperbolic pentagon code. The logical state on the marked pentagon can be reconstructed from either of the two boundary states $|\psi_A\rangle$ and $|\psi_B\rangle$.

2.4.3 Holographic quantum error correction

As a duality between bulk and boundary, AdS/CFT contains a complicated mapping of quantum information between both sides of the duality. Considering subregions of bulk or boundary, the question arises if the information encoded in local regions on one side is contained in a local region on the other side, as well. In general, this does not appear to be the case. Reconstructing a bulk field $\phi(x)$ at a point x generally requires information about a boundary region that increases in size as x is moved further into the bulk; in other words, information about fields close to the boundary can be recovered from a small boundary region, while information deep in the bulk is “smeared out” over the boundary [84]. More precisely, given a region on the boundary there exists a *causal wedge* in the bulk spacetime whose content can be reconstructed [85, 86, 87]. As different boundary regions correspond to sometimes overlapping wedges in the bulk, local bulk information can in fact be reconstructed on *different* boundary regions [88]. This leads to a conundrum: Consider, as shown in Fig. 2.6 (left), two causal wedges \mathcal{W}_A and \mathcal{W}_B containing at point x . If we can reconstruct the bulk field $\phi(x)$ in both of the corresponding boundary regions A and B , does that imply that its information is encoded in $A \cap B$? As we can choose wedges with no overlap, this cannot be correct. The only resolution to this problem — other than assuming that reconstructed operators are all trivial, acting as an identity — is to conclude that $\phi(x)$ can be represented as *different* equivalent operators on different boundary regions. Its information is thus stored redundantly, as removing parts of the boundary required for the reconstruction along one causal wedge does not prevent its recovery via another; in other words, bulk information is stored on the boundary in the manner of a quantum error-correcting code [89].

In its continuum formulation with infinitely many degrees of freedom, the code picture of AdS/CFT is difficult to treat with the language usually used in quantum information. Can we instead build a discrete toy model, based on simple quantum error-correcting codes that are already familiar to us? Such a model was indeed constructed using the previously mentioned five-qubit code, leading to the *hyperbolic pentagon code* [90]: On a regular hyperbolic discretization built from pentagons, each pentagon is identified with a $[[5, 1, 3]]$ code, with each pentagon edge identified with a physical qubit. Representing the code as a six-leg tensor that maps between the logical and physical qubits, the five “physical legs” are then contracted following the adjacency of edges in the discretized geometry. In this construction, visualized in Fig. 2.6 (right), the reconstruction along different causal wedges follows directly from the $[[5, 1, 3]]$ code’s properties: Starting from a set of uncontracted physical sites on the (asymptotic) boundary, we can reconstruct the logical states on the near-boundary pentagons from just three physical sites. Recovering the physical state on the remaining edges, we then use these as inputs on the next layer of pentagons, reconstructing their logical states in turn. Through this procedure, we gradually recover the logical states in the bulk from a boundary region, building up a discretized causal wedge until we can no longer find three physical sites around the same pentagon, i.e., until the edge of the wedge is no longer concave. This process, known as a *greedy algorithm*, can be applied to any given boundary region, the state of which is determined by all logical states within the wedge. Conversely, the logical state on a single pentagon affects all physical boundary states in subsystems whose wedges include it. The hyperbolic pentagon code thus gives a concrete mapping between bulk and boundary states with the quantum error-correcting features of AdS/CFT.

In fact, the hyperbolic pentagon code is only a special case of a large class of tensor networks with similar properties: The crucial ingredient is that of *perfect* tensors, which act as isometries between any bipartition of its indices as long as the number of output indices is at least as large as the number of input indices. Each tensor can then fine-grain a state supported on a small subset of its indices by mapping it onto the remaining ones, turning the tensor network into something akin to an omnidirectional MERA. The perfect tensors can be easily identified with *absolutely maximally entangled* states [91] and in turn, quantum error-correcting codes. These holographic toy models built from perfect tensors are popularly known as *HaPPY codes*, after the alphabetical arrangement of the initials of its creators [90]. Beyond perfect tensors, it is also possible to build similar toy models on the basis of *block-perfect* tensors, which fulfill the isometry condition only between adjacent sets of indices, allowing an implementation of *Calderbank-Shor-Steane* (CSS) codes [92].

The connection between quantum error correction and holography has only recently been established and is the subject of much ongoing research. While a formal review does not yet exist, a short introduction by Beni Yoshida, one of the original HaPPY authors, is available on Caltech’s *Quantum Frontiers* blog [93].

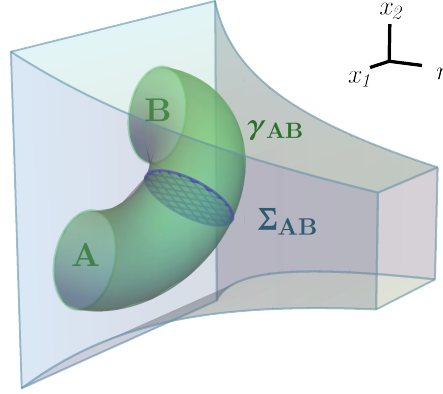


Figure 2.7: Holographic prescription of entanglement of purification E_P for a disjoint boundary region $A \cup B$: The minimal (Ryu-Takayanagi) surface γ_{AB} connects both boundary regions when A and B are close together. The area of the minimal *entanglement wedge cross-section* Σ_{AB} is conjectured to be related to the entanglement of purification via $E_P = |\Sigma_{AB}^{\min}|/4G_N$ [97].

2.4.4 Gravity and entanglement

A particularly fascinating feature of AdS/CFT is that it relates a theory with (quantum) gravity to one without it. This has led to the suggestion that gravity, whose failure at consistent quantization on arbitrarily small scales was one of the driving motivations behind the development of string theory, is indeed not a fundamental force at all, but rather holographically emergent from quantum degrees of freedom. More concretely, Mark Van Raamsdonk suggested that the connectivity between regions of spacetime could be a consequence of entanglement between them [94]: First, he interpreted an earlier setup relating a maximally entangled AdS black hole spacetime to two copies of a CFT [95] as an example of a non-entangled system being spatially separated. An entangled system, on the other hand, would be characterized by a nonvanishing *mutual information*

$$I(A : B) = S_A + S_B - S_{A \cup B} , \quad (2.4.2)$$

between two regions A and B , serving as an upper bound to two-point correlation functions between both regions [96]. In a holographic theory, where such correlators are expected to decay exponentially with geodesic distance through the bulk, an increase in entanglement would thus imply a closer spatial bulk distance.

While this conjectured connection between entanglement and the emergence of gravity remains far from understood, many similar ideas have appeared throughout the decade since its proposal. For example, a similar behavior has been found in the holographic description of quantities other than entanglement entropy. This includes *entanglement of purification*, an entanglement measure for mixed states related holographically to the minimal cross-section of the throat-like RT surface of a two-component region [97, 98] (see Fig. 2.7 for details), again relating spatial connectivity and entanglement.

Another example is the suggestion that the *complexity* of a quantum state, related to the number of local operations required to construct it from a reference state, may possess a holographic dual either in terms of a bulk volume [99] or an action evaluated on a specific bulk region [100]. The validity of either proposal is still hotly debated.

As most of these proposals are motivated around conceptual issues of quantum gravity, it may be surprising that a holographic description of gravity may have a bearing on actual qubit experiments: It was proposed that certain experimental setups for *quantum teleportation*, the transmission of quantum states via entanglement, may be effectively described by a holographic construction involving traversable wormholes [101]. Though no such experiments have yet been conducted, this emphasizes the potential of bridging the fields of quantum computation and fundamental physics.

Many of the early ideas of connecting gravity and entanglement are surveyed in Mark Van Raamsdonk's lecture notes on the same topic [102].

Chapter 3

Roads to holography

3.1 Gravitational approaches

As we have seen in the last chapter, the AdS/CFT correspondence has produced many surprising connections between physical systems that seem quite unconnected at first glance. Commonly, the resulting dualities are useful in one particular direction: Rather than performing computations for strongly interacting quantum field theories, a fairly painful exercise even under the restriction of conformal symmetry, we can carry out conjecturally equivalent calculations in a system of (super)gravity. Gravity is inherently weakly coupled, meaning that small additions of masses and energy to a given spacetime create perturbatively tractable deformations. Thus, even when closed analytical solutions to a dual gravitational setup are not feasible, efficient numerics are in principle possible.

This is especially apparent in the holographic descriptions of entanglement and complexity, which become a problem of extremizing various bulk hypersurfaces on a given spacetime background. The measure explored in the first paper of the cumulative part of this thesis, holographic entanglement entropy, requires the extremal surface computation of the RT/HRT prescription discussed in Sec. 2.4.1. While the computation of such surfaces is clearly amenable to variational methods, we will see that the construction of proper numerical algorithms for this task is still a strenuous exercise. The main obstacle is that surface optimization, which commonly appears in various engineering problems as well as in certain corners of pure mathematics, is not usually applied onto *spacetime* surfaces. This requires the introduction of completely new algorithms taking into account, for example, the nontrivial constraints on the parameter space of solutions placed by the requirement that surfaces be space-like.

Fortunately, analytical techniques already yield many fascinating results from holographic descriptions of entanglement, such as the recent (partial) resolution of the black hole information paradox [103, 104]. Yet, to harness the full power of holographic

methods to achieve an understanding of complicated strongly interacting systems will inevitably require the introduction of increasingly complex numerical approaches. This is especially true for systems with complicated time dependence, where a closed-form expression of the bulk metric may not even exist, requiring numerical lattice approximations of the spacetime itself.

Alternatively, one may attempt to understand the boundary system by using numerical approximations to tackle strongly coupled conformal field theory. In combination with results from the gravitational side, this would also clarify the exact scope of the AdS/CFT correspondence. In the next section, the usefulness of tensor network approaches to this problem will be discussed, including the assumptions necessary for efficient computational realizations.

3.2 Tensor network approaches

Why is the construction of finite-dimensional models of holography, particularly using tensor networks, a worthwhile endeavor? In its continuum formulation, AdS/CFT has shed light on remarkable connections between theories of weak and strong coupling, between those containing gravitational and quantum degrees of freedom, and even between models in different dimensions; as such, its potential for relating complicated theories whose dynamics are yet to be understood to those that are more tractable is tantalizing. Unfortunately, the specific AdS/CFT setups of whose validity we are most certain are also, in some sense, the least practical. While supersymmetry, for example, provides a mathematically elegant simplification to theories of quantum fields and strings, most practical physical systems that we would like to better understand are far from supersymmetrical. The large N limit and conformal symmetry of the boundary gauge theory pose a similar constraint; for example, the strongly interacting low-energy regime of quantum chromodynamics (with $N = 3$ and without conformal symmetry) should not be expected to be describable with AdS/CFT beyond rough approximations.

These constraints, however, may be less of a problem of the holographic principle itself than of the specific setup that AdS/CFT provides. As we have already seen in the formulation of holographic entanglement entropy in the Ryu-Takayanagi formula, many aspects of Juan Maldacena's original proposal seem to become irrelevant as we consider holography through the lens of quantum information. Perhaps a generalization of AdS/CFT, constructed with tools outside of superstring theory, can pave the way to more general dualities? The fundamental challenge in finding such a generalization is the virtuousness of AdS/CFT itself: One side of the duality is always hard to compute in each regime, be it strongly interacting conformal field theory or full quantum gravity. While this allows for a convenient shortcut to this hard theory via its more manageable dual partner, this complicates finding generalizations, whose confirmation requires a detailed understanding of the dynamics of the related theories.

Tensor networks provide a possible path to addressing these issues. They are the lan-

guage of choice for describing physical systems in terms of their entanglement structure and allow efficient computations of a range of properties of finite-dimensional system, easily integrating many useful concepts of quantum information theory. They also appear to reproduce some of the features of AdS/CFT in a range of different models, serving as a useful toolbox to test complicated holographic properties in a well-understood setting. It thus appears reasonable to use tensor networks to understand if and how holography manifests itself in simple quantum systems.

The two new tensor network models introduced in the second and third publication contained in this thesis, built upon fermionic matchgate tensors and Majorana dimers, respectively, rely on the significant simplification of *Gaussianity*. Generic tensor network techniques require a representation of the boundary state in its full Hilbert space — as mentioned in Sec. 2.2, this is unfeasible for more than a few dozen spin sites even with supercomputers. Studying tensor networks with arbitrary geometries thus requires the restriction to a subset of tensors that allows for a more efficient representation. The tensors considered in this thesis furnish such a representation by describing *Gaussian states*. These states can be defined in several different ways that are all equivalent: In particular, they are ground states of non-interacting (or “free”) Hamiltonians that contain only terms quadratic in the fundamental bosonic or fermionic operators. Equivalently, their $2n$ -point correlation functions for $n > 1$ can be expressed by applying *Wick’s theorem* [105] of summing over all combinations of two-point correlators. For example, a four-point function of a fermionic field ψ evaluated at different points x_k would follow the structure

$$\langle \psi_1 \psi_2 \psi_3 \psi_4 \rangle = \langle \psi_1 \psi_2 \rangle \langle \psi_3 \psi_4 \rangle - \langle \psi_1 \psi_3 \rangle \langle \psi_2 \psi_4 \rangle + \langle \psi_1 \psi_4 \rangle \langle \psi_2 \psi_3 \rangle, \quad (3.2.1)$$

writing $\psi_k \equiv \psi(x_k)$. Note the change of signs due to reordering of the anti-commuting field. In terms of Feynman diagrams, the theory only contains propagators but no interaction vertices. The application of Wick’s theorem implies that two-point correlations, often written as a *covariance matrix*, completely determine all correlation functions up to a suitable definition of the vacuum.¹ As we will see, Gaussian states can be represented in forms other than their state vector in the full Hilbert space, essentially by defining quantities that contain the same information as the covariance matrix. By expressing tensor contraction in this language, the study of large tensor networks becomes feasible within the Gaussian constraint.

Of course, the accessibility of a certain class of tensor networks to efficient studies does not necessarily imply that it is useful for building holographic models. On the contrary, the strong/weak coupling duality inherent to AdS/CFT may suggest that a framework that only covers non-interacting states should be far from holographic. Fortunately, early constructions already showed that many features of AdS/CFT appear in non-interacting bulk models, as well. In particular, consider the problem of reconstructing expectation values of bulk fields from those of boundary operators. In the AdS/CFT limit where

¹In order to force all n -point correlations for odd n to vanish, we can add a source term, linear in the fundamental operators, to the vacuum.

both N and Ng_{YM}^2 are large, the boundary $SU(N)$ field theory is strongly coupled, while the boundary can be described by semiclassical gravity. In this pure AdS background, we can define a simple model involving only a non-interacting scalar field $\phi(x)$, whose equation of motion is simply

$$(\square - m^2)\phi = 0, \quad (3.2.2)$$

where $\square = g^{\mu\nu}\partial_\mu\partial_\nu$ is the d'Alembert operator for the AdS metric $g^{\mu\nu}$. The Green's function $G(x, x')$ for (3.2.2) can then be used to compute the bulk field uniquely from the its boundary values. Splitting the coordinate x into a bulk radial direction r (with the AdS boundary at $r \rightarrow 0$) and the remaining boundary coordinates \tilde{x} , the bulk field is then given by convolving the boundary values with G over the bulk [22],

$$\phi(\tilde{x}, r) = \int d\tilde{x}' G(\tilde{x}, \tilde{x}', r, r' \rightarrow 0) \tilde{\phi}(x'). \quad (3.2.3)$$

Here we defined the boundary field $\tilde{\phi}(x) = \phi(x, r \rightarrow 0)$. Correspondingly, correlation functions between bulk points are given by convolving over boundary correlation functions, i.e., those of the boundary CFT, while preserving causality within the AdS space-time [106, 84]. Both for simple scalar fields and $\mathcal{N} = 4$ super-Yang-Mills theory at large N , two- and three-point functions match between direct CFT computations at small coupling and the holographic computation at large coupling [107, 108]. Thus we see that CFT dynamics are well described by holographic models at a large range of interaction strengths.

It is therefore not entirely unreasonable to hope that a suitable non-interacting tensor network ansatz may reproduce features of AdS/CFT. Indeed, this is in alignment with the central notion of the strong/weak coupling duality; bulk dynamics ought to be simpler in their underlying physical description than a generic physical system in the same number of dimensions. Previous work with the MERA tensor network in this direction is encouraging: It can be used as an *exact holographic mapping* that relates non-interacting bulk and boundary states [109, 110], and the RG flow of free fermions can be understood in terms of an exact model of *wavelets* [111].

Given an efficiently computable class of tensor networks, the question of choosing suitable network geometries remains. Starting with the most symmetrical models, the tensor networks that are a primary focus of this thesis follow a *regular* bulk geometry, a setup popularized by the hyperbolic pentagon code model [90]. Unlike the MERA and its generalizations, these geometries have no inherent directionality, reproducing the isotropy of an AdS time-slice, i.e., the hyperbolic Poincaré disk. Though these hyperbolic tessellations appear as a natural choice for holographic tensor network models, they lack one assumption that underlies the MERA: The evaluation of expectation values of local operators is no longer simplified by a *causal cone* within the network.² That means that instead of evaluating a small region of the tensor network that scales with the support of the operator, we generally need to evaluate the entire network. While

²However, a more involved construction on regular tilings, called *hyperinvariant MERA*, attempts to reconcile both approaches [112].

computationally challenging, this property is quite natural given the causal structure of AdS/CFT: If the tensor network is a discrete representation of a time-slice, then correlations between space-like separated points should not exhibit a causal cone, rather decaying exponentially with bulk distance.

Embedding a tensor network into regular hyperbolic tilings yields generic properties that can be derived without using the Gaussian approximation. As will be shown in the fourth paper of this thesis, fixing the *inflation* process by which the discrete geometry is iteratively constructed also bounds the entanglement scaling that boundary states can exhibit. This also bounds the maximal central charge c that a critical theory expressed by such a model can possess. To produce ground states of these models, we further assume that the choice of tensors respects the symmetries of the geometry, i.e., that the tensors are invariant under cyclic index permutation, leading to a bulk configuration resembling an isotropic, “pure” AdS geometry without massive deformations, which we would consider as the bulk dual of CFT ground states in continuum AdS/CFT. Under this assumption the same technical approach that led to central charge bounds now fixes the entanglement scaling and c exactly. As is shown in the fourth paper, the bounds can indeed be saturated by the Majorana dimer model, introduced in the third paper, assuming certain limits. The resulting aperiodic symmetries lead to surprising connections to models that are widely studied in condensed matter applications, giving yet another example of the many connections between subfields engendered by holographic tensor network methods.

3.3 Publication overview

While we so far discussed the general background and motivation to the four publications comprising this cumulative dissertation, this section contains a summary of the core content of each publication to serve as a reading guide. The actual papers are included in the next chapter, sorted by the order of publication.

A. Jahn, T. Takayanagi,

“Holographic Entanglement Entropy of Local Quenches in AdS_4/CFT_3 :

A Finite-Element Approach”

A simple dynamical AdS/CFT model describing local quenches, i.e., local excitations that can be modeled by a Hamiltonian with sudden time dependence, can be constructed by adding a free-falling mass into a pure AdS background geometry. Studying the entanglement entropy induced by this excitation holographically requires the computation of extremal surfaces that becomes analytically challenging in more than 2+1 bulk dimensions. Extending a numerical finite-element approach originally developed in my Master’s thesis, we compute 3+1-dimensional extremal surfaces that correspond to different quench masses and times. For small masses (and dual operator dimensions in the boundary CFT), the results match predictions from the “first law of entanglement

entropy” relating energy density and entanglement entropy. For large masses, numerics show dominant contributions arising from the horizon region, allowing for a generalization to arbitrary dimensions. While the numerical approach cannot be extended to arbitrarily large times after the quench, results suggest deviations from the simple logarithmic time dependence that is quickly reached in the $\text{AdS}_3/\text{CFT}_2$ setup.

*A. Jahn, M. Gluza, F. Pastawski and J. Eisert,
“Holography and criticality in matchgate tensor networks”*

In this paper we initiate a program of investigating generic holographic properties of Gaussian tensor networks using the formalism of *matchgate tensors*. We consider three distinct tensor network geometries: Regular flat tilings, regular hyperbolic tilings, and the MERA geometry. Within the constrained parameter space of bond dimension $\chi = 2$ matchgate tensor networks, the MERA yields translation-invariant critical states, identified with the critical Ising model at central charge $c = 1/2$. Regular hyperbolic tilings lead to boundary states that break translation invariance, but still possess algebraic decay of correlations over the entire parameter space accessible to our matchgate ansatz. We find a special point in this parameter space leading to boundary states with average correlations that, like the MERA, match the $c = 1/2$ critical Ising model. Surprisingly, while flat tilings usually produce exponentially decaying correlations — indicative of gapped, non-critical states — there again exists a special point in their parameter space that leads to average correlations of the critical Ising model. This suggests the existence of a class of tensor networks encoding critical theories that is independent of the network’s curvature.

*A. Jahn, M. Gluza, F. Pastawski and J. Eisert,
“Majorana dimers and holographic quantum error-correcting codes”*

This work establishes a formalism for a class of Gaussian fermionic states characterized by paired Majorana modes, called *Majorana dimers*. We show how tensors representing these states can be contracted by applying a set of simple graphical rules. The resulting tensor networks are thus even easier to contract than the matchgate tensor networks they are a subclass of, and many of their properties can be calculated from geometric features of the connected dimers rather than requiring any numerical contraction algorithm. Having established the theoretical machinery for Majorana dimer tensor network, we then show that these contain the hyperbolic pentagon code (HyPeC) as long as its bulk qubits are fixed to logical basis states. The dimer structure of the resulting boundary states retains the discrete hyperbolic geometry of the bulk, leading to entanglement entropies and correlation decay as expected from a critical theory. These results are shown to extend beyond the basis state restriction on bulk qubits, thus providing new details on HyPeC boundary states previously inaccessible due to the computational difficulties of contracting large non-Gaussian tensor networks. The results also lead to interesting new connections between quantum error correction,

hyperbolic tensor network models, and the *bit thread* model of holographic states as an optimal bulk flow of entangled boundary qubits.

A. Jahn, Z. Zimborás and J. Eisert,
“Central charges of aperiodic holographic tensor network models”

Beyond the behavior of individual tensor network models of AdS/CFT, this paper derives general properties of boundary states produced by tensor networks with the geometry of regular hyperbolic tilings. In particular, it is shown that analogously to continuum AdS/CFT, bulk and boundary symmetries can be directly related, describing the critical boundary theory, e.g. its central charge, in terms of geometric bulk quantities. Making no assumptions on the actual tensor content, effective central charges can be upper-bounded in the regular hyperbolic tensor network setup, with a bound closely resembling its continuum version, the *Brown-Henneaux formula*. We then demonstrate that these bounds can be saturated, using the Majorana dimer state description of the HyPeC, as well as generalizations on other hyperbolic tilings introduced in the previous publication. Interestingly, the RG behavior of the HyPeC can be treated analytically, leading to an appearance of criticality closely resembling *strongly disordered* systems, such as the *Fibonacci XXZ chain*. This result is particularly interesting because it relates the HyPeC, a model of holographic quantum error correction, to a well-understood class of critical systems.

Chapter 4

Publications

This chapter contains the following published articles in their original format.

- A. Jahn and T. Takayanagi,
“Holographic Entanglement Entropy of Local Quenches in AdS_4/CFT_3 : A Finite-Element Approach,”
J. Phys. A **51** (2018) Iss. 1, 015401.
This article is not reproduced electronically as IOP publishing has not licensed online sharing of the Version of Record, which is available as:
DOI: 10.1088/1751-8121/aa8afa
- A. Jahn, M. Gluza, F. Pastawski, and J. Eisert,
“Holography and criticality in matchgate tensor networks,”
Science Advances **5**, eaaw0092 (2019).
This article is reproduced electronically under the Creative Commons Attribution-NonCommercial 4.0 International license. The published version is available as:
DOI: 10.1126/sciadv.aaw0092
- A. Jahn, M. Gluza, F. Pastawski, and J. Eisert,
“Majorana dimers and holographic quantum error-correcting codes,”
Phys. Rev. Research. **1** (2019), Iss. 3, 033079.
This article is reproduced electronically under the Creative Commons Attribution 4.0 International license. The published version is available as:
DOI: 10.1103/PhysRevResearch.1.033079
- A. Jahn, Z. Zimborás, and J. Eisert,
“Central charges of aperiodic holographic tensor network models,”
Phys. Rev. A **102** (2020), 042407.
This article is reproduced electronically under a Reuse and Permissions License by the American Physical Society. The published version is available as:
DOI: 10.1103/PhysRevA.102.042407

PHYSICS

Holography and criticality in matchgate tensor networks

A. Jahn^{1*}, M. Gluza¹, F. Pastawski¹, J. Eisert^{1,2,3}

The AdS/CFT correspondence conjectures a holographic duality between gravity in a bulk space and a critical quantum field theory on its boundary. Tensor networks have come to provide toy models to understand these bulk-boundary correspondences, shedding light on connections between geometry and entanglement. We introduce a versatile and efficient framework for studying tensor networks, extending previous tools for Gaussian matchgate tensors in 1 + 1 dimensions. Using regular bulk tilings, we show that the critical Ising theory can be realized on the boundary of both flat and hyperbolic bulk lattices, obtaining highly accurate critical data. Within our framework, we also produce translation-invariant critical states by an efficiently contractible tensor network with the geometry of the multiscale entanglement renormalization ansatz. Furthermore, we establish a link between holographic quantum error-correcting codes and tensor networks. This work is expected to stimulate a more comprehensive study of tensor network models capturing bulk-boundary correspondences.

INTRODUCTION

The notion of holography in the context of bulk-boundary dualities, most famously expressed through the anti-de Sitter space/conformal field theory (AdS/CFT) correspondence (1), has had an enormously stimulating effect on recent developments in theoretical physics. A key feature of these dualities is the relationship between bulk geometry and boundary entanglement entropies (2–4), prominently elucidated by the Ryu-Takayanagi formula (5). Because of the importance of entanglement in the context of AdS/CFT (6), it was quickly realized that tensor networks are ideally suited for constructing holographic toy models, most notably the multiscale entanglement renormalization ansatz (MERA) (7–9). The realization that quantum error correction could be realized by a holographic duality (10) further connected to ideas from quantum information theory. Despite the successful construction of several tensor network models that reproduce various aspects of AdS/CFT [see, e.g., (11–13)], a general understanding of the features and limits of tensor network holography is still lacking. Particular obstacles are the potentially large parameter spaces of tensor networks and the considerable computational cost of contraction.

In this work, we overcome some of these challenges by applying highly efficient contraction techniques developed for matchgate tensors (14, 15), which replace tensor contraction by a Grassmann-variate integration scheme. These techniques allow us to comprehensively study the interplay of geometry and correlations in Gaussian fermionic tensor networks in a versatile fashion, incorporating toy models for quantum error correction and tensor network approaches for CFT, such as the MERA, into a single framework, highlighting the connections between them. Furthermore, this framework includes highly symmetrical tensor networks based on regular tilings (see Fig. 1, A and B). We are thus in a position to efficiently probe the full space of Gaussian bulk-boundary correspondences from a small set of parameters, including the bulk curvature. We show that matchgate tensor networks with a variety of bulk geometries contain the Ising CFT in their parameter space to remarkably good approximation as a special

case, with properties similar to the wavelet MERA model (16, 17). While regular hyperbolic tilings have recently been considered as a MERA alternative (18), we show that flat tilings can lead to very similar boundary states. In our studies, we restrict ourselves to tensor networks that are nonunitary and real, resembling a Euclidean evolution from bulk to boundary. In particular, we do not require the causal constraints of the MERA for efficient contraction, thus providing new approaches in the context of tensor network renormalization (19, 20). While we provide substantial evidence that tensor networks are capable of describing bulk-boundary correspondences beyond known models and introduce a framework for their study, our work is by no means exhaustive. We do hope to provide a starting point for more systematic studies of holography in tensor networks.

MATERIALS AND METHODS

We constructed two-dimensional planar tensor networks with fermionic bulk and boundary degrees of freedom. The bulk degrees of freedom are associated with a set V of vertices of a tensor network. At each vertex, $v \in V$, a local tensor T_v with k_v indices is placed, which can be interpreted as a local fermionic state on k_v sites. After contraction over all connected bulk indices, the L remaining open indices are interpreted as boundary sites with the boundary state specified by the full contracted tensor. Because of the planarity of the network, the boundary sites form a loop. The bulk geometry can be flat or negatively curved (a positively curved network closes in on itself after finite distance). We visualized our tensor networks by representing each tensor T_v as a k_v -gon whose edges correspond to indices. Thus, the tensor network is represented by a polygon tiling, which determines the bulk geometry. Adjacent edges between two polygons correspond to contracted indices and boundary edges to open ones. See Fig. 1 for examples.

Concretely, each bulk degree of freedom $v \in V$ is associated with a local tensor $T_v : \{0,1\}^{x_r} \rightarrow \mathbb{C}$ of tensor rank r (equal to the number of edges of the corresponding tile), all of which are contracted to form tensors of higher rank. We denote the tensor component at indices $j \in \{0,1\}^{x_r}$ as $T_v(j)$ and the standard computational basis for r boundary spins as $|j\rangle := \otimes_{k=1}^r |j_k\rangle$. Each tensor is then equivalent to a state vector

$$|\psi_v\rangle = \sum_{j \in \{0,1\}^{x_r}} T_v(j) |j\rangle \quad (1)$$

¹Dahlem Center for Complex Quantum Systems, Freie Universität Berlin, 14195 Berlin, Germany. ²Helmholtz-Zentrum Berlin für Materialien und Energie, 14109 Berlin, Germany. ³Department of Mathematics and Computer Science, Freie Universität Berlin, 14195 Berlin, Germany.

*Corresponding author. Email: ajahn@fu-berlin.de

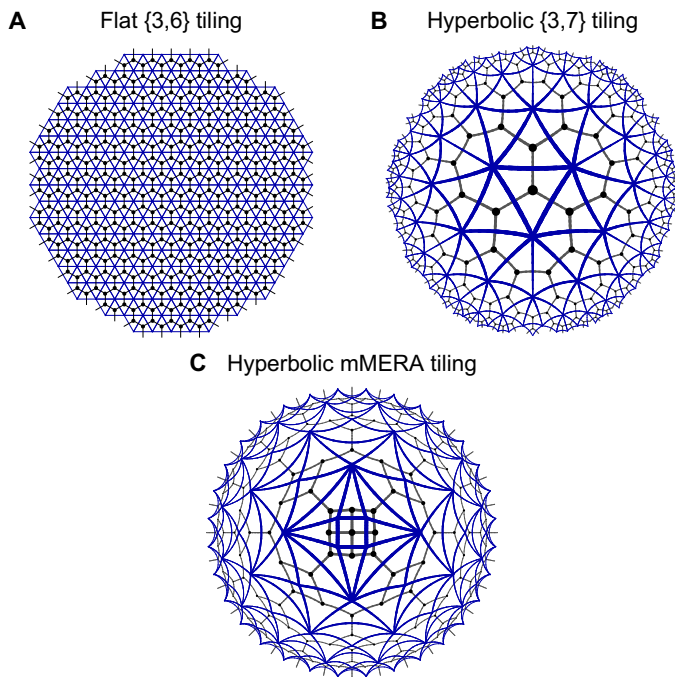


Fig. 1. Geometries of tensor networks. Discretizations of flat (A) and hyperbolic space (B and C) with a triangular tiling (blue edges), into which a tensor network is embedded (black lattice). In the matchgate formalism, joint edges between triangles correspond to an integration over a pair of Grassmann numbers, analogous to tensor network contraction over indices. While (A) and (B) show regular tilings, (C) presents a nonregular MERA-like tiling we call the matchgate MERA (mMERA).

For a broader introduction to tensor networks and their contractions, see (21–24).

Instead of explicit tensor contraction along pairs of indices, we used the formalism from (15) using Grassmann integration. Any tensor T can be represented by a Grassmann-variate characteristic function

$$\Phi_T(\theta) = \sum_{j \in \{0,1\}^{\times r}} T(j) \theta_1^{j_1} \theta_2^{j_2} \dots \theta_r^{j_r} \quad (2)$$

where the θ_k are Grassmann numbers defined by the anticommutation relation $\theta_k \theta_l + \theta_l \theta_k = 0$. The contraction $T_1 *_2$ of two tensors T_1 and T_2 (of rank r_1 and r_2 , respectively) over the last index of T_1 and the first index of T_2 is given by

$$T_1 *_2(x, y) = \sum_{z \in \{0,1\}} T_1(x, z) T_2(z, y) \quad (3)$$

where $x \in \{0,1\}^{\times(r_1-1)}$, $y \in \{0,1\}^{\times(r_2-1)}$. $T_1 *_2$ has rank $r_1 + r_2 - 2$. The characteristic function of the contraction is obtained as

$$\Phi_{T_1 *_2}(\xi) = \int d\eta_1 \int d\theta_{r_1} \Phi_{T_1}(\theta) \Phi_{T_2}(\eta) \exp(\theta_{r_1} \eta_1) \quad (4)$$

where we used $\xi = (\theta_1, \dots, \theta_{r_1-1}, \eta_2, \dots, \eta_{r_2})$ and $\int d\eta_1 \int d\theta_{r_1}$ denotes Grassmann integrals, anticommuting multilinear functionals obeying $\int d\xi_j \xi_j^{z_j} = \delta_{z_j,1}$ [see (15, 25–27) for more details]. A self-contained derivation of the equivalence of (4) with tensor contraction, as well as a note on iterated integrals, is given in the Supplementary Materials. Anticommutativity requires an appropriate labeling of all Grassmann

variables, but such a labeling can always be found for contractions of planar networks (15). These Grassmann integrations are particularly efficient to compute for the case of matchgate tensors, where their computation scales polynomially in the number of tensor indices.

Consider a rank r tensor $T(x)$ with inputs $x \in \{0,1\}^{\times r}$. One calls $T(x)$ a matchgate if there exists an antisymmetric matrix $A \in \mathbb{C}^{r \times r}$ and a $z \in \{0,1\}^{\times r}$ so that one can write

$$T(x) = \text{Pf}(A_{|x \text{ XOR } z}) T(z) \quad (5)$$

where $\text{Pf}(A)$ is the Pfaffian of A and $A_{|x}$ is the principal submatrix of A acting on the subspace supported by x . Furthermore, one calls $T(x)$ an even tensor if $T(x) = 0$ for any x with odd $\sum_j x_j$.

A generic even matchgate has a simple Gaussian characteristic function of the form

$$\Phi_T(\theta) = T(0) \exp\left(\frac{1}{2} \sum_{j,k=1}^r A_{j,k} \theta_j \theta_k\right) \quad (6)$$

where $T(0)$, the tensor component for all-zero input, acts as a normalization factor. Apart from normalization, the full tensor is completely determined by A , which we therefore call the generating matrix. Thus, the rules for contracting matchgate tensors can be written as rules for combining generating matrices. Full derivations of these, including the calculation of physical covariance matrices from the generating matrices, are provided in the Supplementary Materials. With our contraction rules, the computational cost of contracting two tensors is quadratic in the number of indices of the final tensor. Thus, we could bound the total computational cost for contracting an entire network of the type considered here by $O(L^2 N)$, where L is the number of boundary sites and N is the number of contracted tensors [for similar bounds on matchgate contraction, see (15)].

Using Pauli matrices σ^α with $\alpha \in \{x, y, z\}$, one can define Majorana operators γ_i via the Jordan-Wigner transformation

$$\gamma_{2k-1} = (\sigma^z)^{\otimes(k-1)} \otimes \sigma^x \otimes (\mathbb{1}_2)^{\otimes(r-k)} \quad (7)$$

$$\gamma_{2k} = (\sigma^z)^{\otimes(k-1)} \otimes \sigma^y \otimes (\mathbb{1}_2)^{\otimes(r-k)} \quad (8)$$

The computational basis is then equivalent to an occupational basis. In this context, we proved that any fermionic Gaussian state vector in the form of Eq. 1 has coefficients $T(j)$ constituting a matchgate tensor. For details on this proof, refer to the Supplementary Materials. The converse statement is also true, providing a further perspective on the connection to free fermions (28).

RESULTS

The holographic pentagon code

We will now apply our framework to the highly symmetric class of regular bulk tilings, first implementing the holographic error correcting code (HaPPY code) proposed in (12) and then exploiting the versatility of our framework to extend it toward more physical setups. The HaPPY code furnishes a mapping between additional (uncontracted) bulk degrees of freedom on each tensor and the boundary state, realized by a bulk tiling of pentagons. Each pentagon tile encodes

one fault-tolerant logical qubit via the encoding isometry of the five-qubit code. This $[[5,1,3]]$ quantum error-correcting code (29) saturates both the quantum Hamming bound (30, 31) and the singleton bound (31) and can be expressed as a stabilizer code (32).

We observe that fixing the bulk degrees of freedom to computational basis states gives rise to a matchgate tensor network, as the logical computational basis states of the holographic pentagon code can be viewed as ground states of a quadratic fermionic Hamiltonian. This can be seen directly by applying Eqs. 7 and 8 onto the stabilizers S_k of the underlying $[[5,1,3]]$ code, thus expressing it in terms of Majorana operators γ_i and a total parity operator $\mathcal{P}_{\text{tot}} = (\sigma^z)^{\otimes 5}$ as

$$\begin{aligned} S_1 &= \sigma^x \otimes \sigma^z \otimes \sigma^z \otimes \sigma^x \otimes 1_2 = i\gamma_7\gamma_2 \\ S_2 &= 1_2 \otimes \sigma^x \otimes \sigma^z \otimes \sigma^z \otimes \sigma^x = i\gamma_9\gamma_4 \\ S_3 &= \sigma^x \otimes 1_2 \otimes \sigma^x \otimes \sigma^z \otimes \sigma^z = i\mathcal{P}_{\text{tot}}\gamma_6\gamma_1 \\ S_4 &= \sigma^z \otimes \sigma^x \otimes 1_2 \otimes \sigma^x \otimes \sigma^z = i\mathcal{P}_{\text{tot}}\gamma_8\gamma_3 \\ S_5 &= \sigma^z \otimes \sigma^z \otimes \sigma^x \otimes 1_2 \otimes \sigma^x = i\mathcal{P}_{\text{tot}}\gamma_{10}\gamma_5 \end{aligned} \quad (9)$$

As the corresponding stabilizer Hamiltonian is given by $H = -\sum_{k=1}^5 S_k$, we find a doubly degenerate ground state whose degeneracy is lifted by the parity operator \mathcal{P}_{tot} . The resulting two states with parity eigenvalues ± 1 correspond to the logical eigenstates $|\bar{0}\rangle$ and $|\bar{1}\rangle$, which are themselves ground states of purely quadratic Hamiltonians with different parity factors. Thus, both computational basis states are pure Gaussian, leading us to the conclusion that for fixed computa-

tional input in the bulk, the holographic pentagon code yields a matchgate tensor on the boundary (see Fig. 2). The explicit construction is given in the Supplementary Materials. Using the Schläfli symbol $\{p, q\}$, where p is the number of edges per polygon and q is the number of polygons around each corner, we can specify the hyperbolic geometry of the HaPPY model as a regular $\{5, 4\}$ tiling.

We find that the correlation structure of this model is best captured in the Majorana picture. Explicitly, consider the pentagon tiling of (12) with all bulk inputs set to the positive-parity eigenvector $|\bar{0}\rangle$. The entries of the Majorana covariance matrix $\Gamma_{j,k} = \frac{1}{2}\langle \psi | [\gamma_j, \gamma_k] | \psi \rangle$ resulting from successive contraction steps are shown in Fig. 3 (A to C). As

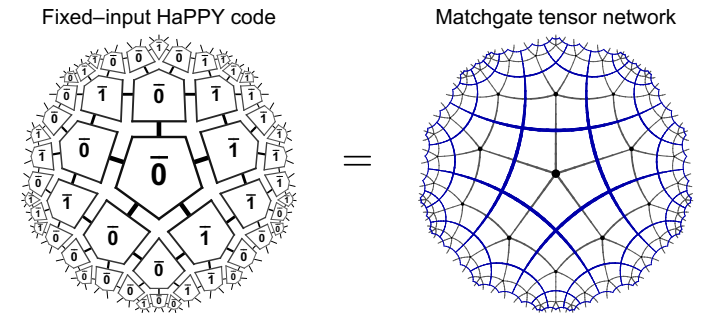


Fig. 2. HaPPY/matchgate equivalence. The holographic pentagon code of the HaPPY model for fixed computational bulk input (left) is equal to a matchgate tensor network on a hyperbolic pentagon tiling (right).

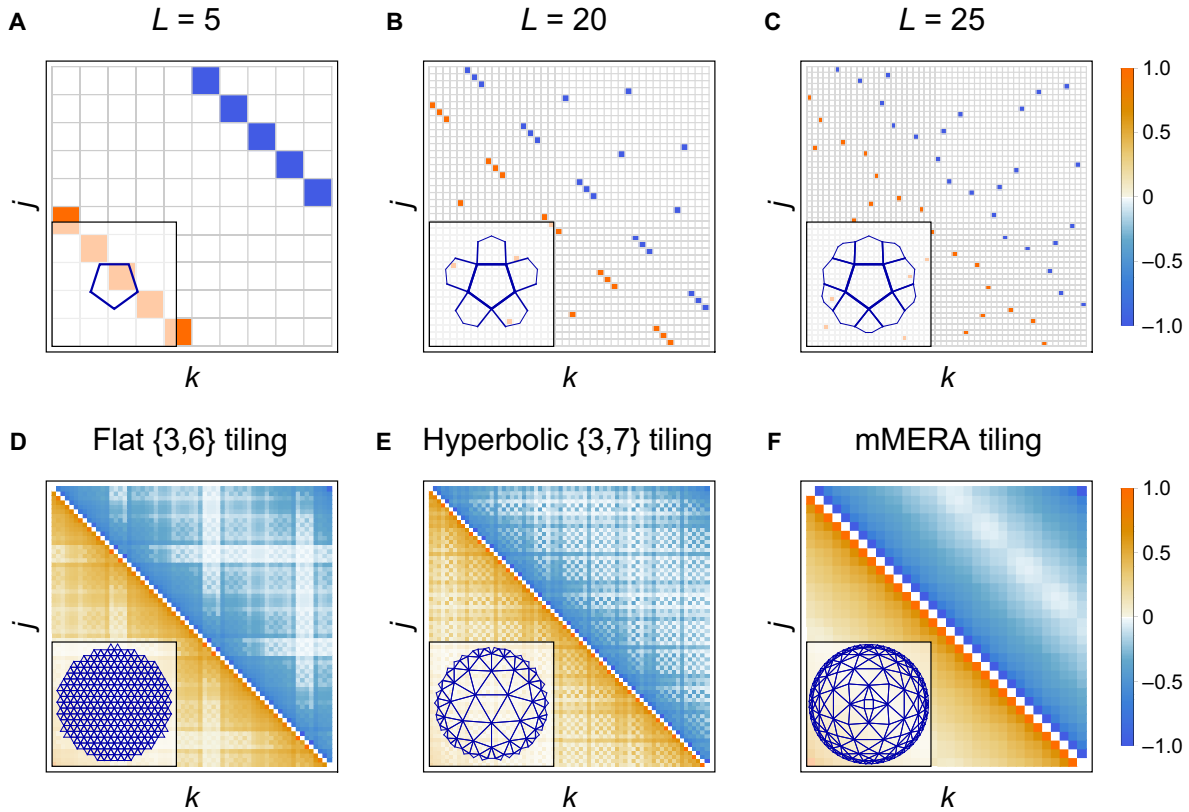


Fig. 3. Boundary state correlations. (A to C) Majorana covariance matrix Γ with color-coded entries for a boundary state of a hyperbolic $\{5,4\}$ tiling of the HaPPY code with fixed $\bar{0}$ input on each tile. Boundary consists of $2L = 10, 40,$ and 50 Majorana sites, respectively. (D to F) Field correlation matrix $\langle \psi_j \psi_k - \psi_k \psi_j \rangle / 2 = (\Gamma_{2j,2k-1} + \Gamma_{2j-1,2k}) / 4$ for boundary states of the $\{3,6\}$, $\{3,7\}$, and mMERA tiling at criticality with $L = 63, 69,$ and 64 boundary sites, respectively. Matrix entries are normalized to the same color scale. The tiling corresponding to each correlation matrix in (A) to (F) is shown in the lower left corner.

we can see, both the individual pentagon state and the larger contracted states are characterized by a nonlocal pairing of Majorana fermions. The contractions effectively connect Majorana pairs from each pentagon to a larger chain, so the pairs on the boundary of the contracted network can be seen as end points of a discretized “geodesic” spanning the bulk. While this discontinuous correlation pattern of $\Gamma_{j,k}$ makes the computation of CFT observables difficult, we can estimate the average correlation falloff by counting the relative frequency $n(d)$ of Majorana pairs at distance $d = |j - k|$ over which they connect points on the boundary. According to the results shown in Fig. 4A, correlation falloff follows a power law $n(d) \propto d^{-1}$, as expected of a CFT. Furthermore, we compute the entanglement entropy S_A of a subsystem A of size l averaged over all boundary positions, defined as

$$\mathbb{E}_l(S) = \sum_{k=1}^L S_{[k,k+l]} \quad (10)$$

The result, shown in Fig. 4B, closely follows the Calabrese-Cardy formula for periodic 1 + 1-dimensional CFTs, given by (33, 34)

$$S_A = \frac{c}{3} \log \left(\frac{L}{\pi \epsilon} \sin \frac{\pi l}{L} \right) \approx \frac{c}{3} \log \frac{l}{\epsilon} + O((l/L)^2) \quad (11)$$

with a numerical fit yielding $c \approx 4.2$ and $\epsilon \approx 1.1$ for a cutoff at $L = 2605$ boundary sites.

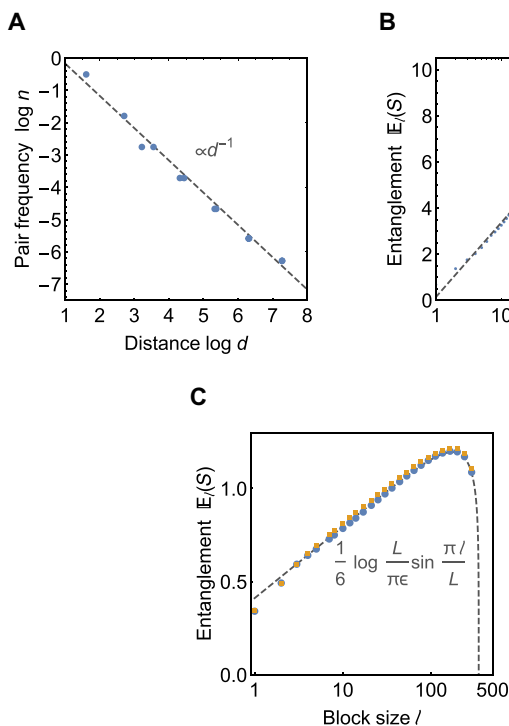


Fig. 4. Critical correlations and entanglement scaling. (A and B) Boundary state properties of the HaPPY code at 2605 boundary sites. (A) shows average correlations at boundary distance d , computed as the relative frequency n of Majorana pairs. Dashed gray line shows an $n(d) \sim 1/d$ numerical fit. (B) shows the scaling of average entanglement entropy $\mathbb{E}_l(S)$ with subsystem size l . Dashed gray line shows numerical fit using (11). (C) $\mathbb{E}_l(S)$ for regular tilings at the critical values $a = 0.580$ for a {3,6} tiling (blue) and at $a = 0.609$ for the {3,7} tiling (yellow) with 348 boundary sites each. The dashed gray line shows the exact $c = 1/2$ CFT solution.

The peculiar pairwise correlation of boundary Majorana modes, suggesting a connection to Majorana dimer models (35), is more deeply explored in a separate publication (36). However, as the correlation structure breaks the translation and scale invariance expected of CFT ground states, we now consider regular tilings with generic matchgate input.

Regular triangulations

As the boundary states of triangular tilings are necessarily Gaussian (15), we can study their properties comprehensively using matchgate tensors. The simplest such tilings are regular and isotropic, i.e., with each local tensor specified by the same antisymmetric 3×3 -generating matrix A . Isotropy constrains its components to one parameter $a = A_{1,2} = A_{1,3} = A_{2,3}$. The bulk topology follows from our choice of tiling. For triangular tilings ($p = 3$), setting $q = 6$ produces a flat tiling, whereas $q > 6$ leads to a hyperbolic one (see Fig. 1, A and B). Triangular tilings with $q < 6$ produce closed polyhedra that are positively curved and lack the notion of an asymptotic boundary. As a convention, we choose the local orientation of the triangles so that the generating matrix for the contracted boundary state satisfies $A'_{ij} > 0$ for $i > j$, corresponding to antiperiodic boundary conditions: Covariance matrix entries Γ_{ij} acquire a sign flip when cyclic permutations push either index i or j over the boundary, as relative ordering is reversed.

We now consider the boundary states of {3, k } bulk tilings. The falloff of correlations along the boundary generally depends on k , i.e., the bulk curvature, as shown in Fig. 5 (A and B) for the $a = 0.25$ case. While correlations between the boundary Majorana fermions of a flat bulk fall off exponentially, a hyperbolic bulk produces a polynomial decay (up to

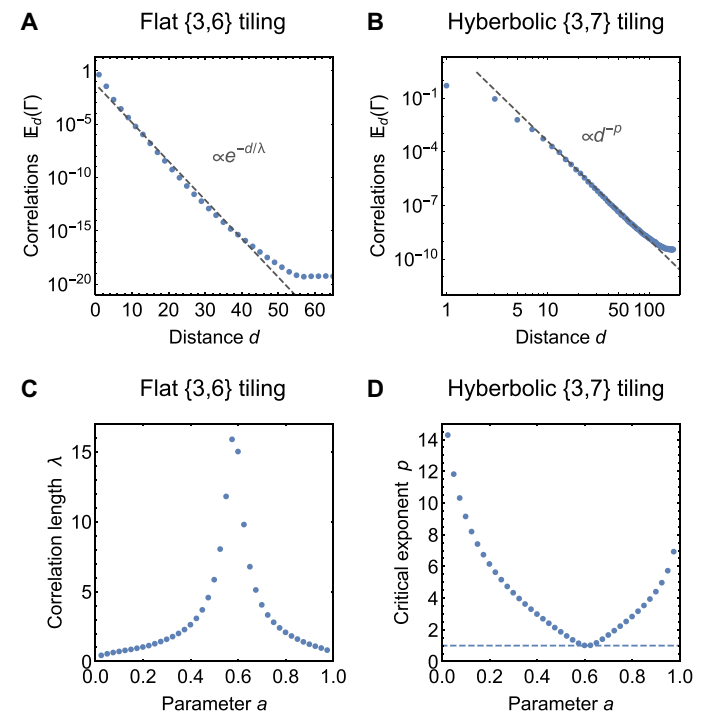


Fig. 5. Boundary correlations for regular tilings. (A and B) Mean value of Majorana covariance $\mathbb{E}_d(\Gamma) = \sum_{k=1}^L |\Gamma_{k,k+d}| / L$ (with $\Gamma_{i,L+j} = \Gamma_{ij}$) at boundary distance d . For {3,6} tiling with 150 boundary Majorana fermions (left) and {3,7} tiling with 348 (right). $a = 0.25$ in both cases. (C and D) Dependence of correlation falloff on a for {3,6} tiling with falloff $\sim e^{-d/\lambda}$ (left) and {3,7} tiling with $\propto d^{-p}$ (right).

finite-size effects at large distances and rounding errors at very small correlations). In the hyperbolic case, geodesics between boundary points scale logarithmically in boundary distance, so the falloff is still exponential in bulk distance, as we would expect in AdS/CFT (37).

Restricting ourselves to the $0 < a < 1$ region, we explore how quickly correlations decay in both settings. At $a = 0$ and $a = 1$, the boundary Majorana fermions only have neighboring pair correlations, either pairing within each edge ($a = 0$) or across the corners ($a = 1$). Thus, correlation decay becomes infinite in the limits $a \rightarrow 0$ and $a \rightarrow 1$, independent of bulk geometry. We use numerical fits to study the remaining region $0 < a < 1$ (see Fig. 5, C and D). For a hyperbolic bulk geometry, the power law is generic with the slowest decay at $a \approx 0.61$, where we see a $\propto d^{-1}$ falloff over distance d . The exponential decay $\propto e^{-d/\lambda}$ generally produced by a flat bulk geometry, however, slows down to a power law (with correlation length λ diverging) around $a \approx 0.58$, where correlations again decay as $\propto d^{-1}$. At their critical values, the boundary states of both bulk geometries have the same average properties.

Up to finite-size effects, this critical boundary theory turns out to be the Ising CFT, as we confirm by computing a range of critical properties from the covariance matrix, shown in Table 1. The entanglement entropy scaling, shown in Fig. 4C, again matches the expected form (11) irrespective of the choice of tiling. The Ising CFT state that we observe at the critical value of a is the ground state of the Hamiltonian

$$H = i \left(\sum_{k=1}^{N-1} \gamma_k \gamma_{k+1} + \gamma_1 \gamma_N \right) \quad (12)$$

where the sign of the boundary term $\gamma_1 \gamma_N$ signifies antiperiodic boundary conditions. Triangular tilings also incorporate more generic models: By associating each edge with a bond dimension $\chi > 2$, it is possible to produce boundary theories with central charges c larger than $1/2$. In the simplest case, we choose a generating matrix that only couples between sets of fermionic modes, resulting in a boundary theory that consists of multiple copies of the Ising CFT and a corresponding central charge that is a multiple of $1/2$ (note that this construction is only possible for $\{n, k\}$ tilings with even k). Furthermore, by changing the tensor content in a central region of the network, a mass gap can be introduced, highlighting how radii in a hyperbolic bulk correspond to a re-

normalization scale on the boundary. Details are provided in the Supplementary Materials.

Translation invariance and MERA

The regular bulk tilings considered so far have a set of discrete symmetries. When choosing identical tensors on each polygon, the boundary states necessarily inherit these symmetries, breaking translation invariance. To recover it, we consider a tiling with the same geometry as the MERA network. As we restrict ourselves to real generating matrices for the three- and four-leg matchgate tensors in this geometry, our model is not a unitary circuit but a model of Euclidean entanglement renormalization resembling imaginary time evolution, extending ideas from (19, 20). This may provide a more realistic representation of the causal structure of an AdS time slice than the standard MERA. Accordingly, the tensors of our matchgate MERA (mMERA) do not correspond to the usual (norm-preserving) isometries and disentanglers. We can still produce almost perfectly translation-invariant boundary states (Fig. 3F) while optimizing over only three parameters and recover the expected CFT properties (Table 1). In particular, at bond dimension $\chi = 2$, the ground-state energy has a relative error of only 0.02% compared to the exact solution. Note that the optimization process only takes a few minutes on a desktop computer for a network with hundreds of tensors. We also find that the $\chi = 2$ mMERA has a symmetry that allows us to write its four-leg tensors as contractions of simpler three-leg tensors (see Fig. 1C), yielding a nonregular triangular tiling. An interesting question to pursue is whether alternating or quasisperiodic tilings with a larger parameter space than regular tilings can also produce translation-invariant states.

DISCUSSION

In this work, we have studied bulk-boundary correspondences in fermionic Gaussian tensor networks, introducing a versatile framework and a highly efficient contraction method based on matchgate tensors (14, 15) for a wide class of flat and hyperbolic bulk tilings. We showed that our framework includes the holographic pentagon code built from five-qubit stabilizer states for fixed bulk inputs. Its boundary states correspond to a nonlocal bulk pairing of Majorana fermions, opening an avenue to studying the state properties of this holographic model at large sizes. We explicitly computed two-point correlators and entanglement entropies, which were found to exhibit critical scaling. Beyond known models, we showed that critical and gapped Gaussian boundary states can be realized by various bulk tilings. In particular, the average scaling properties of the $c = 1/2$ Ising CFT (and multiples thereof) can be reproduced using regular one-parameter bulk triangulations with both flat and hyperbolic curvature. This is particularly unexpected for the flat case where boundary theories are typically gapped and raises the question whether this appearance of criticality is retained in strongly interacting models as well. The appearance of equivalent boundary CFT states for flat and hyperbolic bulks resembles the effect of local Weyl transformations in Euclidean path integrals (38). Our reproduction of conformal properties from an isotropic tensor network with only a single parameter further suggests that isotropy is a powerful symmetry for numerical CFT computations. Furthermore, we constructed the mMERA, a Euclidean matchgate tensor network based on the MERA geometry. Beyond the results achievable with regular triangulations, this tiling, which can also be expressed as a triangulation, recovers the Ising CFT with translation invariance while requiring only three free parameters and little computational cost.

Table 1. Table of conformal data for the regular {3, 6} and {3, 7} bulk tilings as well as the mMERA, compared to the exact results and the wavelet MERA (16). Listed are the ground-state energy density ϵ_0 , central charge c , scaling dimensions Δ_ϕ of the fields $\phi = \psi, \bar{\psi}, \epsilon, \sigma$, and the structure constant $C_{\sigma,\sigma,\epsilon}$. The nonscaling of the identity $\mathbb{1}$ is discussed in the Supplementary Materials.

	Exact	{3, 6} bulk	{3, 7} bulk	mMERA	Wavelets
ϵ_0	-0.6366	-0.6139	-0.5617	-0.6365	-0.6211
c	0.5000	0.5006	0.5018	0.4958	0.4957
$\Delta_\psi, \Delta_{\bar{\psi}}$	0.5000	0.4948	0.4951	0.5023	0.5000
Δ_ϵ	1.0000	0.9856	1.0121	1.0027	1.0000
Δ_σ	0.1250	0.1403	0.1368	0.1417	0.1402
$C_{\sigma,\sigma,\epsilon}$	0.5000	0.5470	0.5336	0.5156	0.4584

SCIENCE ADVANCES | RESEARCH ARTICLE

Within the Gaussian setting, further studies could focus on positively curved bulks, higher-dimensional models, and random tensors. Beyond Gaussianity, one could also explore interacting fermionic tensor networks (39–43) by a weak-coupling expansion or under locally restricted interactions. Both of these possible extensions to our framework would require computations scaling only polynomially in the system size, thus still avoiding the prohibitive computational effort of general methods for exact tensor contraction.

SUPPLEMENTARY MATERIALS

Supplementary material for this article is available at <http://advances.sciencemag.org/cgi/content/full/5/8/eaaw0092/DC1>

Section S1. Tensor contractions in the Grassmann formalism

Section S2. Matchgates and fermionic Gaussian states

Section S3. Conversion of generating matrices to covariance matrices

Section S4. Contraction rules for generating matrices

Section S5. Explicit generating matrices and numerical results

Fig. S1. Combining tiles of matchgates.

Fig. S2. Tile orientations under contraction.

Fig. S3. Constructing the mMERA.

Fig. S4. Energy convergence of the mMERA.

Fig. S5. Determining scaling dimensions of flat tilings.

Fig. S6. Determining scaling dimensions of hyperbolic tilings.

Fig. S7. Determining scaling dimensions of mMERA.

Fig. S8. Determining structure constants.

Fig. S9. Correlations and entanglement with IR cutoff.

Fig. S10. Construction of triangle states with bond dimension $\chi = 2, 4, 8$.

Table S1. Values of the critical generating matrix parameter a for different $\{3, k\}$ triangular tilings and ultraviolet cutoffs.

Table S2. Exact conformal scaling dimension of various (quasi-)primary fields ϕ of the Ising CFT.

References (44–51)

REFERENCES AND NOTES

- J. M. Maldacena, The large N limit of superconformal field theories and supergravity. *Adv. Theor. Math. Phys.* **2**, 231–252 (1998).
- M. Van Raamsdonk, Building up spacetime with quantum entanglement. *Gen. Rel. Grav.* **42**, 2323–2329 (2010).
- F. Pastawski, J. Preskill, Code properties from holographic geometries. *Phys. Rev. X* **7**, 021022 (2017).
- J. Eisert, M. Cramer, M. B. Plenio, *Colloquium: Area laws for the entanglement entropy*. *Rev. Mod. Phys.* **82**, 277–306 (2010).
- S. Ryu, T. Takayanagi, Holographic derivation of entanglement entropy from the anti-de Sitter space/conformal field theory correspondence. *Phys. Rev. Lett.* **96**, 181602 (2006).
- B. G. Swingle, Entanglement renormalization and holography. *Phys. Rev. D* **86**, 065007 (2012).
- G. Vidal, Class of quantum many-body states that can be efficiently simulated. *Phys. Rev. Lett.* **101**, 110501 (2008).
- G. Evenbly, G. Vidal, Algorithms for entanglement renormalization. *Phys. Rev. B* **79**, 144108 (2009).
- C. M. Dawson, J. Eisert, T. J. Osborne, Unifying variational methods for simulating quantum many-body systems. *Phys. Rev. Lett.* **100**, 130501 (2008).
- A. Almheiri, X. Dong, D. Harlow, Bulk locality and quantum error correction in AdS/CFT. *J. High Energy Phys.* **1504**, 163 (2015).
- C. H. Lee, X.-L. Qi, Exact holographic mapping in free fermion systems. *Phys. Rev. B* **93**, 035112 (2016).
- F. Pastawski, B. Yoshida, D. Harlow, J. Preskill, Holographic quantum error-correcting codes: Toy models for the bulk/boundary correspondence. *J. High Energy Phys.* **2015**, 149 (2015).
- P. Hayden, S. Nezami, X.-L. Qi, N. Thomas, M. Walter, Z. Yang, Holographic duality from random tensor networks. *J. High Energy Phys.* **2016**, 9 (2016).
- L. G. Valiant, Quantum circuits that can be simulated classically in polynomial time. *SIAM J. Comput.* **31**, 1229–1254 (2002).
- S. Bravyi, Contraction of matchgate tensor networks on non-planar graphs. *Cont. Math.* **482**, 179–211 (2009).
- G. Evenbly, S. R. White, Entanglement renormalization and wavelets. *Phys. Rev. Lett.* **116**, 140403 (2016).
- J. Haegeman, B. Swingle, M. Walter, J. Cotler, G. Evenbly, V. B. Scholz, Rigorous free fermion entanglement renormalization from wavelet theory. *Phys. Rev. X* **8**, 011003 (2018).
- G. Evenbly, Hyperinvariant tensor networks and holography. *Phys. Rev. Lett.* **119**, 141602 (2017).
- G. Evenbly, G. Vidal, Tensor network renormalization. *Phys. Rev. Lett.* **115**, 180405 (2015).
- G. Evenbly, G. Vidal, Tensor network renormalization yields the multiscale entanglement renormalization ansatz. *Phys. Rev. Lett.* **115**, 200401 (2015).
- R. Orus, A practical introduction to tensor networks: Matrix product states and projected entangled pair states. *Ann. Phys.* **349**, 117–158 (2014).
- N. Schuch, *Lecture notes for the 44th IFF Spring School “Quantum Information Processing” in Juelich* (2013).
- F. Verstraete, J. I. Cirac, V. Murg, Matrix product states, projected entangled pair states, and variational renormalization group methods for quantum spin systems. *Adv. Phys.* **57**, 143–224 (2008).
- J. Eisert, Entanglement and tensor network states. *Mod. Sim.* **3**, 520 (2013).
- F. A. Berezin, *The Method of Second Quantization* (Academic Press, 1966).
- K. E. Cahill, R. J. Glauber, Density operators for fermions. *Phys. Rev. A* **A59**, 1538–1555 (1999).
- S. Bravyi, Lagrangian representation for fermionic linear optics. *Quantum Inf. Comput.* **5**, 216–238 (2005).
- B. M. Terhal, D. P. DiVincenzo, Classical simulation of noninteracting-fermion quantum circuits. *Phys. Rev. A* **65**, 032325 (2002).
- R. Laflamme, C. Miquel, J. P. Paz, W. H. Zurek, Perfect quantum error correcting code. *Phys. Rev. Lett.* **77**, 198–201 (1996).
- D. Gottesman, Class of quantum error-correcting codes saturating the quantum hamming bound. *Phys. Rev. A* **54**, 1862–1868 (1996).
- B. M. Terhal, Quantum error correction for quantum memories. *Rev. Mod. Phys.* **87**, 307–346 (2015).
- D. Gottesman, “Stabilizer codes and quantum error correction,” thesis, California Institute of Technology (1997).
- C. Holzhey, F. Larsen, F. Wilczek, Geometric and renormalized entropy in conformal field theory. *Nucl. Phys. B* **B424**, 443–467 (1994).
- P. Calabrese, J. Cardy, Entanglement entropy and quantum field theory. *J. Stat. Mech.* **0406**, P06002 (2004).
- B. Ware, J. H. Son, M. Cheng, R. V. Mishmash, J. Alicea, B. Bauer, Ising anyons in frustration-free majorana-dimer models. *Phys. Rev. B* **94**, 115127 (2016).
- A. Jahn, M. Gluza, F. Pastawski, J. Eisert, Majorana dimers and holographic quantum error-correcting codes, arXiv:1905.03268 [hep-th] (8 May 2019).
- V. Balasubramanian, S. F. Ross, Holographic particle detection. *Phys. Rev. D* **D61**, 044007 (2000).
- P. Caputa, N. Kundu, M. Miyaji, T. Takayanagi, K. Watanabe, Anti-de Sitter space from optimization of path integrals in conformal field theories. *Phys. Rev. Lett.* **119**, 071602 (2017).
- T. Barthel, C. Pineda, J. Eisert, Contraction of fermionic operator circuits and the simulation of strongly correlated fermions. *Phys. Rev. A* **80**, 042333 (2009).
- P. Corboz, R. Orus, B. Bauer, G. Vidal, Simulation of strongly correlated fermions in two spatial dimensions with fermionic projected entangled-pair states. *Phys. Rev. B* **81**, 165104 (2010).
- C. V. Kraus, N. Schuch, F. Verstraete, J. I. Cirac, Fermionic projected entangled pair states. *Phys. Rev. A* **81**, 052338 (2010).
- C. Wille, O. Buijsscher, J. Eisert, Fermionic topological quantum states as tensor networks. *Phys. Rev. B* **95**, 245127 (2017).
- N. Bultinck, D. J. Williamson, J. Haegeman, F. Verstraete, Fermionic matrix product states and one-dimensional topological phases. *Phys. Rev. B* **95**, 075108 (2017).
- H. N. V. Temperley, M. E. Fisher, Dimer problem in statistical mechanics—an exact result. *Phil. Mag.* **6**, 1061–1063 (1961).
- P. W. Kasteleyn, The statistics of dimers on a lattice: I. The number of dimer arrangements on a quadratic lattice. *Phys. Ther.* **27**, 1209–1225 (1961).
- J.-Y. Cai, V. Choudhary, P. Lu, On the theory of matchgate computations, in *Twenty-Second Annual IEEE Conference on Computational Complexity (CCC’07)* (IEEE, 2007), pp. 305–318.
- C. Bloch, A. Messiah, The canonical form of an antisymmetric tensor and its application to the theory of superconductivity. *Nucl. Phys.* **39**, 95–106 (1962).
- C. V. Kraus, “A quantum information perspective of fermionic quantum many-body systems,” thesis, Universität München (2009).
- S. Bravyi, D. Gosset, Complexity of quantum impurity problems. *Comm. Math. Phys.* **356**, 451–500 (2016).
- P. Francesco, P. Mathieu, D. Sénéchal, *Conformal Field Theory* (Springer, 1997).
- A. Serafini, F. Illuminati, S. De Siena, Von Neumann entropy, mutual information and total correlations of Gaussian states. *J. Phys.* **B37**, L21 (2004).

SCIENCE ADVANCES | RESEARCH ARTICLE

Acknowledgments: We would like to thank A. Kubica for pointing out that $[[5,1,3]]$ code states (29) are ground states of quadratic Majorana Hamiltonians. We also thank X.-L. Qi, T. Takayanagi, and P. Caputa for helpful discussions. **Funding:** We thank the ERC (TAQ), the DFG (CRC 183, EI 519/7-1, EI 519/14-1, and EI 519/15-1), the John Templeton Foundation, the EC (PASQuanS), the Studienstiftung, and the Alexander von Humboldt Foundation for support. **Author contributions:** F.P. and J.E. conceived the project and provided guidance, while A.J. and M.G. performed analytical calculations. A.J. provided the numerical computations and figure design. All authors discussed the results and wrote the manuscript. **Competing interests:** The authors declare that they have no competing interests. F.P. is currently employed by Psi Quantum Inc. but provided his main contribution to this work while being employed at Freie Universität Berlin. **Data and materials**

availability: All data needed to evaluate the conclusions in the paper are present in the paper and/or the Supplementary Materials. All data related to this paper may be requested from the authors.

Submitted 13 November 2018

Accepted 28 June 2019

Published 9 August 2019

10.1126/sciadv.aaw0092

Citation: A. Jahn, M. Gluza, F. Pastawski, J. Eisert, Holography and criticality in matchgate tensor networks. *Sci. Adv.* **5**, eaaw0092 (2019).

advances.sciencemag.org/cgi/content/full/5/8/eaaw0092/DC1

Supplementary Materials for

Holography and criticality in matchgate tensor networks

A. Jahn*, M. Gluza, F. Pastawski, J. Eisert

*Corresponding author. Email: a.jahn@fu-berlin.de

Published 9 August 2019, *Sci. Adv.* **5**, eaaw0092 (2019)
DOI: 10.1126/sciadv.aaw0092

This PDF file includes:

- Section S1. Tensor contractions in the Grassmann formalism
- Section S2. Matchgates and fermionic Gaussian states
- Section S3. Conversion of generating matrices to covariance matrices
- Section S4. Contraction rules for generating matrices
- Section S5. Explicit generating matrices and numerical results
- Fig. S1. Contraction of two triangle states with Grassmann-variable edges $\{\theta_1, \theta_2, \theta_3\}$ and $\{\theta_4, \theta_5, \theta_6\}$ into a state with four edges $\{\Theta_1, \Theta_2, \Theta_3, \Theta_4\}$.
- Fig. S2. Tile orientations under contraction.
- Fig. S3. Constructing the mMERA.
- Fig. S4. Energy convergence of the mMERA.
- Fig. S5. Determining scaling dimensions of flat tilings.
- Fig. S6. Determining scaling dimensions of hyperbolic tilings.
- Fig. S7. Determining scaling dimensions of mMERA.
- Fig. S8. Determining structure constants.
- Fig. S9. Correlations and entanglement with IR cutoff.
- Fig. S10. Construction of triangle states with bond dimension $\chi = 2, 4, 8$.
- Table S1. Values of the critical generating matrix parameter a for different $\{3, k\}$ triangular tilings and ultraviolet cutoffs.
- Table S2. Exact conformal scaling dimension of various (quasi-)primary fields ϕ of the Ising CFT.
- References (44–51)

Supplementary materials

OVERVIEW

These supplementary materials contain additional details, technical calculations and proofs of the assertions made in the main text. We begin by showing how to perform tensor contraction using Grassmann integration in Section S1, followed by a minimal example of contracting two matchgate tensors. In Section S2, we restructure the definitions made in Ref. [15] in order to bring the theory of matchgates closer to the free fermionic formalism. In particular, we prove the correspondence between matchgate tensors and fermionic Gaussian states. In Section S3, we show how to convert a generating matrix of a matchgate tensor to the covariance matrix of the corresponding state, yielding the physically relevant correlations. In Section S4, we provide technical details and calculations for the contraction rules in the Grassmann formalism used in the numerical implementation. In Section S5, we give explicit examples of generating matrices relevant to the main text and present a construction of states with higher central charges.

Section S1. Tensor contractions in the Grassmann formalism

In this section, we review the approach to contraction of matchgate tensor networks through Grassmann integration [15]. In particular we present a simplified version of Lemma 5 from Ref. [15] and explain this result through an example. Grassmann variables will be denoted by θ and are a set of anti-commuting generators of an algebra ($\theta_j\theta_i = -\theta_i\theta_j$) which nevertheless commutes with ordinary scalars x ($x\theta_i = \theta_ix$). A general element in this algebra may be written as

$$z = \sum_{k=0}^n \sum_{i_1, \dots, i_k} c_{i_1 \dots i_k} \theta_{i_1} \cdots \theta_{i_k} \quad (1)$$

where $c_{i_1 \dots i_k}$ can be arbitrary complex coefficients and i_k form an increasing sequence in $\{1, 2, \dots, n\}$. In particular, given a tensor $T : \{0, 1\}^{\times r} \rightarrow \mathbb{C}$ we associate to it a polynomial in Grassmann numbers given by

$$\Phi_T(\theta) = \sum_{j \in \{0, 1\}^{\times r}} T(j) \theta_1^{j_1} \theta_2^{j_2} \cdots \theta_r^{j_r} \quad (2)$$

which we call its characteristic function.

For simplicity, we consider contracting the last index of a rank- r_1 tensor T_1 with the first index of a rank- r_2 tensor T_2 where $r_1, r_2 \geq 1$. Let us denote $r'_1 = r_1 - 1$ and $r'_2 = r_2 - 1$. This operation gives rise to a rank- $(r'_1 + r'_2)$ tensor $T_{1 \star 2}$ with entries

$$T_{1 \star 2}(x, y) = \sum_{z \in \{0, 1\}} T_1(x, z) T_2(z, y) \quad (3)$$

for $x \in \{0, 1\}^{\times r'_1}$ and $y \in \{0, 1\}^{\times r'_2}$ being binary words. The characteristic function for the contraction of two tensors can be obtained by

$$\Phi_{T_{1 \star 2}}(\tilde{\theta}, \tilde{\eta}) = \int d\eta_1 \int d\theta_{r_1} \Phi_{T_1}(\theta) \Phi_{T_2}(\eta) \exp(\theta_{r_1} \eta_1) \quad (4)$$

where $\tilde{\theta} = (\theta_1, \dots, \theta_{r'_1})$, $\tilde{\eta} = (\eta_1, \dots, \eta_{r'_2})$ correspond to uncontracted indices and θ_{r_1} and η_1 are the two Grassmann numbers of the two indices that are being contracted. Let us use $\exp(\theta_{r_1} \eta_1) = 1 + \theta_{r_1} \eta_1$ on the right hand side

$$RHS = \sum_{\substack{x \in \{0, 1\}^{\times r'_1} \\ y \in \{0, 1\}^{\times r'_2}}} \sum_{a, b \in \{0, 1\}} T_1(x, a) T_2(b, y) \int d\eta_1 \int d\theta_{r_1} \theta_1^{x_1} \theta_2^{x_2} \cdots \theta_{r'_1}^{x_{r'_1}} \theta_{r_1}^a \eta_1^b \eta_2^{y_1} \cdots \eta_{r'_2}^{y_{r'_2}} (1 + \theta_{r_1} \eta_1) \quad (5)$$

and observe that the two integrals commute with the first $r_1 - 1$ of the θ 's and exponential factor commutes with the η 's. This gives

$$RHS = \sum_{\substack{x \in \{0, 1\}^{\times r'_1} \\ y \in \{0, 1\}^{\times r'_2}}} \sum_{a, b \in \{0, 1\}} T_1(x, a) T_2(b, y) \theta_1^{x_1} \theta_2^{x_2} \cdots \theta_{r'_1}^{x_{r'_1}} \left[\int d\eta_1 \int d\theta_{r_1} \theta_{r_1}^a \eta_1^b (1 + \theta_{r_1} \eta_1) \right] \eta_2^{y_1} \cdots \eta_{r'_2}^{y_{r'_2}} \quad (6)$$

For the middle bracket, we obtain

$$\int d\eta_1 \int d\theta_{r_1} \theta_{r_1}^a \eta_1^b (1 + \theta_{r_1} \eta_1) = \delta_{a, b} \quad (7)$$

and therefore

$$RHS = \sum_{\substack{x \in \{0, 1\}^{\times r'_1} \\ y \in \{0, 1\}^{\times r'_2}}} \left[\sum_{z \in \{0, 1\}} T_1(x, z) T_2(z, y) \right] \theta_1^{x_1} \theta_2^{x_2} \cdots \theta_{r'_1}^{x_{r'_1}} \eta_2^{y_1} \cdots \eta_{r'_2}^{y_{r'_2}} \quad (8)$$

We see that this is exactly the characteristic function for the tensor contraction. Note that it is important that we contract the last index with the first one. Lemma 5 of Ref. [15] generalizes this calculation to an arbitrary number of indices that are being contracted in an appropriate order – this essentially could be derived by iterating the formula that we derived for the case of self-contractions.

A. Minimal example

As an example, we want to show the contraction of two tensors T_A, T_B with Gaussian characteristic functions of the form

$$\Phi_{T_A}(\theta) = \exp\left(\frac{1}{2} \sum_{j,k=1}^L A_{j,k} \theta_j \theta_k\right), \quad \Phi_{T_B}(\theta) = \exp\left(\frac{1}{2} \sum_{j,k=1}^L B_{j,k} \theta_j \theta_k\right) \quad (9)$$

As we summarize in Fig. S1, we associate the Grassmann numbers $\theta_1, \theta_2, \theta_3$ to A and $\theta_4, \theta_5, \theta_6$ to B , and fix θ_3 and θ_4 on the edges between the triangles to be integrated out, yielding a state with four edges whose correlation matrix C shall be computed from A and B via Grassmann integration

$$\Phi_C(\Theta) = \int d\theta_4 d\theta_3 e^{\theta_3 \theta_4 + \frac{1}{2} \sum_{j,k=1}^6 (A \oplus B)_{j,k} \theta_j \theta_k} \quad (10)$$

where $\Theta = (\theta_1, \theta_2, \theta_5, \theta_6)^\top$ contains the four Grassmann numbers that remain after integration. Taking A, B as input, we find that after the integration Φ_{T_C} is again Gaussian (the technicalities of integration will be dealt with in Section S4) and the generating matrix is

$$C = \begin{pmatrix} 0 & A_{1,2} & A_{1,3}B_{4,5} & A_{1,3}B_{4,6} \\ -A_{1,2} & 0 & A_{2,3}B_{4,5} & A_{2,3}B_{4,6} \\ -A_{1,3}B_{4,5} & -A_{2,3}B_{4,5} & 0 & B_{5,6} \\ -A_{1,3}B_{4,6} & -A_{2,3}B_{4,6} & -B_{5,6} & 0 \end{pmatrix} \quad (11)$$

We observe that the newly created entries in the upper right corner are in fact a dyadic product and this block is a lower-rank matrix.

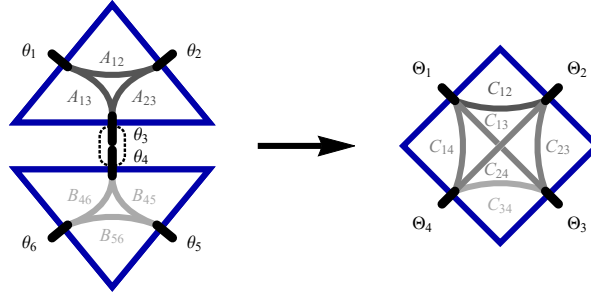


Fig. S1. Combining tiles of matchgates. Contraction of two triangle states with Grassmann-variable edges $\{\theta_1, \theta_2, \theta_3\}$ and $\{\theta_4, \theta_5, \theta_6\}$ into a state with four edges $\{\Theta_1, \Theta_2, \Theta_3, \Theta_4\}$.

Section S2. Matchgates and fermionic Gaussian states

We first discuss definitions of matchgate tensors and then explain the connection to fermionic Gaussian states.

A. Definitions of matchgates

For completeness, we shortly recapitulate the characterization of matchgates by Bravyi in Ref. [15]. Originally matchgates [44] were characterized as the local tensors of a tensor network that can be contracted efficiently through the *Fisher-Kastelyn-Temperley method* [45, 46]. Subsequently, the following algebraic characterization has been found [47].

Definition 1 (Matchgate equations). *A rank- r tensor T is a matchgate if for all $x, y \in \{0, 1\}^{\times r}$ it holds that*

$$\sum_{k: x_k \neq y_k} T(x \text{ XOR } e^k) T(y \text{ XOR } e^k) (-1)^{\sum_{j=1}^{k-1} (x_j + y_j)} = 0 \quad (12)$$

where $(e^k)_q = \delta_{k,q}$.

Proposition 2 of Ref. [15] shows that one can equivalently define matchgates through Pfaffians, leading to the following equivalent definition.

Definition 2 (Matchgates as Pfaffians). *A rank- r tensor T is a matchgate if there exists a reference index $z \in \{0, 1\}^{\times r}$ and an anti-symmetric matrix $A \in \mathbb{C}^{r \times r}$, such that for any $x \in \{0, 1\}^{\times r}$*

$$T(x) = \text{Pf}(A_{|x \text{ XOR } z}) T(z) \quad (13)$$

In particular, A is explicitly given by $A_{j,k} = T(e^j \text{ XOR } e^k \text{ XOR } z)/T(z)$ for $j < k$ if $T(z) \neq 0$ or $A \equiv 0$ if $T \equiv 0$ and we denote by $A_{|x \text{ XOR } z}$ the restriction of A to the entries indicated by $x \text{ XOR } z$.

Proof of the equivalence of these definitions. In particular, proposition 2 of Ref. [15] shows that whenever $T(z) \neq 0$ then a new matchgate tensor T' fulfills $T'(x) = T(x \text{ XOR } z)/T(z) = \text{Pf}(A_{|x})$ which is derived from the matchgate equations. From this we have that $T'(x \text{ XOR } z) = T(x \text{ XOR } z \text{ XOR } z)/T(z) = T(x)/T(z) = \text{Pf}(A_{|x \text{ XOR } z}) T(z)$ and therefore $T(x) = \text{Pf}(A_{|x \text{ XOR } z}) T(z)$. Finally, for the trivial matchgate tensor $T = 0$ both definitions agree, too.

The converse direction can be shown by a simplification of the argument of Theorem 2 of Ref. [15]. We start with $T(x) = \text{Pf}(A_{|x \text{ XOR } z}) T(z)$. If $T(z) = 0$ then T fulfills the matchgate equations trivially. Otherwise we consider T' with entries $T'(x) = T(x \text{ XOR } z)/T(z) = \text{Pf}(A_{|x})$ which has a Gaussian characteristic function

$$\Phi_{T'}(\theta) = \exp\left(\frac{1}{2} \sum_{j,k=1}^r A_{j,k} \theta_j \theta_k\right) \quad (14)$$

This is argued as follows. As this is a Gaussian characteristic function by the theory of Ref. [27] the Lemma 1 in Ref. [15] applies which shows that T' fulfills matchgate equations. Finally, from Proposition 1 in op. cit., or by a shift of variables, we find that T also satisfies these equations.

The following lemma shows that matchgates have Gaussian characteristic functions.

Lemma 3 (Grassmann exponentials). *Let $A = -A^\top \in \mathbb{C}^{r \times r}$ for some positive integer r , then we have*

$$\exp\left(\frac{1}{2} \sum_{j,k=1}^r A_{j,k} \theta_j \theta_k\right) = \sum_{x \in \{0,1\}^{\times r}} \text{Pf}(A_{|x}) \theta_1^{x_1} \theta_2^{x_2} \dots \theta_r^{x_r} \quad (15)$$

We omit the proof which proceeds by using the definition of the exponential series which is truncated to first $\lfloor n/2 \rfloor$ powers of the quadratic form and then regrouping terms that have the same normal ordered Grassmann monomial. Keeping track of the sign in such reordering, yields the sign of the permutation and subsequently the Pfaffian can be identified. From this it follows that an even matchgate with $z = \bar{0}$ and covariance matrix A has a Gaussian characteristic function

$$\Phi_T(\theta) = T(\bar{0}) \exp\left(\frac{1}{2} \sum_{j,k=1}^r A_{j,k} \theta_j \theta_k\right) \quad (16)$$

For matchgates with $z \neq \bar{0}$ we refer the reader to Theorem 2 of Ref. [15] for a general form of the characteristic function. Note that the set of creation operators generates a Grassmann algebra too because $\{f_j^\dagger, f_k^\dagger\} = f_j^\dagger f_k^\dagger + f_k^\dagger f_j^\dagger = 0$. This means that if we calculate $\exp((1/2) \sum_{j,k=1}^r A_{j,k} f_j^\dagger f_k^\dagger)$ from the definition and simplify all terms, we will make the same reordering as in the Grassmann number case, picking up the same sign differences. Hence, (15) is valid if we replace Grassmann numbers by the creation operators, which gives a physical interpretation to the characteristic function as normal-ordered operators.

B. Fermionic Gaussian states

Our statements will concern even Gaussian state vectors of the form $|\psi_G\rangle = U_G |\emptyset\rangle$. This means that we fix the reference state vector $|\emptyset\rangle$ to be the vacuum and use a Gaussian unitary that has an even and quadratic generator

$$H(G) = \frac{i}{4} \sum_{j,k=1}^{2L} G_{j,k} \gamma_j \gamma_k \quad (17)$$

where $G = -G^\top \in \mathbb{R}^{2L \times 2L}$ and the $\{\gamma_j\}$ are the self-adjoint Majorana operators which satisfy the Clifford relations $\{\gamma_j, \gamma_k\} = 2\delta_{j,k} \mathbb{1}$. Alternatively, they can be defined via Jordan-Wigner transformation or by relating them to the canonically

anticommuting creation-annihilation operators through $\gamma_{2j-1} = f_j + f_j^\dagger$ and $\gamma_{2j} = -i(f_j - f_j^\dagger)$. As we are using even generators, the resulting state will conform to the fermionic parity superselection rule. Note that as reference state one could in principle use a Fock-basis state with an odd particle content and again use a Gaussian unitary, however either choice results in the same physics and can be related by an appropriate particle-hole redefinition.

The Bloch-Messiah reduction [48, 49] employs a unitary transformation U_1 of the single particle basis to decouple a given Gaussian state vector as

$$|\psi_G\rangle = U_1 \prod_{k=1}^{L/2} (v_k + u_k f_{2k-1}^\dagger f_{2k}^\dagger) |\emptyset\rangle \quad (18)$$

where the coefficients v, u depend on G . A particle number preserving (PNP) Gaussian transformation is a unitary of the form $U_1 = e^{-iH_1}$ where $H_1 = \sum_{j,k=1}^L h_{j,k} f_j^\dagger f_k$ with $h = h^\dagger \in \mathbb{C}^{L \times L}$. For the above defined Gaussian states we have the following result [48, 49].

Lemma 4 (Bloch-Messiah reduction). *There exists a PNP transformation U_1 decoupling the state vector $|\psi_G\rangle$ in the following sense*

$$|\psi_G\rangle = \prod_{k=1}^{\lfloor L/2 \rfloor} (v_k \mathbb{1} + u_k p_{2k-1}^\dagger p_{2k}^\dagger) |\emptyset\rangle \quad (19)$$

Here, $v, u \in \mathbb{C}^{\times \lfloor L/2 \rfloor}$ and $p_j = U_1 f_j U_1^\dagger$.

Proof. We recapitulate the idea of the proof that can be found in the Appendix A of Ref. [49] or in Ref. [48]. The main idea is to show that there exists a unitary transformation that puts into the normal form both the coherent hopping correlations $C_{j,k} = \langle f_j^\dagger f_k \rangle$ and pairing terms $P_{j,k} = \langle f_j f_k \rangle$. A relation first derived by Bogoliubov between C and P shows that both matrices can be put into a normal form simultaneously by a unitary transformation $U \in \mathbb{C}^{L \times L}$ [48, 49]. For C due to hermiticity we seek a diagonal form, while for P a block diagonal form. The transformation U that achieves this can be viewed as a representation in mode space of a PNP transformation U_1 which defines the special mode operators $p_k = U_1 f_k U_1^\dagger = \sum_{k'} U_{k,k'} f_{k'}$ where the correlation matrices are particularly simple. The state vector $|\psi_G\rangle$ expressed in the $\{p_k\}$ takes the particularly simple form

$$|\psi\rangle = \prod_{k=1}^{L/2} (v_{2k-1} \mathbb{1} + u_{2k} p_{2k-1}^\dagger p_{2k}^\dagger) |\emptyset\rangle \quad (20)$$

where $|v_k|^2 + |u_k|^2 = 1$ and we use the invariance of the vacuum under PNP transformations.

This means that normal-ordering of a generic U_G with respect to the vacuum is again Gaussian, i.e., it is a quadratic operator exponential which now only contains creation operators

$$|\psi\rangle = : U_G : |\emptyset\rangle = \sqrt{Z}^{-1} \exp\left(\frac{1}{2} \sum_{j,k=1}^L A_{j,k} f_j^\dagger f_k^\dagger\right) |\emptyset\rangle \quad (21)$$

Indeed, let us for now assume that $v_k \neq 0$. We now use $f^{\dagger 2} = 0$ to write (19) as

$$|\psi\rangle = \prod_{k=1}^{L/2} v_{2k-1} e^{\frac{u_{2k}}{v_{2k-1}} p_{2k-1}^\dagger p_{2k}^\dagger} |\emptyset\rangle \quad (22)$$

$$= \sqrt{Z}^{-1} e^{\sum_{k=1}^{L/2} \frac{u_{2k}}{2v_{2k-1}} [p_{2k-1}^\dagger, p_{2k}^\dagger]} |\emptyset\rangle \quad (23)$$

where we have defined

$$\sqrt{Z}^{-1} := \prod_{k=1}^{L/2} v_{2k-1} \quad (24)$$

In the next step, we exploit the result that any complex anti-symmetric matrix \tilde{A} can be put into a normal form by a unitary conjugation, i.e., $\tilde{A} = UN(\lambda)U^\dagger$ where

$$N(\lambda) = \bigoplus_k \begin{pmatrix} 0 & \lambda_k \\ -\lambda_k & 0 \end{pmatrix} \quad (25)$$

when L is even, with complex $\{\lambda_k\}$ [48, 49]. If L is odd, it takes the same form, with an additional 1×1 block of 0's. Thus, if U_1 acts as U on modes we will have for $p_k = U_1 f_k U_1^\dagger = \sum_{k'} U_{k,k'} f_{k'}$

$$|\psi\rangle = \sqrt{Z}^{-1} \exp\left(\frac{1}{2} \sum_{j,k=1}^L A_{j,k} f_j^\dagger f_k^\dagger\right) |\emptyset\rangle = :U_G : |\emptyset\rangle \quad (26)$$

where

$$\lambda_k = \frac{u_{2k}}{2v_{2k-1}} \quad (27)$$

Clearly, by tuning u, v we can reach any spectrum so any complex anti-symmetric matrix A can be obtained. For generic states this is enough, while basis states can be expressed as a limit of such expressions.

Finally, we observe that the algebra of creation operators alone is isomorphic to that of Grassmann by replacing θ_j by f_j^\dagger . Then we can rewrite

$$|\psi\rangle = \sum_{j \in \{0,1\}^{\times L}} \mathcal{T}(j) (f_1^\dagger)^{j_1} \dots (f_L^\dagger)^{j_L} |\emptyset\rangle \quad (28)$$

where $\mathcal{T}(j) = \sqrt{Z}^{-1} \text{Pf}(A_{|j})$ which is by definition a matchgate tensor. Conversely, one can go the other direction defining as state using a matchgate tensor which will be a fermionic Gaussian state. An alternative derivation of this fact based on a generalized Wick's theorem [50] is given below.

C. Alternative proof for matchgates corresponding to Gaussian states

We express a fermionic Gaussian state vector in the occupation basis

$$|\psi\rangle = \sum_{x \in \{0,1\}^n} \mathcal{T}(x) |x\rangle \quad (29)$$

where we have defined the *amplitude tensor* \mathcal{T} . Its components can be obtained via $\mathcal{T}(x) = \langle x | \psi \rangle$ where $|x\rangle = (f_1^\dagger)^{x_1} \dots (f_L^\dagger)^{x_L} |\emptyset\rangle$ denotes an occupation basis state. Note, that identifying $|\emptyset\rangle = |\downarrow\rangle^{\otimes L}$ and using the Jordan-Wigner transformation as in the main-text, this ordering of creation operators will yield $|x\rangle = (\sigma_1^+)^{x_1} \dots (\sigma_L^+)^{x_L} |\downarrow\rangle^{\otimes L} = \otimes_{j=1}^L |x_j\rangle$. Fixing a basis state $|z\rangle$, we may define the z -offset basis $|x\rangle_z = (\gamma_{2L-1})^{x_L} \dots (\gamma_1)^{x_1} |z\rangle$. We would like to show that \mathcal{T} is a matchgate tensor by making use of the following result [49].

Lemma 5 (Generalized Wick's theorem). *For two Gaussian state vectors $|\phi_1\rangle, |\phi_2\rangle$ and corresponding covariance matrices M_1, M_2 , we have the generalized Wick's theorem*

$$\langle \phi_1 | (\gamma_1)^{x_1} \dots (\gamma_{2L})^{x_{2L}} | \phi_2 \rangle = \langle \phi_1 | \phi_2 \rangle \text{Pf}(i\Delta_{|x}) \quad (30)$$

where

$$\Delta = (-2\mathbb{1} + iM_1 - iM_2)(M_1 + M_2)^{-1} \quad (31)$$

This general result should also be useful in various settings, in particular for studying non-Gaussian states with the methods of fermionic linear optics as it allows to calculate observables in linear combinations of pure Gaussian states. Here is a first possible application.

Lemma 6 (Matchgates and Gaussian states). *For a Gaussian state vector $|\psi\rangle = U_G |\emptyset\rangle$ define the z -offset such that $\langle z | \psi \rangle \neq 0$. Then the amplitude tensor \mathcal{T} in the z -offset basis representation $|\psi\rangle = \sum_{x \in \{0,1\}^L} \mathcal{T}(x) |x\rangle_z$ is a matchgate tensor.*

Proof. We define $\mathcal{T}(x) = {}_z \langle x | \psi \rangle$. We want to show that there exists an anti-symmetric matrix A such that we have $\mathcal{T}(x) = \mathcal{T}(\bar{0}) \text{Pf}(A_{|x})$ for all x . Let us observe that $|z\rangle$ is Gaussian and we can obtain the components via $\mathcal{T}(x) = \langle z | (\gamma_1)^{x_1} \dots (\gamma_{2L-1})^{x_L} | \psi \rangle$. Next, we use the generalized Wick's theorem as stated above for the Gaussian state vectors $|z\rangle$ and $|\psi\rangle$ which gives us $\mathcal{T}(x) = \langle z | \psi \rangle \text{Pf}(i\Delta_{|\bar{x}}) = \mathcal{T}(\bar{0}) \text{Pf}(i\Delta_{|\bar{x}})$ where $\bar{x} = x \otimes (1, 0)^\top$ and therefore \mathcal{T} is a matchgate tensor because we have $A = i\Delta_{|\bar{1} \otimes (1, 0)^\top}$ such that $\mathcal{T}(x) = \mathcal{T}(\bar{0}) \text{Pf}(A_{|x})$.

Section S3. Conversion of generating matrices to covariance matrices

We now convert generating matrices to their corresponding covariance matrix, the entries of which are given by

$$\Gamma_{j,k}(\psi) = \langle \psi | \frac{1}{2} [\gamma_j, \gamma_k] | \psi \rangle \quad (32)$$

This can be seen as the inverse procedure to the Bloch-Messiah reduction that was used above to calculate the normal ordering. Again, the calculation is based on the normal form of anti-symmetric matrices: We use the fact that any anti-symmetric matrix $A \in \mathbb{C}^{L \times L}$ can be put into a normal form $A = W^\top \Sigma W$ where $W \in O(L)$ and Σ is block-diagonal consisting of 2×2 blocks of the form

$$\frac{1}{2} \begin{pmatrix} 0 & \lambda_k \\ -\lambda_k & 0 \end{pmatrix} \quad (33)$$

for L even and additionally a 0 block if it is odd. If A is real, it is easy to find W from the eigenvectors of the hermitian matrix iA , while in the general case the appendix of Ref. [48] provides implicitly a possible algorithm. In the following we will prove a conversion formula for the case of *real* anti-symmetric generating matrices, as the general case is not necessary for the main-text results. In this case λ_k 's are real and we will assume that W is such that $\lambda_k > 0$ without loss of generality. Using this convention we define a set of angles ϕ_k by identifying

$$\cos(\phi_k) := 1/(1 + \lambda_k^2)^{1/2} \quad \text{and} \quad \sin(\phi_k) := \lambda_k/(1 + \lambda_k^2)^{1/2} \quad (34)$$

With these definitions, we state the following conversion lemma.

Lemma 7 ($A \rightarrow \Gamma$ conversion). *Let $A = -A^\top \in \mathbb{R}^{L \times L}$ with normal form $A = W^\top \Sigma W$ as above. Then the state vector $|\psi\rangle = \sqrt{Z}^{-1} \exp(\frac{1}{2} \sum_{j,k=1}^L A_{j,k} f_j^\dagger f_k^\dagger) |\emptyset\rangle$ has the covariance matrix*

$$\Gamma(\psi) = \Xi \tilde{W} V_\phi \Xi^{-1} \Gamma(\emptyset) (\Xi \tilde{W} V_\phi \Xi^{-1})^\top \quad (35)$$

where $\tilde{W} = W \otimes \mathbb{1}_2$, $V_\phi = \bigoplus_{k=1}^{L/2} (\cos(\phi_k) \mathbb{1} + i \sin(\phi_k) \sigma^y \otimes \sigma^x)$ when L is even, or append $\oplus \mathbb{1}_1$ if it is odd and $\Xi = \bigoplus_{k=1}^n \begin{pmatrix} 1 & 1 \\ -i & i \end{pmatrix}$.

Proof. Let U_W be the Gaussian particle number preserving unitary that implements the W action on the modes

$$f_j = U_W f_j^\dagger U_W^\dagger = \sum_{k=1}^L W_{j,k} f_k^\dagger \quad (36)$$

This choice puts the quadratic form into the normal form because

$$\sum_{j,k=1}^L A_{j,k} f_j^\dagger f_k^\dagger = \sum_{j,k=1}^L \sum_{j',k'=1}^L (W^\top)_{j,j'} \Sigma_{j',k'} W_{k',k} f_j^\dagger f_k^\dagger = \sum_{j',k'=1}^L \Sigma_{j',k'} \tilde{f}_{j'}^\dagger \tilde{f}_{k'}^\dagger \quad (37)$$

which gives

$$|\psi\rangle = \sqrt{Z}^{-1} e^{\sum_{j,k=1}^L A_{j,k} f_j^\dagger f_k^\dagger} |\emptyset\rangle = \sqrt{Z}^{-1} \prod_{k=1}^{L/2} e^{\lambda_k \tilde{f}_{2k-1}^\dagger \tilde{f}_{2k}^\dagger} |\emptyset\rangle = \sqrt{Z}^{-1} \prod_{k=1}^{L/2} (1 + \lambda_k \tilde{f}_{2k-1}^\dagger \tilde{f}_{2k}^\dagger) |\emptyset\rangle \quad (38)$$

For ease of notation all sums and products going up to $\lfloor L/2 \rfloor$ will be denoted with an $L/2$ upper limit. From this form we can read off the normalization of $|\psi\rangle$

$$\langle \psi | \psi \rangle = Z^{-1} \prod_{k=1}^{L/2} (1 + \lambda_k^2) = 1 \quad (39)$$

i.e., $Z = \prod_{k=1}^{L/2} (1 + \lambda_k^2)$. Having found that the state is decoupled, for fixed k each term can be promoted to a unitary with the same action on the vacuum $|\emptyset\rangle$. Using the angles ϕ_k defined above through (34) we find that

$$\frac{1 + \lambda_k \tilde{f}_{2k-1}^\dagger \tilde{f}_{2k}^\dagger}{\sqrt{1 + \lambda_k^2}} |\emptyset\rangle = (\cos \phi_k \mathbb{1} + \sin \phi_k \Omega_k) |\emptyset\rangle \quad (40)$$

where we have defined

$$\Omega_k := \tilde{f}_{2k-1}^\dagger \tilde{f}_{2k}^\dagger + \tilde{f}_{2k-1} \tilde{f}_{2k} \quad (41)$$

which is anti-symmetric and hence can be used as a generator for a unitary operator in Hilbert space. By observing that $\Omega_k^2 |\emptyset\rangle = -|\emptyset\rangle$ we find that $U_{\phi_k} = \cos \phi_k \mathbb{1} + \sin \phi_k \Omega_k = e^{\phi_k \Omega_k}$ and using that the $\{\Omega_k\}$ commute we finally arrive at

$$|\psi\rangle = e^{\sum_{k=1}^{L/2} \phi_k \Omega_k} |\emptyset\rangle =: U_\phi |\emptyset\rangle \quad (42)$$

which is an explicit (even) Gaussian rotation of the vacuum. To summarize this decoupling step, we have decoupled the normal-form of the state with U_W to the Bloch-Messiah form and found the Gaussian unitary U_ϕ that rotates the vacuum into the state vector $|\psi\rangle$. Note, that this allows to split any Gaussian unitary U_G acting on the vacuum into a particle number preserving part U_W and a squeezing part U_ϕ . For Majorana operators $\tilde{\gamma}_{2k-1} = \tilde{f}_k + \tilde{f}_k^\dagger$ and $\tilde{\gamma}_{2k} = -i(\tilde{f}_k - \tilde{f}_k^\dagger)$, we define the matrix $\tilde{\Gamma}$ with entries

$$\tilde{\Gamma}_{j,k}(\psi) := \langle \psi | \frac{i}{2} [\tilde{\gamma}_j, \tilde{\gamma}_k] | \psi \rangle \quad (43)$$

By noting that $\tilde{\gamma}_{2k-1} = \sum_{j=1}^L W_{k,j} \gamma_{2j-1}$ and $\tilde{\gamma}_{2k} = \sum_{j=1}^L W_{k,j} \gamma_{2j}$, we find the relation $\tilde{\Gamma}(\psi) = \tilde{W} \Gamma(\psi) \tilde{W}^t$ where

$$\tilde{W} = W \otimes \begin{pmatrix} 1 & 0 \\ 0 & 1 \end{pmatrix} \quad (44)$$

Denoting by

$$\Gamma(\emptyset) = \bigoplus_{k=1}^L \begin{pmatrix} 0 & 1 \\ -1 & 0 \end{pmatrix} \quad (45)$$

the vacuum covariance matrix, it remains to show that $\tilde{\Gamma} = W_\phi \Gamma(\emptyset) W_\phi^\top$ where W_ϕ is defined by $U_\phi^\dagger \tilde{\gamma}_j U_\phi = \sum_{k=1}^{2L} (W_\phi)_{j,k} \tilde{\gamma}_k$. Indeed we find that for $\tilde{f}_k(\phi) = U_\phi^\dagger \tilde{f}_k U_\phi$ we have the block-decoupled equations of motion

$$\partial_{\phi_k} \begin{bmatrix} \tilde{f}_{2k-1}(\phi) \\ \tilde{f}_{2k-1}^\dagger(\phi) \\ \tilde{f}_{2k}(\phi) \\ \tilde{f}_{2k}^\dagger(\phi) \end{bmatrix} = \begin{bmatrix} 0 & 0 & 0 & 1 \\ 0 & 0 & 1 & 0 \\ 0 & -1 & 0 & 0 \\ -1 & 0 & 0 & 0 \end{bmatrix} \begin{bmatrix} \tilde{f}_{2k-1}(\phi) \\ \tilde{f}_{2k-1}^\dagger(\phi) \\ \tilde{f}_{2k}(\phi) \\ \tilde{f}_{2k}^\dagger(\phi) \end{bmatrix} = i\sigma^y \otimes \sigma^x \begin{bmatrix} \tilde{f}_{2k-1}(\phi) \\ \tilde{f}_{2k-1}^\dagger(\phi) \\ \tilde{f}_{2k}(\phi) \\ \tilde{f}_{2k}^\dagger(\phi) \end{bmatrix} \quad (46)$$

and therefore

$$\begin{bmatrix} \tilde{f}_{2k-1}(\phi) \\ \tilde{f}_{2k-1}^\dagger(\phi) \\ \tilde{f}_{2k}(\phi) \\ \tilde{f}_{2k}^\dagger(\phi) \end{bmatrix} = \begin{bmatrix} \cos(\phi_k) & 0 & 0 & \sin(\phi_k) \\ 0 & \cos(\phi_k) & \sin(\phi_k) & 0 \\ 0 & -\sin(\phi_k) & \cos(\phi_k) & 0 \\ -\sin(\phi_k) & 0 & 0 & \cos(\phi_k) \end{bmatrix} \begin{bmatrix} \tilde{f}_{2k-1} \\ \tilde{f}_{2k-1}^\dagger \\ \tilde{f}_{2k} \\ \tilde{f}_{2k}^\dagger \end{bmatrix} = (\cos(\phi_k) \mathbb{1} + \sin(\phi_k) i\sigma^y \otimes \sigma^x) \begin{bmatrix} \tilde{f}_{2k-1} \\ \tilde{f}_{2k-1}^\dagger \\ \tilde{f}_{2k} \\ \tilde{f}_{2k}^\dagger \end{bmatrix} \quad (47)$$

We collect all such rotations to $V_\phi = \bigoplus_{k=1}^{L/2} (\cos(\phi_k) \mathbb{1} + i \sin(\phi_k) \sigma^y \otimes \sigma^x)$ when L is even, and append $\bigoplus \mathbb{1}_1$ if it is odd. Using the relation $\tilde{m} = \Xi \tilde{f}^\dagger$ with

$$\Xi = \bigoplus_{k=1}^n \begin{pmatrix} 1 & 1 \\ -i & i \end{pmatrix} \quad (48)$$

we can switch between the vector of creation annihilation operators and Majorana operators which gives $W_\phi = \Xi V_\phi \Xi^{-1}$, so we find

$$\Gamma(\psi) = \Xi \tilde{W} V_\phi \Xi^{-1} \Gamma(\emptyset) (\Xi \tilde{W} V_\phi \Xi^{-1})^\top \quad (49)$$

Section S4. Contraction rules for generating matrices

A. Contracting two tensors

Now, we explicitly show how contracting two tensors U and V into a tensor W combines the generating matrices A and B of the two original tensors into a larger generating matrix C . We assume that all three tensors are even matchgates, and can thus be written as

$$U(\Theta_U) = c_U \exp\left(\frac{1}{2}\Theta_U^T A \Theta_U\right) \quad (50)$$

$$V(\Theta_V) = c_V \exp\left(\frac{1}{2}\Theta_V^T B \Theta_V\right) \quad (51)$$

$$W(\Theta_W) = c_W \exp\left(\frac{1}{2}\Theta_W^T C \Theta_W\right) \quad (52)$$

where we have defined the vectors Θ_U , Θ_V , and Θ_W of Grassmann variables θ_i as

$$\Theta_U := (\theta_1, \dots, \theta_{d_U})^T \quad (53)$$

$$\Theta_V := (\theta_{d_U+1}, \dots, \theta_{d_U+d_V})^T \quad (54)$$

$$\Theta_W := (\theta_1, \dots, \theta_{d_U-1}, \theta_{d_U+2}, \dots, \theta_{d_U+d_V})^T \quad (55)$$

Thus, A , B , and C are $d_U \times d_U$, $d_V \times d_V$ and $(d_U + d_V - 2) \times (d_U + d_V - 2)$ matrices, respectively. All are anti-symmetric. Note that we want to trace out the degrees of freedom corresponding to the Grassmann variables θ_{d_U} and θ_{d_U+1} , i.e., the last index of U and the first index of V . As we showed earlier, the contraction is equivalent to the Grassmann integration

$$W(\Theta_W) = \int d\theta_{d_U+1} \int d\theta_{d_U} \exp(\theta_{d_U} \theta_{d_U+1}) U(\Theta_U) V(\Theta_V) \quad (56)$$

$$= c_U c_V \int d\theta_{d_U+1} \int d\theta_{d_U} \exp\left(\theta_{d_U} \theta_{d_U+1} + \frac{1}{2}\Theta_U^T A \Theta_U + \frac{1}{2}\Theta_V^T B \Theta_V\right) \quad (57)$$

Notice that we can easily factorize exponentials because binomial terms in Grassmann variables commute, thus making the Baker-Campbell-Hausdorff formula trivial. This also allows us to remove all terms independent of θ_{d_U} and θ_{d_U+1} from the integral

$$\begin{aligned} W(\Theta_W) &= c_U c_V \exp\left(\sum_{i=1}^{d_U-2} \sum_{j=i+1}^{d_U-1} A_{i,j} \theta_i \theta_j + \sum_{i=2}^{d_V-1} \sum_{j=i+1}^{d_V} B_{i,j} \theta_{d_U+i} \theta_{d_U+j}\right) \\ &\cdot \int d\theta_{d_U+1} \int d\theta_{d_U} \exp\left(\theta_{d_U} \theta_{d_U+1} + \sum_{i=1}^{d_U-1} A_{i,d_U} \theta_i \theta_{d_U} + \sum_{j=2}^{d_V} B_{1,j} \theta_{d_U+1} \theta_{d_U+j}\right) \end{aligned} \quad (58)$$

The expansion of the integrand exponential is fairly simple, as all powers higher than two vanish, according to

$$\begin{aligned} \exp\left(\theta_{d_U} \theta_{d_U+1} + \sum_{i=1}^{d_U-1} A_{i,d_U} \theta_i \theta_{d_U} + \sum_{j=2}^{d_V} B_{1,j} \theta_{d_U+1} \theta_{d_U+j}\right) &= 1 + \theta_{d_U} \theta_{d_U+1} + \sum_{i=1}^{d_U-1} A_{i,d_U} \theta_i \theta_{d_U} + \sum_{j=2}^{d_V} B_{1,j} \theta_{d_U+1} \theta_{d_U+j} \\ &+ \sum_{i=1}^{d_U-1} \sum_{j=2}^{d_V} A_{i,d_U} B_{1,j} \theta_i \theta_{d_U} \theta_{d_U+1} \theta_{d_U+j} \end{aligned} \quad (59)$$

Applying the integral leaves us with

$$\begin{aligned} W(\Theta_W) &= c_U c_V \exp\left(\sum_{i=1}^{d_U-2} \sum_{j=i+1}^{d_U-1} A_{i,j} \theta_i \theta_j + \sum_{i=2}^{d_V-1} \sum_{j=i+1}^{d_V} B_{i,j} \theta_{d_U+i} \theta_{d_U+j}\right) \left(1 + \sum_{i=1}^{d_U-1} \sum_{j=2}^{d_V} A_{i,d_U} B_{1,j} \theta_i \theta_{d_U+j}\right) \\ &= c_U c_V \exp\left(\sum_{i=1}^{d_U-2} \sum_{j=i+1}^{d_U-1} A_{i,j} \theta_i \theta_j + \sum_{i=2}^{d_V-1} \sum_{j=i+1}^{d_V} B_{i,j} \theta_{d_U+i} \theta_{d_U+j} + \sum_{i=1}^{d_U-1} \sum_{j=2}^{d_V} A_{i,d_U} B_{1,j} \theta_i \theta_{d_U+j}\right) \end{aligned} \quad (60)$$

We were able to turn the last factor into an exponential because higher powers of the contraction sum are zero, i.e.,

$$\left(\sum_{i=1}^{d_U-1} \sum_{j=2}^{d_V} A_{i,d_U} B_{1,j} \theta_i \theta_{d_U+j} \right)^2 = \left(\sum_{i=1}^{d_U-1} A_{i,d_U} \theta_i \right)^2 \left(\sum_{j=2}^{d_V} B_{1,j} \theta_{d_U+j} \right)^2 = 0 \quad (61)$$

where we have used the fact that any linear combination of Grassmann numbers $\sum_i a_i \theta_i$ is again a Grassmann number, squaring to zero. We can now write the explicit structure of $W(\Theta_W)$ in terms of c_W and C in (52). Obviously, $c_W = c_U c_V$. The matrix C is composed of A and B according the pattern

$$C = \begin{pmatrix} A_{1,1} & \cdots & A_{1,d_U-1} & A_{1,d_U} B_{1,2} & \cdots & A_{1,d_U} B_{1,d_V} \\ \vdots & \ddots & \vdots & \vdots & \ddots & \vdots \\ -A_{1,d_U-1} & \cdots & A_{d_U-1,d_U-1} & A_{d_U-1,d_U} B_{1,2} & \cdots & A_{d_U-1,d_U} B_{1,d_V} \\ -A_{1,d_U} B_{1,1} & \cdots & -A_{d_U-1,d_U} B_{1,1} & B_{2,2} & \cdots & B_{2,d_V} \\ \vdots & \ddots & \vdots & \vdots & \ddots & \vdots \\ -A_{1,d_U} B_{1,d_V} & \vdots & -A_{d_U-1,d_U} B_{1,d_V} & B_{d_V,2} & \cdots & B_{d_V,d_V} \end{pmatrix} \quad (62)$$

$$= \begin{pmatrix} & & & \begin{pmatrix} A_{1,d_U} \\ \vdots \\ A_{d_U-1,d_U} \end{pmatrix} & \begin{pmatrix} B_{1,2} & \cdots & B_{1,d_V} \end{pmatrix} \\ & A_{UL} & & & \\ - \begin{pmatrix} B_{1,2} \\ \vdots \\ B_{1,d_V} \end{pmatrix} & \begin{pmatrix} A_{1,d_U} & \cdots & A_{d_U-1,d_U} \end{pmatrix} & & & B_{BR} \end{pmatrix} \quad (63)$$

The submatrices A_{UL} and B_{BR} are the upper-left and bottom-right part of the matrices A and B , respectively, with one row and column removed. anti-symmetry of A_{UL} and B_{BR} , and by extensions C , implies that all diagonal elements are zero.

This result is indeed quite natural, seen from a diagrammatic perspective, where the matrix C defines the 2-point correlators of the contracted state. The correlation between uncontracted Grassmann variables that lie either completely in Θ_U or Θ_V remains unaffected by the contraction. Correlators $C_{i,j}$ between a θ_i in Θ_U and a θ_j in Θ_V are simply given by $A_{i,d_U} B_{1,j}$, i.e., the product of the correlators over the contracted edge $(\theta_{d_U}, \theta_{d_U+1})$.

B. Self-contractions

Now, consider the more complicated case of self-contraction. We start with the tensor $T(\Theta)$ given by

$$T(\Theta) = c \exp \left(\frac{1}{2} \Theta^T A \Theta \right) = c \exp \left(\sum_{i=1}^{d-1} \sum_{j=i+1}^d A_{i,j} \theta_i \theta_j \right) \quad (64)$$

using the d Grassmann variables $\Theta = (\theta_1, \dots, \theta_d)$. Without loss of generality (we can always perform index permutation), we want to contract the first two indices of T , i.e., contract over θ_1 and θ_2 . Again writing the contraction as a Grassmann integration, we find

$$\begin{aligned} T(\Theta)_{1*2} &= c \int d\theta_2 \int d\theta_1 \exp \left(\theta_1 \theta_2 + \sum_{i=1}^{d-1} \sum_{j=i+1}^d A_{i,j} \theta_i \theta_j \right) \\ &= c \exp \left(\sum_{i=3}^{d-1} \sum_{j=i+1}^d A_{i,j} \theta_i \theta_j \right) \int d\theta_2 \int d\theta_1 \exp \left((1 + A_{1,2}) \theta_1 \theta_2 + \sum_{j=3}^d (A_{1,j} \theta_1 \theta_j + A_{2,j} \theta_2 \theta_j) \right) \end{aligned} \quad (65)$$

Again, we can expand the exponential explicitly, as all terms beyond second order vanish

$$\begin{aligned} \exp \left((1 + A_{1,2}) \theta_1 \theta_2 + \sum_{j=3}^d (A_{1,j} \theta_1 \theta_j + A_{2,j} \theta_2 \theta_j) \right) &= 1 + (1 + A_{1,2}) \theta_1 \theta_2 + \sum_{j=3}^d (A_{1,j} \theta_1 \theta_j + A_{2,j} \theta_2 \theta_j) \\ &\quad + \sum_{i=3}^{d-1} \sum_{j=i+1}^d (A_{i,1} A_{2,j} - A_{i,2} A_{1,j}) \theta_1 \theta_2 \theta_i \theta_j \end{aligned} \quad (66)$$

Only the second and fourth term survive the integration, giving us

$$\begin{aligned}
T(\Theta)_{1\star 2} &= c \exp \left(\sum_{i=3}^{d-1} \sum_{j=i+1}^d A_{i,j} \theta_i \theta_j \right) \left(1 + A_{1,2} + \sum_{i=3}^{d-1} \sum_{j=i+1}^d (A_{i,1} A_{2,j} - A_{i,2} A_{1,j}) \theta_i \theta_j \right) \\
&= c(1 + A_{1,2}) \exp \left(\sum_{i=3}^{d-1} \sum_{j=i+1}^d A_{i,j} \theta_i \theta_j \right) \exp \left(\sum_{i=3}^{d-1} \sum_{j=i+1}^d \frac{A_{i,1} A_{2,j} - A_{i,2} A_{1,j}}{1 + A_{1,2}} \theta_i \theta_j \right) \\
&= c(1 + A_{1,2}) \exp \left(\sum_{i=3}^{d-1} \sum_{j=i+1}^d \left(A_{i,j} + \frac{A_{i,1} A_{2,j} - A_{i,2} A_{1,j}}{1 + A_{1,2}} \right) \theta_i \theta_j \right)
\end{aligned} \tag{67}$$

To get to the second line, we require that the square (and thus higher powers) of the $O(\theta_i \theta_j)$ term vanish

$$\begin{aligned}
\left(\sum_{i=3}^{d-1} \sum_{j=i+1}^d (A_{i,1} A_{2,j} - A_{i,2} A_{1,j}) \theta_i \theta_j \right)^2 &= \left(\sum_{i=3}^d \sum_{j=3}^d A_{i,1} A_{2,j} \theta_i \theta_j \right)^2 \\
&= \left(\sum_{i=3}^d A_{i,1} \theta_i \right)^2 \left(\sum_{j=3}^d A_{2,j} \theta_j \right)^2 = 0
\end{aligned} \tag{68}$$

Thus, we can express the contracted tensor in the form

$$T(\Theta)_{1\star 2} = c_{1\star 2} \exp \left(\frac{1}{2} \Theta_{1\star 2}^T A_{1\star 2} \Theta_{1\star 2} \right) \tag{69}$$

where $\Theta_{1\star 2} = (\theta_3, \theta_4, \dots, \theta_d)$ contains the uncontracted Grassmann variables, and the constant $c_{1\star 2}$ and $(d-2) \times (d-2)$ matrix $A_{1\star 2}$ are given by the original constant c and matrix A according to

$$\begin{aligned}
c_{1\star 2} &= (1 + A_{1,2})c, \\
(A_{1\star 2})_{i,j} &= A_{i,j} + \frac{A_{i,1} A_{2,j} - A_{i,2} A_{1,j}}{1 + A_{1,2}} \\
&= \frac{A_{i,j} + A_{i,j} A_{1,2} + A_{i,1} A_{2,j} - A_{i,2} A_{1,j}}{1 + A_{1,2}}
\end{aligned} \tag{70}$$

$$= \frac{A_{i,j} + A_{i,j} A_{1,2} + A_{i,1} A_{2,j} - A_{i,2} A_{1,j}}{1 + A_{1,2}} \tag{71}$$

The self-contraction integrates out the $A_{1,2}$ correlator, redefining our “vacuum term” c . $(A_{1\star 2})_{i,j}$ now contains all connected and disconnected correlations between site i and j , divided by the vacuum contributions.

C. Cyclic permutations

In order to contract smaller matchgate tensors into larger ones, we need one additional ingredient: rules for cyclic permutation. Our prescription for contracting two tensors U and V works by contracting the last index of U with the first index V , while in the self-contraction case we contracted the first two indices of a tensor T . Clearly, we can satisfy both conditions by cyclically permuting the indices of the tensors in question, i.e., relabeling the Grassmann variables. We write a cyclic permutation by n bits as $\sigma_n(\Theta)$, for example

$$\sigma_1(\theta_1 \theta_2 - \theta_2 \theta_3) = \theta_1 \theta_3 + \theta_2 \theta_3 \tag{72}$$

It is easy to see that the cyclic permutation of a Gaussian matchgate tensor $T(\Theta)$ is given by

$$\sigma_n(T(\Theta)) = \sigma_n \left(c \exp \left(\frac{1}{2} \Theta^T A \Theta \right) \right) = c \exp \left(\frac{1}{2} \Theta^T \sigma_n(A) \Theta \right) \tag{73}$$

where the new correlation matrix $\sigma_n(A)$ is simply A where the i -th row and j -th column is replaced by the $(i+n)$ th row and the $(j+n)$ th column modulo m (where m is the length of the vector of Grassman variables Θ). With these rules for permutations, contractions and self-contractions, we can contract any planar network of Gaussian matchgate tensors. For odd tensors, where an integral over an additional source term of auxiliary Grassmann variables is required, the rules become significantly more complicated.

D. Graph orientation and boundary conditions

We now show how a complete network is contracted using the tools developed earlier. As a concrete example, consider the contraction of 11 pentagons (i.e., tensors with five indices) in a $\{5, 4\}$ tiling shown in Fig. S2. We start with an initial labeling of all pentagon edges in a clockwise orientation, with each index i corresponding to an independent Grassmann variable θ_i . Starting from the central tensor, we start contracting adjacent tensors, using cyclic permutations of the indices to ensure that the largest index of the first tensor is adjacent to the smallest index of the second tensor. This process can be easily repeated until a tensor with two adjacent edges is encountered. We then contract from the edge with the smaller index (in clockwise orientation), which leaves a protruding double-edge that can be removed through self-contraction.

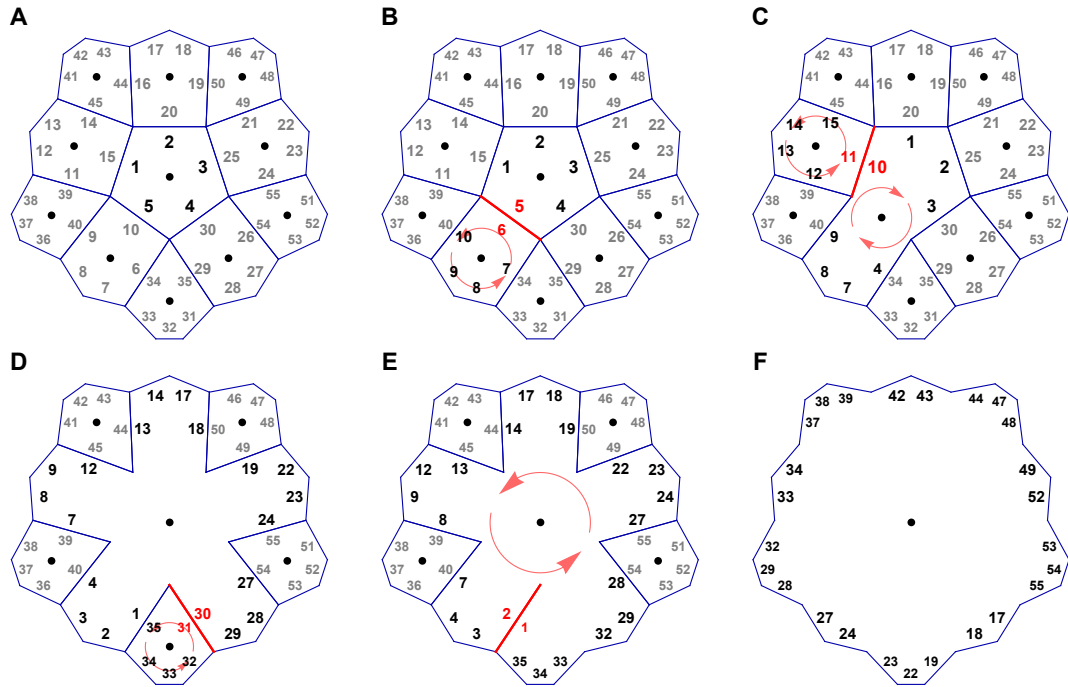


Fig. S2. Tile orientations under contraction. Schematic contraction of 11 pentagons (steps A-F), using contractions over joint edges, self-contraction and cyclic permutation of indices. Contracted edges and indices are marked in red, while cyclic permutations are shown by circular arrows.

After all tensors are contracted, we are left with a boundary of edges whose indices are still clockwise-oriented, provided that our initial labeling of pentagon edges followed the order in which we contracted the respective tensors. We can think of the remaining indices as specifying our boundary sites, and the contracted indices being bulk sites that were “integrated out”. Note that this contraction process is possible for planar graphs for which a Kasteleyn orientation is guaranteed to exist [46].

In principle, we have the freedom to cyclically permute the indices of each initial tensor. We can fix this freedom by using symmetry constraints on the generating matrix $A_{i,j}$. For anti-periodic boundary conditions, we require $A_{i,j}$ to be positive for $i > j$ and negative for $i < j$. The condition is retained for the full contracted state if we restrict ourselves to applying cyclic permutations only on the indices of the “inner” tensor from which we contract outwards, and affix the lowest index of each “outer tensor” to the edge over which it is first contracted. These conditions on $A_{i,j}$ allowed us to produce physical covariance matrices with $\Gamma_{i,j} > 0$ for $i > j$, as well.

For periodic boundary conditions, $A_{i,j}$ should be positive for $|i - j| < L/2$ (with number of indices L) and negative otherwise. This can be achieved using the same index labeling rules, but choosing *only* the central tensor’s generating matrix to produce a locally anti-periodic state, while keeping the states corresponding to all other local tensors as periodic.

Periodic boundary conditions are less convenient for numerical studies, as overlap between positive and negative correlations can occur for networks of finite size. For this reason, we have focused on anti-periodic boundary conditions in our work. In the infinite-size limit, of course, both choices of boundary conditions should lead to the same physical properties of the boundary states.

Table S1. Values of the critical generating matrix parameter a for different $\{3, k\}$ triangular tilings and ultraviolet cutoffs.

d_c	$k = 6:$	r_c	$k = 7:$	$k = 8:$	$k = 9:$	$k = 10:$	$k = 11:$	$k = 12:$
10	0.5779	0.95	0.6063	0.6213	0.6378	0.6482	0.6529	0.6650
15	0.5804	0.98	0.6051	0.6203	0.6404	0.6447	0.6618	0.6639
20	0.5806	0.99	0.6082	0.6244	0.6393	0.6502	0.6575	0.6661

Section S5. Explicit generating matrices and numerical results**A. Regular tilings**

We start by discussing the correlations achieved for regular tilings. We can produce the boundary theory with $\sim 1/d$ falloff using a regular $\{3, k\}$ tiling with $k \geq 6$. The critical parameter $a = a_{\text{crit}}$ for each k can be found by maximizing mean long-range correlations $(2/L) \sum_{k=1}^{L/2} |\Gamma_{k, k+L/2}|$ in the covariance matrix. For $k > 6$, the tilings can be embedded into the Poincaré disk with metric

$$ds^2 = 4 \frac{dr^2 + r^2 d\phi^2}{(1 - r^2)^2} \quad (74)$$

using polar coordinates (r, ϕ) with $0 \leq r < 1$ and $0 \leq \phi < 2\pi$. As the Poincaré disk represents an infinite volume, we cut off our tilings at a radius $r = r_c$. For the flat case $k = 6$, we simply cut off at Euclidean distance d_c (with all edges set to unit length). The resulting values of a_{crit} for a given d ($k = 6$) or r_c ($k > 6$) are shown in Table S1. Note that increasing k leads to a larger a_c . We argue that this may compensate for the “leaking” of correlations into the higher-curvature bulk. While in principle it is possible to extend this reasoning to positive-curvature (spherical) tilings, the largest triangular tiling $\{3, 5\}$ corresponds to an icosahedron with only 20 triangles. Thus, no proper choice of an asymptotic boundary can be made.

B. MERA

We now turn to discussing how the MERA framework can be related to our approach. The MERA tensor network consists of two types of tensors, isometries and disentanglers with three and four legs, respectively. Thus, the lattice for the equivalent matchgate tensor consists of triangles and quadrilaterals. In the matchgate setting, the MERA tensors are thus fully specified by a 3×3 generating matrix S and a 4×4 matrix B , corresponding to isometries and disentanglers, respectively. For norm-preserving tensors, i.e. unitary disentanglers and isometries, real generating matrices are restricted to the components

$$A = \begin{pmatrix} 0 & \sqrt{1+x^2} \cos \theta & \sqrt{1+x^2} \sin \theta \\ -\sqrt{1+x^2} \cos \theta & 0 & x \\ -\sqrt{1+x^2} \sin \theta & -x & 0 \end{pmatrix} \quad (75)$$

$$B = \begin{pmatrix} 0 & y & \sqrt{1+y^2} \cos \phi & \sqrt{1+y^2} \sin \phi \\ -y & 0 & -\sqrt{1+y^2} \sin \phi & \sqrt{1+y^2} \cos \phi \\ -\sqrt{1+y^2} \cos \phi & \sqrt{1+y^2} \sin \phi & 0 & y \\ -\sqrt{1+y^2} \sin \phi & -\sqrt{1+y^2} \cos \phi & -y & 0 \end{pmatrix} \quad (76)$$

with $x, y \in \mathbb{R}$ and $\theta, \phi \in [0, 2\pi]$. These free parameters of the model can be set by numerically minimizing the ground-state energy of the translation-invariant Ising Hamiltonian

$$H = i \left(\sum_{i=1}^{L-1} \gamma_i \gamma_{i+1} + \gamma_1 \gamma_L \right) \quad (77)$$

However, with these inputs we were unable to find boundary states that are any more translation-invariant than the regular tilings considered earlier. Instead, we consider a more generic “matchgate MERA” (mMERA) with three- and four-leg generating matrices

$$A = \begin{pmatrix} 0 & a & a \\ -a & 0 & b \\ -a & -b & 0 \end{pmatrix}, \quad B = \begin{pmatrix} 0 & c & e & f \\ -c & 0 & d & e \\ -e & -d & 0 & c \\ -f & -e & -c & 0 \end{pmatrix} \quad (78)$$

with the parameters $a, b, \dots, f \in \mathbb{R}$. Now, again minimizing according to (77), we find that numerical solutions obey the symmetries $c \approx e$ and $a \approx d \approx f$, thus leaving us with three free parameters to optimize. Intriguingly, these symmetries allow us to express the 4-leg “disentangler” as contractions of a 3-leg tensor with its conjugate, visualized in Fig. S3. While the individual tensors of our model are no longer norm-preserving, we show in the next section that for large networks, norm preservation can still be achieved. Note that while the usual MERA identities for isometries and disentanglers no longer hold, contractions of the mMERA are still efficient, owing to the matchgate setting.

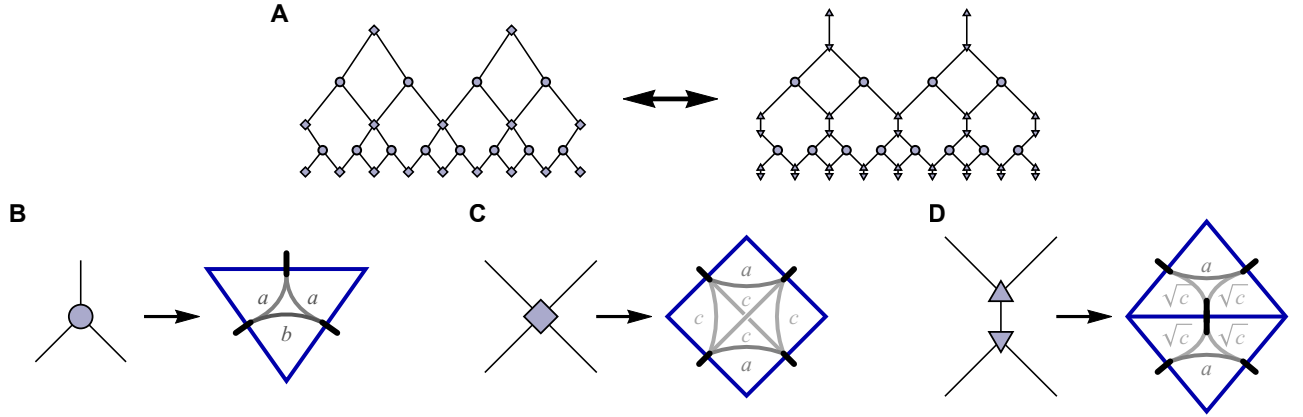


Fig. S3. Constructing the mMERA. **A:** The standard MERA tensor network (left) in our numerical matchgate setting is equivalent to a network of purely 3-leg tensors (right). **B-D:** Isometries, disentanglers, and triangulated disentanglers (from left to right) expressed as matchgate tensors. The free parameters a, b, c fix the components of the generating matrices (78).

The central 4-leg tensor of the MERA describes a CFT ground state on four sites, for which the generating matrix A_0 and normalization c_0 can be given explicitly:

$$A_0 = \begin{pmatrix} 0 & a_0 & b_0 & a_0 \\ -a_0 & 0 & a_0 & b_0 \\ -b_0 & -a_0 & 0 & a_0 \\ -a_0 & -b_0 & -a_0 & 0 \end{pmatrix}, \quad c_0 = \frac{1}{\sqrt{1 + 4a_0^2 - 2b_0^2 + (2a_0^2 - b_0^2)^2}} \quad (79)$$

where the constants a_0 and b_0 are found by analytically minimizing (77), yielding

$$a_0 = \sqrt{1 + \frac{1}{\sqrt{2}}} - 1 \approx 0.3066, \quad b_0 = \frac{68 + 8a_0 + 532a_0^2 - 616a_0^3 - 290a_0^4 - 58a_0^5}{43 + 16a_0 - 340a_0^2 - 474a_0^3 - 250a_0^4 - 50a_0^5} \approx 0.2346 \quad (80)$$

All remaining tensors are numerically optimized within our three-parameter model. As shown in Fig. S4, the minimal energy density $\epsilon = \langle H \rangle / L$ converges quadratically with the number of boundary sites L . The optimal values for a, b, c converge as well. At $L = 1024$, those are given by $a = 0.6854$, $b = 0.5246$, and $c = 0.2172$, yielding a ground-state energy density $\epsilon_0 = -0.636533$ (decimals given up to convergent digits). The relative error with respect to the continuum solution $\epsilon_0 = 2/\pi$ is about 0.014%. Note that this MERA model only has bond dimension $\chi = 2$, and that increasing χ would increase the size of the generating matrices and the number of free parameters, presumably allowing for even higher accuracy.

C. Conformal data

In this subsection, we show how to obtain conformal data from the approach taken here. The Ising theory at criticality can be described by a 1+1-dimensional conformal field theory (CFT) [51]. The operator content of this theory is defined by its primary fields, whose scaling behavior is exactly known. This is because two-dimensional CFTs can be solved exactly, usually by mapping the space and time coordinates (x, t) to a complex number $z = x + it$ and its complex conjugate $\bar{z} = x - it$. (Quasi-)primary fields $\phi(z)$ have associated *conformal weights* h_ϕ and \bar{h}_ϕ , with correlations between different space-time points z and w being given by

$$\langle \phi(z)\phi(w) \rangle = \frac{C_{\phi,\phi}}{(z-w)^{2h_\phi}(\bar{z}-\bar{w})^{2\bar{h}_\phi}} \quad (81)$$

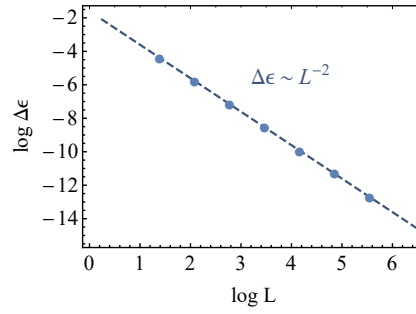


Fig. S4. Energy convergence of mMERA. Energy density ϵ of the mMERA boundary state of L sites, minimized with respect to the Ising Hamiltonian (77). Plotted are the differences $\Delta\epsilon = \epsilon(2L) - \epsilon(L)$ between two mMERA layers, with a quadratic falloff, fitted from the data, shown as a gray line.

Table S2. Exact conformal scaling dimension of various (quasi-)primary fields ϕ of the Ising CFT.

Field ϕ	$\mathbb{1}$	ϵ	σ	ψ	$\bar{\psi}$
h_ϕ	0	1/2	1/16	1/2	0
\bar{h}_ϕ	0	1/2	1/16	0	1/2
Δ_ϕ	0	1	1/8	1/2	1/2

The constant $C_{\phi,\phi}$ is not a fundamental CFT parameter, but determined by the normalization of ϕ . As we are restricting ourselves to correlations on time-slices, we will find correlators of the form

$$\langle \phi(x)\phi(y) \rangle = \frac{C_{\phi,\phi}}{|x-y|^{2(h_\phi+\bar{h}_\phi)}} = \frac{C_{\phi,\phi}}{|x-y|^{2\Delta_\phi}} \quad (82)$$

expressed in terms of the *scaling dimension* $\Delta_\phi = h_\phi + \bar{h}_\phi$. The three-point functions of primary fields ϕ, χ and ω have the form

$$\langle \phi(x)\chi(y)\omega(z) \rangle = \frac{\sqrt{C_{\phi,\phi}C_{\chi,\chi}C_{\omega,\omega}} C_{\phi,\chi,\omega}}{|x-y|^{\Delta_\phi+\Delta_\chi-\Delta_\omega} |y-z|^{\Delta_\chi+\Delta_\omega-\Delta_\phi} |z-x|^{\Delta_\omega+\Delta_\phi-\Delta_\chi}} \quad (83)$$

with the *structure constants* $C_{\phi,\chi,\omega}$ being fundamental CFT quantities.

For the Ising CFT in two dimensions, there are three primary fields: The identity $\mathbb{1}$, the energy density ϵ and the spin (or “order parameter”) σ . The Jordan-Wigner transformation gives us an alternative description in terms of the fermionic fields ψ and $\bar{\psi}$. The corresponding scaling dimensions are given in Table S2. Furthermore, the structure constants in the spin sector are given by $C_{\sigma,\sigma,\mathbb{1}} = 1$ and $C_{\sigma,\sigma,\epsilon} = \frac{1}{2}$.

For the Gaussian states produced by our matchgate tensor networks, all the information on correlators is stored in the Majorana covariance matrix with entries $\Gamma_{j,k} = \langle \frac{i}{2}[\gamma_j, \gamma_k] \rangle$. Before calculating the scaling dimensions, let us first prove a useful identity regarding the covariance matrix of odd-pairing Hamiltonians of the form

$$H_{\text{OP}} = i \sum_{k,d} J_{k,d} \gamma_k \gamma_{k+2d-1} \quad (84)$$

with the couplings $J_{k,d} \in \mathbb{R}$ between Majorana sites at odd distance. In particular, this includes Hamiltonians with only nearest-neighbor Majorana coupling with $J_{k,d} = \delta_{d,1} J_k$, such as the Ising model considered above.

Lemma 8 (Covariance matrices of odd-pairing Majorana Hamiltonians). *Eigenstates of Hamiltonians H_{OP} of the form (84) are described by a covariance matrix Γ whose entries $\Gamma_{j,k}$ vanish for even $j+k$.*

Proof. Consider an eigenstate $|\psi\rangle = \sum_{x \in \{0,1\}^n} \mathcal{T}(x) |x\rangle$ of H_{OP} with eigenenergy E . We will first prove that $\mathcal{T}(x) \in \mathbb{R}$ for all $x \in \{0,1\}^n$. We first note that we can write

$$\begin{aligned} H_{\text{OP}} &= i \sum_{i,d} (J_{2i-1,d} \gamma_{2i-1} \gamma_{2i+2d-2} + J_{2i,d} \gamma_{2i} \gamma_{2i+2d-1}) \\ &= \sum_{i,d} \left(J_{2i-1,d} (f_i + f_i^\dagger)(f_{i+d-1} - f_{i+d-1}^\dagger) + J_{2i,d} (f_i - f_i^\dagger)(f_{i+d} + f_{i+d}^\dagger) \right) \end{aligned} \quad (85)$$

which implies that the Hamiltonian is not only Hermitian but also invariant under complex conjugation $H_{\text{OP}}^* = H_{\text{OP}}$. We now decompose our eigenstate into its real and imaginary part denoted by $|\psi\rangle = \Re[|\psi\rangle] + i \Im[|\psi\rangle]$. The eigenequation reads

$$H_{\text{OP}} |\psi\rangle = E |\psi\rangle \quad (86)$$

and its complex conjugate can be expressed as

$$(H_{\text{OP}} |\psi\rangle)^* = H_{\text{OP}} |\psi\rangle^* = H_{\text{OP}} \Re[|\psi\rangle] - i H_{\text{OP}} \Im[|\psi\rangle] \stackrel{\text{!}}{=} E \Re[|\psi\rangle] - i E \Im[|\psi\rangle] \quad (87)$$

where the only difference to the original equation is the minus sign. Adding and subtracting these two equations yields

$$H_{\text{OP}} \Re[|\psi\rangle] = E \Re[|\psi\rangle] \quad (88)$$

and

$$H_{\text{OP}} \Im[|\psi\rangle] = E \Im[|\psi\rangle] \quad (89)$$

which means that $\Re[|\psi\rangle]$ and $\Im[|\psi\rangle]$ are both eigenvectors. If the spectrum is non-degenerate then they are collinear and hence we can assume that $|\psi\rangle^* = |\psi\rangle$ up to a phase. If the spectrum is degenerate then we can also choose real eigenstates because $\text{span}(|\psi\rangle, |\psi\rangle^*) = \text{span}(\Re[|\psi\rangle], \Im[|\psi\rangle])$. In the context of matchgates, this means that all eigenstates are expressed by real generating matrices, which are therefore a suitable ansatz for ground states of such Hamiltonians.

Next, we show that the matrix elements of the covariance matrix vanish for even $j+k$. For $j=k$ this is true by definition, so we assume $j \neq k$. For even j and k we find $\frac{1}{2}[\gamma_j, \gamma_k] = i \gamma_j \gamma_k = -i (f_{j/2} - f_{j/2}^\dagger)(f_{k/2} - f_{k/2}^\dagger)$ while for odd j and k we have $\frac{1}{2}[\gamma_j, \gamma_k] = i \gamma_j \gamma_k = i (f_{(j+1)/2} + f_{(j+1)/2}^\dagger)(f_{(k+1)/2} + f_{(k+1)/2}^\dagger)$. Either way, these Hermitian operators have purely imaginary coefficients in terms of creation and annihilation operators. Evaluated in a state with real amplitudes, as shown above, the expectation value can only be imaginary. As all observables are real, it must therefore vanish altogether.

Now let us relate the covariance matrix entries $\Gamma_{j,k}$ to the primary fields. By construction of our covariance matrix in Section S3, $\langle \psi | \psi \rangle = 1$ and thus the identity $\mathbb{1}$ does not scale. However, the normalization factor Z in (39) can in principle scale with the size of the contracted network. To ensure normalization, we have to act on each of the N_T contracted tensors with a scaling factor $f = Z^{-1/(2N_T)}$. We find that this factor f converges for large systems, ensuring $\Delta_{\mathbb{1}} = 0$. Explicitly, $f_{\{3,6\}} \approx 0.972$ and $f_{\{3,7\}} \approx 0.941$ for the regular tilings and $f_{\text{mMERA}} \approx 0.959$ for the mMERA.

We identify the fermionic fields ψ and $\bar{\psi}$ with physical operators $\psi_k := f_k = \frac{1}{2}(\gamma_{2k-1} + i \gamma_{2k})$ and $\bar{\psi}_k := i f_k^\dagger = \frac{1}{2}(i \gamma_{2k-1} + \gamma_{2k})$. We then find that

$$\langle \psi_j \psi_k \rangle = \langle \bar{\psi}_j \bar{\psi}_k \rangle = \frac{1}{4} (\Gamma_{2j,2k-1} + \Gamma_{2j-1,2k}) \quad (90)$$

Note that we have used Lemma 8 to simplify the result. As we are considering Gaussian states, $\langle \psi_k \rangle = \langle \bar{\psi}_k \rangle = 0$ for any k , so we do not have to consider expectation values of the individual fields. Next, we compute the energy density ϵ . On site k , we simply consider the local operator $\epsilon_k := i \psi_k \bar{\psi}_k = \frac{1}{2} \gamma_{2k-1} \gamma_{2k}$. With this definition, $\langle \epsilon \rangle \neq 0$, so we need to subtract the field's expectation value to compute physical two-point correlators, equivalent to using a field $\epsilon' = \epsilon - \langle \epsilon \rangle$. Using Wick's theorem, the two-point functions then follow as

$$\langle \epsilon_j \epsilon_k \rangle - \langle \epsilon_j \rangle \langle \epsilon_k \rangle = \frac{1}{4} (-\langle \gamma_{2j-1} \gamma_{2j} \gamma_{2k-1} \gamma_{2k} \rangle + \langle \gamma_{2j-1} \gamma_{2j} \rangle \langle \gamma_{2k-1} \gamma_{2k} \rangle) = \frac{1}{4} \Gamma_{2j-1,2k} \Gamma_{2j,2k-1} \quad (91)$$

The order σ is a nonlocal operator in the Majorana picture but corresponds to a σ^x operator in the spin picture, obtained through a Jordan-Wigner transformation (similarly, ϵ can be related to the σ^z operator, which only acts locally in terms of Majorana operators). A two-point correlator of σ_k^x at different sites j and k corresponds to a chain of Majorana operators,

$$\langle \sigma_k^x \sigma_{k+1}^x \rangle = -i \langle \gamma_{2k} \gamma_{2k+1} \rangle = -\text{Pf} \begin{pmatrix} \Gamma_{2k,2k} & \Gamma_{2k,2k+1} \\ \Gamma_{2k+1,2k} & \Gamma_{2k+1,2k+1} \end{pmatrix} \quad (92)$$

$$\langle \sigma_k^x \sigma_{k+2}^x \rangle = -\langle \gamma_{2k} \gamma_{2k+1} \gamma_{2k+2} \gamma_{2k+3} \rangle = \text{Pf} \begin{pmatrix} \Gamma_{2k,2k} & \Gamma_{2k,2k+1} & \Gamma_{2k,2k+2} & \Gamma_{2k,2k+3} \\ \Gamma_{2k+1,2k} & \Gamma_{2k+1,2k+1} & \Gamma_{2k+1,2k+2} & \Gamma_{2k+1,2k+3} \\ \Gamma_{2k+2,2k} & \Gamma_{2k+2,2k+1} & \Gamma_{2k+2,2k+2} & \Gamma_{2k+2,2k+3} \\ \Gamma_{2k+3,2k} & \Gamma_{2k+3,2k+1} & \Gamma_{2k+3,2k+2} & \Gamma_{2k+3,2k+3} \end{pmatrix} \quad (93)$$

$$\langle \sigma_j^x \sigma_k^x \rangle = (-i)^{k-j} \langle \gamma_{2j} \gamma_{2j+1} \cdots \gamma_{2k-2} \gamma_{2k-1} \rangle = (-1)^{k-j} \text{Pf} (\Gamma_{|2j,2k-1|}) \quad (94)$$

The absolute value of the Pfaffian is given by $|\text{Pf}(M)| = \sqrt{\det M}$. Note that because σ_k^x is an odd product of Majorana operators, $\langle \sigma_k^x \rangle = 0$.

Additionally, we compute the structure constant $C_{\sigma,\sigma,\epsilon}$ from the corresponding three-point correlator:

$$\langle \sigma_j^x \sigma_k^x \epsilon_l \rangle - \langle \sigma_j^x \sigma_k^x \rangle \langle \epsilon_l \rangle = \frac{-1}{2} \left((-i)^{k-j+1} \langle \gamma_{2j} \gamma_{2j+1} \cdots \gamma_{2k-2} \gamma_{2k-1} \gamma_{2l-1} \gamma_{2l} \rangle + (-1)^{k-j} \text{Pf}(\Gamma_{|[2j,2k-1]}) \Gamma_{2l-1,2l} \right) \quad (95)$$

$$= \frac{(-1)^{k-j}}{2} \left(\text{Pf}(\Gamma_{|[2j,2k-1] \cap \{2l-1,2l\}}) - \text{Pf}(\Gamma_{|[2j,2k-1]}) \Gamma_{2l-1,2l} \right) \quad (96)$$

In order to use this result to compute the value of $C_{\sigma,\sigma,\epsilon}$ as in (83), we consider the special case $k - j = l - k = d$, for some integer distance d . We then expect a scaling

$$\langle \sigma_j^x \sigma_{j+d}^x \epsilon_{j+2d} \rangle - \langle \sigma_j^x \sigma_{j+d}^x \rangle \langle \epsilon_{j+2d} \rangle = \frac{C_{\sigma,\sigma} \sqrt{C_{\epsilon,\epsilon}} C_{\sigma,\sigma,\epsilon}}{2 \Delta_\epsilon d^{2\Delta_\sigma + \Delta_\epsilon}} \quad (97)$$

Using these tools for extracting two- and three-point correlators, we compute the scaling powers p_ϕ for the various fields ϕ by fitting the dependence of $\langle \phi_i \phi_{i+d} \rangle$ on distance d . The resulting graphs for $\phi \in \{\psi, \epsilon, \sigma\}$ are presented for the regular $\{3, 6\}$ and $\{3, 7\}$ tilings as well as for the mMERA tiling in figures S7, S8 and S9, respectively. We also compute $C_{\sigma,\sigma,\epsilon}$ with (95) and (97), using the scaling dimensions $\Delta_\sigma, \Delta_\epsilon$ and normalizations $C_{\sigma,\sigma}, C_{\epsilon,\epsilon}$ from the previous fits as inputs. Furthermore, we compute the energy density $\epsilon_0 = \langle H \rangle / L$ with respect to the Ising Hamiltonian (77). Note that the regular $\{3, 6\}$ and $\{3, 7\}$ tilings are not translation invariant, leading to irregularities on small scales and amplified finite-size effects. This also leads to larger deviations from the exact ground state energy density $\epsilon_0 = -2/\pi$.

Finally, we can also compute the *central charge* c characterizing the CFT. This is achieved by considering the scaling of the entanglement entropy S_A with the subsystem size $\ell = |A|$. The exact result for a critical theory is given by [33, 34]

$$S_A = \frac{c}{3} \ln \left(\frac{L}{\pi \epsilon} \sin \frac{\pi \ell}{L} \right) \simeq \frac{c}{3} \ln \frac{\ell}{\epsilon} + O((\ell/L)^2) \quad (98)$$

where L is again the size of the total system. For the Ising CFT, we expect $c = 1/2$. The entanglement entropy S_A for $A = [k, k + \ell]$ can be computed from the symplectic eigenvalue spectrum of the partial covariance matrix $\Gamma_{|A}$ [52]. In detail, one performs an orthogonal transformation $\Gamma_{|A} = Q \tilde{\Gamma}_{|A} Q^T$ into the form

$$\tilde{\Gamma}_{|A} = \bigoplus_{i=1}^L \begin{pmatrix} 0 & \lambda_i \\ -\lambda_i & 0 \end{pmatrix} \quad (99)$$

which is most conveniently achieved using numerical Schur decomposition, and then reading off the entanglement entropy as

$$S_A = \sum_{i=1}^L \left(-\frac{1 + \lambda_i}{2} \log \frac{1 + \lambda_i}{2} - \frac{1 - \lambda_i}{2} \log \frac{1 - \lambda_i}{2} \right) \quad (100)$$

Our combined results for scaling dimensions, the structure constant $C_{\sigma,\sigma,\epsilon}$, the ground state energy ϵ_0 and the central charge c are summarized in Fig. 4 of the main text.

D. IR cutoff

While the matchgate model is restricted to planar graphs, it is possible to construct an effective IR cutoff, i.e. a ‘‘black hole horizon’’, by changing the tensor content of tensors in the center of the network. For a regular $\{3, k\}$ tiling with $k \geq 7$ this cutoff is simply a cutoff radius r_{cut} in the Poincaré disk with $0 \leq r_{\text{cut}} < 1$. For a flat $\{3, 6\}$ tiling r_{cut} becomes a radius in the flat Euclidean plane with $0 \leq r_{\text{cut}} < \infty$. While the MERA can also be embedded in the Poincaré disk, it is more convenient to define a cutoff layer n_{cut} , with the first n_{cut} MERA layers (isometries and disentanglers) and the central tensor being affected.

There are two natural choices for the tensor’s generating matrices A in the cutoff region: Either setting all components $A_{i,j}$ with $i < j$ to zero or to one, corresponding to a local vacuum or a fully occupied state, respectively. We find that both produce gapped states on the boundary, but that the former choice leads to periodic boundary conditions, while the latter produces anti-periodic ones. As we have been considering the anti-periodic case in the previous examples, we also choose this case here.

The results are shown in Fig. S9 with regard to the scaling of the fermionic field ψ and the dependence of the entanglement entropy S_A on the length l of the subsystem A . Outside of the cutoff region, the tensor content is identical to the one used to produce a boundary Ising CFT in the previous section.

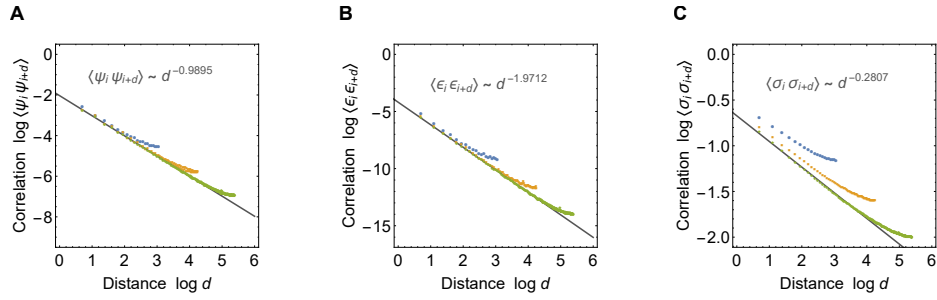


Fig. S5. Determining scaling dimensions of flat tilings. Scaling of primary operators ψ , ϵ and σ (A-C) in the regular $\{3,6\}$ tiling for boundary states of 84, 282, and 870 Majorana sites (blue, yellow and green points, respectively). Numerical fit of scaling power law shown as grey line. Correlators $\langle \phi_i \phi_{i+d} \rangle$ of fields ϕ at distance d are averaged over all sites i .

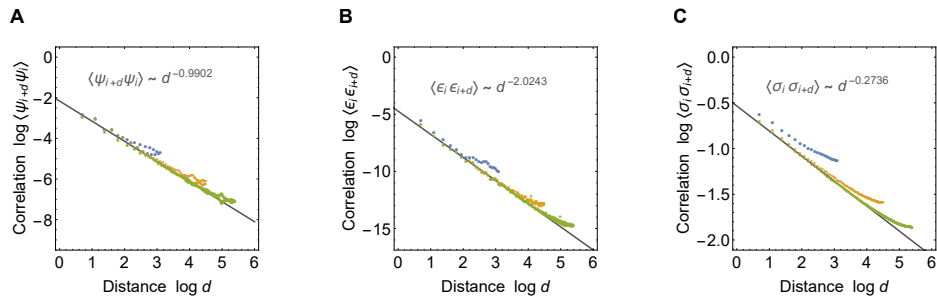


Fig. S6. Determining scaling dimensions of hyperbolic tilings. Scaling of primary operators ψ , ϵ and σ (A-C) in the regular $\{3,7\}$ tiling for boundary states of 90, 360, and 876 Majorana sites (blue, yellow and green points, respectively). Numerical fit of scaling power law shown as grey line. Correlators $\langle \phi_i \phi_{i+d} \rangle$ of fields ϕ at distance d are averaged over all sites i .

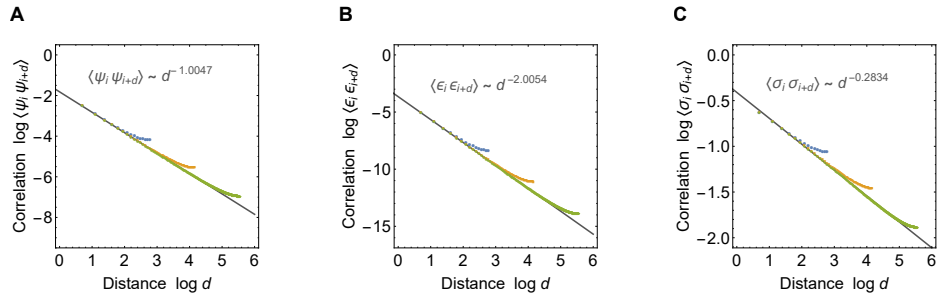


Fig. S7. Determining scaling dimensions of mMERA. Scaling of primary operators ψ , ϵ and σ (A-C) in the mMERA tiling for boundary states of 64, 256, and 1024 Majorana sites (blue, yellow and green points, respectively). Numerical fit of scaling power law shown as grey line. Correlators $\langle \phi_i \phi_{i+d} \rangle$ of fields ϕ at distance d are averaged over all sites i .

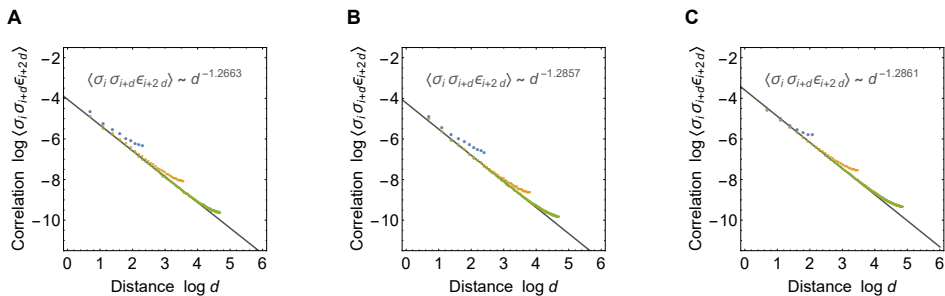


Fig. S8. Determining structure constants. Scaling of the three-point function $\langle \sigma_i \sigma_{i+d} \epsilon_{i+2d} \rangle$ at distance d , averaged over all sites i , for the regular $\{3,6\}$ and $\{3,7\}$, as well as the mMERA tilings (A-C). Numerical fit of scaling power law, based on the data from Fig. S5-S7, shown as grey line.

After a characteristic length scale ξ depending on the cutoff, we see that the ψ field's power law scaling transitions to an exponential falloff, as would be expected in a gapped (massive) theory. Furthermore, S_A saturates for $l > \xi$, which allows us to directly extract ξ from the entanglement entropy formula for a massive QFT [34],

$$S_A = \frac{c}{3} \log \frac{\xi}{a}, \quad (101)$$

which holds in the limit where ξ is much larger than the lattice spacing a . The values for c and a are given by the full entanglement entropy scaling (98) at zero cutoff (note that a depends on the tiling). Without a cutoff, ξ can be identified with the length of the system, which is infinite in the CFT limit.

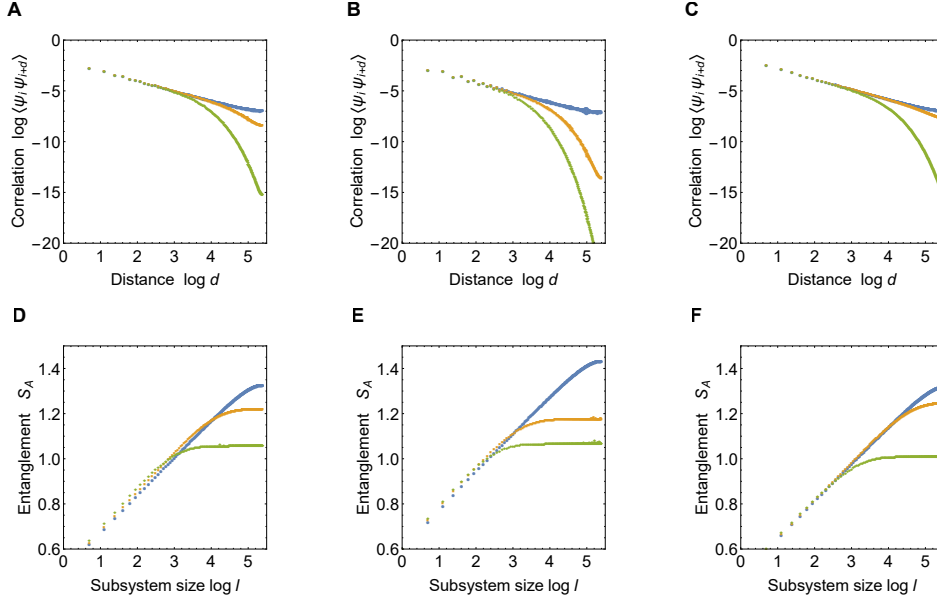


Fig. S9. Correlations and entanglement with IR cutoff. Scaling of the $\langle \psi_i \psi_{i+d} \rangle$ correlator with distance d (A-C) as well as the entanglement entropy S_A with subsystem length $l = |A|$ (D-F) at various cutoffs for the $\{3, 6\}$, $\{3, 7\}$ and MERA tiling (left to right). The cutoffs are $r_c = 0, 50, 75$ ($\{3, 6\}$ case with 870 Majorana boundary sites), $r_c = 0.0, 0.8, 0.9$ ($\{3, 7\}$ case with 876 sites), and $n_c = 0, 2, 4$ (MERA case with 1024 sites), the data for each cutoff plotted in blue, yellow and green, respectively.

E. Pentagon code for quantum error correction

First, consider the boundary state of a single pentagon. Explicitly, the $+1$ logical state vector of the quantum error correcting code is given by

$$|\bar{0}\rangle = N \exp \left(\frac{1}{2} \sum_{i,j} A_{i,j}^+ f_i^\dagger f_j^\dagger \right) |\emptyset\rangle, \quad (102)$$

with a normalization factor $N = \frac{1}{4}$ and the 5×5 generating matrix

$$A^+ = \begin{pmatrix} 0 & -1 & 1 & 1 & -1 \\ 1 & 0 & -1 & 1 & 1 \\ -1 & 1 & 0 & -1 & 1 \\ -1 & -1 & 1 & 0 & -1 \\ 1 & -1 & -1 & 1 & 0 \end{pmatrix}.$$

Correspondingly, the -1 logical state vector is given by

$$|\bar{1}\rangle = N \exp \left(\frac{1}{2} \sum_{i,j} A_{i,j}^- f_i^\dagger f_j^\dagger \right) \int d\eta \exp \left(\eta \sum_i B_i^- f_i^\dagger \right) |\widetilde{\emptyset}\rangle, \quad (103)$$

containing an integration over the auxiliary Grassmann variable η , fulfilling $\eta f_i^\dagger = -f_i^\dagger \eta$. The generating matrix A^- and coupling matrix B^- between η and the f_i^\dagger are given by

$$A^- = \begin{pmatrix} 0 & 0.2 & -0.6 & 0.6 & -0.2 \\ -0.2 & 0 & 0.2 & -0.6 & 0.6 \\ 0.6 & -0.2 & 0 & 0.2 & -0.6 \\ -0.6 & 0.6 & -0.2 & 0 & 0.2 \\ 0.2 & -0.6 & 0.6 & -0.2 & 0 \end{pmatrix}, \quad B^- = \begin{pmatrix} 1 & 1 & 1 & 1 & 1 \end{pmatrix} \quad (104)$$

However, we can also write this state in a purely Gaussian form by acting with annihilation operators on the fully occupied state vector $|\widetilde{0}\rangle = \prod_i f_i^\dagger |\emptyset\rangle$

$$|\bar{1}\rangle = -N \exp\left(\frac{1}{2} \sum_{i,j} A_{i,j}^+ f_i f_j\right) |\widetilde{0}\rangle \quad (105)$$

Note that the generating matrix A^+ in this form is the same as for the positive-parity state, highlighting the symmetry between the positive- and negative-parity eigenstate. The additional minus sign can be removed by redefining either N or $|\widetilde{0}\rangle$.

F. Higher central charges and critical scaling of entanglement entropies

By associating a higher bond dimension $\chi = 2^n$ with each geometric edge, it is possible to increase the central charge c of the conformal field theory capturing the boundary state. The corresponding $3n \times 3n$ correlation matrix A of each triangle state can be chosen so that correlations separate into n parts. An example for $\chi = 4$ is given by

$$A = \begin{pmatrix} 0 & 0 & a & 0 & b & 0 \\ 0 & 0 & 0 & a & 0 & b \\ -a & 0 & 0 & 0 & c & 0 \\ 0 & -a & 0 & 0 & 0 & c \\ -b & 0 & -c & 0 & 0 & 0 \\ 0 & -b & 0 & -c & 0 & 0 \end{pmatrix} \quad (106)$$

where $a = b = c$ again corresponds to a rotation-invariant state. The construction of states with higher χ is visualized in Fig. S10. Note that this separation into n independent ‘‘channels’’ can only be sustained in contracted $\{p, q\}$ tilings if q is even; otherwise, self-contractions lead to mixing between different channels. Also shown in Fig. S10 is the entanglement entropy scaling of the boundary states of such triangular bulks, yielding a central charge of the equivalent CFT description of $c = n/2 = \log_2 \sqrt{\chi}$. The expected entanglement growth (98) is only reached when the subsystem size l is larger than the size of one geometrical edge, i.e. $2n$ Majorana fermions. Indeed, by construction of our Gaussian model, a site of one Majorana fermion always has an entanglement entropy of $1/2 \log 2$, independent of χ .

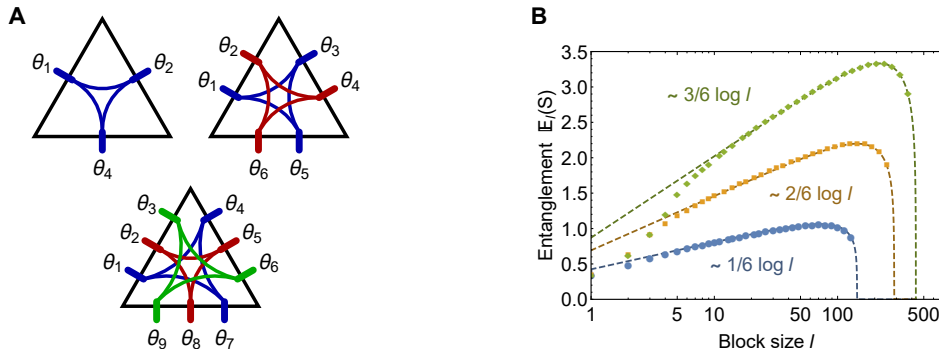



Fig. S10. Construction of triangle states with bond dimension $\chi = 2, 4, 8$. **A:** Visualization of correlations, with colored connections between sites θ_k denoting non-zero correlations. **B:** Mean value of entanglement entropy $\mathbb{E}_\ell(S) = \sum_{k=1}^L S_{[k, k+\ell]}$ of a boundary subsystem of size ℓ . Results for $\{3, 8\}$ tiling with bond dimension $\chi = 2, 4, 8$ (bottom to top; with 144, 288, 432 boundary sites, respectively).

Majorana dimers and holographic quantum error-correcting codes

A. Jahn , M. Gluza, F. Pastawski, and J. Eisert

Dahlem Center for Complex Quantum Systems, Freie Universität Berlin, 14195 Berlin, Germany



(Received 15 July 2019; published 6 November 2019)

Holographic quantum error-correcting codes have been proposed as toy models that describe key aspects of the anti-de Sitter/conformal field theory (AdS/CFT) correspondence. In this work, we introduce a versatile framework of Majorana dimers capturing the intersection of stabilizer and Gaussian Majorana states. This picture allows for an efficient contraction with a simple diagrammatic interpretation and is amenable to analytical study of holographic quantum error-correcting codes. Equipped with this framework, we revisit the recently proposed hyperbolic pentagon code (HyPeC). Relating its logical code basis to Majorana dimers, we efficiently compute boundary-state properties even for the non-Gaussian case of generic logical input. The dimers characterizing these boundary states coincide with discrete bulk geodesics, leading to a geometric picture from which properties of entanglement, quantum error correction, and bulk/boundary operator mapping immediately follow. We also elaborate upon the emergence of the Ryu-Takayanagi formula from our model, which realizes many of the properties of the recent bit thread proposal. Our work thus elucidates the connection among bulk geometry, entanglement, and quantum error correction in AdS/CFT and lays the foundation for new models of holography.

DOI: [10.1103/PhysRevResearch.1.033079](https://doi.org/10.1103/PhysRevResearch.1.033079)

I. INTRODUCTION

The holographic principle—the idea that certain theories of gravity are dual to lower dimensional quantum field theory—has had wide-ranging applications within theoretical physics. In particular, the AdS/CFT correspondence has changed our understanding of theories of both (quantum) gravity and quantum field theory by giving a specific relationship between gravity on $(d+1)$ -dimensional negatively curved *anti-de Sitter* spacetime (AdS) and d -dimensional conformal field theory (CFT) [1,2]. A number of simple models capturing key aspects of holography have been constructed [3–8], largely relying on *tensor network* descriptions of bulk AdS geometry and boundary states. Tensor networks have long been understood as describing a state in terms of its entanglement structure [9], thus serving as an ideal tool to study holography in terms of notions of quantum information theory [10–14]. The basis of this work is the tensor network construction of the *hyperbolic pentagon code* (HyPeC), a class of holographic models often named *HaPPY codes* after the authors' initials [5]. These codes explicitly realize *holographic quantum error correction* [3] by providing an error-correctable mapping from bulk to boundary degrees of freedom, reproducing many of the features of AdS/CFT. However, the boundary states of the HyPeC differ from other tensor network models specifically designed to produce physical CFTs, such as the multi-scale entanglement renormalization ansatz (MERA) [15]. For computational basis bulk inputs, where the tensor network

becomes Gaussian and efficiently contractible, earlier studies revealed a pairwise correlation structure in terms of boundary Majorana modes [16]. As we show in this work, HyPeC states are in fact a special case of a *Majorana dimer model* and can be described by entangled fermionic pairs. Majorana dimers have previously been used to describe superconducting phases on lattices [17,18] as instances of tensor networks that have a fermionic component [19–23]. We show that the contraction of dimer-based tensor networks is equivalent to combining entangled Majorana pairs, replacing the computational difficulties of contraction by simple rules on dimer diagrams. This graphical language directly visualizes parities, physical correlations, and the entanglement structure of quantum states spanning the entire fermionic Hilbert space. By deriving the holographic properties of the HyPeC merely from emergent entangled pairs, we connect to recent proposals of AdS/CFT models based on bit threads [24,25]. Thus, our work is also an important step toward integrating discrete tensor network models of AdS/CFT into a unified setting.

II. A SIMPLE MODEL OF HOLOGRAPHY

Consider the *boundary* and *bulk* Hilbert spaces denoted by \mathcal{H}_∂ and $\mathcal{H}_{\text{bulk}}$ respectively. A holographic quantum error-correcting code is formed by an *encoding isometry* E from the logical states in $\mathcal{H}_{\text{bulk}}$ to boundary states in $\mathcal{H}_{\text{code}} \subset \mathcal{H}_\partial$. Indeed, EE^\dagger is the projector onto the code $\mathcal{H}_{\text{code}}$ of the boundary Hilbert space \mathcal{H}_∂ . Any bulk operator \mathcal{O} acting on the states in $\mathcal{H}_{\text{bulk}}$ can be represented by at least one operator \mathcal{O}_∂ acting on $|\psi_{\text{code}}\rangle \in \mathcal{H}_{\text{code}}$ with the property $E^\dagger \mathcal{O}_\partial E = \mathcal{O}$ while preserving the code subspace ($[\mathcal{O}_\partial, EE^\dagger] = 0$). The specific form of such a mapping from bulk to boundary is the *holographic dictionary* obtained in continuum AdS/CFT by equating bulk and boundary partition functions [2], which is equivalent to considering boundary CFT operators \mathcal{O}_∂ as

Published by the American Physical Society under the terms of the Creative Commons Attribution 4.0 International license. Further distribution of this work must maintain attribution to the author(s) and the published article's title, journal citation, and DOI.

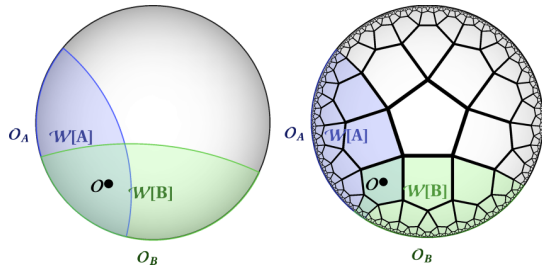


FIG. 1. Continuous (left) and discretized (right) reconstruction of an AdS bulk operator \mathcal{O} along two (causal) wedges $\mathcal{W}[A]$ and $\mathcal{W}[B]$ [3], leading to two boundary operators \mathcal{O}_A and \mathcal{O}_B with support on boundary regions A and B . The AdS time slice is projected onto the Poincaré disk, with the AdS boundary corresponding to the black outer circle. The discretization is a $\{5, 4\}$ tiling.

limits of fields on the gravitational AdS background [26]. As we visualize in Fig. 1 (left), oftentimes \mathcal{O}_θ acts nontrivially only on a subregion of the total boundary. Given a subregion A on the boundary, one can perform the so-called *AdS-Rindler reconstruction* [26–31] to associate to any boundary operator \mathcal{O}_A a corresponding bulk operator \mathcal{O} acting within the wedge $\mathcal{W}[A]$ which is a subset of the bulk.

Because of the computational difficulties in studying continuum AdS/CFT, discrete toy models often provide an easier approach to understanding its properties. These models usually consider a spacelike slice of the full AdS spacetime, discretized by a tiling whose open boundary edges correspond to the AdS boundary. Subsets of these open edges are then identified with subregions of the boundary CFT (see Fig. 1, right).

What properties should the discretized boundary states in $\mathcal{H}_{\text{code}}$ fulfill? As a bulk operator can be represented equivalently on different parts of the boundary, e.g., two regions A and B , we are led to the condition

$$\mathcal{O}_A |\psi_{\text{code}}\rangle = \mathcal{O}_B |\psi_{\text{code}}\rangle, \quad (1)$$

where \mathcal{O}_A and \mathcal{O}_B are boundary representations on A and B of an operator \mathcal{O} inserted somewhere in the bulk. For this condition to hold for any \mathcal{O} and any suitable A and B , the states in $\mathcal{H}_{\text{code}}$ must necessarily possess multipartite and nonlocal entanglement to allow for operators that act equivalently on distant parts of the boundary.

In this work, we show that the *holographic pentagon code* implements these properties through an underlying fermionic structure. To motivate the use of fermions in the context of holographic quantum error correction, consider a simple toy model of entangled fermionic modes. Throughout, we denote fermionic canonically anticommuting operators by f_j satisfying $f_j^\dagger f_k + f_k f_j^\dagger = \delta_{j,k}$ and distinguish the vacuum state vector $|\emptyset\rangle$ satisfying $f_j |\emptyset\rangle = 0$ for any j . The counterpart of a Bell pair for fermions is the so-called BCS state which has the form

$$|\psi_{\text{BCS}}\rangle = (1 + f_j^\dagger f_k^\dagger) |\emptyset\rangle. \quad (2)$$

By a simple calculation, we find that

$$f_j |\psi_{\text{BCS}}\rangle = f_k^\dagger |\psi_{\text{BCS}}\rangle = f_k^\dagger |\emptyset\rangle, \quad (3)$$

which implies that if j, k are boundary indices, we found a mapping between boundary operators that resembles (1). For holographic quantum error correction, however, this mapping is insufficient: After acting with the operator, the result (3) is an unentangled Fock state vector $f_k^\dagger |\emptyset\rangle$, which is no longer in the desired code space of entangled states. Furthermore, $|\psi_{\text{BCS}}\rangle$ does not exhibit any multipartite entanglement necessary for holography [32]. Fortunately, both problems can be resolved by fermionic mode fractionalization by means of *Majorana dimers*. Consider the action of Majorana operators, defined as

$$\gamma_{2k-1} = f_k^\dagger + f_k, \quad \gamma_{2k} = i(f_k^\dagger - f_k), \quad (4)$$

and fulfilling $\{\gamma_j, \gamma_k\} = 2\delta_{j,k}$, on the BCS state vector (2) as

$$\gamma_{2j-1} |\psi_{\text{BCS}}\rangle = -i \gamma_{2k} |\psi_{\text{BCS}}\rangle = (f_j^\dagger + f_k^\dagger) |\emptyset\rangle, \quad (5)$$

$$\gamma_{2k-1} |\psi_{\text{BCS}}\rangle = i \gamma_{2j} |\psi_{\text{BCS}}\rangle = (f_j^\dagger - f_k^\dagger) |\emptyset\rangle. \quad (6)$$

This shows that a mapping between Majorana operators, unlike one relying on standard fermionic operators as in Eq. (3), can be performed without destroying entanglement. To achieve multipartite entanglement, BCS-type states are insufficient. However, a suitable model is provided by the hyperbolic pentagon code (HyPeC). Let us briefly review its construction: The HyPeC is an isometry between bulk and boundary degrees of freedom. An AdS time slice is discretized by a finite tiling of M pentagons, the Poincaré disk projection of which is shown in Fig. 1. Each pentagon is associated with one logical qubit, i.e., one bulk degree of freedom, encoded in five spins (the pentagon edges) via the $[[5, 1, 3]]$ quantum error-correcting code. This code can be expressed by a six-leg tensor, with one “bulk” leg corresponding to the logical qubit and the remaining five to the physical spins. The tiling is connected by tracing out spins on the edges of two adjacent pentagon tiles, i.e., by contracting the corresponding tensor indices. This contraction can be understood as a projection of the spins on the two connected edges onto a Bell pair. In this paper, we will usually consider this setup with each bulk input fixed to a certain state. Before contraction, the bulk is then effectively composed of a product state of M local quantum states on five spins each. Contraction locally entangles the spins with each other, thus leading to a larger entangled state on the remaining N spins at the boundary of the pentagon tiling. If we consider instead an arbitrary bulk input on each pentagon,¹ contraction combines the local five-spin Hilbert spaces into a larger N -spin Hilbert space that defines our code space $\mathcal{H}_{\text{code}}$.

By merit of the $[[5, 1, 3]]$ code, the five spins on the edges of each pentagon are *absolutely maximally entangled*. A pure state of n qubits is absolutely maximally entangled if all of its reductions to $\lfloor n/2 \rfloor$ subsystems are maximally mixed [33–35] and hence the states are maximally entangled over all such cuts. The isometric properties of the code follow from this construction.

¹For the purposes of this paper, bulk inputs between different pentagons are assumed to be unentangled.

A useful approach to understanding these states is to represent this spin picture of the HyPeC in terms of Majorana fermions [16]. This is achieved by a Jordan-Wigner transformation between L spins and $2L$ Majorana modes:

$$\begin{aligned}\gamma_{2k-1} &= Z_1 Z_2 \dots Z_{k-1} X_k, \\ \gamma_{2k} &= Z_1 Z_2 \dots Z_{k-1} Y_k,\end{aligned}\quad (7)$$

where we have used the k -site Pauli operators defined as

$$\begin{aligned}X_k &:= \mathbb{1}_2^{\otimes(k-1)} \otimes \sigma_x \otimes \mathbb{1}_2^{\otimes(L-k)}, \\ Y_k &:= \mathbb{1}_2^{\otimes(k-1)} \otimes \sigma_y \otimes \mathbb{1}_2^{\otimes(L-k)}, \\ Z_k &:= \mathbb{1}_2^{\otimes(k-1)} \otimes \sigma_z \otimes \mathbb{1}_2^{\otimes(L-k)},\end{aligned}\quad (8)$$

in terms of the Pauli matrices $\sigma_x, \sigma_y, \sigma_z$. It will be useful to define the total parity operator

$$\mathcal{P}_{\text{tot}} = Z_1 Z_2 \dots Z_L = (-i)^L \gamma_1 \gamma_2 \dots \gamma_{2L}. \quad (9)$$

In the HyPeC, we take $L = 5$ spins for each pentagon. The logical eigenvectors $|\bar{0}\rangle$ and $|\bar{1}\rangle$ of the $[[5, 1, 3]]$ code have \mathcal{P}_{tot} eigenvalues $+1$ and -1 , respectively, corresponding to even and odd fermionic parity. For fixed bulk input (and thus parity), the stabilizers are quadratic in Majorana operators. Thus, $|\bar{0}\rangle$ and $|\bar{1}\rangle$ are ground-state vectors of a Hamiltonian describing free Majorana modes, given by

$$H = i \sum_{j=1}^{L=5} (P_{\text{tot}})^j \gamma_j \gamma_{j+5}, \quad (10)$$

where $P_{\text{tot}} = \pm 1$ is the eigenvalue of \mathcal{P}_{tot} and indices follow periodic boundary conditions. If we replace $P_{\text{tot}} \rightarrow \mathcal{P}_{\text{tot}}$, we recover the original $[[5, 1, 3]]$ stabilizer Hamiltonian with its twofold degenerate ground state. Before considering contractions of these fermionic code states, we now develop a comprehensive framework for Majorana dimers that allows us to study the fermionic HyPeC in detail.

III. MAJORANA DIMERS

A. Definition

Majorana dimers are effectively a reordering of the vacuum state in terms of Majorana modes. The L -fermion vacuum state vector is defined by being annihilated by all of the fermionic annihilation operators f_k for $k \in \{1, 2, \dots, L\}$ as

$$f_k |\emptyset\rangle = \frac{1}{2} (\gamma_{2k-1} + i \gamma_{2k}) |\emptyset\rangle = 0. \quad (11)$$

Thus, the vacuum state effectively relates L pairs of Majorana modes $(2k-1, 2k)$ in an operator equation. By permuting Majorana indices, we can generalize this state to any pairing of modes. Such a *Majorana dimer state* is determined via L conditions on distinct pairs (j, k) (choosing $j < k$ as convention) of Majorana operators

$$(\gamma_j + i p_{j,k} \gamma_k) |\psi\rangle = 0. \quad (12)$$

The *dimer parities* $p_{j,k} \in \{-1, 1\}$ give each pair an ‘‘orientation’’ with respect to the index ordering. We refer to $p_{j,k} = 1$ as ‘‘even’’ and $p_{j,k} = -1$ as ‘‘odd.’’ To restate this, a Majorana dimer state is defined to be a (normalized) state vector of L fermionic modes which is annihilated by L independent

conditions of the form (12). Note that we have fixed a vacuum state which under the Jordan-Wigner transformation corresponds to a product state in spins, but nontrivial Majorana dimer states can be highly entangled, as we shall see.

Equivalently, we may characterize Majorana dimer state vectors $|\psi\rangle$ as ground states of specific quadratic Hamiltonians: Multiplying (12) with its Hermitian conjugate from the left yields

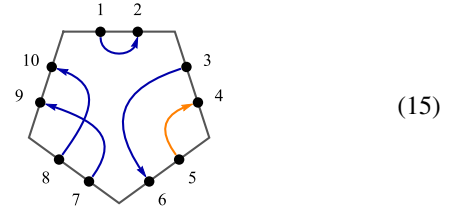
$$\langle \psi | (2 + 2i p_{j,k} \gamma_j \gamma_k) | \psi \rangle = 0, \quad (13)$$

which implies that the Hermitian operator $i \gamma_j \gamma_k$ has expectation value $-p_{j,k}$. We can now construct the Hamiltonian

$$H = \frac{i}{2} \sum_{(j,k) \in \Omega} p_{j,k} \gamma_j \gamma_k, \quad (14)$$

where we sum over all L Majorana dimers $\Omega = \{(j, k)\}$. H is a *parent Hamiltonian* of $|\psi\rangle$, meaning that $|\psi\rangle$ is the unique ground-state vector of H with energy $-L$, being in the -1 eigenspace of all the summands.

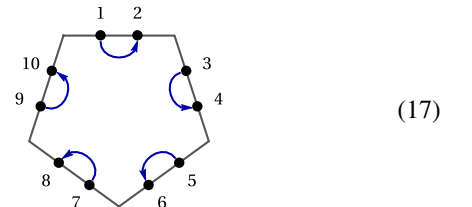
These two equivalent characterizations are most intuitively visualized through a diagrammatic notation. Consider L fermionic modes, ordered as a chain visualized by an L gon, with the Majorana modes shown as dots on the edge (mode). Arrows between the Majorana modes represent the pairing. For example, for $L = 5$, the state visualized by



is the ground state of the Hamiltonian

$$H = \frac{i}{2} (\gamma_1 \gamma_2 + \gamma_3 \gamma_6 - \gamma_4 \gamma_5 + \gamma_7 \gamma_9 + \gamma_8 \gamma_{10}). \quad (16)$$

An arrow $j \rightarrow k$ along the index orientation ($j < k$, blue) corresponds to a dimer parity $p_{j,k} = +1$, while an arrow against it ($j > k$, orange) corresponds to $p_{j,k} = -1$. Note that these diagrams only specify the state up to a scalar $c \in \mathbb{C}$, as c affects neither the ground-state property nor the dimer conditions (12). A particularly symmetric case is the aforementioned vacuum $|\emptyset\rangle$ represented by a diagram



for $L = 5$. Unsurprisingly, $|\emptyset\rangle$ is also the ground-state vector of the Hamiltonian $H_0 = \sum_k n_k$ with the local number operators $n_k = f_k^\dagger f_k = (1 + i \gamma_{2k-1} \gamma_{2k})/2$. We can construct any Majorana dimer state from the vacuum by applying swap operators $S_{j,k} := \mathcal{P}_{\text{tot}} (\gamma_j - \gamma_k) / \sqrt{2}$ onto $|\emptyset\rangle$, with \mathcal{P}_{tot} being the total parity operator defined in the last section. For example,

the state expressed by diagram (15) is given by $S_{8,9}S_{4,6}|\emptyset\rangle$. It should be noted that while these swap operators violate the fermionic superselection rule in an actual fermionic systems, we are merely interested in Majorana dimers as an effective representation of spins (such as the HyPeC).

As Majorana dimer states are Gaussian, all expectation values are determined by the entries of the *covariance matrix* with entries

$$\Gamma_{j,k}^\psi = \frac{i}{2} \langle \psi | [\gamma_j, \gamma_k] | \psi \rangle. \quad (18)$$

We can read off $\Gamma_{j,k}^\psi$ directly from the corresponding diagram: As $|\psi\rangle$ is constructed from $|\emptyset\rangle$ by acting with a product \mathcal{S} of swap operators mapping each index k to an index $S(k)$, $\Gamma_{j,k}^\psi$ is simply $\Gamma_{j,k}^\emptyset$ with interchanged rows and columns:

$$\Gamma_{j,k}^\psi = \frac{i}{2} \langle \emptyset | \mathcal{S}^\dagger [\gamma_i, \gamma_j] \mathcal{S} | \emptyset \rangle \quad (19)$$

$$= \frac{i}{2} \langle \emptyset | [\gamma_{S(i)}, \gamma_{S(j)}] | \emptyset \rangle = \Gamma_{S(j),S(i)}^\emptyset. \quad (20)$$

The only nonzero entries of the vacuum covariance matrix are $\Gamma_{2k,2k-1}^\emptyset = -\Gamma_{2k-1,2k}^\emptyset = 1$. We can thus infer $\Gamma_{j,k}^\psi$ from its diagram using the rules

$$\Gamma_{j,k}^\psi = \begin{cases} -1 & \text{for an arrow } j \rightarrow k \\ 1 & \text{for an arrow } k \rightarrow j \\ 0 & \text{if no arrow connects } j \text{ and } k \end{cases}. \quad (21)$$

For example, the covariance matrix for diagram (15) is

$$\Gamma_{j,k}^\psi = \begin{matrix} & \begin{matrix} 1 & 2 & 3 & 4 & 5 & 6 & 7 & 8 & 9 & 10 \end{matrix} \\ \begin{matrix} 1 \\ 2 \\ 3 \\ 4 \\ 5 \\ 6 \\ 7 \\ 8 \\ 9 \\ 10 \end{matrix} & \begin{matrix} & & & & & & & & & & \\ & & & & & & & & & & \\ & & & & & & & & & & \\ & & & & & & & & & & \\ & & & & & & & & & & \\ & & & & & & & & & & \\ & & & & & & & & & & \\ & & & & & & & & & & \\ & & & & & & & & & & \\ & & & & & & & & & & \\ & & & & & & & & & & \end{matrix} \end{matrix} \quad (22)$$

with color-coded entries (orange = +1, blue = -1). Note that we have chosen the colors to match with the dimer parities when reading the entries above the main diagonal ($j < k$). We assume that the state vector $|\psi\rangle$ is normalized. Equivalently, we can think of the swap operators as acting on the Hamiltonian, yielding $H_\psi = \mathcal{S} H_0 \mathcal{S}^\dagger$. Clearly, the spectrum of H_ψ is simply a permutation of the spectrum of H_0 , consistent with the covariance matrix picture.

By Eq. (10), the $[[5, 1, 3]]$ code states are ground states of Hamiltonians quadratic in Majorana operators and can thus

be represented as Majorana dimers. As diagrams, they are given by

$$|\bar{0}\rangle_5 = \begin{matrix} & \begin{matrix} 1 & 2 \end{matrix} \\ \begin{matrix} 10 \\ 9 \\ 8 \\ 7 \\ 6 \end{matrix} & \begin{matrix} & & & & & & & & & & \\ & & & & & & & & & & \\ & & & & & & & & & & \\ & & & & & & & & & & \\ & & & & & & & & & & \\ & & & & & & & & & & \\ & & & & & & & & & & \\ & & & & & & & & & & \\ & & & & & & & & & & \end{matrix} \end{matrix}, \quad (23)$$

$$|\bar{1}\rangle_5 = \begin{matrix} & \begin{matrix} 1 & 2 \end{matrix} \\ \begin{matrix} 10 \\ 9 \\ 8 \\ 7 \\ 6 \end{matrix} & \begin{matrix} & & & & & & & & & & \\ & & & & & & & & & & \\ & & & & & & & & & & \\ & & & & & & & & & & \\ & & & & & & & & & & \\ & & & & & & & & & & \\ & & & & & & & & & & \\ & & & & & & & & & & \\ & & & & & & & & & & \\ & & & & & & & & & & \end{matrix} \end{matrix}. \quad (24)$$

As we will see in the next section, the code distance $d = 3$ between these two states in terms of Pauli operations can be shown graphically.

B. Pauli operations and total parity

As the Majorana operators are obtained from spin operators through a Jordan-Wigner transformation, local Pauli operations in the spin picture generally act nonlocally on the Majorana dimers. Specifically, the reverse transformation of (7) is given by

$$\begin{aligned} X_k &= (-i)^{k-1} \prod_{j=1}^{2k-1} \gamma_j, \\ Y_k &= (-i)^{k-1} \left(\prod_{j=1}^{2k-2} \gamma_j \right) \gamma_{2k}, \\ Z_k &= -i \gamma_{2k-1} \gamma_{2k}. \end{aligned} \quad (25)$$

A Majorana operator γ_k acting on a Majorana dimer state flips the parity of the dimer ending on site k . We show this by noting that if a state vector $|\psi\rangle$ is annihilated by the operator $\gamma_a + i p \gamma_b$ (with dimer parity $p \in \{-1, +1\}$ and $a \neq b$), then both $\gamma_a |\psi\rangle$ and $\gamma_b |\psi\rangle$ are annihilated by $\gamma_a - i p \gamma_b$:

$$(\gamma_a - i p \gamma_b) \gamma_a |\psi\rangle = \gamma_a (\gamma_a + i p \gamma_b) |\psi\rangle = 0, \quad (26)$$

$$(\gamma_a - i p \gamma_b) \gamma_b |\psi\rangle = -\gamma_b (\gamma_a + i p \gamma_b) |\psi\rangle = 0. \quad (27)$$

All other dimer conditions remain unaffected. As a graphical notation, we highlight the affected edges of the state in red. Some examples of these operations on a Majorana dimer state

vector $|\psi\rangle$ are shown here:

$$X_2 |\psi\rangle = \text{Diagram 1} = \text{Diagram 2} \quad (28)$$

$$Y_3 |\psi\rangle = \text{Diagram 3} = \text{Diagram 4} \quad (29)$$

$$Z_4 |\psi\rangle = \text{Diagram 5} = \text{Diagram 6} \quad (30)$$

When both ends of a dimer are acted upon with a Majorana operator, the local parity stays the same. Note that Z_k operations only affect the k th edge, while X_k and Y_k combine a local Majorana operation with a Z string on the first $k-1$ edges. Using this graphical calculus, we can now see that it requires three Pauli operations to map (23) into (24) or each into itself. These correspond to bit flip (e.g., $i\gamma_1\gamma_3\gamma_5 = X_1Y_2X_3$) and phase flip errors (e.g., $i\gamma_1\gamma_6 = Y_1Z_2Y_3$), respectively.

Now consider the total parity operator $\mathcal{P}_{\text{tot}} = \prod_i Z_i$, which affects all Majorana sites at once. Clearly, acting with \mathcal{P}_{tot} leaves the state invariant (up to the parity eigenvalue), which implies that all Majorana dimer states have definite total parity p_{tot} . In fact, this parity is given by

$$p_{\text{tot}} = (-1)^{N_c} \prod_{(j,k)} p_{j,k}, \quad (31)$$

depending on the dimer parities $p_{j,k}$ of all dimers (j, k) as well the number N_c of crossings between dimers. This statement can be proven inductively: We start with the vacuum $|\emptyset\rangle$ with $p_{\text{tot}} = +1$. It corresponds to a diagram with $p_k = +1$ for all dimers k and no crossings. We can now construct any state vector $|\psi\rangle$ from $|\emptyset\rangle$ by applying swap operators $S_{j,k} = \mathcal{P}_{\text{tot}}(\gamma_j - \gamma_k)/\sqrt{2}$. Since $S_{i,j}$ anticommutes with \mathcal{P}_{tot} , each swap inverts p_{tot} . To see that (31) reflects this, consider how a swap $S_{j,k}$ affects the pairs ending in j and k for each possible initial configuration as

$$\begin{matrix} \text{Diagram 1} & \text{Diagram 2} & \text{Diagram 3} & \text{Diagram 4} \\ \downarrow S_{3,4} & \downarrow S_{1,3} \uparrow S_{2,4} & \downarrow S_{3,4} \uparrow S_{1,5} & \downarrow S_{5,6} \\ \text{Diagram 5} & \text{Diagram 6} & \text{Diagram 7} & \text{Diagram 8} \end{matrix} \quad (32)$$

Up to mirroring, relabeling, and relative shifting of indices, all possible swaps belong to one of the four categories shown above. The first two swaps flip one local parity but create no additional crossings; the last two either add or remove one crossing while flipping an even number of parities. Thus, (31) is always satisfied. Note that we are free to move around the dimer curve between the fixed endpoints, which means we can make two (or more) paths overlap. However, this will always change the number of crossings by an even number. For example, the logical $\bar{0}$ state of the $[[5, 1, 3]]$ code corresponds to both of the following diagrams (each with ten crossings):

$$|\bar{0}\rangle_5 = \text{Diagram 9} = \text{Diagram 10} \quad (33)$$

As expected, (31) tells us that this state has positive parity. For a fixed dimer configuration but variable dimer parities p_k , only the second factor of (31) is relevant. Thus, we find that acting with an X_k or Y_k operator, which changes an odd number of dimer parities, also flips the total parity. A Z_k error, which always flips two dimer parities, leaves the total parity invariant.

C. Contracting dimers

We will now show how the notion of tensor network contraction applies to Majorana dimer states. To begin with, consider a state of N spins

$$|\psi_T\rangle = \sum_{j \in \{0,1\}^{\times N}} T_{j_1, \dots, j_N} |j_1, \dots, j_N\rangle. \quad (34)$$

Here, the amplitudes $T_{j_1, \dots, j_N} = \langle j_1, \dots, j_N | \psi \rangle$ can be viewed as a tensor T which fully specifies the state vector $|\psi_T\rangle$. A tensor network is a means of specifying a tensor describing a state of a large number of spins through multiple contractions of tensors of a smaller rank. Specifically, the contraction of two tensors S and T of ranks N_S and N_T between the last index of S and the first index of T is defined to be a new tensor U of rank $N_U = N_S + N_T - 2$, with entries

$$U_{k_1, k_2, \dots, k_{N_U}} = S_{k_1, k_2, \dots, k_{N_S-1}, 0} T_{0, k_{N_S}, k_{N_S+1}, \dots, k_{N_U}} + S_{k_1, k_2, \dots, k_{N_S-1}, 1} T_{1, k_{N_S}, k_{N_S+1}, \dots, k_{N_U}}. \quad (35)$$

We see that by contracting the respective tensors, this operation allows us to merge two state vectors $|\psi_S\rangle$ and $|\psi_T\rangle$ into a larger one $|\psi_U\rangle$ given by

$$|\psi_U\rangle = \sum_{k \in \{0,1\}^{\times N'}} U_{k_1, k_2, \dots, k_{N'}} |k_1, \dots, k_{N'}\rangle. \quad (36)$$

A tensor network state can thus describe a large state by the relatively few entries of its contracted tensors. This process can be generalized to fermions by identifying the spin basis with a fermionic one as

$$|j_1, \dots, j_N\rangle \leftrightarrow (f_1^\dagger)^{j_1} (f_2^\dagger)^{j_2} \dots (f_N^\dagger)^{j_N} |\emptyset\rangle. \quad (37)$$

In this picture, tensors are associated with pure fermionic states. As these expressions only use creation operators, they

obey a *Grassmann algebra*. The tensor contraction (35) can then be expressed by a Grassmann integration over fermionic degrees of freedom [36]. Specifically, a contraction of two fermionic state vectors $|\phi\rangle$ and $|\psi\rangle$ into a state vector $|\omega\rangle$ over the same indices as in Eq. (35) has the form

$$|\omega\rangle = \int df_{M+1}^\dagger df_M^\dagger (1 + f_M^\dagger f_{M+1}^\dagger) |\phi\rangle |\psi\rangle \quad (38)$$

$$= \int df_{M+1}^\dagger df_M^\dagger e^{f_M^\dagger f_{M+1}^\dagger} |\phi\rangle |\psi\rangle, \quad (39)$$

where we have used the Grassmann integration $\int df_k^\dagger f_k^{\dagger n} = \delta_{n,1}$ (for more information, see Refs. [36–39]). Note that $\int df_k^\dagger$ acts like an annihilator f_k on a fermionic state, with a subsequent projection onto the fermionic subspace excluding the k th mode. This requires a relabeling of the remaining degrees of freedom and a truncation of the Jordan-Wigner string in the corresponding spin representation.

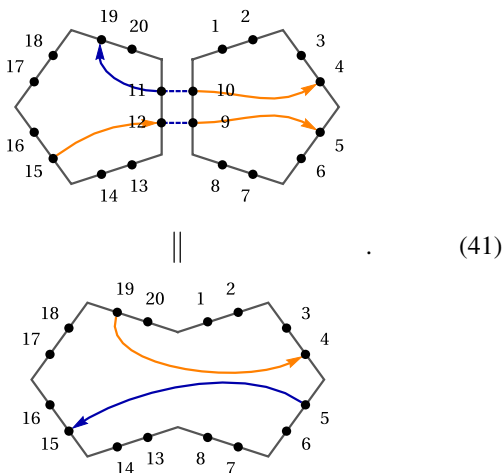
We can now apply this machinery to Majorana dimer states. In our graphical language, tensor contraction is equivalent to connecting two polygon edges and integrating out the four Majorana modes on them. What happens to the dimers of the original states? It is easy to see that dimers (j, k) of a state vector $|\phi\rangle$ not connected to the contracted edges remain dimers, i.e., if $(\gamma_j + i p_{j,k} \gamma_k) |\phi\rangle$ vanishes, we also find

$$\begin{aligned} & (\gamma_j + i p_{j,k} \gamma_k) \int df_{M+1}^\dagger df_M^\dagger e^{f_M^\dagger f_{M+1}^\dagger} |\phi\rangle |\psi\rangle \\ &= \int df_{M+1}^\dagger df_M^\dagger e^{f_M^\dagger f_{M+1}^\dagger} (\gamma_j + i p_{j,k} \gamma_k) |\phi\rangle |\psi\rangle = 0, \end{aligned} \quad (40)$$

as γ_j and γ_k commute with the integration. We now claim that the dimers connected to the contracted edge become new dimers of the contracted state ω . This leads to the following statement.

Theorem 1 (Contractions of Majorana dimer states). The contraction of two Majorana dimer state vectors $|\phi\rangle$ and $|\psi\rangle$ yields either a new Majorana dimer state vector $|\omega\rangle$ or zero.

An example for the contraction of two pentagon state vectors $|\phi\rangle$ and $|\psi\rangle$ is given by



We have visualized the contraction by a pair of dashed lines. In this example, dimers not connected to the contracted edges are omitted. The upper diagram corresponds to the conditions

$$(\gamma_4 - i \gamma_{10}) |\phi\rangle = 0, \quad (\gamma_{11} + i \gamma_{19}) |\psi\rangle = 0, \quad (42)$$

$$(\gamma_5 - i \gamma_9) |\phi\rangle = 0, \quad (\gamma_{12} - i \gamma_{15}) |\psi\rangle = 0. \quad (43)$$

We now prove that (42) implies $(\gamma_4 - i \gamma_{19}) |\omega\rangle = 0$ for the contracted state vector $|\omega\rangle$, i.e., that the two original dimers fuse into a larger one:

$$\begin{aligned} & (\gamma_4 - i \gamma_{19}) |\omega\rangle \\ &= \int df_6^\dagger df_5^\dagger e^{f_5^\dagger f_6^\dagger} (\gamma_4 - i \gamma_{19}) |\psi\rangle |\phi\rangle \\ &= \int df_6^\dagger df_5^\dagger e^{f_5^\dagger f_6^\dagger} (i \gamma_{10} + \gamma_{11}) |\psi\rangle |\phi\rangle \\ &= \int df_6^\dagger df_5^\dagger e^{f_5^\dagger f_6^\dagger} (-f_5^\dagger + f_6^\dagger + f_5 + f_6) |\psi\rangle |\phi\rangle \\ &= \int df_6^\dagger df_5^\dagger (-f_5^\dagger + f_6^\dagger - f_6^\dagger f_5^\dagger f_5 + f_5^\dagger f_6^\dagger f_6) |\psi\rangle |\phi\rangle \\ &= 0, \end{aligned} \quad (44)$$

where we have used the identities $\int df_k^\dagger f_k = 0$ and $\{f_k, f_l^\dagger\} = \delta_{k,l}$. A similar proof using (43) leads to $(\gamma_5 + i \gamma_{15}) |\omega\rangle = 0$.

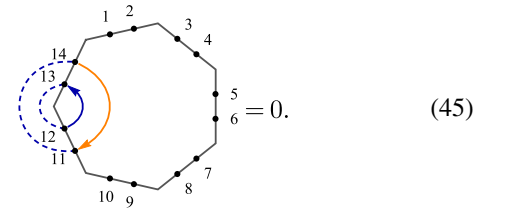
The full proof for all possible dimer contractions is given in Appendix A. The resulting rules are the following:

(1) Contracting neighboring edges k and $k+1$ removes the Majorana modes $\{2k-1, 2k, 2k+1, 2k+2\}$. The dimers ending on $2k-1$ and $2k+2$ as well as $2k$ and $2k+1$ are fused into larger dimers.

(2) The dimer parity $p_{j,k}$ of a fused dimer is the product of parities of the original dimers. In addition, every crossing of the path of a contracted dimer with itself reverses $p_{j,k}$.

(3) Every contraction that creates closed loops leads to a vanishing contracted state if at least one loop has an odd dimer parity.

The last case refers to diagrams such as the following:

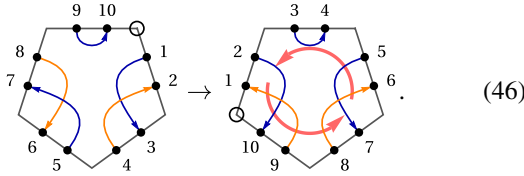


Loops with even total dimer parity only change the contracted state by a nonzero constant.

D. Ordering and cyclic permutations

As fermionic operators anticommute, defining a chain of fermionic sites requires a definite ordering of the site indices. This is also true for the Majorana modes that make up Majorana dimer states. For convention, we assume clockwise-oriented indices starting from an initial index which we call the *pivot* and mark by a little circle in the following diagrams. Shifting the pivot corresponds to a cyclic permutation of all

indices:



How does this transformation affect the dimer parities? First, let us interpret (46) as a cyclic permutation of Majorana indices through an operator \mathcal{M}_4 acting on Majorana modes. For example, in the initial labeling we find $(\gamma_5 + i\gamma_7)|\psi\rangle = 0$. After a cyclic permutation $|\psi\rangle \mapsto |\psi'\rangle = \mathcal{M}_4|\psi\rangle$ with $\mathcal{M}_4 \gamma_k \mathcal{M}_4^{-1} = \gamma_{(k+4) \bmod 10}$, it follows that

$$(\gamma_9 + i\gamma_1)|\psi'\rangle \propto (\gamma_1 - i\gamma_9)|\psi'\rangle = 0. \quad (47)$$

Hence, while a cyclic permutation of Majorana operators does not change the direction of the arrows, it flips the local parities of dimers ending on the edges between the initial and final pivot (with indices $i, i+1, \dots, f$), effectively acting like a product of all Majorana operators $\gamma_{2i-1}, \gamma_{2i}, \dots, \gamma_{2f}$ on these edges.

However, in our use of Majorana dimers as a description of the HyPeC, the underlying physical system is one of spins, where (Pauli) operators on different sites commute. Hence, we are interested in cyclic permutations not of Majorana modes but of the underlying spin degrees of freedom. This modifies the previous result, as each spin permutation effects a different Jordan-Wigner transformation. Consider an initial spin state vector

$$|\psi\rangle = \sum_{k \in \{0,1\}^{\times N}} T_{k_1, k_2, \dots, k_N} |k_1, k_2, \dots, k_N\rangle. \quad (48)$$

A permutation $i \mapsto \sigma(i)$ of indices i gives rise to the spin state vector $|\tilde{\psi}\rangle = \mathcal{S}_\sigma |\psi\rangle$, where \mathcal{S}_σ is the spin-picture unitary permutation operator. Explicitly,

$$\begin{aligned} |\tilde{\psi}\rangle &= \sum_{k \in \{0,1\}^{\times N}} T_{k_1, k_2, \dots, k_N} |\sigma(k_1), \sigma(k_2), \dots, \sigma(k_N)\rangle \\ &= \sum_{j \in \{0,1\}^{\times N}} \tilde{T}_{j_1, j_2, \dots, j_N} |j_1, j_2, \dots, j_N\rangle \end{aligned} \quad (49)$$

with

$$\tilde{T}_{j_1, j_2, \dots, j_N} = T_{\sigma^{-1}(j_1), \sigma^{-1}(j_2), \dots, \sigma^{-1}(j_N)}. \quad (50)$$

In terms of fermionic operators, the initial- and final-state vectors $|\psi\rangle$ and $|\tilde{\psi}\rangle$ are identified as

$$|\psi\rangle = \sum_{k \in \{0,1\}^{\times N}} T_{k_1, k_2, \dots, k_N} (f_1^\dagger)^{k_1} (f_2^\dagger)^{k_2} \dots (f_N^\dagger)^{k_N} |\emptyset\rangle, \quad (51)$$

$$|\tilde{\psi}\rangle = \sum_{k \in \{0,1\}^{\times N}} \tilde{T}_{k_1, k_2, \dots, k_N} (\tilde{f}_1^\dagger)^{k_1} (\tilde{f}_2^\dagger)^{k_2} \dots (\tilde{f}_N^\dagger)^{k_N} |\emptyset\rangle. \quad (52)$$

The operators f_k^\dagger and \tilde{f}_k^\dagger are fermionic operators defined by the respective Jordan-Wigner transformations. Consider a one-step cyclic spin permutation $i \mapsto (i+1) \bmod N$ through a permutation operator \mathcal{S}_{+1} . The Majorana operators transform as $\gamma_k \mapsto \mathcal{S}_{+1} \gamma_k \mathcal{S}_{+1}^\dagger$ and explicitly as

$$\begin{aligned} \gamma_1 &= X_1 \mapsto X_2 = Z_1 \tilde{\gamma}_3, \\ \gamma_2 &= Y_1 \mapsto Y_2 = Z_1 \tilde{\gamma}_4, \\ \gamma_3 &= Z_1 X_2 \mapsto Z_2 X_3 = Z_1 \tilde{\gamma}_5, \\ &\dots \end{aligned} \quad (53)$$

$$\gamma_{2N-2} = Z_1 \dots Z_{N-2} Y_{N-1} \mapsto Z_2 \dots Z_{N-1} Y_N = Z_1 \tilde{\gamma}_N,$$

$$\gamma_{2N-1} = Z_1 \dots Z_{N-1} X_N \mapsto X_1 Z_2 \dots Z_N = -Z_1 \tilde{\gamma}_1 \mathcal{P}_{\text{tot}},$$

$$\gamma_{2N} = Z_1 \dots Z_{N-1} Y_N \mapsto Y_1 Z_2 \dots Z_N = -Z_1 \tilde{\gamma}_2 \mathcal{P}_{\text{tot}}.$$

Hence, the transformed Majorana operators are *not* the Majorana operators defined by the new Jordan-Wigner transformation. Instead, under the cyclic permutation \mathcal{S}_{+1} , all γ_k for $k < 2N-1$ transform as $\gamma_k \mapsto Z_1 \tilde{\gamma}_{k+2}$, while γ_{2N-1} and γ_{2N} transform with an additional total parity $\mathcal{P}_{\text{tot}} = Z_1 Z_2 \dots Z_N$. This changes the dimer conditions: If the state vector $|\psi\rangle$ is annihilated by the operator $\gamma_j + i p_{j,k} \gamma_k$ (with $j < k$), then this operator changes under cyclic spin permutation to

$$\begin{aligned} (\gamma_j + i p_{j,k} \gamma_k)|\psi\rangle &\mapsto \mathcal{S}_{+1}(\gamma_j + i p_{j,k} \gamma_k) \mathcal{S}_{+1}^\dagger \mathcal{S}_{+1} |\psi\rangle \\ &= (\mathcal{S}_{+1} \gamma_j \mathcal{S}_{+1}^\dagger + i p_{j,k} \mathcal{S}_{+1} \gamma_k \mathcal{S}_{+1}^\dagger) |\tilde{\psi}\rangle. \end{aligned} \quad (54)$$

Let us distinguish this result by the parity of $|\tilde{\psi}\rangle$. For even parity $\mathcal{P}_{\text{tot}} |\tilde{\psi}\rangle = |\tilde{\psi}\rangle$, we find

$$(\mathcal{S}_{+1} \gamma_j \mathcal{S}_{+1}^\dagger + i p_{j,k} \mathcal{S}_{+1} \gamma_k \mathcal{S}_{+1}^\dagger) |\tilde{\psi}\rangle = \begin{cases} Z_1 (\tilde{\gamma}_{j+2} + i p_{j,k} \tilde{\gamma}_{k+2}) |\tilde{\psi}\rangle, & j, k < 2N-1, \\ Z_1 (\tilde{\gamma}_{j+2} - i p_{j,k} \tilde{\gamma}_{k+2-2N}) |\tilde{\psi}\rangle, & j < 2N-1, k \geq 2N-1, \\ -Z_1 (\tilde{\gamma}_1 + i p_{j,k} \tilde{\gamma}_2) |\tilde{\psi}\rangle, & j = 2N-1, k = 2N. \end{cases} \quad (55)$$

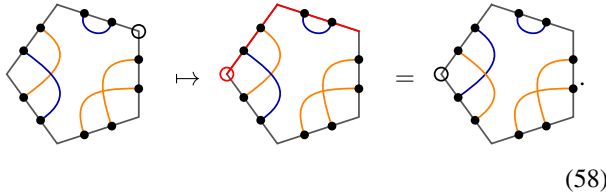
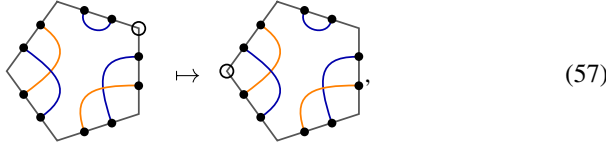
For odd parity $\mathcal{P}_{\text{tot}} |\tilde{\psi}\rangle = -|\tilde{\psi}\rangle$, the result is given by

$$(\mathcal{S}_{+1} \gamma_j \mathcal{S}_{+1}^\dagger + i p_{j,k} \mathcal{S}_{+1} \gamma_k \mathcal{S}_{+1}^\dagger) |\tilde{\psi}\rangle = \begin{cases} Z_1 (\tilde{\gamma}_{j+2} + i p_{j,k} \tilde{\gamma}_{k+2}) |\tilde{\psi}\rangle, & j, k < 2N-1, \\ Z_1 (\tilde{\gamma}_{j+2} + i p_{j,k} \tilde{\gamma}_{k+2-2N}) |\tilde{\psi}\rangle, & j < 2N-1, k \geq 2N-1, \\ Z_1 (\tilde{\gamma}_1 + i p_{j,k} \tilde{\gamma}_2) |\tilde{\psi}\rangle, & j = 2N-1, k = 2N. \end{cases} \quad (56)$$

For odd-parity states, we thus find from (56) that the dimer parities flip as one dimer endpoint moves past the pivot, just as

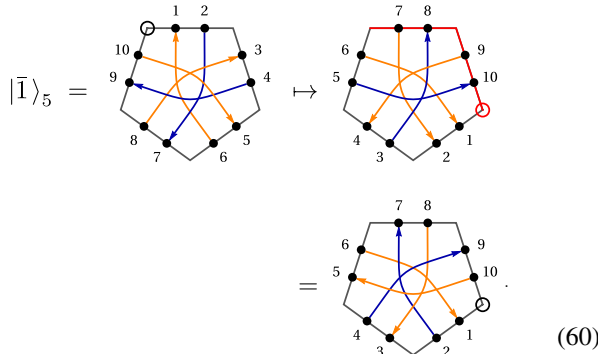
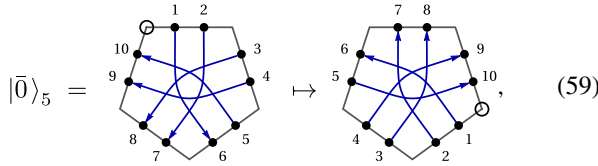
in Eq. (47). However, for an even-parity state, (55) tells us that the dimer parities remain invariant under spin permutations.

This is the only difference between cyclic permutations of Majorana modes and of the underlying spin sites. Omitting arrows and showing only dimer parities, spin cyclic permutation correspond to diagrams such as



These two diagrams illustrate a more general observation. Namely, the upper diagram shows a parity-even Majorana dimer state, where changing the index labeling (i.e., shifting the pivot) does not change the dimer parities. The lower one, however, is parity odd: The red-shaded edges, following the path along which the pivot was moved, represent Majorana operators on the edges that flip the connected dimer parities. Note that there are two possible paths (clockwise and anti-clockwise) between the initial and final position of the pivot and that both lead to the same final state up to a total sign.

As a special case, consider the behavior of the logical code state vectors $|\bar{0}\rangle_5$ and $|\bar{1}\rangle_5$ of the $[[5,1,3]]$ code under cyclic permutations (here, for a clockwise shift of two edges):



We see that a cyclic permutation of these states is equivalent to a rotation of its dimer parities, which is simply a rotation of the corresponding diagram. This is because the tensors T corresponding to these states are invariant under cyclic permutations of indices, i.e., $T_{i,j,k,l,m} = T_{m,i,j,k,l}$. The explicit construction of these states can be easily performed using *matchgate tensors* [16].

E. Computing entanglement

The entanglement entropy $S_A = -\text{tr}_A(\rho_A \log \rho_A)$ of a subsystem A and its corresponding reduced density matrix

$\rho_A = \text{tr}_{A^C}(\rho_{\text{tot}})$ can be evaluated diagrammatically. Given the $2M \times 2M$ Majorana covariance matrix Γ^A of the subspace belonging to A (i.e., the rows and columns of the full $2L \times 2L$ covariance matrix Γ whose Majorana modes are contained in A), we can perform a special orthogonal transformation $\Gamma^A = Q\tilde{\Gamma}^AQ^T$ to the form

$$\tilde{\Gamma}^A = \bigoplus_{i=1}^M \begin{pmatrix} 0 & \lambda_i \\ -\lambda_i & 0 \end{pmatrix}, \quad (61)$$

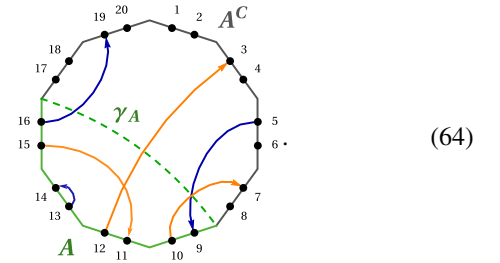
where $\pm i\lambda_k$ are the eigenvalues of Γ^A , some of which may be zero. From this form, the entanglement entropy follows as

$$S_A = \sum_{i=1}^M \left(-\frac{1+\lambda_i}{2} \log \frac{1+\lambda_i}{2} - \frac{1-\lambda_i}{2} \log \frac{1-\lambda_i}{2} \right). \quad (62)$$

As we have found in Sec. III, the covariance matrix entries $\Gamma_{j,k}$ of Majorana dimer states can only be ± 1 or zero. Consider the j th row (or column) of the submatrix Γ^A : The dimer connected to Majorana mode j ends on another mode k (with $1 \leq k \leq 2L$). If $j, k \in A$, the j and k th row will jointly contribute to a λ_i of ± 1 , i.e., zero entanglement entropy. However, if $j \in A, k \notin A$, the j th row of Γ^A will be zero. As the number of such ‘‘dimer leaks’’ must be even, each pair contributes to a vanishing λ_i . Thus, each dimer connecting A with its complement A^C contributes an entanglement entropy of $\frac{1}{2} \log 2$, i.e., half of an EPR pair, a maximally entangled pair of qubits. Graphically, the entanglement entropy reduces to counting such dimers

$$S_A = (\# \text{ dimers between } A \text{ and } A^C) \times \frac{\log 2}{2}. \quad (63)$$

Consider the following example state:



The subsystem A comprises four edges with the Majorana modes 9 to 16. As four dimers connect A with A^C , the entanglement entropy is given by $S_A = 2 \log 2$. Effectively, S_A counts the number of dimers across the cut γ_A separating A from A^C (shown as a dashed line). For contracted states, $S_A \leq |\gamma_A| \log 2$, where $|\gamma_A|$ is the length of the shortest cut through the contracted network. Thus, we recover the tensor network interpretation of the Ryu-Takayanagi surface γ_A , which appears in continuum AdS/CFT in the holographic entanglement entropy formula [40]

$$S_A = \frac{|\gamma_A|}{4G_N}, \quad (65)$$

which expresses S_A in terms of the area of the minimal surface γ_A , denoted $|\gamma_A|$, and Newton’s constant G_N . In our two-dimensional bulk space, γ_A is simply a geodesic and $|\gamma_A|$ is its length. We will see later how the discrete analog of (65), where $1/(4G_N) \rightarrow \log 2$, is saturated in the HyPeC.

The definition of entanglement entropy S_A can be ambiguous under a mapping from spins to fermions, as fermionic operators on different sites do not commute. As long as we consider connected subsystems A , such a mapping (37) yields the same S_A , as both are related only by cyclical permutation of fermionic sites, which only leads to a sign flip along the permuted rows and columns of the covariance matrix Γ . For a region A composed of disconnected parts, S_A is generally not preserved by a mapping from spins to fermions. If, as in the HyPeC model, we want to compute the spin entanglement entropy in the effective fermionic picture, we first need to permute the spin degrees of freedom so that A becomes connected and then apply the mapping to fermions. However, such a spin transposition usually breaks the Majorana dimer structure, as it leads to fermionic states that are not ground states of Hamiltonians quadratic in Majorana operators. Thus, (63) describes fermionic entanglement that remains valid in the spin picture only for connected regions A .

In the fermionic picture, we can easily generalize (63) to disjoint subsystems, such as the *mutual information*

$$I(A : B) = S_A + S_B - S_{AB} = (\# \text{ dimers between } A \text{ and } B) \times \log 2. \quad (66)$$

Compared to (63), each dimer in Eq. (66) is counted twice. In terms of the geometry of the dimer graph itself, (66) corresponds to a system with an *exact area law* [41]. One of the properties of this form of the mutual information is an always vanishing *tripartite information* [42]

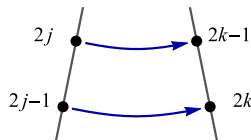
$$I_3(A : B : C) = I(A : B) + I(A : C) - I(A : BC) = 0. \quad (67)$$

This implies that Majorana dimer models are compatible with holographic theories, where $I_3 \leq 0$ [43]. Furthermore, as we show in Appendix B, the spectrum of Rényi entropies

$$S_A^{(n)} = \frac{1}{1-n} \log \text{tr}(\rho_A^n) \quad (68)$$

is flat, a property of the underlying stabilizer state structure [44]. We show in Appendix B that this property also follows from the Majorana dimer picture for arbitrary local superpositions of bulk input in the HyPeC under certain constraints on the (compact) boundary region considered.

To clarify the connection between Majorana dimers and EPR pairs, we can explicitly construct Bell states from pairs of dimers. Consider the following two even-parity dimers connecting edges j and k (with $j < k$) without crossing:



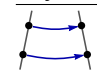
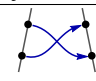
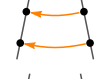
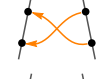
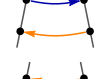
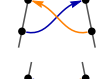
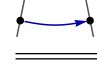
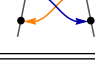
$$\quad (69)$$

This corresponds to two conditions on the total state vector $|\psi\rangle$,

$$(\gamma_{2j-1} + i \gamma_{2k})|\psi\rangle = (f_j^\dagger + f_j - f_k^\dagger + f_k)|\psi\rangle = 0, \\ (\gamma_{2j} + i \gamma_{2k-1})|\psi\rangle = i(f_j^\dagger - f_j + f_k^\dagger + f_k)|\psi\rangle = 0. \quad (70)$$

As no entanglement between edges j and k and the rest of the system exists, $|\psi\rangle$ should be factorizable with regards to these

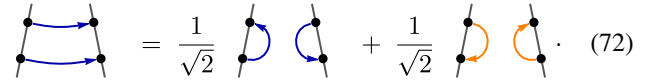
TABLE I. Bell states expressed as Majorana dimers.

Majorana dimer	Bell state	Majorana dimer	Bell state
	$\frac{ 0\rangle 0\rangle + 1\rangle 1\rangle}{\sqrt{2}}$		$\frac{ 0\rangle 1\rangle + i 1\rangle 0\rangle}{\sqrt{2}}$
	$\frac{ 0\rangle 0\rangle - 1\rangle 1\rangle}{\sqrt{2}}$		$\frac{ 0\rangle 1\rangle - i 1\rangle 0\rangle}{\sqrt{2}}$
	$\frac{ 0\rangle 1\rangle + 1\rangle 0\rangle}{\sqrt{2}}$		$\frac{ 0\rangle 0\rangle + i 1\rangle 1\rangle}{\sqrt{2}}$
	$\frac{ 0\rangle 1\rangle - 1\rangle 0\rangle}{\sqrt{2}}$		$\frac{ 0\rangle 0\rangle - i 1\rangle 1\rangle}{\sqrt{2}}$

degrees of freedom:

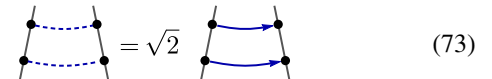
$$|\psi\rangle \propto (a + bf_j^\dagger + cf_k^\dagger + df_j^\dagger f_k^\dagger)(\dots)|\emptyset\rangle, \quad (71)$$

where (\dots) includes terms containing creation operators f_i^\dagger with $i \neq j, k$. Up to a complex phase, the parameters $a, b, c, d \in \mathbb{C}$ can be fixed using (70), which leads to $b = c = 0$ and $a = d = 1/\sqrt{2}$ (assuming normalization). This corresponds to a Bell state vector $|\Phi^+\rangle = (|0\rangle|0\rangle + |1\rangle|1\rangle)/\sqrt{2}$ on sites j and k . This analysis can be repeated for all possible dimer configurations, yielding Table I. Conveniently, this allows us to form superpositions of dimers, for example,



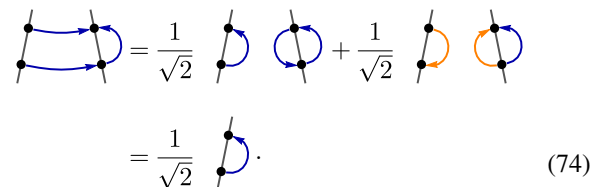
$$\quad (72)$$

Each diagram in this expression corresponds to a normalized Majorana dimer state. Note that this diagram confirms our intuition that a contraction, which is the sum of projections onto $|0\rangle$ and $|1\rangle$, is equivalent to connecting pairs of Majoranas via dimers. In a mild abuse of notation, we may thus write



$$\quad (73)$$

to express a contraction (dashed lines). This also allows us to fix relative factors that appear through contraction, such as in the following projection of (72) onto a $|0\rangle$ state vector:



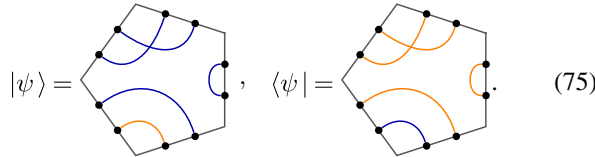
$$\quad (74)$$

The second term vanishes from the condition $\langle 0|1\rangle = 0$, in agreement with the rule that loops of total odd parity vanish [compare Eq. (45)]. Note that the arrow orientation of the dimer for $\langle 0|$ is reversed, as it is used in its adjoint form $\langle 0|$ (more on Hermitian conjugates in the next section). Projections like (74) can be evaluated for each of the entries in Table I, always leading to a resulting factor of $1/\sqrt{2}$. This result is heavily used in Appendix B, where we study the entanglement properties of superpositions of HyPeC code

states, where norms of Majorana dimer states become relevant.

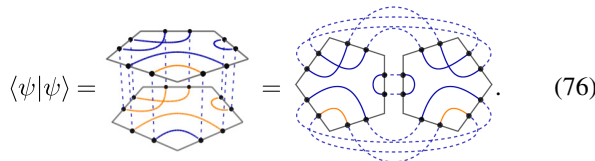
F. Orthogonality and completeness

Our diagrammatic notation can also express inner products. Consider the bra $\langle\psi|$ corresponding to a ket $|\psi\rangle$. Clearly, if $(\gamma_j + i\gamma_k)|\psi\rangle = 0$ then $\langle\psi|(\gamma_j - i\gamma_k) = 0$ holds for the adjoint. Thus, we can visualize adjoints by inverting all arrows and corresponding parities, for example (omitting labels):



$$|\psi\rangle = \text{diagram}, \quad \langle\psi| = \text{diagram}. \quad (75)$$

The inner product $\langle\psi|\psi\rangle$ is a contraction between $|\psi\rangle$ and $\langle\psi|$ over all indices, expressed as



$$\langle\psi|\psi\rangle = \text{diagram} = \text{diagram}. \quad (76)$$

The right-hand side, showing a “flipped” $\langle\psi|$, represents a Choi-Jamiołkowski isomorphism expressing $\langle\psi|$ in the same Hilbert space as $|\psi\rangle$. This involves an inversion of the orientation which flips all dimer parities. As all diagrams are defined for normalized state vectors that satisfy $\langle\psi|\psi\rangle = 1$. Furthermore, we can easily evaluate whether two diagrams correspond to orthogonal states as a contraction $\langle\psi|\phi\rangle$ of $|\psi\rangle$ and $|\phi\rangle$ vanishes for any odd-parity loop (see Appendix A). In particular, $|\psi\rangle$ and $|\phi\rangle$ are orthogonal if they share the same correlation structure (i.e., pairing of Majorana modes) but differ in at least one dimer parity. This allows us to construct the complete Hilbert space with Majorana dimer states on N edges by fixing a correlation structure and then flipping through all 2^N possible dimer parities, resulting in 2^N mutually orthogonal state vectors. Since the Hilbert space is also 2^N dimensional, we can express any state in it by a superposition of Majorana dimer states under the given correlation structure. This is equivalent to obtaining a orthogonal stabilizer state basis by considering all 2^N sign combinations of N stabilizer generators.

IV. THE HYPEC WITH MAJORANA DIMERS

A. Overview

As we saw in the previous section, the computational basis logical code states of the $[[5, 1, 3]]$ quantum error-correcting code can be expressed as Majorana dimers. Furthermore, we showed that identifying Majorana dimer states as tensors and contracting them yields new Majorana dimer states and that these contractions are easy to evaluate diagrammatically. Because the HyPeC is built from tensors each representing the $[[5, 1, 3]]$ code, we find the following key result.

Theorem 2 (Representing the HyPeC with Majorana dimers). The hyperbolic pentagon code (HyPeC) with logical bulk input fixed to local basis states $\bar{0}$ or $\bar{1}$ yields a Majorana

dimer state on the boundary. Each input corresponds to a (unique) pattern of dimer parities on the boundary state.

While fermionic modes require an explicit ordering, we show in Appendix C that different contraction orderings lead to equivalent boundary states. We will now show how the geometry of the dimers in the HyPeC determines its properties, using the tools developed in the previous section.

B. Dimers and entanglement structure

First, we will consider the physical properties of the HyPeC for logical inputs fixed locally to $\bar{0}$ or $\bar{1}$. The code is constructed from a hyperbolic $\{5, 4\}$ tiling,² with each tile now set to (23) or (24) (the full HyPeC also allows for superpositions between the two). As the model consists of asymptotically infinite tiles, we have to define a UV cutoff at which the tiling is truncated. We do this by starting with a central tile and iteratively adding tiles on all free edges. The number n of iterations thus gives the graph distance between each boundary tile and the center, determining the cutoff. Such a series of iterations for an all- $\bar{0}$ bulk input is visualized in Fig. 2.

The contracted dimers are drawn as geodesics in the Poincaré disk. This is not an arbitrary choice, as the dimers follow discrete geodesics (i.e., shortest paths) in the $\{5, 4\}$ tiling. Figure 3 shows the $n \rightarrow \infty$ limit both for an example of two dimers and the whole contraction. Because of the particular property of the $\{5, 4\}$ tiling that the pentagon edges connect to continuous geodesics, the asymptotic endpoints of a contracted dimer are also endpoints of such a geodesic.³ Tracing this geodesic back into the bulk, we see that it passes along all tiles that contained the uncontracted dimer pieces. Furthermore, as Fig. 3 also shows, there are always two dimers with the same pair of asymptotic boundary points, resulting in a bulk geodesic that is dual to a boundary Bell state. While Fig. 3 only shows a uniform $\bar{0}$ bulk input, the dimer parities generally differ with the input. The dimer pairs then correspond to different types of Bell states, as in Table I. Note that the Majorana modes composing the effective fermions of these Bell states are located on neighboring boundary edges at any finite cutoff. This elucidates the code’s error-correction properties: Any product of pairs of Majorana operators $i\gamma_j\gamma_k$ acting on dimer endpoints (j, k) can only change the state up to a total sign and is thus a representation of a logical parity operation in the bulk. While single Majorana operators are nonlocal in terms of spins, pairs of Majorana operators on neighboring sites can be expressed by a local pair of Pauli operators [compare (25)]. For each pair of HyPeC dimers, there then exists a boundary operator \mathcal{O} of weight $|\mathcal{O}| = 4$, i.e., consisting of four Pauli operators acting on the boundary, which represents a logical bulk operation. Thus, even for an infinitely large number of HyPeC tiles, the code distance d never exceeds $d = 3$, as such an \mathcal{O} represents an error on the code space.

²This *Schläfli symbol* denotes a polygon tiling with four pentagons at each vertex.

³In the dual $\{4, 5\}$ tiling, each four-sided tile contains an intersection of two such geodesics meeting at right angles.

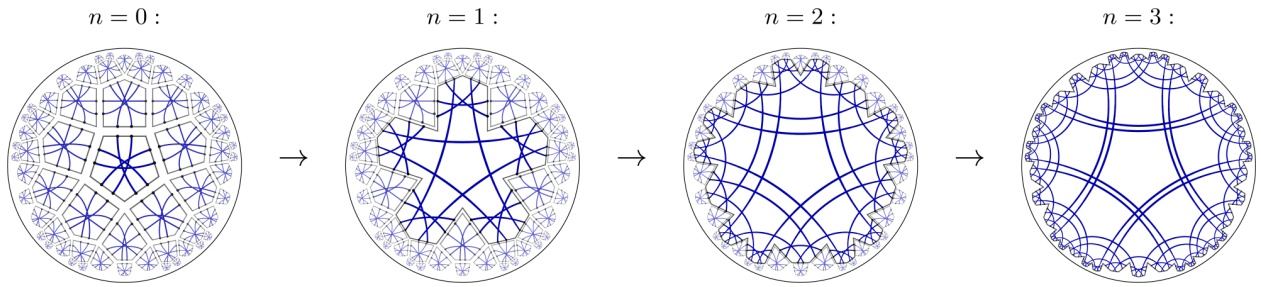


FIG. 2. Iterative contraction of the HyPeC for fixed bulk inputs of $|\bar{0}\rangle_5$ state vectors, with a cutoff after 3 iterations. Each step involves contracting a further layer of tiles, starting from the center at $n = 0$. The asymptotic boundary of the Poincaré disk is drawn as a black circle.

Given this picture of pair entanglement on the boundary through bulk geodesics, the dependence of the entanglement entropy S_A on the boundary subsystem size $|A| = \ell$ can be explicitly computed. Clearly, the position of this subsystem affects the value of S_A , as the distribution of entangled pairs in Fig. 3 does not respect translation invariance on the boundary. Thus, we consider the average expectation value $\mathbb{E}_\ell(S)$ of the entanglement entropy instead. The results in Fig. 4 show an approximate logarithmic growth $S_A \propto \log \ell$, as expected of a critical theory. Fitting against the expected logarithmic scaling expected for a CFT [45],

$$S_A = \frac{c}{3} \log \left(\frac{L}{\pi \epsilon} \sin \frac{\pi \ell}{L} \right) \simeq \frac{c}{3} \log \frac{\ell}{\epsilon} + O((\ell/L)^2), \quad (77)$$

we find a central charge $c \approx 4.2$ (dashed line in Fig. 4). For a finite system of boundary size L , S_A reaches its maximum at $\ell = L/2$, in agreement with the full form of (77). Each iteration preserves the entanglement entropy scaling of the previous one up to $\ell \approx L/4$. We already observed this behavior in a previous analysis using *matchgate tensors* [16].

The logarithmic entanglement entropy scaling saturates the bound we observed in Eq. (64): The maximum entanglement between two boundary regions A and A^C is proportional to the maximum number of dimers that can connect them, or equivalently, the number of edges $|\gamma_A|$ of a minimal cut γ_A through the bulk separating A from A^C . Because of the hyperbolic geometry of the $\{5, 4\}$ tiling, $|\gamma_A| \propto \log |A|$. As γ_A is a geodesic in this discrete geometry, no other geodesic—and thus no dimer—can pass through it twice (up to cases such as in Fig. 6), turning the upper bound into an equality:

$$S_A = |\gamma_A| \log 2 \propto \log \ell. \quad (78)$$

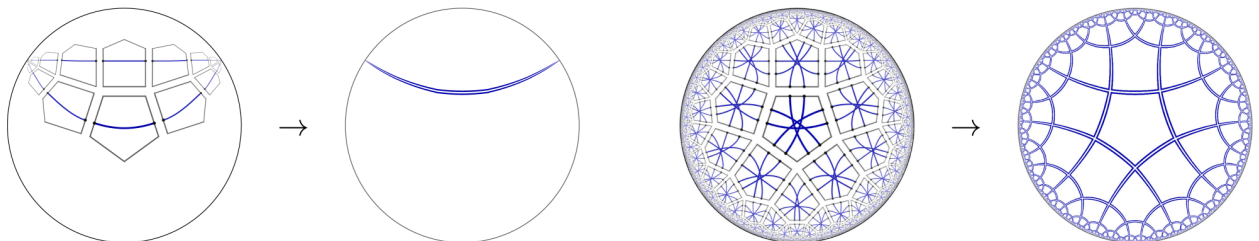


FIG. 3. Left: A Majorana dimer pair in an infinitely large contraction of HyPeC tiles. The endpoints of both dimers meet at the asymptotic boundary, and thus the dimer pair can be drawn as a double geodesic. Right: Full contraction for a $|\bar{0}\rangle$ input on all tiles, with all dimers pairing up.

Clearly, this result is the same for each computational basis state input, as changing this input only changes dimer parities, leaving S_A invariant.

We can modify the infrared (IR) structure of our boundary states by modifying the central tiles. There are two possible approaches: One is the replacement of the dimer structure in these tiles, and the other is the complete removal of the tiles. In the first case, we simply reconnect the dimers with each other, so that they no longer follow geodesics. This breaks the conditions for the saturation of the bound (78), so that we reduce the entanglement of the boundary states. The more tiles in the center are changed [e.g., to the vacuum (17)], the further long-range entanglement is suppressed, so that we approach a *gapped* boundary state with constant (i.e., area-law) entanglement.

The second case was already considered in the original HyPeC model: When removing entire tiles, auxiliary bulk degrees of freedom (open edges, or open legs in tensor network language) are opened up. The usual interpretation of this setup is that of a black hole, or when extending the open edges to a noncontracted auxiliary system, that of a *wormhole*. In both cases, the boundary state of this setup should exhibit an additional thermal entropy, which the Ryu-Takayanagi formula interprets as a deformation of geodesics around the horizon. In the language of Majorana dimers, this additional entropy is explained by dimers ending on the open edges: Following (62), any dimer in a region A that connects to a site outside of A contributes $\log(2)/2$ to the entanglement entropy S_A . When A becomes large, this entropy contribution scales with the “horizon area” of the black hole, i.e., the number of fermionic modes on the open edges. As we increase the radius of the black hole, S_A will begin to grow linearly with the size of A , as expected of a thermal CFT.

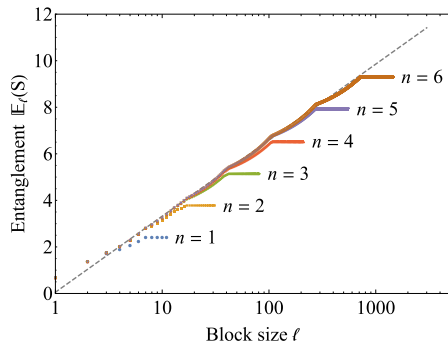


FIG. 4. Entanglement entropy scaling with the size ℓ of the subsystem block for successive iterations n of the contraction. Dashed line is a logarithmic fit of the $n \rightarrow \infty$ limit.

As we show in Appendix B, the entanglement entropy S_A of compact subsystems A of the HyPeC for logical bulk input can be generalized to arbitrary *local* input, i.e., superpositions of $\bar{0}$ and $\bar{1}$ that factorize between the tiles. Without additional entanglement between bulk sites, S_A is independent of the specific bulk input, as long as the boundary regions A and its complement A^C are reducible to the same discrete bulk geodesic γ_A via the *greedy algorithm* [5], which can be completely rederived using Majorana dimers. This algorithm iteratively removes tiles with three or four open edges (see Fig. 5), deforming A into a region A' further in the bulk, while keeping $S_A = S_{A'}$ invariant. Figure 6 illustrates how some boundary regions B are not reducible to the same geodesic γ_B as their complement regions B^C . In these cases, no cut along the pentagon edges can completely separate dimers with endpoints in B from those with endpoints in B^C , leaving dimers in a *residual bulk region*. While (63) still holds if local bulk inputs are fixed to basis states $\bar{0}$ or $\bar{1}$, the entanglement entropy S_B for local superpositions can generally be larger, as there is additional input-dependent entanglement between the residual dimers. For example, in the setup of Fig. 6 (bottom),

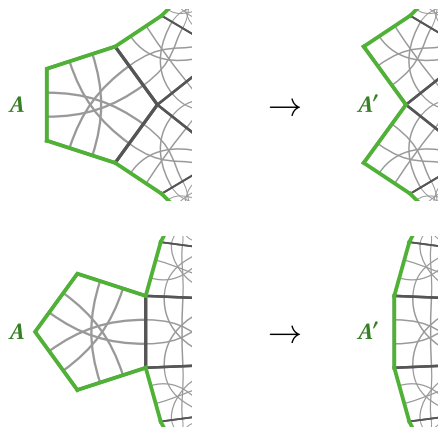


FIG. 5. The greedy algorithm: The boundary region A is pushed into the bulk to a new region A' by removing pentagon tiles with three (top) and four (bottom) open edges. Each pentagon can be in an arbitrary local superposition of $\bar{0}$ and $\bar{1}$, shown as gray-shaded dimers.

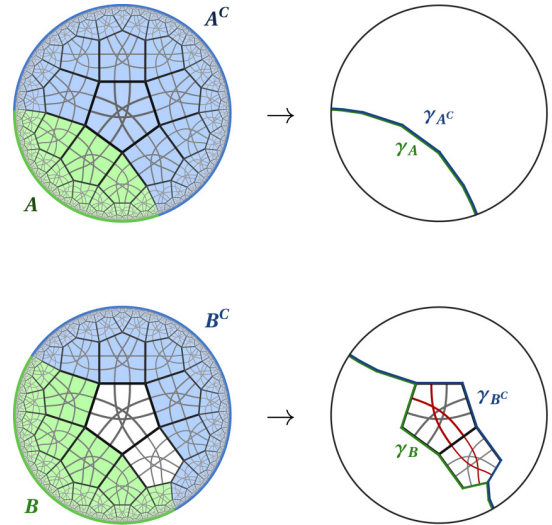


FIG. 6. Reducing boundary regions in the HyPeC with the greedy algorithm, for two boundary regions A and B . A reduces to the same geodesic $\gamma_A = \gamma_{A^C}$ as its complement A^C , while B does not. On the left-hand side, the corresponding “greedy wedge” is shaded in the same color as the boundary regions. The residual dimers are shaded in red.

S_B can be up to $\log 2$ larger than the fixed-input result (see Appendix B for details).

C. Scaling and RG flow

As we saw in Fig. 3, contracting the HyPeC produces effective boundary EPR pairs connected along geodesics through the bulk. This allows for a naive interpretation in terms of IR/UV scaling: Longer geodesics that probe deeper into the bulk are then associated with the IR scale, while short-range geodesics close to the boundary correspond to UV modes. The iteration of contractions in Fig. 2 is then interpreted as a renormalization group (RG) flow, with each new iteration adding additional degrees of freedom. As each tile connects to either one or two tiles of the previous iteration, there are two possible local scaling steps, both of which are shown in Fig. 7. Thus, either one or three new dimers are added in each local step.

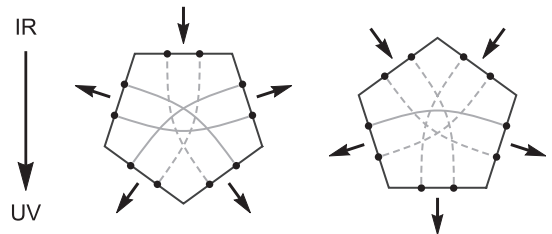


FIG. 7. Each tile in the HyPeC can act as a mapping of $1 \rightarrow 4$ edges (left) or $2 \rightarrow 3$ edge (right). Arrows distinguish between “input” (IR) and “output” (UV) edges. Dimers extended from previous tiles are drawn as dashed curves, while new ones are drawn as solid curves. The dimer parities depend on the actual logical input on the tile.

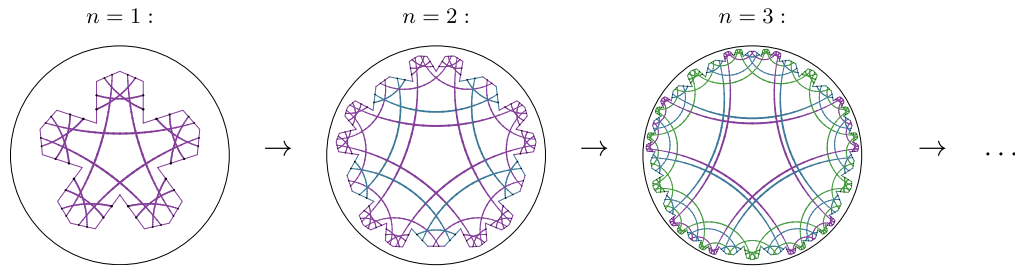


FIG. 8. Iterative contraction of the HyPeC, with Majorana dimers belonging to decoupled fermionic subsystems drawn in different colors. The number of such subsystems increases with iteration number n .

This IR \rightarrow UV renormalization step has a well-defined UV \rightarrow IR inverse constructed from the Hermitian conjugate of a specific tile. Consider the $2 \rightarrow 3$ step from Fig. 7: The IR \rightarrow UV step consists of contracting the edges 1 and 2 of $|\psi\rangle = \alpha|\bar{0}\rangle_5 + \beta|\bar{1}\rangle_5$ (with $|\alpha|^2 + |\beta|^2 = 1$) onto the boundary state. To inverse this operation, we trace out the edges 3,4,5 of $|\psi\rangle\langle\psi|$, which we can express using Majorana dimers [full calculation (B10) in Appendix B]:

$$\text{tr}_{(3,4,5)} |\psi\rangle\langle\psi| = \frac{|\alpha|^2 + |\beta|^2}{2} \text{ (dimer diagram) } = \frac{\mathbb{1}_4}{4}. \quad (79)$$

Note the representation of the identity as a set of dimers directly connecting two pairs of edges: Any Majorana dimer state is left invariant by contraction with such a state, and hence any other state, which we can always express in a dimer basis, as well. We can similarly find that $\text{tr}_{(2,3,4,5)} |\psi\rangle\langle\psi| = \mathbb{1}_2/2$. The inverse renormalization step is thus simply the reversal of Fig. 7: Some dimers are closed into loops, thus tracing out the associated degrees of freedom. In fact, this result is closely related to the *perfect tensor* property of the HyPeC, whereby any pentagon tile can act as an isometry of $k \rightarrow 5 - k$ edges as long as $k \leq 5 - k$. We also use it in Appendix B to prove the greedy algorithm with Majorana dimers.

While we saw that Majorana dimers form effective EPR pairs in the asymptotic limit of infinitely many contractions, we can also observe a separation of the boundary into separate fermionic subsystems at finite cutoff. The physical fermion corresponding to each uncontracted edge can be coupled to at most two other fermions or edges via the dimers it contains. These two fermions are again coupled to further fermions, so we end up with a—necessarily closed—chain of fermions, each only coupled to its two nonlocal “neighbors.” However, as we contract more tiles, we find that our boundary fermions are separated into an increasing number of independent chains. This is shown in Fig. 8 for the first few iterations, where the dimers are colored according to the decoupled fermionic chain they belong to. The appearance of additional decoupled subsystems at larger iterations is another sign of an RG flow: Increasing the number of iterations encodes more subsystems of varying sizes on the boundary. For the full HyPeC beyond basis-state input, correlations between these subsystems can be nonzero. As we will show next, however, such correlations can only be captured by n -point correlators with $n > 2$.

D. Correlation functions for general bulk input

By counting the dimers by the boundary distance over which they reach, the average correlation falloff of the Majorana covariance matrix Γ defined in Eq. (18) can be determined. For fixed input, this leads to a polynomial $\Gamma_{j,k} \propto |j - k|^{-1}$ falloff of two-point correlations [16], again resembling a CFT scaling. Naively, this holds only for the case of a fixed logical input $\bar{0}$ or $\bar{1}$ on each tile, as superpositions of Majorana dimer states are generally non-Gaussian and have a complicated two-point correlation structure.

However, we will now show that two-point correlations for the HyPeC with general bulk input, where local superpositions of $\bar{0}$ and $\bar{1}$ inputs are allowed, are surprisingly similar to the fixed-input case. First, consider the dimer parity structure caused by local $\bar{1}$ inputs. As we showed in Fig. 2, using even-parity $\bar{0}$ input over the entire bulk leads to a simple contracted state, where all resulting dimer parities are even. When contracting over odd-parity $\bar{1}$ inputs, index permutations necessary during the contraction process can lead to additional dimer parity flips caused by Z operators on some of the pentagon edges. After going through the contraction process, which is laid out in Appendix C, we find that these dimer parity flips can be grouped into strings of Z operators between the tiles with $\bar{1}$ input. Possible configurations are shown in Fig. 9 for two and four $\bar{1}$ insertions. While neither the pairing of $\bar{1}$ tiles with Z strings nor the paths of these strings are unique, we can freely deform them without changing the boundary state (bottom diagrams in Fig. 9). Furthermore, we can freely add closed Z loops around a set of tiles with an even number of $\bar{1}$ tiles in it, as this is equivalent to evaluating the total (even) parity of the contained tiles. Intriguingly, we can relate this to physical rotations of tiles: While the dimer parities of $\bar{0}$ tiles are invariant under cyclic permutations (in the spin picture), we showed in Eq. (60) that a rotation of a tile with $\bar{1}$ input is equivalent to tracing the shifted endpoint of the local ordering with a Z string. A full “rotation” (leading to a closed Z loop around a $\bar{1}$ tile) changes the state by a total minus sign. In other words, as shown in Fig. 9, Z string loops around tiles with an even number of $\bar{1}$ insertions leave the state invariant. Thus, it is tempting to interpret the $\bar{0}$ tiles as local fermionic vacua and the $\bar{1}$ tiles as logical fermions, emergent from the underlying spin degrees of freedom.

The set of boundary states for all possible basis-state bulk inputs ($\bar{0}$ or $\bar{1}$ on each tile) gives us a basis set for the states of the full HyPeC. In general, boundary n -point functions for an arbitrary input can have a correlation structure completely different from the dimer structure we saw for logical

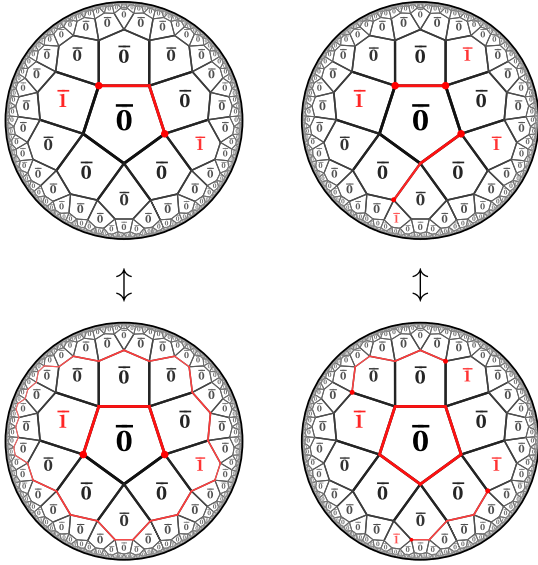


FIG. 9. Top: Inserting two (left) and four (right) $\bar{1}$ tiles in the HyPeC. Beyond the local dimer parity flips in each tile, pairs of $\bar{1}$ tiles are connected by Z strings (red lines), which flip dimer parities nonlocally. The endpoints of these strings (red dots) set the local orientation of the $\bar{1}$ tiles connected to it. Bottom: Equivalent Z string configuration of the upper two states.

basis-state input, and overlaps between different basis states can change the entanglement structure. Fortunately, as we show in Appendix C, the HyPeC boundary states for different basis inputs are all distinct by an operator of *Majorana weight* $\mathfrak{w} > 2$, i.e., at least three Majorana operators γ_k are required to map one basis state to another. This leads us to the following conclusion:

Theorem 3. For a contraction of N pentagon tiles of the HyPeC, two-point correlation functions of the boundary states are convex combinations of the covariance matrices for any logical basis input.

Proof. We denote by $|b\rangle := |b_1, b_2, \dots, b_N\rangle$ the state vector for a fixed basis-state input b_k on the k th pentagon. A general HyPeC boundary state vector is given by the superposition

$$|\omega\rangle = \sum_{b \in \{\bar{0}, \bar{1}\}^{\times N}} c_b |b\rangle, \quad (80)$$

with $c_b \in \mathbb{C}$. A fermionic two-point correlation function with entries

$$G_{j,k}^{(2)} = \frac{i}{2} \langle \omega | [\gamma_j, \gamma_k] | \omega \rangle \quad (81)$$

$$= \sum_{b, b' \in \{\bar{0}, \bar{1}\}^{\times N}} \frac{i c_b^* c_{b'}}{2} \langle b | [\gamma_j, \gamma_k] | b' \rangle \quad (82)$$

is generally a sum of 2^{2N} terms. However, we assumed that two boundary states for different basis-state inputs b and b' are separated by a $\mathfrak{w} > 2$ operator, i.e., fulfill the conditions

$$\langle b | b' \rangle = 0, \quad (83)$$

$$\langle b | \gamma_j | b' \rangle = 0, \quad (84)$$

$$\langle b | \gamma_j \gamma_k | b' \rangle = 0. \quad (85)$$

In other words, the expectation values of operators with Majorana weight $\mathfrak{w} \leq 2$ are diagonal in the logical basis. This implies

$$\begin{aligned} G_{j,k}^{(2)} &= \sum_{b \in \{\bar{0}, \bar{1}\}^{\times N}} \frac{i c_b^* c_b}{2} \langle b | [\gamma_j, \gamma_k] | b \rangle \\ &= \sum_{b \in \{\bar{0}, \bar{1}\}^{\times N}} |c_b|^2 \Gamma_{j,k}^b, \end{aligned} \quad (86)$$

where $\Gamma_{j,k}^b = i \langle b | [\gamma_j, \gamma_k] | b \rangle / 2$ are the covariance matrices for the Gaussian boundary state for a basis-state input b . ■

This enormously simplifies the computation of fermionic two-point correlation functions. For example, consider the contraction of only two pentagon states: There are four possible fixed logical bulk inputs, with a $\bar{0}$ or $\bar{1}$ input on either pentagon. When contracted, these lead to the “boundary” state vectors $|\bar{0}, \bar{0}\rangle_8$, $|\bar{0}, \bar{1}\rangle_8$, $|\bar{1}, \bar{0}\rangle_8$, and $|\bar{1}, \bar{1}\rangle_8$ on eight edges. Now consider a general logical input, i.e., a state vector $\alpha_1 |\bar{0}\rangle_5 + \beta_1 |\bar{1}\rangle_5$ on the first tile and $\alpha_2 |\bar{0}\rangle_5 + \beta_2 |\bar{1}\rangle_5$ on the second (with $|\alpha_k|^2 + |\beta_k|^2 = 1$). As tensor contraction is a linear operation, the contracted state vector is given by

$$|\omega\rangle = \alpha_1 \alpha_2 |\bar{0}, \bar{0}\rangle_8 + \beta_1 \beta_2 |\bar{1}, \bar{1}\rangle_8 \quad (87)$$

$$+ \alpha_1 \beta_2 |\bar{0}, \bar{1}\rangle_8 + \beta_1 \alpha_2 |\bar{1}, \bar{0}\rangle_8. \quad (88)$$

In dimers, the explicit basis-state contractions are

$$|\bar{0}, \bar{0}\rangle_8 = \text{Diagram with 16 vertices and 8 edges, showing blue and orange dimer parity flips.} \quad (89)$$

$$|\bar{0}, \bar{1}\rangle_8 = \text{Diagram with 16 vertices and 8 edges, showing blue and orange dimer parity flips.} \quad (90)$$

$$|\bar{1}, \bar{0}\rangle_8 = \text{Diagram with 16 vertices and 8 edges, showing blue and orange dimer parity flips.} \quad (91)$$

$$|\bar{1}, \bar{1}\rangle_8 = \text{Diagram with 16 vertices and 8 edges, showing blue and orange dimer parity flips.} \quad (92)$$

Note that in this labeling, the first pentagon is on the right. As we can see, each of these state vectors is distinguished from the others by at least three dimer parity flips; i.e., it requires more than two Majorana operators to map between them. As

a result, $G^{(2)}$ only contains four diagonal terms,

$$G_{j,k}^{(2)} = |\alpha_1|^2 |\alpha_2|^2 \Gamma_{j,k}^{\bar{0},\bar{0}} + |\beta_1|^2 |\beta_2|^2 \Gamma_{j,k}^{\bar{1},\bar{1}} + |\alpha_1|^2 |\beta_2|^2 \Gamma_{j,k}^{\bar{0},\bar{1}} + |\beta_1|^2 |\alpha_2|^2 \Gamma_{j,k}^{\bar{1},\bar{0}}, \quad (93)$$

with the covariance matrix $\Gamma_{j,k}^{b_1,b_2}$ containing two-point correlations for the basis state vector $|b_1, b_2\rangle_8$.

This example, as well as the general case of Theorem 3, implies that two-point functions $G^{(2)}$ preserve the correlation structure of the fixed-input covariance matrices Γ , whose entries only differ by signs (i.e., dimer parities). Hence, if $\Gamma_{j,k} = 0$ for a fixed logical input (no dimer connecting Majorana modes j and k), then two-point correlations between the two modes vanish for *any* bulk input. This is even true for the case of superpositions with entangled bulk input, where $G^{(2)}$ is still a convex sum. Higher order correlation functions separate into a Gaussian part that follows Wick's theorem and has the form of products of dimer terms, and a non-Gaussian part which contains contributions from overlaps between boundary states for different logical inputs. To illustrate, consider a single pentagon with arbitrary logical input, described by $|\psi\rangle = \alpha|\bar{0}\rangle_5 + \beta|\bar{1}\rangle_5$ (with $|\alpha|^2 + |\beta|^2 = 1$). The n -point correlators $G^{(n)}$ until $n = 4$ are given by

$$G_j^{(1)} = \langle \psi | \gamma_j | \psi \rangle = 0, \quad (94)$$

$$G_{j,k}^{(2)} = i \langle \psi | \gamma_{[j} \gamma_{k]} | \psi \rangle = |\alpha|^2 \Gamma_{j,k}^{\bar{0}} + |\beta|^2 \Gamma_{j,k}^{\bar{1}}, \quad (95)$$

$$G_{j,k,l}^{(3)} = -i \langle \psi | \gamma_{[j} \gamma_{k} \gamma_{l]} | \psi \rangle = -i \alpha^* \beta \langle \bar{0} | \gamma_{[j} \gamma_{k} \gamma_{l]} | \bar{1} \rangle + \text{H.c.}, \quad (96)$$

$$G_{j,k,l,m}^{(4)} = \langle \psi | \gamma_{[j} \gamma_{k} \gamma_{l} \gamma_{m]} | \psi \rangle = |\alpha|^2 (\Gamma_{i,j}^{\bar{0}} \Gamma_{k,m}^{\bar{0}} - \Gamma_{i,k}^{\bar{0}} \Gamma_{j,m}^{\bar{0}} + \Gamma_{i,m}^{\bar{0}} \Gamma_{j,k}^{\bar{0}}) + |\beta|^2 (\Gamma_{i,j}^{\bar{1}} \Gamma_{k,m}^{\bar{1}} - \Gamma_{i,k}^{\bar{1}} \Gamma_{j,m}^{\bar{1}} + \Gamma_{i,m}^{\bar{1}} \Gamma_{j,k}^{\bar{1}}). \quad (97)$$

We have used square brackets around indices to denote antisymmetrization. Gaussian contributions can occur only for even n , as only pairs of Majorana operators can map a dimer state onto itself. As $|\bar{0}\rangle_5$ and $|\bar{1}\rangle_5$ are mapped to each other by a $\mathfrak{w} = 3$ operator, the non-Gaussian part appears at $n = 3$: The correlator $G_{j,k,l}^{(3)}$ can have nonzero entries for $j \in \{1, 6\}$, $k \in \{3, 8\}$, $l \in \{5, 10\}$ and its permutations, corresponding to the dimers differing between both input states [compare (23) and (24)]. As the exact entries of $G^{(3)}$ depend on the complex phases with which we define $|\bar{0}\rangle_5$ and $|\bar{1}\rangle_5$, they are not determined by the Majorana dimer structure.

Our example generalizes to large HyPeC contractions: The Gaussian part of n -point correlations $G^{(n)}$ is described by a convex combination of Gaussian covariance matrices, while all boundary states for fixed logical input that differ by n dimer parities contribute to its non-Gaussian part. We can think of the latter as an ‘‘interaction’’ between code words that depends on how much the logical bulk input is in a superposition of the basis state vectors $\bar{0}$ and $\bar{1}$. For a completely classical version of the code, no non-Gaussianity appears.

V. GENERALIZED CODES WITH MAJORANA DIMERS

A. Other stabilizer codes

We have extensively focused on the $[[5, 1, 3]]$ stabilizer code as the building block of the HyPeC. However, we can construct Majorana dimer models for states on other n gons, i.e., more general $[[n, 1, d]]$ stabilizer codes. We now show that these have properties very similar to the $n = 5$ case.

We set a number of requirements to such generalizations:

(I) Stabilizer code: We require $n - 1$ stabilizers (commuting products of Pauli operators) that lead to a twofold degenerate ground state, stabilizing one logical qubit.

(II) Majorana dimer representation: All stabilizers should be products of two Majorana operators, up to a total parity operator \mathcal{P}_{tot} .

(III) Rotational symmetry: All stabilizers S_k should be cyclic permutations of S_1 .

We may also wish to construct n -qubit codes that correspond to *perfect tensors*. For fixed input \bar{b} with $b \in \{0, 1\}$, this requires an isometric reduced density matrix

$$\rho_A = \text{tr}_{A^c} |\bar{b}\rangle_n \langle \bar{b}|_n \propto \mathbb{1}_{2^{|A|}} \quad (98)$$

for any subset A of sites with size $|A| \leq n/2$. To hold for arbitrary input (i.e., superpositions of $\bar{0}$ and $\bar{1}$), it is also necessary that $\bar{0}$ and $\bar{1}$ are partially orthogonal on A^c , i.e.,

$$\text{tr}_{A^c} |\bar{0}\rangle_n \langle \bar{1}|_n = \text{tr}_{A^c} |\bar{1}\rangle_n \langle \bar{0}|_n = 0, \quad (99)$$

again assuming $|A| \leq n/2$. Unfortunately, perfect tensors for qubits require states that are maximally entangled for any subdivision of sites, a condition which cannot be satisfied for $n = 4$ or any $n > 6$ [46,47]. As $n < 3$ does not correspond to a physical tile and we already covered the $n = 5$ case, this leaves only $n = 3$ and $n = 6$ to be studied with Majorana dimers. However, as we will see below, none of the corresponding Majorana dimer codes can be perfect for arbitrary bulk input.

Let us start with the $n = 3$ case. We can easily find a stabilizer code that conditions I–III. The stabilizers S are

$$Y_1 Y_2 = i \gamma_1 \gamma_4, \quad Y_1 Y_3 = i \mathcal{P}_{\text{tot}} \gamma_2 \gamma_5, \quad Y_2 Y_3 = i \gamma_3 \gamma_6. \quad (100)$$

The twofold degenerate ground state of the stabilizer Hamiltonian $H = -\sum_k S_k$ is spanned by one parity-even and one parity-odd Majorana dimer state with pairing between modes on opposite sites. Furthermore, for a fixed logical input $\bar{0}$ or $\bar{1}$ (but not its superpositions), the boundary state is described by a perfect tensor. This implies that adding such triangular tiles into the pentagon code preserves its entanglement structure only for logical basis-state input. Note that this code is equivalent to a repetition code under $Y_k \rightarrow Z_k$. We will explore the connection to GHZ states in the next section. Contrary to the pentagon code, embedding the states of this ‘‘triangle code’’ into a regular $\{3, k\}$ bulk tiling does not lead to interesting bulk/boundary relations, as the dimers close into loops.

Similarly, we can consider a ‘‘square code’’ for $n = 4$, where we find yet another stabilizer code with similar properties. The following stabilizers lead to a familiar Majorana

form:

$$\begin{aligned} X_1 X_2 Z_3 Z_4 &= -i \mathcal{P}_{\text{tot}} \gamma_1 \gamma_4, & Z_1 X_2 X_3 Z_4 &= -i \mathcal{P}_{\text{tot}} \gamma_3 \gamma_6, \\ Z_1 Z_2 X_3 X_4 &= -i \mathcal{P}_{\text{tot}} \gamma_5 \gamma_8, & X_1 Z_2 Z_3 X_4 &= -i \gamma_2 \gamma_7. \end{aligned} \quad (101)$$

Note that by applying a total parity operator, we can map this to an equivalent code with stabilizers $S = \langle Y_1 Y_2, Y_2 Y_3, Y_3 Y_4, Y_1 Y_4 \rangle$ (which again highlights the GHZ-type entanglement). As in the triangle code, Majorana dimers at a distance of three Majorana sites are paired up. Again, this implies trivial bulk loops of dimers for a regular $\{4, k\}$ tiling. Furthermore, this code does not lead to a perfect tensor for any logical input, as this is impossible to achieve with four-leg tensors. One may be tempted to construct a stabilizer code with $S = \langle X_1 Z_2 X_3, X_2 Z_3 X_4, X_1 X_3 Z_4, Z_1 X_2 X_4 \rangle$, where each element of S can also be written as a product of two Majorana operators on opposite edges (see Table II). However, this choice of S only stabilizes a single state instead of a full qubit, as the ground state is nondegenerate. Interestingly, this ground state does fulfill the perfect tensor property for connected subsets of the boundary legs.

Beyond the familiar $n = 5$ case (with permutations of $X_1 Z_2 Z_3 X_4$ as stabilizers), we can construct another code by exchanging $X_k \leftrightarrow Y_k$, which is equivalent to exchanging $\gamma_{2k-1} \leftrightarrow \gamma_{2k}$ and leads to the stabilizers

$$\begin{aligned} Y_1 Y_3 Z_4 Z_5 &= i \mathcal{P}_{\text{tot}} \gamma_2 \gamma_5, & Y_1 Z_2 Z_3 Y_4 &= i \gamma_1 \gamma_8, \\ Z_1 Y_2 Y_4 Z_5 &= i \mathcal{P}_{\text{tot}} \gamma_4 \gamma_7, & Y_2 Z_3 Z_4 Y_5 &= i \gamma_3 \gamma_{10}, \\ Z_1 Z_2 Y_3 Y_5 &= i \mathcal{P}_{\text{tot}} \gamma_6 \gamma_9. \end{aligned} \quad (102)$$

Naturally, this code inherits the properties of the original $[[5, 1, 3]]$ code, including the perfect tensor property for any logical input.

Attempting to generalize to $n = 6$, we find the following choice for the elements of S :

$$\begin{aligned} X_1 X_4 Z_5 Z_6 &= -i \mathcal{P}_{\text{tot}} \gamma_1 \gamma_8, & X_1 Z_2 Z_3 X_4 &= -i \gamma_2 \gamma_7, \\ Z_1 X_2 X_5 Z_6 &= -i \mathcal{P}_{\text{tot}} \gamma_3 \gamma_{10}, & X_2 Z_3 Z_4 X_5 &= -i \gamma_4 \gamma_9, \\ Z_1 Z_2 X_3 X_6 &= -i \mathcal{P}_{\text{tot}} \gamma_5 \gamma_{12}, & X_3 Z_4 Z_5 X_6 &= -i \gamma_6 \gamma_{11}. \end{aligned} \quad (103)$$

The $n = 6$ case resembles the $n = 3$ result, as partial traces $\text{tr}_{A^c} |\bar{0}\rangle \langle \bar{1}|$ do not usually vanish. Contrary to the $n = 3$ case, it is also possible to form subsystems A of size $|A| \leq n/2$ that are disjoint. In both cases, the reduced density matrix ρ_A is not an isometry. In other words, this code is only perfect for basis-state inputs and connected subsystems A .

We find similar properties for $n > 6$ codes: While it is impossible to construct a perfect tensor for all (possibly disjoint) boundary regions A , we can always construct a Majorana dimer code with basis states $\bar{0}$ and $\bar{1}$ that are each perfect for connected subsystems A by connecting Majorana dimer modes on opposite edges. For $n = 4k+1, k \in \mathbb{N}$, this construction even leads to codes where $\text{tr}_{A^c} |\bar{0}\rangle \langle \bar{1}| = 0$ for a connected subsystem A with $|A| \leq n/2$. Such a *block perfect* code leads to an isometric ρ_A for superpositions of bulk input for any connected A . The $n = 9$ case, whose stabilizers are permutations of $X_1 Z_2 Z_3 Z_4 Z_5 X_6$, is visualized in Table II. Note

TABLE II. Possible generalizations of the $[[5, 1, 3]]$ pentagon code (fourth row) to an n gon code. All stabilizers are cyclic permutations of the one given in the second column. The last column indicates whether boundary states lead to block perfect tensors (\checkmark) or fully perfect tensors ($\checkmark\checkmark$).

n	Stabilizer	$ \bar{0}\rangle_n$	$ \bar{1}\rangle_n$	P
3	$Y_1 Y_2$			\times
4	$X_1 Z_2 Z_3 X_4$			\times
4	$X_1 Z_2 X_3$		-	\checkmark
5	$X_1 Z_2 Z_3 X_4$			$\checkmark\checkmark$
5	$Y_1 Z_2 Z_3 Y_4$			$\checkmark\checkmark$
6	$X_1 Z_2 Z_3 X_4$			\times
\vdots				
9	$X_1 Z_2 Z_3 Z_4 Z_5 X_6$			\checkmark

that block perfect holographic codes can also be constructed from Calderbank-Shor-Steane (CSS) codes [48].

While we would expect a bulk tiling of each of the two $n = 5$ codes to lead to similar boundary properties, it would be interesting to investigate codes built from combinations of perfect and block perfect tensors.

B. GHZ states

The $n = 3$ code considered previously possesses a peculiar property: The logical eigenstates are GHZ states in the Y basis, i.e., $|\bar{0}\rangle_3 = |Y+\rangle_3^{\text{GHZ}}$ and $|\bar{1}\rangle_3 = |Y-\rangle_3^{\text{GHZ}}$, using the definition

$$\begin{aligned} |Y+\rangle_n^{\text{GHZ}} &= \frac{1}{\sqrt{2}}(|y_+\rangle^{\otimes n} - |y_-\rangle^{\otimes n}), \\ |Y-\rangle_n^{\text{GHZ}} &= \frac{1}{\sqrt{2}}(|y_+\rangle^{\otimes n} + |y_-\rangle^{\otimes n}), \end{aligned} \quad (104)$$

where $|y_{\pm}\rangle$ are the eigenstates of σ^y with $\sigma^y|y_{\pm}\rangle = \pm|y_{\pm}\rangle$. This is because $|\pm\rangle_n^{\text{GHZ}}$ is in the $+1$ eigenspace of the stabilizer $S_1 = Y_1 Y_2$ and its permutations, and thus in the ground-state space of corresponding stabilizer Hamiltonian. The total parity $\mathcal{P}_{\text{tot}}|\pm\rangle_n^{\text{GHZ}} = \pm|\pm\rangle_n^{\text{GHZ}}$ follows from the relation $\sigma_z|y_{\pm}\rangle = -|y_{\mp}\rangle$.

We can easily generalize these Y -basis GHZ states to higher n . Using (25), we find $Y_k Y_{k+1} = i \gamma_{2k-1} \gamma_{2k+2}$ for $k < n$ and $Y_1 Y_n = i \mathcal{P}_{\text{tot}} \gamma_2 \gamma_{2n-1}$. This fixes the Majorana dimers for any n to a $(2k+2 \bmod 2n) \mapsto (2k-1)$ pairing ($k \in \{1, \dots, n\}$), with the last dimer parity flipped in the $Y-$ state. For example, the GHZ state vectors on a pentagon are

$$|Y+\rangle_5^{\text{GHZ}} = \text{Diagram (105)}$$

$$|Y-\rangle_5^{\text{GHZ}} = \text{Diagram (106)}$$

Similarly, we can construct n -qubit GHZ states in the X basis: As $X_k X_{k+1} = -i \gamma_{2k} \gamma_{2k+1}$ and $X_1 X_n = i \mathcal{P}_{\text{tot}} \gamma_1 \gamma_{2n}$, we find a $2k \rightarrow 2k+1 \bmod 2n$ pairing, with the last dimer flipped in the $X+$ state. For the $n = 5$ case, the corresponding diagrams are

$$|X+\rangle_5^{\text{GHZ}} = \text{Diagram (107)}$$

$$|X-\rangle_5^{\text{GHZ}} = \text{Diagram (108)}$$

As a general rule, the positive-parity GHZ states are rotationally invariant in dimer parities, while the negative-parity GHZ states are rotationally invariant in dimer orientation (i.e., direction of arrows). As shown in Sec. III D, this means that the underlying spin degrees of freedom are invariant under

a cyclic permutation of indices of the tensors specifying the GHZ states.

In the Majorana dimer language, we can also see that the $[[5, 1, 3]]$ logical code states are extensions of GHZ states: All have a completely symmetric entanglement structure, but whereas the X_{\pm} and Y_{\pm} GHZ states connect Majorana modes at a distance of $d = 1$ and $d = 3$ modes, respectively, the $\bar{0}$ and $\bar{1}$ logical eigenstates pair modes five sites apart. While an even d cannot lead to rotational symmetry, we can systematically construct all of these states by considering all odd d . For example, the $n = 9$ case in Table II corresponds to a $d = 9$ pairing.

C. Majorana dimers and Majorana codes

So far, we have only discussed quantum error correction in a system of spins which we effectively described by fermionic degrees of freedom. Another approach is to build quantum error correction in fundamentally fermionic systems and then describe the actions of Majorana operators in such codes [49]. While superficially similar to our treatment of the HyPeC, there are fundamental differences: The advantage of actual Majorana codes is the use of fermion super-selection to reduce the occurrence of logical errors by encoding them in operators that are odd in Majorana operators and thus cannot occur if the system is in a purely bosonic environment. However, our Majorana dimer model encodes the $\bar{0}$ and $\bar{1}$ states in *different* fermionic parity sectors, superpositions of which would thus be forbidden in a system composed of actual fermions. It follows that our Majorana dimer description of the $[[5, 1, 3]]$ stabilizer code is different from the Bravyi-Terhal-Leemhuis prescription to turn stabilizer into Majorana codes, which uses four Majorana modes to encode one spin degrees of freedom. However, Majorana dimers can still be a useful tool for studying Majorana codes. Consider a simple *Kitaev chain* [50] of $2N$ Majorana modes in the ground state of the stabilizer Hamiltonian

$$H = -i \sum_{k=1}^{N-1} \gamma_{2k} \gamma_{2k+1}. \quad (109)$$

The ground state is twofold degenerate but can be spanned by two Majorana dimer state vectors $|\pm\rangle_N$. Explicitly for $N = 6$,

$$|+\rangle_6 = \text{Diagram (110)}$$

$$|-\rangle_6 = \text{Diagram (111)}$$

From (31), we immediately see that $|\pm\rangle_N$ has fermionic parity ± 1 . While the logical code states can be easily mapped into each other by applying the operator γ_1 or γ_{12} (which flips the parity of the $1 \rightarrow 12$ dimer), any physical error has to respect fermion parity and locality and is therefore restricted to the form $\gamma_k \gamma_{k+1}$, i.e., even nearest-neighbor terms. Thus, a phase error requires a string $\gamma_1 \gamma_2 \dots \gamma_{12}$ of Majorana operators with $w = 2N$, endowing the ground state of the Kitaev chain with *topological protection*. Clearly, this approach can be generalized to any Majorana dimer state of $2N$ Majorana

modes: By fixing $N-k$ dimers, we leave a k -dimensional logical qubit subspace on the remaining k possible dimers. If these remaining k modes are far apart, then they will be robust against errors that are both even and local in Majorana operators.

Furthermore, we can express Majorana stabilizer codes with dimers even if the stabilizer generators are not quadratic in Majorana operators. Consider $N = 4$ edges with eight Majorana modes under the stabilizers $S = \langle -\gamma_1 \gamma_3 \gamma_5 \gamma_7, -\gamma_2 \gamma_4 \gamma_6 \gamma_8 \rangle$. The $+1$ eigenspace of each S_k is spanned by two Majorana dimer states on the corresponding modes, one where both dimer parities are even and one where they are odd. We can thus define the logical 2-qubit state vectors $|\bar{b}_1, \bar{b}_2\rangle$ as follows:

$$\begin{aligned}
 |\bar{0}, \bar{0}\rangle &= \begin{array}{c} \text{Diagram 1: Circle with 8 nodes, blue arcs connecting (1,2), (2,3), (3,4), (4,5), (5,6), (6,7), (7,8), (8,1).} \end{array}, & |\bar{0}, \bar{1}\rangle &= \begin{array}{c} \text{Diagram 2: Circle with 8 nodes, blue arcs connecting (1,2), (2,3), (3,4), (4,5), (5,6), (6,7), (7,8), (8,1). Orange arcs connecting (1,4), (2,5), (3,6), (4,7), (5,8).} \end{array}, \\
 |\bar{1}, \bar{0}\rangle &= \begin{array}{c} \text{Diagram 3: Circle with 8 nodes, orange arcs connecting (1,4), (2,5), (3,6), (4,7), (5,8). Blue arcs connecting (1,2), (2,3), (3,4), (4,5), (5,6), (6,7), (7,8), (8,1).} \end{array}, & |\bar{1}, \bar{1}\rangle &= \begin{array}{c} \text{Diagram 4: Circle with 8 nodes, orange arcs connecting (1,4), (2,5), (3,6), (4,7), (5,8). Blue arcs connecting (1,2), (2,3), (3,4), (4,5), (5,6), (6,7), (7,8), (8,1).} \end{array}.
 \end{aligned}
 \tag{112}$$

If we again assume physical errors to correspond to even nearest-neighbour Majorana operators, we find a code distance $d = 2$ with regards to these errors. Explicitly, two such operators are required for both bit-flip and phase-flip errors, e.g., $\gamma_1 \gamma_2 \gamma_2 \gamma_3 = \gamma_1 \gamma_3$ for a phase flip and $\gamma_3 \gamma_4 \gamma_5 \gamma_6$ for a bit flip. We identify these types of errors by the Majorana dimers whose parity differs between the logical code states: In the former case, we identify operators acting on both ends of one of these dimers, while the latter case corresponds to operators on one endpoint of each of them. We can thus systematically evaluate the error correction properties of any Majorana stabilizer code by expressing its logical basis in Majorana dimers.

VI. MAJORANA DIMERS AND BIT THREADS

Our model bears close resemblance to the *bit thread* proposal [24], a model for holographic states that rederives the Ryu-Takayanagi (RT) formula by postulating that such states are composed by a flow of EPR pairs between boundary regions. In this proposal, the entanglement entropy S_A of a boundary region A is then equivalent to the *maximal flow* of EPR pairs between A and A^C through the bulk, which is equivalent to the area of the minimal surface γ_A in the standard RT prescription.

Clearly, this picture is satisfied by the Majorana dimer description of the HyPeC for compact regions A [for which (63) holds]. While each dimer only carries half the entanglement of an EPR pair, the phenomenological behavior is identical: S_A is determined by the number of dimers between A and A^C , which is restricted by the minimal cut through the bulk tiling from the endpoints of A . The HyPeC leads to a special dimer

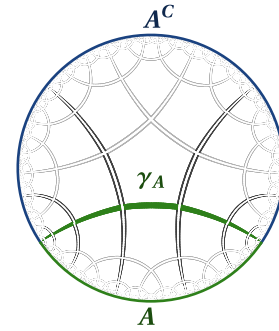


FIG. 10. Effective bit thread picture in the asymptotically large HyPeC: All dimers are paired along bulk geodesics and any boundary region A has a maximal flow of bit threads (dimer pairs) through the Ryu-Takayanagi surface γ_A . The threads that pass γ_A , each contributing $\log 2$ to the entanglement entropy S_A , are highlighted. Note that both the number of such threads and S_A are UV divergent.

configuration in which this bound is saturated for any compact region A (up to degenerate cases shown in Fig. 6). It thus defines a *global* bit thread configuration, i.e., one independent of the choice of A . A special property of this configuration is that the dimers and bit threads follow discrete geodesics through the bulk, so that the bulk metric is emergent from the entanglement structure. Note that in the asymptotic limit of infinitely many tiles, shown in Fig. 10, each geodesic can be identified with a pair of dimers, thus forming an effective EPR pair. Curiously, the resulting entanglement entropy resembles a classical fracton models on a $\{4, 5\}$ tiling, where the Shannon entropy scales with the number of dual geodesics, each doubling the ground-state degeneracy [51].

However, global bit thread configurations are generally not sufficient to reproduce the RT formula for disjoint subsystems; in such cases, the bit thread flow must differ according to the choice of the subsystems to reproduce the correct holographic multipartite entanglement [25]. This cannot be fulfilled with fermionic dimers, as the global entanglement structure is fixed for a specific state. However, the HyPeC is only a Majorana dimer model effectively, with its underlying spin degrees of freedom converted to fermionic modes through a Jordan-Wigner transformation. Thus in general, when considering disjoint subsystems, the entanglement entropy cannot be determined by a dimer counting. It is an interesting future question whether the entanglement between disjoint subsystems (or equivalently, for transpositions of boundary regions) leads to a multipartite entanglement of the HyPeC also resembling the bit thread picture.

VII. DISCUSSION

In this work, we have studied the intersection of stabilizer states and fermionic Gaussian states, both efficiently describable classes of quantum states with a wide range of applications in quantum information theory and both condensed-matter and high-energy physics. For this purpose, we have introduced a graphical formalism for describing Majorana dimer states, free fermionic states characterized by entangled Majorana modes. These can describe stabilizer states such as those of the $[[5, 1, 3]]$ quantum error-correcting code. We

applied this formalism to the recently constructed hyperbolic pentagon code (HyPeC), a discrete toy model of the AdS/CFT correspondence [5]. For logical bulk input fixed to code basis states, the HyPeC was found to correspond to Majorana dimers along discrete bulk geodesics. With the bulk geometry thus encoded in boundary-state entanglement, we reproduced the logarithmic scaling of the entanglement entropy S_A with its subsystem size for connected subsystems A , reproducing the Ryu-Takayanagi formula through a calculation that sharply resembles the recent *bit thread* proposal. We also extended our results to bulk inputs containing local superpositions on each pentagon tile. For this case, where boundary states are generally non-Gaussian, Majorana dimers quantify the dependence of the entanglement entropy on residual bulk regions. We also provided a method for computing non-Gaussian n -point correlations function of the HyPeC for arbitrary bulk input, finding that the Majorana dimer structure—i.e., boundary correlations only between pairs of Majorana modes—is preserved for $n = 2$, a feature related to the quantum error-correcting properties of the code. Furthermore, we showed that Majorana dimers can describe a range of entangled states, including GHZ states and models such as the Kitaev chain, while also allowing for complicated non-Gaussian states by expansion in a Majorana dimer basis. Finally, tensor networks based on Majorana dimers provide a particularly simple model of an RG flow, where an IR \rightarrow UV transformation is interpreted as an addition of new dimer degrees of freedom upon contraction.

As this work has focused on the specific Majorana dimer structure of the [[5, 1, 3]] code and the HyPeC that is built upon it, we have only glimpsed the general relationship between Majorana fermions and stabilizers. While our graphical formalism for Majorana dimers can be used to describe a wide range of entangled quantum states, including generalized stabilizer codes, only a subset of these could be covered here. As this formalism allows for the construction of quantum states from their entanglement symmetries, a more systematic study of Majorana dimer states and their symmetries would be useful in the future. With our approach allowing for a direct analytical contraction of dimer-based tensor networks through simple graphical rules and a possible description of non-Gaussian states through dimer superpositions, there appears to be a vast number of potential applications. Within the Gaussian setting, an interesting question is the deformation of Gaussian stabilizer states. As each Majorana dimer state can be expressed by a *matchgate tensor* [16], one may consider smooth deformation of the HyPeC (and other stabilizer models) while retaining an efficiently contractible tensor network. Under such deformations, it is conceivable that a picture with some effective degrees of freedom localized to geodesics is retained. For example, there exists a possible connection to *ribbon operators* [52] which appear in the study of topological phases of matter away from fixed point models. This would also involve exploring the similarities between Majorana dimers and anyon models. One may also wish to address the actual recovery rates of logical qubits in holographic codes, which have been studied both in the original HyPeC proposal [5] and in extensions such as the Calderbank-Shor-Steane (CSS) holographic heptagon code [48]. Their remarkable property of a resilience of logical

qubits further in the bulk may be studied more directly with Majorana dimers, where an explicit mapping between bulk and boundary degrees of freedom is provided. While the toy models studied here are inherently discrete, the many properties of the HyPeC resembling a *conformal field theory* (CFT) motivate further studies on its continuum limits, analogous to continuous MERA [53,54]. While rigorous studies of the continuum quantum fields corresponding to lattice models are ongoing [55], the *quasiregular* symmetries expected on the boundary of regular hyperbolic bulk tilings [56] may require a different notion of a CFT for regular discretizations than the familiar continuum formulation. We hope that the present work stimulates further endeavors in this direction.

ACKNOWLEDGMENTS

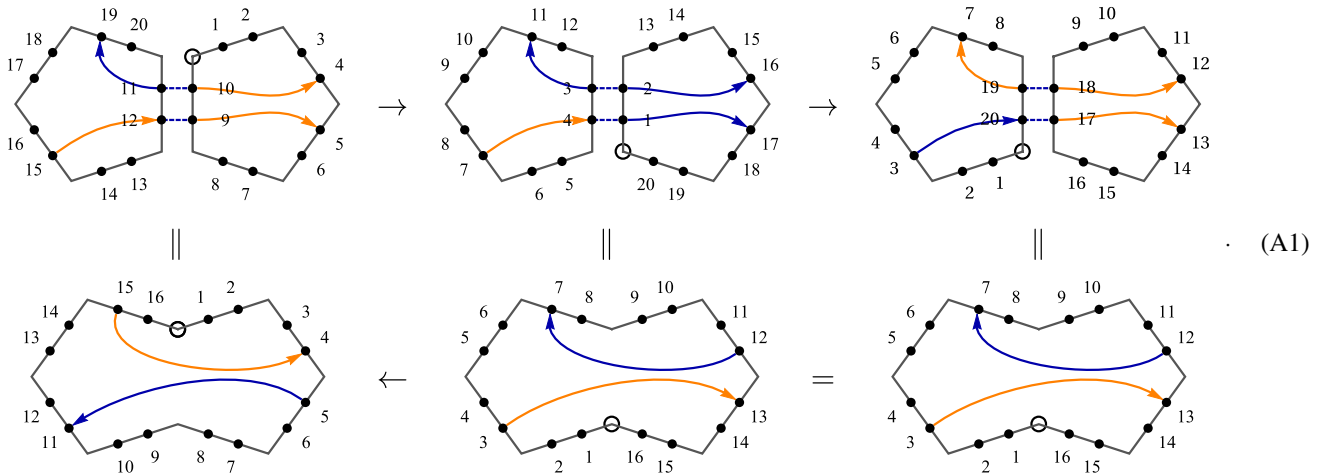
We would like to thank Pawel Caputa, Xiao-Liang Qi, Tadashi Takayanagi, Nicholas Tarantino, Han Yan, Michael Walter, and Carolin Wille for valuable comments and discussions. This work has been supported by the European Research Council (ERC-SG TAQ), the Templeton Foundation, the Studienstiftung des Deutschen Volkes, and the DFG (EI 519/14-1, EI 519/15-1, CRC 183 B1, FOR 2724). This work has also received funding from the European Union's Horizon 2020 research and innovation programme under Grant Agreement No. 817482 (PASQuanS).

APPENDIX A: DIMER CONTRACTION RULES

We will now prove the contraction rules from the main text by considering all possible Majorana dimer configurations that can be contracted, showing that they either result in a new Majorana dimer state or vanish. As the Majorana dimer diagrams are defined as an effective representation of spins, we define contractions in the Majorana picture to be consistent with the result obtained by reversing the Jordan-Wigner transformation, contracting the corresponding spin degrees of freedom, and applying a new Jordan-Wigner transformation on the remaining ones. This is equivalent to always contracting the first two fermionic degrees of freedom under the given ordering, as this requires no reordering when projecting onto the $|0, 0\rangle$ and $|1, 1\rangle$ subspaces in the spin picture during contraction.

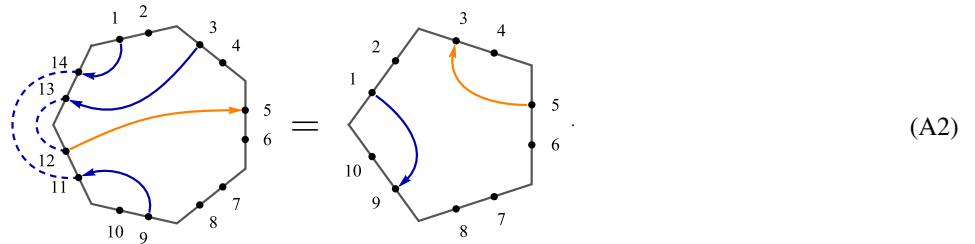
Note that any contraction is equivalent to a self-contraction. For example, when contracting two state vectors $|\phi\rangle$ and $|\psi\rangle$ over some fermionic degree of freedom, we can simply view this as a self-contraction of the tensor product $|\phi\rangle|\psi\rangle$. By using cyclic permutations, we can relate the contraction of any edge index pair (j, k) with $j < k$ to the canonical case $(i, j) = (1, 2)$. Equivalently, as we will consider below, we can apply the contraction rules to the last two edges under a given ordering (which avoids renumbering all the edges). As we will see throughout this section, the contraction rules rely purely on the dimer parities of dimers connected to contracted edges, so changing the index ordering for states with even total parity does not affect the result, as dimer parities are left invariant. To see that the same logic holds for parity-odd states, consider the following reordered versions of the contraction (41) from the main text, where we assume the product state vector $|\phi\rangle|\psi\rangle$ to have odd total parity,

and again omit dimers that are not connected to the contracted edge:



The two diagrams on the left correspond to the contraction (41) proved in the main text. Cyclic permutations relate this to a self-contraction of the first two fermions (Majorana modes 1 to 4, center) and alternatively of the two last fermions (Majorana modes 17 to 20, right). The pivot of the permutation is again represented by a small circle. As we see, applying the dimer contraction rules from the main text leads to equivalent results under cyclic permutations. Note, however, that forming product state vectors $|\phi\rangle|\psi\rangle$ requires an ordering of the modes in $|\phi\rangle$ before the ones in $|\psi\rangle$, which can still lead to additional parity shifts when contracting in parity-odd states. We resolve these ambiguities in Appendix C.

Let us now prove the general case of the previous diagram, written as a self-contraction of an arbitrary Majorana dimers state (of which a product state is only a special case). We start with contractions of the form



We start with an N -fermion state vector $|\chi\rangle$ [$N = 7$ in Eq. (A2)] that obeys the Majorana dimer conditions

$$(\gamma_a + i p_{a,2N} \gamma_{2N})|\chi\rangle = 0, \quad (\gamma_b + i p_{b,2N-3} \gamma_{2N-3})|\chi\rangle = 0, \quad (\text{A3})$$

$$(\gamma_c + i p_{c,2N-1} \gamma_{2N-1})|\chi\rangle = 0, \quad (\gamma_d + i p_{d,2N-2} \gamma_{2N-2})|\chi\rangle = 0, \quad (\text{A4})$$

where we assume for now that $a < b$ and $c < d$, so that the dimer lines do not cross [$a = 1, b = 9, c = 3, d = 5$ in Eq. (A2)]. We claim that after contraction, the contracted state vector $|\omega\rangle$ is again a Majorana dimer state with conditions

$$(\gamma_a + i p_{a,2N} p_{b,2N-3} \gamma_b)|\omega\rangle = 0, \quad (\text{A5})$$

$$(\gamma_c + i p_{c,2N-1} p_{d,2N-2} \gamma_d)|\omega\rangle = 0, \quad (\text{A6})$$

which means that the parities along a contracted path are multiplied. We write these conditions as $O_k|\omega\rangle = 0$ with $k \in \{1, 2\}$ denoting the two cases. Using the tools developed in Sec. III C, we will now prove them simultaneously:

$$\begin{aligned} O_k|\omega\rangle &= O_k \int df_N^\dagger df_{N-1}^\dagger e^{f_{N-1}^\dagger f_N^\dagger} |\chi\rangle \\ &= \int df_N^\dagger df_{N-1}^\dagger e^{f_{N-1}^\dagger f_N^\dagger} \begin{cases} (\gamma_a + i p_{a,2N} p_{b,2N-3} \gamma_b)|\chi\rangle & \text{for } k = 1 \\ (\gamma_c + i p_{c,2N-1} p_{d,2N-2} \gamma_d)|\chi\rangle & \text{for } k = 2 \end{cases} \end{aligned} \quad (\text{A7})$$

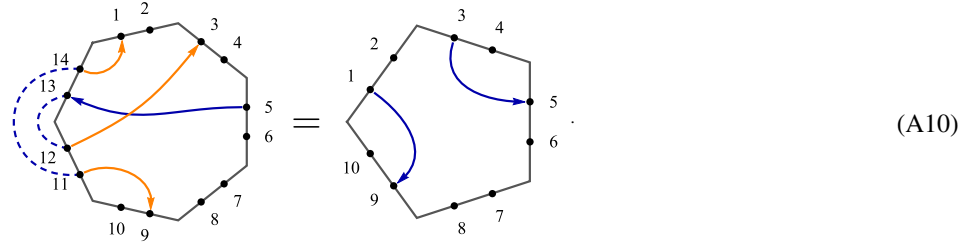
Using (A3) and (A4), we can rewrite this purely in terms of operators acting locally on the contracted edges:

$$\begin{aligned}
O_k|\omega\rangle &= \int df_N^\dagger df_{N-1}^\dagger e^{f_{N-1}^\dagger f_N^\dagger} \begin{cases} p_{a,2N}(\gamma_{2N-3} - i \gamma_{2N})|\chi\rangle & \text{for } k = 1 \\ p_{c,2N-1}(\gamma_{2N-3} - i \gamma_{2N-1})|\chi\rangle & \text{for } k = 2 \end{cases} \\
&\propto \int df_N^\dagger df_{N-1}^\dagger e^{f_{N-1}^\dagger f_N^\dagger} \begin{cases} (f_{N-1} + f_{N-1}^\dagger - f_N + f_N^\dagger)|\chi\rangle \\ (f_{N-1} - f_{N-1}^\dagger + f_N + f_N^\dagger)|\chi\rangle \end{cases} \\
&= \int df_N^\dagger df_{N-1}^\dagger \begin{cases} (f_{N-1}^\dagger + f_N^\dagger - f_N^\dagger f_{N-1}^\dagger f_{N-1} - f_{N-1}^\dagger f_N^\dagger f)|\chi\rangle \\ (-f_{N-1}^\dagger + f_N^\dagger - f_N^\dagger f_{N-1}^\dagger f_{N-1} + f_{N-1}^\dagger f_N^\dagger f_N)|\chi\rangle \end{cases} \\
&= \int df_N^\dagger df_{N-1}^\dagger \begin{cases} (f_{N-1} f_{N-1}^\dagger f_N^\dagger + f_{N-1}^\dagger f_N f_N^\dagger)|\chi\rangle \\ (f_{N-1} f_{N-1}^\dagger f_N - f_{N-1}^\dagger f_N f_N^\dagger)|\chi\rangle \end{cases} = 0. \tag{A8}
\end{aligned}$$

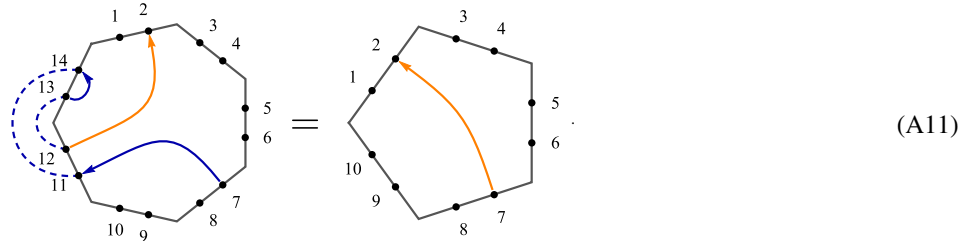
We previously assumed $a < b$ and $c < d$. What happens if, e.g., $c > d$? As the condition (A6) for the contracted state vector $|\omega\rangle$ still hold, we just multiply both sides by $-i p_{c,2N-1} p_{d,2N-2}$, yielding

$$(\gamma_d - i p_{c,2N-1} p_{d,2N-2} \gamma_c)|\omega\rangle = 0. \tag{A9}$$

In other words, contracting out two Majorana dimers that cross each other flips the parity of the resulting dimer. For our example, the corresponding diagram has the form



Self-contractions also allow for special cases involving dimers on the contracted edge itself, which we will now prove, as well. First, consider the case where one of the contracted edges contains a local dimer, such as the contraction



The contracted path contains contributions from three parities. Without loss of generality, we assume that the local dimer is located on the N th edge, so that we start with the conditions

$$(\gamma_{2N-1} + i p_{2N-1,2N} \gamma_{2N})|\chi\rangle = [(1 - p_{2N-1,2N})f_N^\dagger + (1 + p_{2N-1,2N})f_N]|\chi\rangle = 0, \tag{A12}$$

$$(\gamma_a + i p_{a,2N-2} \gamma_{2N-2})|\chi\rangle = 0, \quad (\gamma_b + i p_{b,2N-3} \gamma_{2N-3})|\chi\rangle = 0. \tag{A13}$$

In our example (A11), $a = 2$ and $b = 7$. The first line simply becomes $f_N^\dagger|\chi\rangle = 0$ for $p_{2N-1,2N} = -1$ and $f_N|\chi\rangle = 0$ for $p_{2N-1,2N} = +1$. The latter case implies that $\int df_N^\dagger|\chi\rangle = 0$ as well, as Grassmann integrations and annihilators act equivalently. We now prove that these assumptions for the uncontracted $|\chi\rangle$ imply that

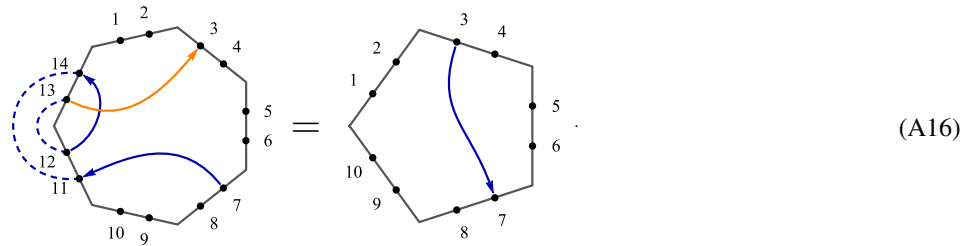
$$(\gamma_a + i p_{a,2N-2} p_{2N-1,2N} p_{b,2N-3} \gamma_b)|\omega\rangle = 0 \tag{A14}$$

for the contracted $|\omega\rangle$, similar to (A5) and (A6). The proof is similar to the previous setup:

$$\begin{aligned}
(\gamma_a + i p_{a,2N-2} p_{2N-1,2N} p_{b,2N-3} \gamma_b)|\omega\rangle &= \int df_N^\dagger df_{N-1}^\dagger e^{f_{N-1}^\dagger f_N^\dagger} (\gamma_a + i p_{a,2N-2} p_{2N-1,2N} p_{b,2N-3} \gamma_b)|\chi\rangle \\
&= p_{a,2N-2} \int df_N^\dagger df_{N-1}^\dagger e^{f_{N-1}^\dagger f_N^\dagger} (p_{2N-1,2N} \gamma_{2N-3} - i \gamma_{2N-2})|\chi\rangle
\end{aligned}$$

$$\begin{aligned}
&= 2p_{a,2N-2} \int df_N^\dagger df_{N-1}^\dagger e^{f_{N-1}^\dagger f_N^\dagger} \begin{cases} -f_{N-1} |\chi\rangle & \text{for } p_{2N-1,2N} = -1 \\ f_{N-1}^\dagger |\chi\rangle & \text{for } p_{2N-1,2N} = +1 \end{cases} \\
&= 2p_{a,2N-2} \begin{cases} -\int df_N^\dagger df_{N-1}^\dagger f_{N-1}^\dagger f_N^\dagger f_{N-1} |\chi\rangle \\ \int df_N^\dagger df_{N-1}^\dagger f_{N-1}^\dagger |\chi\rangle \end{cases} \\
&= 2p_{a,2N-2} \begin{cases} \int df_N^\dagger df_{N-1}^\dagger f_{N-1}^\dagger f_{N-1} f_N^\dagger |\chi\rangle \\ \int df_{N-1}^\dagger f_{N-1}^\dagger \int df_N^\dagger |\chi\rangle \end{cases} \\
&= 0.
\end{aligned} \tag{A15}$$

Again, crossing the two initial paths so that $a > b$ introduces an additional minus sign to the contracted parity. The next case to consider contains a Majorana pair across the two contracted edges, such as in the diagram



Note that this kind of contraction always contains a crossing. Again without loss of generality, we assume that the dimer on the contracted edges connects Majorana modes $2N - 3$ and $2N$. The full conditions for the uncontracted state are

$$(\gamma_{2N-2} + i p_{2N-2,2N} \gamma_{2N}) |\chi\rangle = [i (f_{N-1}^\dagger - f_{N-1}) - p_{2N-2,2N} (f_N^\dagger - f_N)] |\chi\rangle = 0, \tag{A17}$$

$$(\gamma_a + i p_{a,2N-1} \gamma_{2N-1}) |\chi\rangle = 0, \quad (\gamma_b + i p_{b,2N-3} \gamma_{2N-3}) |\chi\rangle = 0, \tag{A18}$$

with $a = 3$ and $b = 7$ in Eq. (A16). The first condition can be rewritten into the form

$$(p_{2N-2,2N} f_{N-1}^\dagger + i f_N^\dagger) |\chi\rangle = (p_{2N-2,2N} f_{N-1} + i f_N) |\chi\rangle. \tag{A19}$$

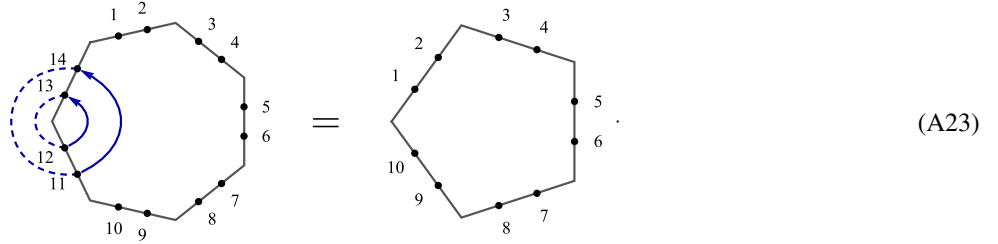
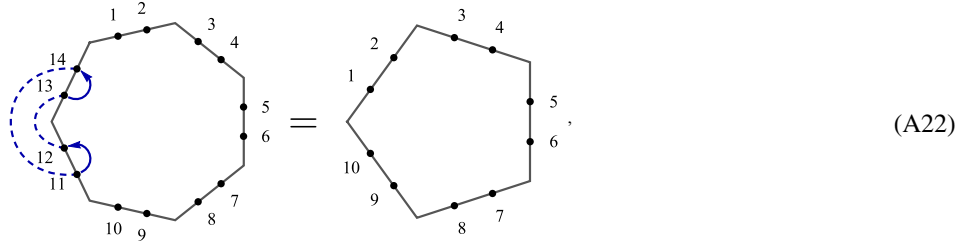
We now prove the contracted state fulfills

$$(\gamma_a - i p_{a,2N-1} p_{2N-2,2N} p_{b,2N-3} \gamma_b) |\omega\rangle = 0. \tag{A20}$$

Note that additional minus sign in comparison to (A14) due to the crossing. The proof is given by

$$\begin{aligned}
(\gamma_a - i p_{a,2N-1} p_{2N-2,2N} p_{b,2N-3} \gamma_b) |\omega\rangle &= \int df_N^\dagger df_{N-1}^\dagger e^{f_{N-1}^\dagger f_N^\dagger} (\gamma_a - i p_{a,2N-1} p_{2N-2,2N} p_{b,2N-3} \gamma_b) |\chi\rangle \\
&= -p_{a,2N-1} \int df_N^\dagger df_{N-1}^\dagger e^{f_{N-1}^\dagger f_N^\dagger} (p_{2N-2,2N} \gamma_{2N-3} + i \gamma_{2N-1}) |\chi\rangle \\
&= -2p_{a,2N-1} \int df_N^\dagger df_{N-1}^\dagger e^{f_{N-1}^\dagger f_N^\dagger} (p_{2N-2,2N} f_{N-1}^\dagger + i f_N^\dagger) |\chi\rangle \\
&= -2p_{a,2N-1} \int df_N^\dagger df_{N-1}^\dagger (p_{2N-2,2N} f_{N-1}^\dagger + i f_N^\dagger) |\chi\rangle \\
&= -2p_{a,2N-1} \int df_N^\dagger df_{N-1}^\dagger (p_{2N-2,2N} f_{N-1} + i f_N) |\chi\rangle \\
&= 0.
\end{aligned} \tag{A21}$$

Finally, consider contractions that involve paths that get completely removed by contraction. Up to parities, there are two possible dimer configurations for such contractions:



Clearly, such contractions can only affect the state on the remaining edges by an overall constant C . Unless $C = 0$, this constant can be absorbed into an appropriate normalization. But when does $C = 0$ occur? Let us consider the first diagram (A22), which can be generalized to the conditions

$$(\gamma_{2N-3} + i p_{2N-3,2N-2} \gamma_{2N-2})|\chi\rangle = 0, \tag{A24}$$

$$(\gamma_{2N-1} + i p_{2N-1,2N} \gamma_{2N})|\chi\rangle = 0. \tag{A25}$$

We claim that the contracted state vector $|\omega\rangle$ vanishes if $(p_{2N-3,2N-2}, p_{2N-1,2N}) \in \{(1, -1), (-1, 1)\}$. These two cases correspond to either $f_{N-1}|\chi\rangle = 0$ and $f_N^\dagger|\chi\rangle = 0$ or $f_{N-1}^\dagger|\chi\rangle = 0$ and $f_N|\chi\rangle = 0$. It is easy to see that the contraction

$$|\omega\rangle = \int df_N^\dagger df_{N-1}^\dagger e^{f_{N-1}^\dagger f_N^\dagger} |\chi\rangle = \int df_N^\dagger df_{N-1}^\dagger |\chi\rangle + \int df_N^\dagger df_{N-1}^\dagger f_{N-1}^\dagger f_N^\dagger |\chi\rangle \tag{A26}$$

is annihilated in either case (recall that integrals $\int df_k^\dagger$ act like annihilation operators f_k). The second diagram (A22), corresponding to the conditions

$$(\gamma_{2N-3} + i p_{2N-3,2N} \gamma_{2N})|\chi\rangle = 0, \tag{A27}$$

$$(\gamma_{2N-2} + i p_{2N-2,2N-1} \gamma_{2N-1})|\chi\rangle = 0, \tag{A28}$$

is more involved. We seek to prove that $|\omega\rangle$ vanishes if $(p_{2N-3,2N}, p_{2N-2,2N-1}) \in \{(1, -1), (-1, 1), (-1, -1)\}$, i.e., for at least one odd parity. In terms of creation and annihilation operators, these three cases can be rewritten as

$$f_{N-1}|\chi\rangle = \begin{cases} f_N|\chi\rangle & \text{for } (p_{2N-3,2N}, p_{2N-2,2N-1}) = (1, -1) \\ f_N|\chi\rangle & \text{for } (p_{2N-3,2N}, p_{2N-2,2N-1}) = (-1, 1) \\ -f_N^\dagger|\chi\rangle & \text{for } (p_{2N-3,2N}, p_{2N-2,2N-1}) = (-1, -1) \end{cases}, \tag{A29}$$

$$f_{N-1}^\dagger|\chi\rangle = \begin{cases} f_N^\dagger|\chi\rangle & \text{for } (p_{2N-3,2N}, p_{2N-2,2N-1}) = (1, -1) \\ -f_N^\dagger|\chi\rangle & \text{for } (p_{2N-3,2N}, p_{2N-2,2N-1}) = (-1, 1) \\ f_N|\chi\rangle & \text{for } (p_{2N-3,2N}, p_{2N-2,2N-1}) = (-1, -1) \end{cases}. \tag{A30}$$

For the first two cases, the contraction (A26) turns into

$$|\omega\rangle = \int df_N^\dagger df_{N-1}^\dagger |\chi\rangle \pm \int df_N^\dagger df_{N-1}^\dagger f_{N-1}^\dagger f_N^\dagger |\chi\rangle = 0. \tag{A31}$$

For the third case, we get

$$|\omega\rangle = \int df_N^\dagger df_{N-1}^\dagger (1 - f_N^\dagger f_N) |\chi\rangle = \int df_N^\dagger df_{N-1}^\dagger f_N^\dagger f_N |\chi\rangle = 0. \tag{A32}$$

To summarize, we see that a self-contracted loop leads to vanishing contracted state if the total parity of the loop is odd, as postulated in the main text. Even-parity loops contribute an overall constant $C \neq 0$ to the contracted state.

APPENDIX B: GRAPHICAL COMPUTATION OF ENTANGLEMENT ENTROPIES

In this section, we derive formula (63) for the entanglement entropy S_A of a Majorana dimer state using diagrammatic tools and extend it to the computation of Rényi entropies $S_A^{(n)}$. Furthermore, we generalize these proofs to full the HyPeC with arbitrary bulk input, recovering previously known conditions on the boundary regions A [5]. Following (75), we can visualize a density matrix $\rho = |\psi\rangle\langle\psi|$ of some Majorana dimer state vector $|\psi\rangle$ as

$$\rho = \left(\begin{array}{c} \text{Diagram 1} \\ \text{Diagram 2} \end{array} \right)^\dagger = \text{Diagram 3} \cdot \text{Diagram 4} \tag{B1}$$

Here we are effectively using a Choi-Jamiolkowski isomorphism, representing a density matrix as a state in a doubled Hilbert space. In order to produce a reduced density matrix ρ_A of some subsystem A , we sum over a complete set of states projected onto the edges that are part of A^C (the complement of A), which we saw in Eq. (72) to be equivalent to a contraction. For instance, the green-shaded subsystem A in the following example leads to a reduced density matrix of the form

$$\rho_A = \text{Diagram 1} = \text{Diagram 2} + \text{Diagram 3} + \text{Diagram 4} + \text{Diagram 5} + \text{Diagram 6} = \frac{1}{2} \text{Diagram 7} + \frac{1}{2} \text{Diagram 8} = \frac{1}{\sqrt{2}} \text{Diagram 9} \tag{B2}$$

We have omitted Majorana labels for clarity. In the first step, we used (72) to relate partial trace and contraction, and then applied (74) in the second, yielding proper normalization factors. The third step merely uses (72) in reverse. In summary, we see that normalization (requiring $\text{tr}\rho_A = 1$ at each step) leads to a simple rule: Each contraction that glues two pairs of dimer together produces a factor of $1/\sqrt{2}$.

The entanglement entropy now follows from the eigenvalue spectrum of ρ_A . We can compute the eigenstates by projecting a full basis of Majorana dimer states onto the contracted edges of $|\psi\rangle$. For simplicity, we choose the basis of local Fock states, i.e., with dimers only between the Majorana modes on each edge. As two edges are contracted out, there are four such basis states, of which only two are nonvanishing. These eigenvectors $|\psi_{A,1}\rangle$ and $|\psi_{A,2}\rangle$ are given by

$$|\psi_{A,1}\rangle = \sqrt{2} \text{Diagram 1} = \text{Diagram 2}, \quad |\psi_{A,2}\rangle = \sqrt{2} \text{Diagram 3} = \text{Diagram 4} \tag{B3}$$

Here, both diagrams represent normalized states. To see that our construction indeed yields eigenstates of ρ_A , consider the eigenvalue equation for the second eigenvector $|\psi_{A,2}\rangle$:

$$\rho_A |\psi_{A,2}\rangle = \frac{1}{\sqrt{2}} \left[\text{Diagram 1} + \text{Diagram 2} \right] = \frac{1}{2} \left[\text{Diagram 3} + \text{Diagram 4} \right]. \quad (\text{B4})$$

With a similar diagram for $\rho_A |\psi_{A,1}\rangle$ it is found that both eigenvalues are $1/2$. Thus, the entanglement entropy is given by

$$S_A = -\text{tr}_A \rho_A \log \rho_A = -\frac{1}{2} \log \frac{1}{2} - \frac{1}{2} \log \frac{1}{2} = \log 2. \quad (\text{B5})$$

We find that evaluating S_A reduces to counting the dimers connecting the “ket” edges with the “bra” edges, which determines how mixed ρ_A is. In general, any reduced density matrix contains $2m$ “mixing dimers” that span an eigenspace of 2^m orthogonal dimer states (whose diagrammatic representation is not unique for $m > 1$). The entanglement entropy follows as

$$S_A = -2^m \left(\frac{1}{2^m} \log \frac{1}{2^m} \right) = m \log 2. \quad (\text{B6})$$

Equivalently, as $2m$ dimers connect A with the complementary (contracted) region A^C , each dimer contributes $\frac{1}{2} \log 2$ to the entanglement entropy S_A , as in Eq. (63).

Using a similar strategy, we can compute the Rényi entropy $S_A^{(n)} = \log(\text{tr} \rho_A^n)/(1-n)$. This requires evaluating the n th power of the reduced density matrix ρ_A . As an example, consider the square of (B2):

$$\rho_A^2 = \left(\frac{1}{\sqrt{2}} \left[\text{Diagram 1} + \text{Diagram 2} \right] \right)^2 = \frac{1}{2} \left[\text{Diagram 3} + \text{Diagram 4} \right] = \frac{1}{2\sqrt{2}} \left[\text{Diagram 5} + \text{Diagram 6} \right] = \frac{1}{2} \rho_A. \quad (\text{B7})$$

Thus, it follows that $\rho_A^n = \rho_A/2^{n-1}$, and hence $S_A^{(n)} = \log(\text{tr} \rho_A/2^{n-1})/(1-n) = \log 2$. This property of a “flat Rényi spectrum,” i.e., $S_A^{(n)} = S_A$, holds for any Majorana dimer state. For a generic ρ_A , (B7) involves $n - 1$ contractions of $2m$ mixing dimers, leading to the following analog of (B6) for Rényi entropies:

$$S_A^{(n)} = \frac{1}{1-n} \log \text{tr} \rho_A^n = \frac{1}{1-n} \log \frac{\text{tr} \rho_A}{2^{m(n-1)}} = m \log 2 = S_A. \quad (\text{B8})$$

Note that this property of a flat entanglement spectrum is a proven feature of stabilizer codes states [44], thus making Majorana dimers ideal for the study of stabilizers. Contrary to the stabilizer picture, however, we can also diagrammatically evaluate the entanglement entropy for classes of superpositions, as we will now see. First, we take a look at superpositions of input states of the HyPeC. Consider a single tile of the $[[5, 1, 3]]$ code. For arbitrary bulk input, the boundary state is given by

$$|\psi\rangle = \alpha |\bar{0}\rangle_5 + \beta |\bar{1}\rangle_5 = \alpha \left[\text{Diagram 1} \right] + \beta \left[\text{Diagram 2} \right] \equiv \left[\text{Diagram 3} \right] \alpha, \beta. \quad (\text{B9})$$

On the right-hand side, we have used a new notation for superpositions of $[[5, 1, 3]]$ computational basis states with complex factors α and β . Normalization requires $|\alpha|^2 + |\beta|^2 = 1$. We now show that the reduced density matrix ρ_A of this superposition

becomes an identity on the subsystem A when it consists of only two edges [$A = (1, 2)$] or one edge [$A = (1)$]:

$$\begin{aligned}
 \rho_{(1,2)} &= \text{Diagram 1} = \alpha\alpha^* \text{Diagram 2} + \alpha\beta^* \text{Diagram 3} \\
 &+ \alpha^*\beta \text{Diagram 4} + \beta\beta^* \text{Diagram 5} \\
 &= \frac{\alpha\alpha^* + \beta\beta^*}{2} \text{Diagram 6} = \frac{\mathbb{1}_4}{4}. \tag{B10}
 \end{aligned}$$

$$\begin{aligned}
 \rho_{(1)} &= \text{Diagram 1} = \alpha\alpha^* \text{Diagram 2} + \alpha\beta^* \text{Diagram 3} \\
 &+ \alpha^*\beta \text{Diagram 4} + \beta\beta^* \text{Diagram 5} \\
 &= \frac{\alpha\alpha^* + \beta\beta^*}{\sqrt{2}} \text{Diagram 6} = \frac{\mathbb{1}_2}{2}. \tag{B11}
 \end{aligned}$$

Note that the actual values for α and β do not change ρ_A , and thus the entanglement spectrum is the same for *any* superposition of the $[[5, 1, 3]]$ logical code states. As we can easily see, $S_{(1)} = \log 2$ and $S_{(1,2)} = 2 \log 2$, identical to the result for the logical code states. The corresponding eigenstates are simply a complete basis of Majorana dimers on one or two edges, respectively.

Let us now consider the $|A| = 3$ case. We easily find the entanglement entropy $S_A = S_{A^c} = 2 \log 2$. The eigenstates of ρ_A can be found, as in Eq. (B3), by starting with the state vector $|\psi\rangle$ and contracting a complete basis on the edges in A^c , yielding four

eigenstates. We compute the first one explicitly:

$$|\psi_A^{0,0}\rangle = \begin{array}{c} \text{Diagram 1} \\ \alpha, \beta \end{array} = \alpha \begin{array}{c} \text{Diagram 2} \\ \alpha, \beta \end{array} + \beta \begin{array}{c} \text{Diagram 3} \\ \alpha, \beta \end{array} = \frac{\alpha}{2} \begin{array}{c} \text{Diagram 4} \\ \alpha, \beta \end{array} + \frac{\beta}{2} \begin{array}{c} \text{Diagram 5} \\ \alpha, \beta \end{array}. \quad (\text{B12})$$

The remaining three eigenstates are given by

$$|\psi_A^{0,1}\rangle = \begin{array}{c} \text{Diagram 6} \\ \alpha, \beta \end{array} \quad |\psi_A^{1,0}\rangle = \begin{array}{c} \text{Diagram 7} \\ \alpha, \beta \end{array} \quad |\psi_A^{1,1}\rangle = \begin{array}{c} \text{Diagram 8} \\ \alpha, \beta \end{array}. \quad (\text{B13})$$

To see that these are eigenstates, we do not need to actually evaluate these contractions. Instead, using (B10), we compute the eigenvalue equation for the first eigenvector as follows:

$$\begin{aligned} \rho_A |\psi_A^{0,0}\rangle &= \begin{array}{c} \text{Diagram 9} \\ \alpha, \beta \end{array} = \frac{1}{2} \begin{array}{c} \text{Diagram 10} \\ \alpha, \beta \end{array} \\ &= \frac{1}{4} \begin{array}{c} \text{Diagram 11} \\ \alpha, \beta \end{array} = \frac{1}{4} |\psi_A^{0,0}\rangle. \end{aligned} \quad (\text{B14})$$

The equations for the other eigenstates follow equivalently, leading to an entanglement entropy $S_A = 2 \log 2$ (i.e., $m = 2$). For more than one tile, we can generalize (B14) for local superpositions, i.e., superpositions that factorize along the tiles. As an example, consider a $|\psi'\rangle$ resulting from contracting two states of the form (B9):

$$|\psi'\rangle = C_{1 \leftrightarrow 4} (\alpha_1 |\bar{0}\rangle_5 + \beta_1 |\bar{1}\rangle_5) (\alpha_2 |\bar{0}\rangle_5 + \beta_2 |\bar{1}\rangle_5) = \begin{array}{c} \text{Diagram 12} \\ \alpha_1, \beta_1 \end{array} \begin{array}{c} \text{Diagram 13} \\ \alpha_2, \beta_2 \end{array}. \quad (\text{B15})$$

Here we have defined the contraction operator $C_{j \leftrightarrow k}$ contracting the j th edge of the first dimer state on the k th edge of the second. We can now show that (B14) generalizes if we extend region $A \rightarrow A'$ onto a neighboring pentagon tile. The reduced density matrix becomes

$$\rho'_{A'} = 2 \begin{array}{c} \text{Diagram 14} \\ \alpha_1, \beta_1 \end{array} \begin{array}{c} \text{Diagram 15} \\ \alpha_2, \beta_2 \end{array} \begin{array}{c} \text{Diagram 16} \\ \alpha_2^*, \beta_2^* \end{array} \begin{array}{c} \text{Diagram 17} \\ \alpha_1^*, \beta_1^* \end{array}. \quad (\text{B16})$$

Note that a normalization factor of 2 appears as a result of the unresolved contraction within both $|\psi'\rangle$ and $\langle\psi'|$. To see that the eigenvalue spectrum of $\rho'_{A'}$ is the same as that of ρ_A , we simply extend the eigenvectors (B12) and (B13) onto the region A' by contracting them with the first pentagon, which is equivalent to contracting a complete basis on the extended vector $|\psi'\rangle$. For the

first eigenvector, we thus find

$$|\psi'_{A'}{}^{0,0}\rangle = \text{[Diagram of two tiles with parameters } \alpha_1, \beta_1 \text{ and } \alpha_2, \beta_2 \text{]} \quad (\text{B17})$$

The complete eigenvalue equation can be resolved by applying (B10) and (B11) successively:

$$\begin{aligned} \rho'_{A'} |\psi'_{A'}{}^{0,0}\rangle &= 2 \text{ [Diagram of a chain of six tiles with parameters } \alpha_1, \beta_1, \alpha_2, \beta_2, \alpha_2^*, \beta_2^*, \alpha_1^*, \beta_1^* \text{]} \\ &= \sqrt{2} \text{ [Diagram of a chain of four tiles with parameters } \alpha_1, \beta_1, \alpha_2, \beta_2, \alpha_2^*, \beta_2^* \text{]} \\ &= \text{ [Diagram of a chain of four tiles with parameters } \alpha_1, \beta_1, \alpha_2, \beta_2, \alpha_2^*, \beta_2^* \text{]} \\ &= \frac{1}{2} \text{ [Diagram of a chain of four tiles with parameters } \alpha_1, \beta_1, \alpha_2, \beta_2 \text{]} \\ &= \frac{1}{4} \text{ [Diagram of two tiles with parameters } \alpha_1, \beta_1 \text{ and } \alpha_2, \beta_2 \text{]} = \frac{1}{4} |\psi'_{A'}{}^{0,0}\rangle. \end{aligned} \quad (\text{B18})$$

Again, this procedure holds for all eigenstates, leading to the same eigenvalue spectrum as for ρ_A . Thus, we see that “gluing” $[[5, 1, 3]]$ tiles onto a region A on an original tile only projects the eigenvalues onto a larger space of Majorana dimer states, leaving their eigenvalues invariant. This procedure can also be extended to cases where a subsystem B and its complement B^C

both cover different tiles, as in the following example:

Here, we have rotated the configuration (B15) for easier visualization; as before, the adjoint part of ρ'_B is on the right. Even in this configuration, we can construct a set of eigenvectors by projecting a complete dimer basis onto B^C :

Explicitly, the eigenvalue equation for $|\psi_B^{0,0,0}\rangle$ is given by

Again, after repeating this procedure for all eight eigenstates, we find that the entanglement entropy corresponds to the result for a fixed logical input, $S_B = 3 \log 2$. An important condition for computing reduced density matrix eigenstates in this way is that when projecting a complete basis of eigenvectors onto $|\psi\rangle$, the resulting states must be orthogonal. This is always the case when no dimers connect sites within region A^C . If they do, we can still simplify the reduced density matrix to an effective density

matrix of a reduced state, as in the following example for a region C :

$$\rho_C = 2 = \frac{1}{\sqrt{2}} \tag{B22}$$

$$= \frac{1}{2\sqrt{2}} = \frac{1}{8} \tag{B23}$$

Instead of $2^{|C^c|} = 32$ eigenstates, as in the previous example, we now only find $2^{|\gamma_C|} = 8$, where γ_C is the complement region of C after simplifying ρ_C (with $\partial\gamma_C = \partial C$; here, $\gamma_C = C$). This is because a basis set contracted onto C^c of the original state does not lead to fully orthogonal states, for example,

$$\tag{B24}$$

Thus, we conclude that if by applying (B10) and (B11) a reduced density matrix ρ_A can be simplified so that no dimers connect sites within γ_A , then there are $2^{|\gamma_A|}$ eigenstates with equal eigenvalues and an entanglement entropy $S_A = |\gamma_A| \log 2$. When such a simplification is not possible, the entanglement entropy can depend on the bulk input. If we extend the region $C \rightarrow D$ onto half of the two-pentagon system, we cannot apply (B10) and (B11):

$$\rho_D = 2 \tag{B25}$$

Because of a dimer connecting Majorana modes *within* D , an eigenbasis projected onto its edges becomes mixed. Indeed, the reduced density matrix ρ_D separates into a sum of parity-even and parity-odd terms, as cross-terms between both vanish:

$$= 0. \tag{B26}$$

We can thus write

$$\begin{aligned} \rho_D &= \text{tr}_{D^c}(\alpha_1\alpha_2|\bar{0}, \bar{0}\rangle + \beta_1\beta_2|\bar{1}, \bar{1}\rangle)(\alpha_1^*\alpha_2^*\langle\bar{0}, \bar{0}| + \beta_1^*\beta_2^*\langle\bar{1}, \bar{1}|) + \text{tr}_{D^c}(\alpha_1\beta_2|\bar{0}, \bar{1}\rangle + \beta_1\alpha_2|\bar{1}, \bar{0}\rangle)(\alpha_1^*\beta_2^*\langle\bar{0}, \bar{1}| + \beta_1^*\alpha_2^*\langle\bar{1}, \bar{0}|) \\ &\equiv \text{tr}_{D^c}|\psi^+\rangle\langle\psi^+| + \text{tr}_{D^c}|\psi^-\rangle\langle\psi^-|. \end{aligned} \tag{B27}$$

We have defined as $|\psi^\pm\rangle$ the parity-even and parity-odd part of the total state vector $|\psi\rangle$. For each of the two states, we can still apply our previous approach of finding the eigenbasis by projecting a complete dimer basis on the state itself, yielding $S_D(\psi^+) = S_D(\psi^-) = 3 \log 2$, as three dimers connect D and D^c . Following the rules for the entanglement of superpositions for biorthogonal states [57], we can now compute the entanglement entropy of the full state as

$$\begin{aligned} S_D &= \langle\psi^+|\psi^+\rangle S_D(\psi^+) + \langle\psi^-|\psi^-\rangle S_D(\psi^-) + h_2(\langle\psi^+|\psi^+\rangle) \\ &= 3 \log 2 + h_2(|\alpha_1\alpha_2|^2 + |\beta_1\beta_2|^2) \leq 4 \log 2, \end{aligned} \tag{B28}$$

where we have used the binary entropy function $x \mapsto h_2(x) := -x \log x - (1-x) \log(1-x)$. We are thus in a position to compute the entanglement entropy even for complicated superpositions of dimer states.

Assuming a boundary region A that can be simplified using (B10) and (B11), however, we can easily compute the entanglement entropy of the full HyPeC *independent of the bulk input*. For this, we follow the steps laid out in Eqs. (B18), (B21), and (B22) for the construction of reduced density matrices and their eigenstates. Using our previous notation for superpositions, an example is given by

$$|\psi\rangle = 2^{N_c/2} \tag{B29}$$

The normalization depends on the number N_C of internal contractions. We omitted the superposition labels α, β for clarity, but still assume only local superpositions within each tile. Given a boundary region A , we first simplify the reduced density matrix ρ_A as in Eq. (B22), being left with a wedge \mathcal{W} bounded by minimal cut (or “bulk geodesic”) γ_A :

$$\begin{aligned}
 \rho_A &= 2^{N_C} \cdot \text{Diagram 1} \\
 &= 2^{N_{C,\mathcal{W}}} \cdot \text{Diagram 2} \tag{B30}
 \end{aligned}$$

Here, $N_{C,\mathcal{W}}$ is the number of (still unresolved) contractions in the wedge \mathcal{W} . The eigenstate basis of ρ_A can again be constructed by projecting a complete basis of dimer states onto the edges of γ_A , leading to a $2^{|\gamma_A|}$ -dimensional space of states, where $|\gamma_A|$ is the number of edges along the cut. For illustration, we consider the eigenstate with all-even projections:

$$|\psi_A^{0,0,0,0,0}\rangle = \text{Diagram 3} \tag{B31}$$

The eigenvalue equation can be evaluated with the same techniques that we have used for reducing (B18) and (B21),

$$\begin{aligned}
 \rho_A |\psi_A^{0,0,0,0,0}\rangle &= 2^{N_{C,w}} \\
 &= \frac{1}{2^{|\gamma_A|}} \cdot
 \end{aligned}$$

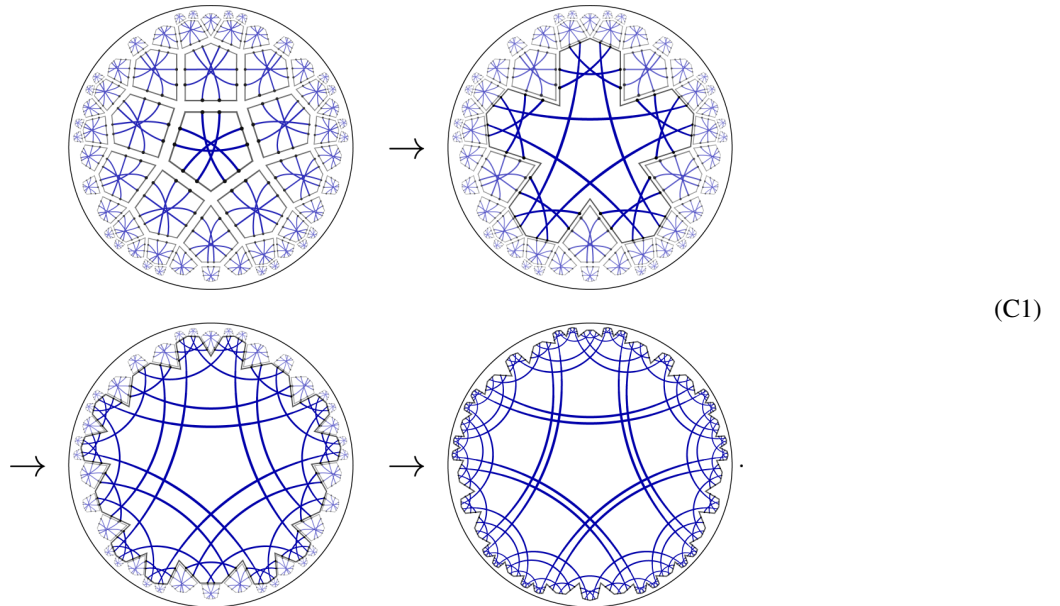
Thus, we find the same entanglement entropy as for the case of fixed logical input states, $S_A = |\gamma_A| \log 2$ (with $|\gamma_A| = 5$). Our procedure is equivalent to the *greedy algorithm* [5], which in dimer language is manifested through the reduction steps (B11) and (B10). As for the greedy algorithm, our approach only applies when both A and its complement A^C are reduced to the same γ_A after simplification. In that case, we can draw the following conclusion about the reduced density matrix:

$$\begin{aligned}
 \rho_A^2 &= 2^{2N_{C,w}} \\
 &= \frac{2^{N_{C,w}}}{2^{|\gamma_A|}} \cdot \frac{\rho_A}{2^{|\gamma_A|}} \cdot
 \end{aligned}$$

As a result, we find a flat spectrum of Rényi entropies $S_A^{(n)} = S_A = |\gamma| \log 2$. When reductions from A and A^C are not equivalent, i.e., when the greedy algorithm does not converge to a geodesic, dimers will be “lost” during each power of ρ_A , and $S_A^{(n)}$ will decrease with n .

APPENDIX C: CONTRACTION ORDER

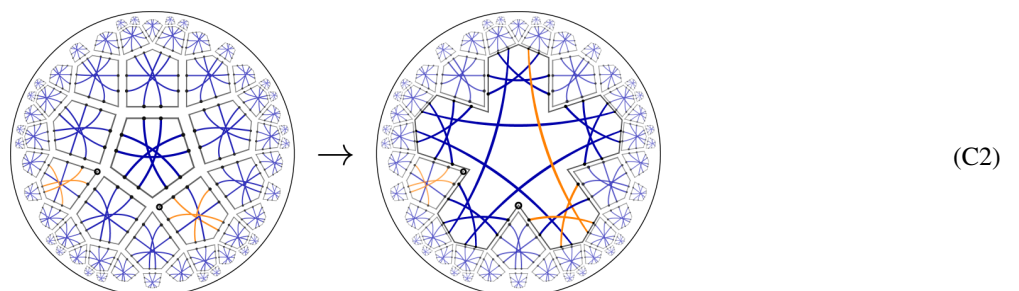
Contracting Majorana dimer states on a given tiling can give rise to ambiguities regarding contraction order: Before contraction, each tile has its own ordering of indices, some of which are contracted out and some remain on the edges of the final geometry. We consider here the HyPeC with its underlying spin tensor network description, of which the Majorana dimers form an effective representation. Let us start with the simplest case of a $\bar{0}$ (read: “logical zero”) input everywhere in the bulk and a successive contraction of neighboring tiles, starting from the center:



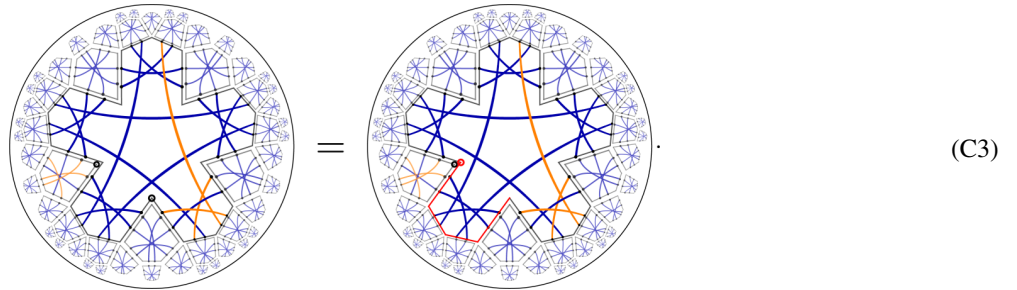
As all tiles have been filled with even-parity input states, the dimer parities of the fully contracted state is entirely independent of the initial ordering: As shown in Eq. (59), any cyclic permutation (i.e., pivot shifts) of the initial tiles or at intermediate contraction steps would have left the dimer parities invariant. For a general bulk input, however, the initial index labeling does matter: The $\bar{1}$ input has odd parity and its dimer parities thus change under cyclic permutations, as shown in Eq. (60). Thus, whenever a $\bar{1}$ tile is contracted in, the total parity of the contraction changes, and while the total parity is odd, any cyclic permutation leads to a string of Z edge operator, as discussed in Sec. III D. This leads to the following contraction rule for arbitrary fixed bulk input:

Lemma 4 (Dimer parities of the fixed-input HyPeC). Contracting fixed $[[5, 1, 3]]$ code states on a pentagon tiling is equivalent to multiplying dimer parities of contracted dimer pairs (regardless of the initial orientation of tiles) and adding Z strings between the pivots of pairs of tiles with $\bar{1}$ input. If the number of $\bar{1}$ inputs is odd, then an additional Z string connects the pivot of the unpaired $\bar{1}$ tile with the pivot of the full contraction.

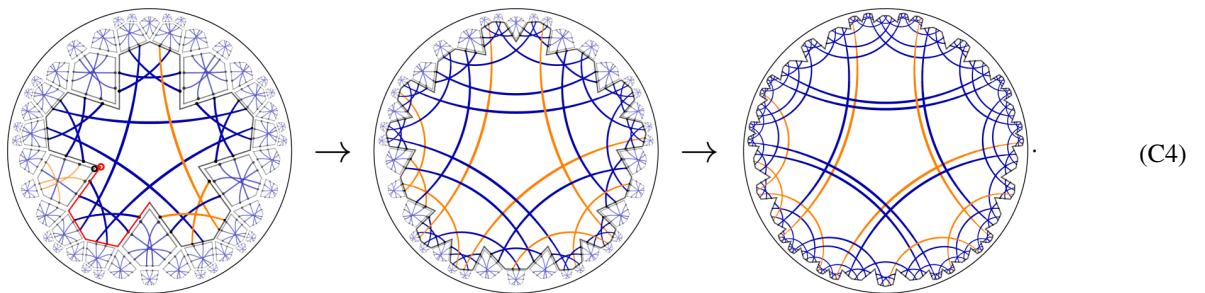
Proof. Without loss of generality, consider a particular contraction order and initial tile orientation. Whenever the total parity of the contraction at any step is even, contracting a $\bar{1}$ tile will cause pivot shifts in all following contraction steps to produce Z strings, until another $\bar{1}$ tile is reached and total parity becomes even again. The starting and end points of these Z strings are the pivots of the first and second $\bar{1}$ tiles. If the number of $\bar{1}$ tiles is even, then the final contraction will contains Z strings between each successive pair of $\bar{1}$ tile pivots. If it is odd, then the Z string from the last $\bar{1}$ tile will continue until the boundary of the full contraction. Consider the previous contraction for a pair of $\bar{1}$ tiles, with pivots of the odd tiles (whose orientation is now relevant) shown by a small circle:



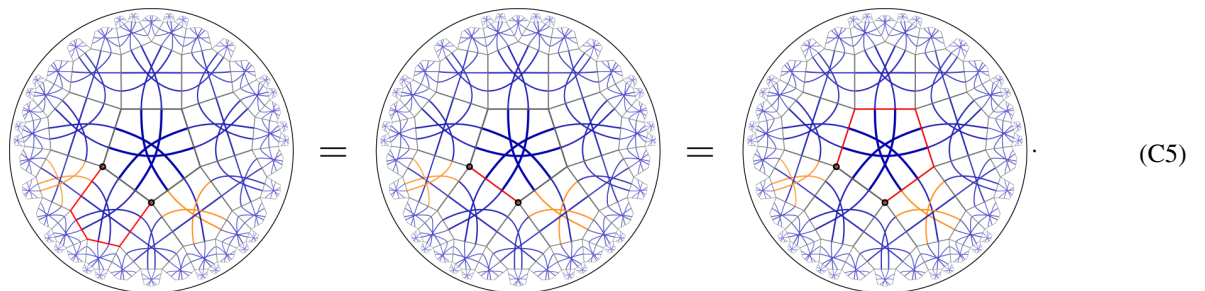
During the first iteration of contractions, the last contraction involves the first $\bar{1}$ tile and makes the contraction parity odd. We thus need to mark it with a pivot, which is simply the pivot of the original $\bar{1}$ tile. To contract the other $\bar{1}$ tile, a pivot shift is required, which produces a Z string (red line):



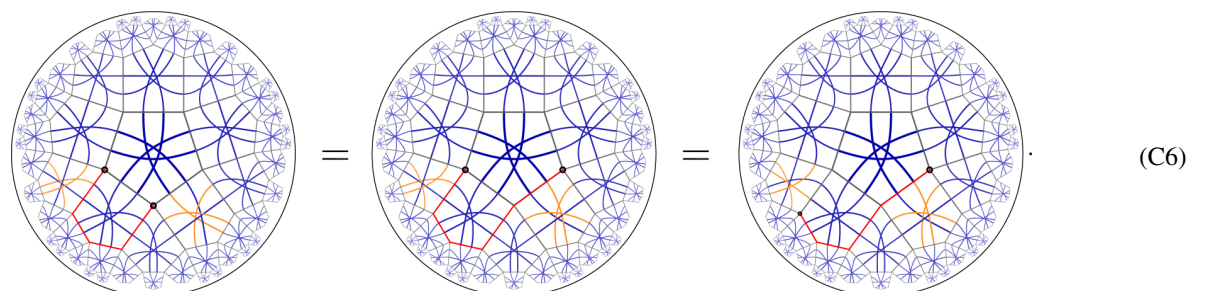
The contraction is now again parity even (the pivots “cancel each other out”), and the rest of the contraction can be performed without worrying about orientations:



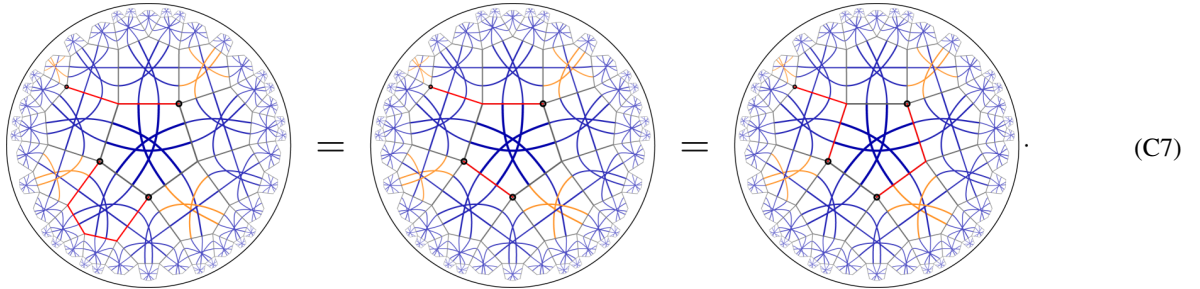
This result is independent of the ordering of the previous contraction, as we can freely deform the Z strings through the $\bar{0}$ tiles:



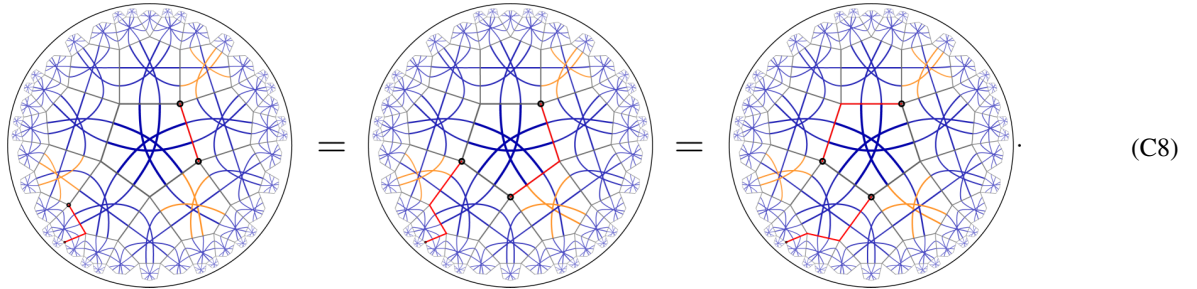
To indicate the action of the Z strings on the full contraction, we have omitted the spaces between tiles in the previous diagram. Furthermore, the result is independent of the initial orientations of the $\bar{1}$ tiles, as rotating these is equivalent to extending or shortening the Z strings, as we have found in Eq. (59):



Contracting more than two \bar{I} tiles will create Z strings between pairs of them, in the order in which we contracted. This ordering, however, also does not affect the final contraction, as we can change this pairing using the same rules:



The same rules apply if we have an odd number of \bar{I} tiles in the bulk. As the entire contraction now has odd parity, it also requires a pivot, which pairs up with the last \bar{I} tile in the ordering. Again, this choice of a “last” tile does not change the outcome:

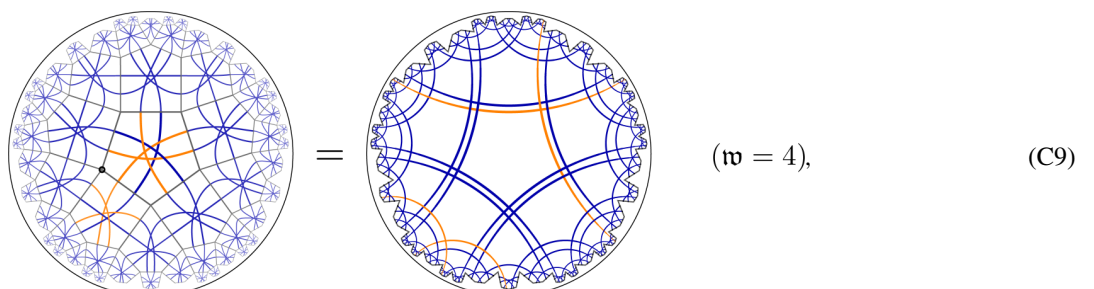


Note that in the last step, we pushed Z strings through two pentagon tiles. Consistent with the lemma above, moving the boundary pivot of the full contraction extends the Z string attached to it along the boundary, which is the expected behavior for a cyclic permutation of an odd-parity dimer state. ■

Lemma 4 now allows us to make some statements on the distance between Majorana boundary states for different bulk inputs. Let us define the *Majorana weight* \mathfrak{w} as the number of Majorana operators (i.e., dimer parity flips) required to transform one state into another. Given a boundary state vector $|\bar{0}, \bar{1}, \bar{1}, \bar{0}, \dots\rangle$ for an arbitrary bulk input, what is the lowest \mathfrak{w}_{\min} with respect to a state with any other bulk input? We claim the following:

Lemma 5 (Majorana distance of HyPeC boundary states). The boundary states of the HyPeC for fixed logical input in the bulk have a code distance $\mathfrak{w} > 2$ between any two inputs.

Proof. We will now show that starting from any fixed-input HyPeC boundary state, no number of logical input flips in the bulk can lead to a state which is closer that $\mathfrak{w} = 3$ to the original one. This bound is clearly saturated for such an input flip $\bar{0} \leftrightarrow \bar{1}$ of a tile on the boundary, which flips three dimer parities. If we instead push the input flip further into the bulk, we will produce a Z string from the boundary (or annihilate one, if the original contraction is parity odd). The further in the bulk the flip occurs, the longer the Z string grows, increasing \mathfrak{w} . Because of the hyperbolic geometry, there is also no way that the dimer flips by neighboring $\bar{1}$ insertions can cancel each out. For neighboring pairs of $\bar{1}$ insertions, we always find $\mathfrak{w} > 3$:



($\mathfrak{w} = 4$). (C10)

We have defined \mathfrak{w} relative to the all- $\bar{0}$ input, but the result clearly holds for insertions on any fixed code input. When non-neighboring pairs are added, the resulting Z strings cause additional dimer flips:

($\mathfrak{w} = 8$). (C11)

Similarly, adding even more pairs to make two Z strings “cancel” out does not bring down \mathfrak{w} :

($\mathfrak{w} = 8$). (C12)

As a result, it is impossible to produce Majorana dimer states on the boundary of the fixed-input HyPeC that can be mapped to each other with less than $\mathfrak{w} = 3$ Majorana operators. The underlying reason for this can be found in the geometrical construction: The number of possible boundary configurations 2^M on L boundary edges increases much faster than the 2^N configurations on the N bulk tiles, as the geometry is hyperbolic. ■

The property $\mathfrak{w} > 2$ resembles the code properties of the HyPeC: Because the tiles corresponding to $[[5, 1, 3]]$ code states, it requires three Pauli-type operations (“errors”) to map one code state to another. Thus, it requires at least three Pauli errors on the boundary to map any HyPeC state to another one. Here, we found that it also requires at least three “Majorana errors” to perform such a mapping. This is not a trivial result, as the number of Pauli operations corresponding to just two Majorana operations already grows in the distance between the two sites on which the Majorana operators act. For example,

$$\gamma_2 \gamma_{2k-1} = i X_1 Z_2 Z_3 \dots Z_{k-1} X_k. \tag{C13}$$

In general, applying two Majorana operators γ_j and γ_k at some distance on the boundary produces a Z string between the edges on which γ_j and γ_k act. Fortunately, the $[[5, 1, 3]]$ code states upon which the HyPeC are built allow for the expression of long Z strings as an action of just two Pauli operators as

$$Z_1 Z_2 Z_3 |\bar{0}\rangle = X_1 X_3 |\bar{0}\rangle, \tag{C14}$$

$$Z_1 Z_2 Z_3 Z_4 |\bar{0}\rangle = \begin{array}{c} \text{Diagram 1: A square lattice with vertices 1-10. Blue arrows point from 1 to 2, 2 to 3, 3 to 4, 4 to 5, 5 to 6, 6 to 7, 7 to 8, 8 to 9, 9 to 10, and 10 to 1. Red arrows point from 1 to 4, 2 to 5, 3 to 6, 4 to 7, 5 to 8, 6 to 9, 7 to 10, 8 to 1, 9 to 2, and 10 to 3.} \end{array} = \begin{array}{c} \text{Diagram 2: A square lattice with vertices 1-10. Blue arrows point from 1 to 2, 2 to 3, 3 to 4, 4 to 5, 5 to 6, 6 to 7, 7 to 8, 8 to 9, 9 to 10, and 10 to 1. Red arrows point from 1 to 4, 2 to 5, 3 to 6, 4 to 7, 5 to 8, 6 to 9, 7 to 10, 8 to 1, 9 to 2, and 10 to 3.} \end{array} = X_2 X_3 |\bar{0}\rangle. \quad (\text{C15})$$

Here, we have used the $\bar{0}$ input for illustration. The relative sign between the left- and right-hand side of these equations changes when using the $\bar{1}$ input instead, corresponding to a “phase flip” in the language of quantum error correction. We conclude that a pair of Majorana operators on the boundary of the HyPeC is related, up to a complex phase, to no more than two Pauli operators acting on tiles on the boundary. As each of these tiles corrects one Pauli errors, no overlap between states for different bulk inputs can be produced with such an operation, supporting our earlier geometrical explanation.

-
- [1] J. M. Maldacena, *Int. J. Theor. Phys.* **38**, 1113 (1999); *Adv. Theor. Math. Phys.* **2**, 231 (1998).
- [2] E. Witten, *Adv. Theor. Math. Phys.* **2**, 253 (1998).
- [3] A. Almheiri, X. Dong, and D. Harlow, *J. High Energy Phys.* **04** (2015) 163.
- [4] C. H. Lee and X.-L. Qi, *Phys. Rev. B* **93**, 035112 (2016).
- [5] F. Pastawski, B. Yoshida, D. Harlow, and J. Preskill, *J. High Energy Phys.* **06** (2015) 149.
- [6] P. Hayden, S. Nezami, X.-L. Qi, N. Thomas, M. Walter, and Z. Yang, *J. High Energy Phys.* **11** (2016) 009.
- [7] E. Minton, J. Polchinski, and V. Rosenhaus, *Phys. Rev. Lett.* **115**, 151601 (2015).
- [8] B. Swingle, *Phys. Rev. D* **86**, 065007 (2012).
- [9] F. Verstraete and J. I. Cirac, *Phys. Rev. B* **73**, 094423 (2006).
- [10] M. Fannes, B. Nachtergaele, and R. F. Werner, *Commun. Math. Phys.* **144**, 443 (1992).
- [11] F. Verstraete, J. I. Cirac, and V. Murg, *Adv. Phys.* **57**, 143 (2008).
- [12] U. Schollwöck, *Ann. Phys.* **326**, 96 (2011).
- [13] R. Orús, *Ann. Phys.* **349**, 117 (2014).
- [14] J. Eisert, M. Cramer, and M. B. Plenio, *Rev. Mod. Phys.* **82**, 277 (2010).
- [15] G. Vidal, *Phys. Rev. Lett.* **101**, 110501 (2008).
- [16] A. Jahn, M. Gluza, F. Pastawski, and J. Eisert, *Sci. Adv.* **5**, eaaw0092 (2019).
- [17] B. Ware, J. H. Son, M. Cheng, R. V. Mishmash, J. Alicea, and B. Bauer, *Phys. Rev. B* **94**, 115127 (2016).
- [18] N. Tarantino and L. Fidkowski, *Phys. Rev. B* **94**, 115115 (2016).
- [19] T. Barthel, C. Pineda, and J. Eisert, *Phys. Rev. A* **80**, 042333 (2009).
- [20] C. V. Kraus, N. Schuch, F. Verstraete, and J. I. Cirac, *Phys. Rev. A* **81**, 052338 (2010).
- [21] P. Corboz, R. Orús, B. Bauer, and G. Vidal, *Phys. Rev. B* **81**, 165104 (2010).
- [22] C. Wille, O. Buerschaper, and J. Eisert, *Phys. Rev. B* **95**, 245127 (2017).
- [23] N. Bultinck, D. J. Williamson, J. Haegeman, and F. Verstraete, *Phys. Rev. B* **95**, 075108 (2017).
- [24] M. Freedman and M. Headrick, *Commun. Math. Phys.* **352**, 407 (2017).
- [25] S. X. Cui, P. Hayden, T. He, M. Headrick, B. Stoica, and M. Walter, *Commun. Math. Phys.* (2019), doi:10.1007/s00220-019-03510-8.
- [26] D. Harlow and D. Stanford, [arXiv:1104.2621](https://arxiv.org/abs/1104.2621) [hep-th].
- [27] L. Susskind and E. Witten, [arXiv:hep-th/9805114](https://arxiv.org/abs/hep-th/9805114) [hep-th].
- [28] T. Banks, M. R. Douglas, G. T. Horowitz, and E. J. Martinec, [arXiv:hep-th.9808016](https://arxiv.org/abs/hep-th.9808016) [hep-th].
- [29] V. Balasubramanian, P. Kraus, A. Lawrence, and S. P. Trivedi, *Phys. Rev. D* **59**, 104021 (1999).
- [30] X. Dong, D. Harlow, and A. C. Wall, *Phys. Rev. Lett.* **117**, 021601 (2016).
- [31] A. Hamilton, D. Kabat, G. Lifschytz, and D. A. Lowe, *Phys. Rev. D* **74**, 066009 (2006).
- [32] M. Walter, D. Gross, and J. Eisert, [arXiv:1612.02437](https://arxiv.org/abs/1612.02437).
- [33] N. Gisin and H. Bechmann-Pasquinucci, *Phys. Lett. A* **246**, 1 (1998).
- [34] A. Higuchi and A. Sudbery, *Phys. Lett. A* **273**, 213 (2000).
- [35] W. Helwig, W. Cui, J. I. Latorre, A. Riera, and H.-K. Lo, *Phys. Rev. A* **86**, 052335 (2012).
- [36] S. Bravyi, *Cont. Math.* **482**, 179 (2009).
- [37] F. Berezin, *The Method of Second Quantization* (Academic Press, New York, 1966).
- [38] K. E. Cahill and R. J. Glauber, *Phys. Rev. A* **59**, 1538 (1999).
- [39] S. Bravyi, *Quantum Inf. Comp.* **5**, 216 (2005).
- [40] S. Ryu and T. Takayanagi, *Phys. Rev. Lett.* **96**, 181602 (2006).
- [41] N. Bao, C. Cao, M. Walter, and Z. Wang, *J. High Energy Phys.* **09** (2015) 203.
- [42] H. Casini and M. Huerta, *J. High Energy Phys.* **03** (2009) 048.
- [43] P. Hayden, M. Headrick, and A. Maloney, *Phys. Rev. D* **87**, 046003 (2013).
- [44] S. T. Flammia, A. Hamma, T. L. Hughes, and X.-G. Wen, *Phys. Rev. Lett.* **103**, 261601 (2009).
- [45] P. Calabrese and J. Cardy, *J. Stat. Mech.* (2004) P06002.
- [46] D. Goyeneche, D. Alsina, J. I. Latorre, A. Riera, and K. Zyczkowski, *Phys. Rev. A* **92**, 032316 (2015).
- [47] F. Huber, O. Gühne, and J. Siewert, *Phys. Rev. Lett.* **118**, 200502 (2017).
- [48] R. J. Harris, N. A. McMahon, G. K. Brennen, and T. M. Stace, *Phys. Rev. A* **98**, 052301 (2018).
- [49] S. Bravyi, B. M. Terhal, and B. Leemhuis, *New J. Phys.* **12**, 083039 (2010).
- [50] A. Y. Kitaev, *Phys.-Usp.* **44**, 131 (2001).
- [51] H. Yan, *Phys. Rev. B* **99**, 155126 (2019).
- [52] J. C. Bridgeman, S. T. Flammia, and D. Poulin, *Phys. Rev. B* **94**, 205123 (2016).

- [53] M. Miyaji, T. Numasawa, N. Shiba, T. Takayanagi, and K. Watanabe, *Phys. Rev. Lett.* **115**, 171602 (2015).
- [54] J. Haegeman, T. J. Osborne, H. Verschelde, and F. Verstraete, *Phys. Rev. Lett.* **110**, 100402 (2013).
- [55] T. J. Osborne, [arXiv:1901.06124](https://arxiv.org/abs/1901.06124) [quant-ph].
- [56] L. Boyle, B. Dickens, and F. Flicker, [arXiv:1805.02665](https://arxiv.org/abs/1805.02665) [hep-th].
- [57] N. Linden, S. Popescu, and J. A. Smolin, *Phys. Rev. Lett.* **97**, 100502 (2006).

Central charges of aperiodic holographic tensor-network models

Alexander Jahn¹, Zoltán Zimborás^{2,3,4} and Jens Eisert^{1,5}


¹*Dahlem Center for Complex Quantum Systems, Freie Universität Berlin, 14195 Berlin, Germany*

²*Institute for Particle and Nuclear Physics, Wigner Research Centre for Physics, 1121 Budapest, Hungary*

³*BME-MTA Lendület Quantum Information Theory Research Group, 1111 Budapest, Hungary*

⁴*Institute for Mathematics, Budapest University of Technology and Economics, 1111 Budapest, Hungary*

⁵*Department of Mathematics and Computer Science, Freie Universität Berlin, 14195 Berlin, Germany*

 (Received 17 January 2020; revised 8 April 2020; accepted 1 October 2020; published 21 October 2020)

Central to the AdS/CFT correspondence is a precise relationship between the curvature of an anti-de Sitter (AdS) space-time and the central charge of the dual conformal field theory (CFT) on its boundary. Our work shows that such a relationship can also be established for tensor network models of AdS/CFT based on regular bulk geometries, leading to an analytical form of the maximal central charges exhibited by the boundary states. We identify a class of tensors based on Majorana dimer states that saturate these bounds in the large curvature limit, while also realizing perfect and block-perfect holographic quantum error correcting codes. Furthermore, the renormalization group description of the resulting model is shown to be analogous to the strong disorder renormalization group, thus giving an example of an exact quantum error correcting code that gives rise to a well-understood critical system. These systems exhibit a large range of fractional central charges, tunable by the choice of bulk tiling. Our approach thus provides a precise physical interpretation of tensor network models on regular hyperbolic geometries and establishes quantitative connections to a wide range of existing models.

DOI: [10.1103/PhysRevA.102.042407](https://doi.org/10.1103/PhysRevA.102.042407)

I. INTRODUCTION

Years before the formulation of the holographic principle, Brown and Henneaux noticed a peculiar property of anti-de Sitter (AdS) space-time, a solution to Einstein's equation with constant negative curvature: At its asymptotic boundary, the generators of the symmetry group $SO(2, 2)$ of $(2+1)$ -dimensional AdS_3 space-time form a *Virasoro algebra* describing a two-dimensional *conformal field theory* (CFT) with an effective *central charge* depending on the curvature of the AdS bulk. Rather than a mathematical coincidence, the AdS/CFT correspondence [1] propelled this observation to the cornerstone of a holographic duality between gravity in $(d+2)$ -dimensional AdS_{d+2} space-time and a CFT on its $(d+1)$ -dimensional boundary, with an equivalent action describing both sides of the duality [2]. A key motivation for the holographic principle was the discovery that a black hole's entropy scales with its horizon area rather than its volume [3,4]. The Bekenstein-Hawking entropy formula

$$S_{\text{BH}} = \frac{A_{\text{hor}}}{4G}, \quad (1)$$

where A_{hor} is the horizon area and G the gravitational constant, has a surprising generalization in the context of AdS/CFT: The entanglement entropy S_A [5] of a boundary region A follows the Ryu-Takayanagi (RT) formula [6]

$$S_A = \frac{|\gamma_A|}{4G}, \quad (2)$$

where $|\gamma_A|$ is the area of an extremal surface γ_A in the bulk whose boundary $\partial\gamma_A$ matches the boundary ∂A . In $2+1$

dimensions, γ_A is simply a geodesic curve and $|\gamma_A|$ its length. Both formulas (1) and (2) suggest an encoding of information in Planckian pieces of area of size $\sim G = l_p^2$ (in $3+1$ bulk dimensions).

While the AdS/CFT correspondence is formulated in the continuum, *tensor networks* [5,7–10] have become a popular approach for models built on a discretized AdS space-time, as they naturally incorporate the RT formula in the form of an upper bound on entanglement and yield boundary quantum states that can be efficiently computed. The *multiscale entanglement renormalization ansatz* (MERA) [11], a tensor network that well approximates critical boundary states, was identified as a possible realization of discrete holography [12,13], but the bulk geometry of the MERA cannot be directly related to an AdS time slice [14–16]. Instead, regular hyperbolic tilings have recently been used as the basis of numerous discrete holographic models [17–23], elucidating many aspects of AdS/CFT, particularly its deep connection to *quantum error correction* [17,24]. However, a clear interpretation of the resulting boundary states in terms of a critical system, as is possible for the MERA, remained elusive.

Resolving this question, we show that tensor networks on regular tilings lead to boundary quantum states whose symmetries naturally discretize conformal symmetries on time slices, allowing their maximal central charges to be analytically computed for any tiling. Relating this central charge to the scalar curvature of the tiling then results in a discrete generalization of the Brown-Henneaux (BH) formula [25]. We demonstrate these properties using a class of tensor networks based on *Majorana dimer states*, whose exact central charges

are computed and are shown to saturate the upper bound in the strong-curvature limit. This class of states includes the widely studied *hyperbolic pentagon code* (HyPeC), an instance of the HaPPY codes [17], a toy model for quantum error correction in AdS/CFT. In this paper, we argue that these dimer models are a discrete approximation of a CFT with an aperiodic structure, the inflation rules of the tiling providing a local renormalization group transformation identified with the strong-disorder renormalization group (SDRG). The discrete boundary thus exhibits quasiregular symmetries, describing a CFT discretization that breaks translation invariance and possesses disorder on all length scales. Such critical systems have been extensively studied in the condensed matter literature, but no connection to holographic models had been known until now.

II. CENTRAL CHARGES AND CURVATURE

In *global* AdS coordinates, AdS₃ space-time takes the form

$$ds^2 = -(1 + r^2/\alpha^2)dt^2 + \frac{\alpha^2 dr^2}{\alpha^2 + r^2} + r^2 d\phi, \quad (3)$$

where α is the *AdS radius*. The scalar curvature or *Ricci scalar* R of AdS _{d} space-time with $d = 2+1$ dimensions is given by

$$R = -\frac{d(d-1)}{\alpha^2} = -\frac{6}{\alpha^2}, \quad (4)$$

corresponding to a negative cosmological constant $\Lambda = -1/\alpha^2$. An AdS₃ time slice can be more conveniently mapped to the *Poincaré disk* with

$$ds^2 = 4\alpha^2 \frac{d\rho^2 + \rho^2 d\phi^2}{(1 - \rho^2)^2}. \quad (5)$$

Global and Poincaré disk coordinates are related by a radial transformation $r = 2\alpha\rho/(1 - \rho^2)$ and the time-slice constraint $dt = 0$. The global radius is defined in $r \in [0, \infty[$, so the AdS boundary is mapped from $r = \infty$ to $\rho = 1$. Consider an *asymptotically* AdS space-time, i.e., one described by Eq. (5) near the AdS boundary. In this asymptotic region $\rho \rightarrow 1$, a bulk geodesic γ_A corresponding to a boundary region A will be unaffected by massive deformations further in the bulk, simply following a radial direction (see Fig. 1). At two different cutoff radii $\rho_1 < \rho_2$ close to unity, the subsystem

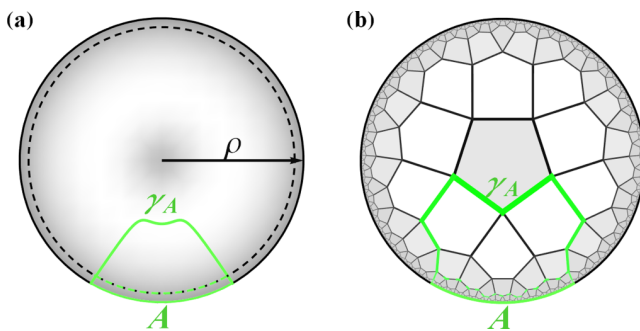


FIG. 1. (a) Continuous and (b) discretized geodesic γ_A in the Poincaré disk with a deformation in the center and a boundary cutoff shown as a dashed curve. In the asymptotic region towards the boundary, the shape of γ_A is independent of bulk deformations.

length $\ell = |A|$ at each cutoff is given by

$$\ell^{(k)} = \frac{2\alpha\rho_k}{1 - \rho_k^2} \Delta\phi \approx \frac{\alpha}{1 - \rho_k} \Delta\phi, \quad (6)$$

where $\Delta\phi$ is the Poincaré disk angle subtended by A . The difference in geodesic length $|\gamma_A|$ between both cutoffs is given by the lengths of two radial segments:

$$|\gamma_A^{(2)}| - |\gamma_A^{(1)}| = 2 \int_{\rho_1}^{\rho_2} \frac{2\alpha}{1 - \rho^2} d\rho \approx 2\alpha \ln \frac{\ell^{(2)}}{\ell^{(1)}}. \quad (7)$$

Compare this with the entanglement entropy of a conformal field theory for a small subsystem ($\Delta\phi \ll 2\pi$), given by [26]

$$S_A = \frac{c}{3} \ln \left(\frac{2\ell}{\Delta\phi\epsilon} \sin \frac{\Delta\phi}{2} \right) \approx \frac{c}{3} \ln \frac{\ell}{\epsilon}, \quad (8)$$

where ϵ denotes the lattice spacing and c is the central charge of the CFT. Assuming that the RT prescription holds, we recover the Brown-Henneaux formula [25]

$$c = \frac{3\alpha}{2G}. \quad (9)$$

III. DISCRETE TENSOR NETWORK MODELS

A natural discretization of an AdS time slice, or equivalently, the Poincaré disk, is given by a *regular* hyperbolic tiling (Fig. 1). A regular $\{n, k\}$ tiling, with k n -gon tiles at each vertex, is hyperbolic if the sum of inner angles of each n -gon is smaller than $(n - 2)\pi$, i.e., when $1/n + 1/k < 1/2$. We can relate such a discretized bulk geometry to a quantum state by identifying each n -gon tile with a rank- n tensor and contracting them over all edges, forming a *tensor network* [5,7–10]. The uncontracted edges on the boundary are then identified as the physical sites of a boundary state. As the Poincaré disk (1) can contain infinitely many tiles, a prescription for constructing the tiling towards the asymptotic boundary is needed. Starting with a given tile/tensor, we iteratively “grow” our geometry by contracting layers of tensors in *inflation steps*, each step corresponding to a UV cutoff. A discretized boundary region A at such a discrete cutoff does not follow a constant radius ρ in the Poincaré disk, with its length ℓ being larger than expected for a radial cutoff in the continuum. Similarly, as shown in Fig. 1, discretized geodesic cuts γ_A no longer follow a smooth curve, with their lengths $|\gamma_A|$ also being larger than in the continuum. However, we can still define a discrete analog to the RT formula (2) as a bound on the entanglement entropy of a boundary region A , given by

$$S_A \leq \frac{|\gamma_A|}{s} \ln \chi, \quad (10)$$

with $\partial A = \partial\gamma_A$ and s being the length of each individual edge. The *bond dimension* χ of each tensor index is assumed to be constant throughout the network.

In analogy to the previous section, we now derive a discretized form of the Brown-Henneaux formula (9) from the relative growth of boundary and geodesic lengths $\ell = |A|$ and $|\gamma_A|$ under inflation of the tiling. We specifically consider *vertex inflation*, whereby an inflation step consists of filling each open vertex with tiles. Vertices are labeled by their number

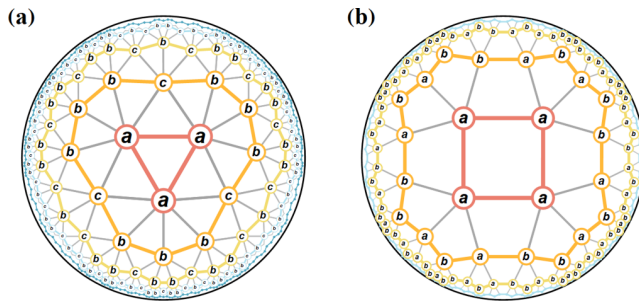


FIG. 2. Vertex inflation of (a) the $\{3, 7\}$ and (b) the $\{4, 5\}$ tiling, with vertices labeled by type and each inflation layer color-coded.

of neighbors up to the given inflation level. First consider the $n = 3$ case, the triangular hyperbolic tiling, whose vertex inflation is shown in Fig. 2 (left). We start with a single triangle with three vertices, each of which has two neighbors. The first inflation step gives each vertex $k-2$ additional neighboring vertices, two of which are shared with its previous neighbors. Thus, the inflation step adds $k-3$ new vertices for each old one. After the first inflation step, all boundary vertices have either three or four neighbors, two of which are other boundary vertices. Denoting vertices with two, three, and four neighbors with the letters a , b , and c , respectively, this pattern is summarized in the *inflation rule*

$$a \mapsto b^{k-4}c, \quad b \mapsto b^{k-5}c, \quad c \mapsto b^{k-6}c, \quad (11)$$

where we encode the boundary vertices as a string of a , b , and c , a^k denoting k repetitions of a . The inflation rule for any hyperbolic $\{n, k\}$ tiling produces a *quasiregular* sequence [27] exhibiting self-similarity: After sufficiently many inflation steps, any starting sequence will lead to a sequence with the same distribution of letters. In this *steady state* the relative frequency of letters is given by the largest eigenvalue of the *substitution matrix* M , where $M_{i,j}$ is the number of j vertices resulting from applying the inflation rule on an i vertex. For the $\{3, k\}$ tiling, it is given by

$$M = \begin{pmatrix} 0 & k-4 & 1 \\ 0 & k-5 & 1 \\ 0 & k-6 & 1 \end{pmatrix}. \quad (12)$$

Here the rows and columns correspond to (a, b, c) vertices. The largest eigenvalue of M ,

$$\lambda = \frac{1}{2}(\sqrt{k^2 - 8k + 12} + k - 4), \quad (13)$$

is the scaling factor of the sequence (and sufficiently large subsystems thereof) in the steady state, i.e., after many inflation steps. The scaling of discrete geodesics can also be computed: Coarse-graining a subsystem A of the sequence by a *deflation* step maps the two vertices that bound A (and a few of its neighbors) onto two vertices at a lower inflation layer. For the $\{3, 7\}$ tiling, this corresponds to removing two edges from the geodesic γ_A , one on either end. Thus, the average difference in entanglement entropy between both layers, denoted as $\overline{\Delta S_A}$, is bounded by $2 \ln \chi$. Relating this to (8) leads to the

central charge bound

$$c_{\{3,k\}} = \frac{3 \overline{\Delta S_A}}{\ln \lambda} \leq \frac{6 \ln \chi}{\ln \frac{\sqrt{k^2 - 8k + 12} + k - 4}{2}} =: c_{\{3,k\}}^{\max}. \quad (14)$$

Generalizing this result to arbitrary hyperbolic $\{n, k\}$ tilings leads to further complications. For the $\{4, k\}$ tiling (Fig. 2, right), the vertex inflation rule is

$$a \mapsto b(ab)^{k-3}, \quad b \mapsto b(ab)^{k-4}. \quad (15)$$

Again a and b denote vertices with two and three neighbors up to a given inflation layer. The substitution matrix and its largest eigenvalues are found to be

$$M = \begin{pmatrix} k-3 & k-2 \\ k-4 & k-3 \end{pmatrix}, \quad \lambda = \sqrt{k^2 - 6k + 8} + k - 3. \quad (16)$$

Unfortunately, the change of geodesic length under deflation now depends on the vertices involved: As we can see in Fig. 2 (right), the deflation $a \leftarrow b$ still only involves moving along one edge, but the deflation $a \leftarrow a$ involves two. To determine the average change in geodesic length per deflation step, we first compute the left and right eigenvectors of M for the eigenvalue λ , given by

$$\vec{l} = \begin{pmatrix} \sqrt{8 - 6k + k^2} \\ k - 2 \end{pmatrix}, \quad \vec{r} = \begin{pmatrix} \sqrt{8 - 6k + k^2} \\ k - 4 \end{pmatrix}. \quad (17)$$

When divided by their total sum, the components of \vec{l} give the relative frequencies $P(a)$ and $P(b)$ of a and b vertices in the steady state. This is not a probabilistic process; however, the relative frequencies can be captured on the formal level by a *discrete Markov chain*. In this sense, we now wish to compute the probability of a deflation step $i \leftarrow j$. Each vertex type corresponds to a state with transition probabilities to other states under a deflation step. After sufficiently many steps, the probability of reaching any given state becomes independent of the starting point. While $M_{i,j} \propto P(i \mapsto j|i)$ is the (relative) transition probability of reaching a j vertex from an i one, we can construct the *deflation matrix* D giving the probability of the reverse process,

$$\begin{aligned} D_{i,j} &= P(i \leftarrow j|j) = \frac{P(i \mapsto j|i)P(i)}{\sum_k P(k \mapsto j|k)P(k)} \\ &= \frac{M_{i,j}l_i}{\sum_k M_{k,j}l_k} = \frac{M_{i,j}l_i}{\lambda l_j}. \end{aligned} \quad (18)$$

The eigenvector \vec{p} of D with eigenvalue 1 now encodes the average probability of reaching each vertex type through deflation. We find $p_i = l_i r_i$, as

$$\sum_j D_{i,j} p_j = \sum_j \frac{M_{i,j} l_i r_j}{\lambda} = l_i r_i = p_i. \quad (19)$$

We normalize \vec{p} so that $\sum_i p_i = 1$. If an inflation step $i \mapsto j$ adds $E_{i,j}$ edges to a geodesic ending at an i vertex, i.e., adding $E_{i,j} \ln \chi$ to the entanglement bounded by the cut, then the average entanglement entropy loss per deflation step is given by

$$\overline{\Delta S_A} \leq \sum_{i,j} D_{i,j} E_{i,j} p_j \ln \chi = \frac{1}{\lambda} \sum_{i,j} M_{i,j} E_{i,j} l_i r_j \ln \chi. \quad (20)$$

TABLE I. Maximal central charges c^{\max} for the boundary state of a bond dimension χ tensor network embedded into a vertex-inflated regular $\{n, k\}$ tiling. The last column contains the slope of c^{\max} with respect to the AdS radius α , given in terms of the geodesic edge length d . Full derivations are given in Appendix A.

	Maximal central charge c^{\max}					Slope c^{\max}/α	
	$k = 3$	$k = 4$	$k = 5$	$k = 6$	General k	$k \rightarrow \infty$	$k \rightarrow \infty$
$n = 3$					$\frac{6 \ln \chi}{\ln \frac{\sqrt{k^2 - 8k + 12 + k - 4}}{2}}$	$\frac{6 \ln \chi}{\ln(k-4)}$	$\frac{12 \ln \chi}{s}$
$n = 4$			$\frac{9 \ln \chi}{\ln(\sqrt{3+2})}$	$\frac{9 \ln \chi}{\ln(2\sqrt{2+3})}$	$\frac{9 \ln \chi}{\ln(\sqrt{k^2 - 6k + 8 + k - 3})}$	$\frac{9 \ln \chi}{\ln(2k-6)}$	$\frac{18 \ln \chi}{s}$
$n = 5$		$\frac{10 \ln \chi}{\ln(\sqrt{3+2})}$	$\frac{10 \ln \chi}{\ln \frac{3\sqrt{5}+7}{2}}$	$\frac{10 \ln \chi}{\ln \frac{4\sqrt{6}+10}{2}}$	$\frac{10 \ln \chi}{\ln \frac{\sqrt{9k^2 - 48k + 60 + 3k - 8}}{2}}$	$\frac{10 \ln \chi}{\ln(3k-8)}$	$\frac{20 \ln \chi}{s}$
$n = 6$		$\frac{12 \ln \chi}{\ln(2\sqrt{2+3})}$	$\frac{12 \ln \chi}{\ln(2\sqrt{6+5})}$	$\frac{2 \ln \chi}{\ln(4\sqrt{3+7})}$	$\frac{12 \ln \chi}{\ln(2\sqrt{k^2 - 5k + 6 + 2k - 5})}$	$\frac{12 \ln \chi}{\ln(4k-10)}$	$\frac{24 \ln \chi}{s}$
$n = 7$	$\frac{66 \ln \chi}{5 \ln \frac{3+\sqrt{5}}{2}}$	$\frac{66 \ln \chi}{5 \ln(\sqrt{15+4})}$	$\frac{66 \ln \chi}{5 \ln \frac{\sqrt{165}+13}{2}}$	$\frac{66 \ln \chi}{5 \ln(\sqrt{15+4})}$	$\frac{66 \ln \chi}{5 \ln \frac{5k-12+\sqrt{(5k-10)(5k-14)}}{2}}$	$\frac{66 \ln \chi}{5 \ln(5k-12)}$	$\frac{132 \ln \chi}{5s}$
$n = 8$	$\frac{15 \ln \chi}{\ln(\sqrt{3+2})}$	$\frac{15 \ln \chi}{\ln(2\sqrt{6+5})}$	$\frac{15 \ln \chi}{\ln(3\sqrt{7+8})}$	$\frac{15 \ln \chi}{\ln(2\sqrt{30+11})}$	$\frac{15 \ln \chi}{\ln(\sqrt{9k^2 - 42k + 48 + 3k - 7})}$	$\frac{15 \ln \chi}{\ln(6k-14)}$	$\frac{30 \ln \chi}{s}$
$n = 9$	$\frac{114 \ln \chi}{7 \ln \frac{5+\sqrt{21}}{2}}$	$\frac{114 \ln \chi}{7 \ln(\sqrt{35+6})}$	$\frac{114 \ln \chi}{119 \ln \frac{2+\sqrt{357}}{2}}$	$\frac{114 \ln \chi}{7 \ln(2\sqrt{42+13})}$	$\frac{114 \ln \chi}{7 \ln \frac{7k+\sqrt{(16-7k)^2 - 4 - 16}}{2}}$	$\frac{114 \ln \chi}{7 \ln(7k-16)}$	$\frac{228 \ln \chi}{7s}$
$n \rightarrow \infty$	$\frac{3(n+2) \ln \chi}{2 \ln(n-4)}$	$\frac{3(n+2) \ln \chi}{2 \ln(2(n-3))}$	$\frac{3(n+2) \ln \chi}{2 \ln(3n-8)}$	$\frac{3(n+2) \ln \chi}{2 \ln(4n-10)}$	$\frac{3(n+2) \ln \chi}{2 \ln((n-2)(k-2)-2)}$	$\frac{3n \ln \chi}{2 \ln(nk)}$	$\frac{3n \ln \chi}{s}$

We thus call E the *entanglement matrix*. The central charge bound for the hyperbolic $\{n, k\}$ tiling thus becomes

$$c_{\{n,k\}} \leq c_{\{n,k\}}^{\max} = \frac{6 \sum_{i,j} M_{i,j} E_{i,j} l_i r_j \ln \chi}{\lambda \ln \lambda}. \quad (21)$$

For the $\{4, k\}$ case, the entanglement matrix is simply

$$E = \begin{pmatrix} 1 & 2 \\ 1 & 2 \end{pmatrix}, \quad (22)$$

which yields a central charge bound

$$c_{\{4,k\}}^{\max} = \frac{9 \ln \chi}{\ln(\sqrt{k^2 - 6k + 8 + k - 3})}. \quad (23)$$

Equation (21) can be used to derive central charge bounds for arbitrary $\{n, k\}$ tilings. For $k > 3$, the inflation rules are as follows:

$$\begin{aligned} n = 3 : & & n > 3 : \\ a \mapsto b^{k-4}c, & & a \mapsto a^{n-4}b(a^{n-3}b)^{k-3}, \\ b \mapsto b^{k-5}c, & & b \mapsto a^{n-4}b(a^{n-3}b)^{k-4}. \\ c \mapsto b^{k-6}c. & & \end{aligned} \quad (24)$$

As before, the letters a, b, c correspond to vertices with two, three, and four neighbors. In the $k = 3$ case we also require three letters a, b, c , where c now denotes a vertex to the right of a b -type vertex, leading to

$$a \mapsto c a^{n-5}b, \quad b \mapsto c a^{n-6}b, \quad c \mapsto \emptyset. \quad (25)$$

Here \emptyset is the *empty set*, i.e., the letter disappears. While (24) and (25) reproduce the quasiregular sequences resulting from vertex inflation, these forms are not sufficient to describe the propagation of geodesics for $n > 4$. This requires distinguishing vertices by the graph distance of their neighboring vertices to the center, which determines which paths from one inflation layer to the next correspond to discretized radial geodesics. As in the continuous case, where we considered radial geodesics in an asymptotically AdS geometry, our tiling can be nonregular in the center; only the tiling structure near the boundary of the Poincaré disk is relevant to the central

charge of the boundary state. The maximum central charges resulting from the full calculation for an arbitrary $\{n, k\}$ tiling are summarized in Table I. The corresponding inflation rules and matrices M and E are given in Appendix A.

IV. CURVATURE OF REGULAR TILINGS

An $\{n, k\}$ tiling embedded into the Poincaré disk is constructed of identical n -gons with an angle of $2\pi/k$ at each corner (see Fig. 3). The geodesic length $P_1P_2 = s$ between two points P_1 and P_2 of the tiling determines the length between all other points in the tiling. The parameters n and k further fix the angles $\beta = \angle(OP_1, OP_2) = 2\pi/n$ and $\gamma = \angle(P_1P_2, P_1O) = \angle(P_2O, P_2P_1) = \pi/k$. The hyperbolic law of cosines then states that

$$\cos \beta = -\cos^2 \gamma + \sin^2 \gamma \cosh \frac{s}{\alpha}. \quad (26)$$

Note that this form of the law of cosines holds for a *Gaussian curvature* $K = R/2 = -1/\alpha^2$ of the time-slice metric. Using this relation we can now express the AdS₃ radius in terms of

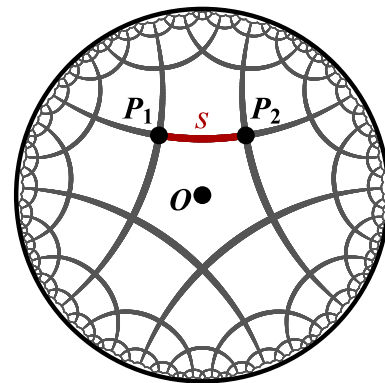


FIG. 3. Sketch of a $\{5, 4\}$ tiling in the Poincaré disk with three reference points and one edge marked.

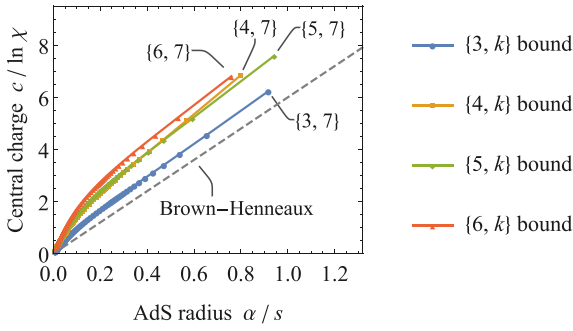


FIG. 4. Central charge bounds and AdS radii for $\{n, k\}$ tilings, with the continuum Brown-Henneaux formula for $G = s/4 \ln \chi$ shown as a dashed line. The data series start at $k = 7$ for $n = 3$, $k = 5$ for $n = 4$, and $k = 4$ for both $n = 5$ and $n = 6$ (first data point of each series in the upper-right corner).

the tiling parameters as

$$\frac{s}{\alpha} = 2 \operatorname{arccosh} \left(\frac{\cos \frac{\pi}{n}}{\sin \frac{\pi}{k}} \right) = 2 \ln \left(\frac{2k}{\pi} \cos \frac{\pi}{n} \right) + O(k^{-2}). \quad (27)$$

Thus, s/α diverges logarithmically in the large k limit. Note that the hyperbolic area $A = \alpha^2(n - 2n/k - 2)$ is finite in this limit.

We can now directly relate the previously derived bounds on central charges c to the AdS radius α of the corresponding AdS geometry, with the results for various choices of n shown in Fig. 4. These bounds can be compared to the continuum Brown-Henneaux prescription (9), with the gravitational constant G fixed through the RT formula: The length of a discretized minimal geodesic γ_A corresponding to a boundary region A can be written as $|\gamma_A| = Ns$, where N is the number of edges that γ_A consists of (note that $N \rightarrow \infty$ in the asymptotic limit). As each edge contributes $\ln \chi$ to S_A , we find

$$S_A = \frac{|\gamma_A|}{4G} = \frac{Ns}{4G} \stackrel{!}{=} N \ln \chi. \quad (28)$$

We can thus rewrite (9) as

$$c^{\max} = \frac{6\alpha \ln \chi}{s}. \quad (29)$$

Comparing this to the behavior of boundary states of $\{n, k\}$ tilings in Fig. 4, we find that these bounds are always above (29). This implies that tensor networks with the same bulk curvature and entanglement entropy growth as a continuum model can always be constructed by choosing appropriate tensors. Furthermore, we find a linear regime at large k in all tilings with the slope depending on n . For example,

$$\lim_{k \rightarrow \infty} \frac{c_{\{3,k\}}^{\max} s}{\alpha_{\{3,k\}} \ln \chi} = 12, \quad \lim_{k \rightarrow \infty} \frac{c_{\{4,k\}}^{\max} s}{\alpha_{\{4,k\}} \ln \chi} = 18. \quad (30)$$

The general coefficients are given in Table I. Note that they are significantly larger than the continuum value at small curvature, and increase monotonically with n . At small k , a second linear regime appears, with a slope much closer to the Brown-Henneaux form, e.g.,

$$\frac{c_{\{3,7\}}^{\max} - c_{\{3,8\}}^{\max}}{\alpha_{\{3,7\}} - \alpha_{\{3,8\}}} \approx 6.38 \frac{\ln \chi}{s}. \quad (31)$$

As a tiling of lower curvature is a better approximation of a continuous geometry, a result closer to the BH formula is not unexpected; however, fixing n while varying k appears to produce a central charge shift relative to the BH result that remains constant for a large range of k , even as the curvature increases significantly.

V. STRONG DISORDER RENORMALIZATION

Having established the previous bounds on entanglement entropy asymptotics, we will consider cases when the central charge can be calculated exactly. Interestingly, the method that allows for such an exact calculation is deeply related to a very early approach to real-space renormalization group transformations that were originally introduced in Ref. [28] and later extended in Ref. [29] to study the ground states, low-energy excitations, and spatiotemporal correlations of random quantum spin chains. This technique, called the SDRG [30] has recently again gained considerable attention due to its role in studying *many-body localization* [31], quantum critical *Floquet dynamics* [32], and models with highly area-law breaking ground states (rainbow states) [33] (see Ref. [34], and references therein for recent development).

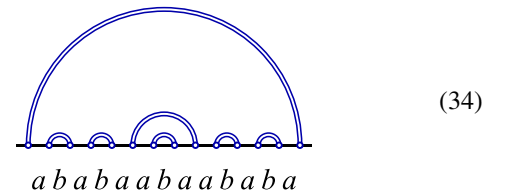
We now describe the basic results of SDRG on some aperiodic singlet models that share the quasiregular symmetries of the boundary states described previously. One example is given by the *Fibonacci XXZ chain* that is defined by the Hamiltonian

$$H = \sum_i J_i (S_i^x S_{i+1}^x + S_i^y S_{i+1}^y + \Delta S_i^z S_{i+1}^z), \quad (32)$$

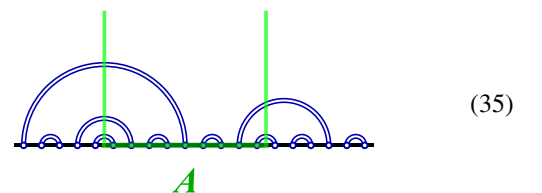
where S_i^α (with $\alpha = x, y, z$) refers to spin- $\frac{1}{2}$ operators. The site-dependent couplings $J_b > J_a > 0$ are modulated according to the aperiodic Fibonacci sequence obtained from the inflation rule

$$a \mapsto ababa, \quad b \mapsto aba. \quad (33)$$

The SDRG procedure predicts that for this aperiodic Hamiltonian the ground state (in the large system size limit) is characterized by fully entangled pairs of sites [35,36]. For example, inflating the letter b twice leads to a Hamiltonian with the ground state given by



where each double line denotes a singlet bond. The entanglement entropy of a subsystem A of such a singlet state is simply computed by counting the number of singlets connecting it to its complement A^C . For example, in the state



graphically as

$$|\bar{0}\rangle_5 = \begin{array}{c} \text{Diagram 1: Pentagon with 10 vertices labeled 1-10. Blue arrows connect vertices in a specific pattern, representing dimer parity +1 for j < k.} \end{array}, \quad |\bar{1}\rangle_5 = \begin{array}{c} \text{Diagram 2: Pentagon with 10 vertices labeled 1-10. Orange arrows connect vertices in a specific pattern, representing dimer parity -1 for j > k.} \end{array}. \quad (41)$$

In this visualization, each edge of a pentagon tile is identified with two Majorana modes, with each arrow $j \rightarrow k$ between two modes j and k corresponding to a term $i\gamma_j\gamma_k$ in the stabilizer Hamiltonian. The orientation of each arrow relative to the mode ordering gives it an associated *dimer parity* $p_{j,k}$, with $p_{j,k} = +1$ for $j < k$ (blue) and $p_{j,k} = -1$ for $j > k$ (orange). The dimer pattern becomes clearer when exchanging the ordering of odd and even Majorana modes, leading to

$$|\bar{0}'\rangle_5 = \begin{array}{c} \text{Diagram 3: Pentagon with 10 vertices labeled 1-10. Blue arrows connect vertices in a different pattern than Diagram 1.} \end{array}, \quad |\bar{1}'\rangle_5 = \begin{array}{c} \text{Diagram 4: Pentagon with 10 vertices labeled 1-10. Orange arrows connect vertices in a different pattern than Diagram 2.} \end{array}. \quad (42)$$

We will use this dual representation in all bulk plots, as it makes the dimer paths along the tiling more apparent. The usefulness of the Majorana dimer picture comes from the simplicity of contracting tensors representing Majorana dimer states such as (41): Contraction pairs up dimers along the contracted edges, with each new dimer's parity being the product of the old parities [23]. In addition, computing the entanglement entropy S_A of a connected subsystem A of a Majorana dimer state (or contraction thereof) reduces to simply counting the dimers between A and its complement A^C , each contributing $\ln(2)/2$ to S_A . While the HyPeC is generally composed of arbitrary logical bulk states, i.e., superpositions of $\bar{0}$ and $\bar{1}$, orthogonality conditions between the contracted states ensure that two-point correlation functions still exhibit a dimer structure, i.e., vanishing correlations between Majorana modes unconnected by dimers. Similarly, basis state superpositions affect the entanglement entropies of the HyPeC by corrections that depend on the logical states in *residual bulk regions* only for certain boundary regions [17].

Beyond the HyPeC, whose logical states on each tile are represented by *perfect tensors* that maximally entangle each possible subsystem A with the remaining sites, Majorana dimer states also represent *block perfect tensors*, where this condition is relaxed to only hold for connected subsystems. A suitable pair of logical eigenstates $\bar{0}_n$ and $\bar{1}_n$ can be found for any $n = 4m + 1, m \in \mathbb{N}$. For instance, for $n = 9$ the logical basis is given by

$$|\bar{0}\rangle_9 = \begin{array}{c} \text{Diagram 5: 9-sided polygon with 18 vertices labeled 1-18. Blue arrows connect vertices in a complex pattern.} \end{array}, \quad |\bar{1}\rangle_9 = \begin{array}{c} \text{Diagram 6: 9-sided polygon with 18 vertices labeled 1-18. Orange arrows connect vertices in a complex pattern.} \end{array}, \quad (43)$$

or equivalently,

$$|\bar{0}'\rangle_9 = \begin{array}{c} \text{Diagram 7: 9-sided polygon with 18 vertices labeled 1-18. Blue arrows connect vertices in a complex pattern.} \end{array}, \quad |\bar{1}'\rangle_9 = \begin{array}{c} \text{Diagram 8: 9-sided polygon with 18 vertices labeled 1-18. Orange arrows connect vertices in a complex pattern.} \end{array}, \quad (44)$$

With the tools developed in the previous sections, the average entanglement entropy [5], and by extension the central charge, can be computed for any regular tiling based on Majorana dimer states. We begin with the $n = 5$ case of the HyPeC. For simplicity, we consider *edge inflation* rather than vertex inflation in the following calculation: At each step, the tiles on all open edges are added to the contraction. The more complicated case of vertex inflation, which is more generalizable to arbitrary $\{n, k\}$ tilings, will be treated in Appendix B. The edge inflation rules for the $\{5, 4\}$ tiling are

$$a \mapsto caab, \quad b \mapsto cab, \quad c \mapsto \emptyset. \quad (45)$$

where the letters label boundary edges. On the level of the $\{5, 4\}$ tiling, these inflation rules can be visualized as follows:

$$\begin{array}{c} \text{Diagram 9: A boundary edge labeled 'a' with a blue arc above it.} \end{array} \mapsto \begin{array}{c} \text{Diagram 10: A boundary edge labeled 'c' with a blue arc above it, and a blue arc labeled 'a' below it.} \end{array}, \quad (46)$$

$$\begin{array}{c} \text{Diagram 11: A boundary edge labeled 'b' with a blue arc above it, and a blue arc labeled 'c' below it.} \end{array} \mapsto \begin{array}{c} \text{Diagram 12: A boundary edge labeled 'c' with a blue arc above it, and a blue arc labeled 'a' below it.} \end{array}. \quad (47)$$

We have combined the rules for b and c as they always appear in the combination bc . A boundary region ending at the marked letter, as well as its inflated version, is highlighted in green. Figure 6 (bottom) shows how these inflation rules act on the whole tiling, starting with a central pentagon (the sequence a^5). To see the change in dimer structure more clearly, one can project the boundary onto a line. The inflation rules are then given by

$$\begin{array}{c} \text{Diagram 13: A horizontal line with a blue arc above it labeled 'a' at its center.} \end{array} \mapsto \begin{array}{c} \text{Diagram 14: A horizontal line with blue arcs above it labeled 'c', 'a', 'a', 'b' from left to right.} \end{array}, \quad (48)$$

$$\begin{array}{c} \text{Diagram 15: A horizontal line with blue arcs above it labeled 'b' and 'c' at its ends.} \end{array} \mapsto \begin{array}{c} \text{Diagram 16: A horizontal line with blue arcs above it labeled 'c', 'a', 'b' from left to right.} \end{array}. \quad (49)$$

The new dimers added at each step are drawn in a lighter color, while the ones that are extended from the previous layer are drawn darker. As we are interested in entanglement properties, the dimer parities (which we previously color-coded) are irrelevant here.

Having associated geometrical features of the inflated tiling with a specific dimer configuration, we can now exactly calculate the entanglement entropy that each inflation step produces. As in the previous section, first consider a deflation

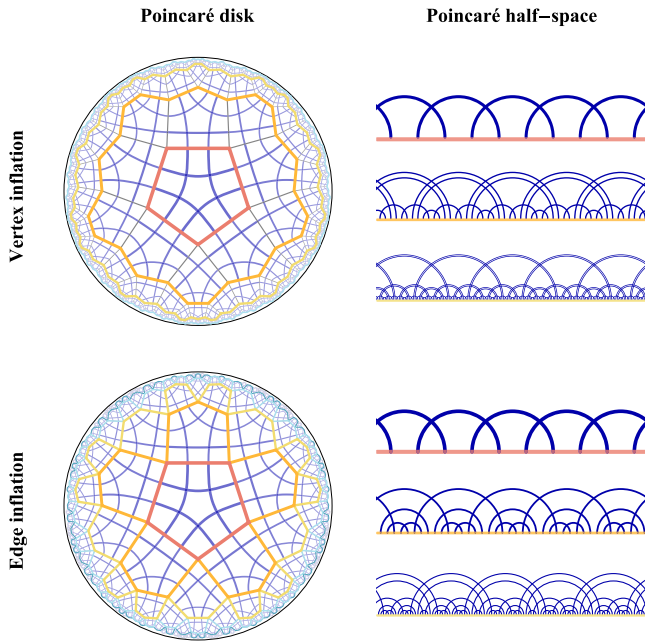


FIG. 6. Edge- and vertex-based inflation of the $\{5, 4\}$ HyPeC in the form (42), with inflation layers color-coded. The full tiling in the original Poincaré disk projection is shown on the left, while the dimers at the first three inflation layers are shown on the right, unfolded onto a line (Poincaré half-space projection).

or coarse-graining step that removes dimers and thus, entanglement entropy. Consider how a cut (green line) changes throughout a deflation step:

$$\begin{array}{c}
 \begin{array}{c} 1 \\ \leftarrow \\ \text{---} \\ a \end{array} \\
 \end{array}
 \quad \leftarrow \quad
 \begin{array}{c}
 \begin{array}{c} 3 \quad 3 \quad 3 \quad 0 \\ \leftarrow \\ \text{---} \\ c \quad a \quad a \quad b \end{array} \\
 \end{array}
 , \quad (50)$$

$$\begin{array}{c}
 \begin{array}{c} 0 \\ \leftarrow \\ \text{---} \\ b \quad c \end{array} \\
 \end{array}
 \quad \leftarrow \quad
 \begin{array}{c}
 \begin{array}{c} 4 \quad 4 \quad 2 \\ \leftarrow \\ \text{---} \\ c \quad a \quad b \end{array} \\
 \end{array}
 . \quad (51)$$

The green number counts the dimers that pass through the cut to the right of it, i.e., the local entanglement of a boundary region ending on a given edge. From these diagrams, we now construct the substitution and entanglement matrices M and E that describe the Markov process underlying vertex inflation. While M is constructed as before, the entries of E are now composed of half the difference in dimer cuts between two inflation layers for a given substitution, as each dimer carries $\ln(2)/2$ entanglement. We thus find

$$M = \begin{pmatrix} 2 & 1 & 1 \\ 1 & 1 & 1 \\ 0 & 0 & 0 \end{pmatrix}, \quad E = \begin{pmatrix} 1 & 0 & 1 \\ 2 & 1 & 2 \\ 0 & 0 & 0 \end{pmatrix}. \quad (52)$$

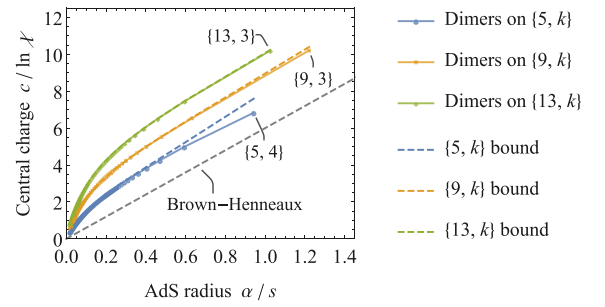


FIG. 7. Central charges for the $\{5, k\}$, $\{9, k\}$, and $\{13, k\}$ Majorana dimer models (solid curves, bottom to top) and corresponding geodesic bounds (dashed curves). The continuum Brown-Henneaux formula for $G = s/4 \ln \chi$ is shown as a dashed line.

Using (21), which now becomes an equality rather than an upper bound, this leads to an effective central charge

$$c_{\{5,4\}_e}^d = \frac{6 \ln 2}{\ln \frac{3+\sqrt{5}}{2}} \approx 4.32, \quad (53)$$

a result in agreement with previous numerical studies [23]. Note that we used the subscript of $\{5, 4\}_e$ to denote edge inflation, while all values without such a subscript in this text refer to vertex inflation. The computation of effective central charges follows analogously for vertex inflation, which we can generalize to arbitrary $\{5, k\}$ tiling with a finite number of letters. We can further extend this approach to the block-perfect tensors associated with $\{4m+1, k\}$ tilings. The central charges for these general cases are computed in Appendix B. The results for $m = 1, 2, 3$, i.e., the hyperbolic pentagon code and the block-perfect *nonagon* and *tridecagon codes*, are shown in Fig. 7. For all of these codes, the central charges saturate to their maximum allowed value at large k , with a slope at small k similar to the Brown-Henneaux value. Explicitly, at large n and k both the central charge bound and the exact Majorana dimer value scale as

$$c_{\{4m+1, k\}}^d = c_{\{4m+1, k\}}^{\max} = \frac{(6m + \frac{9}{2}) \ln \chi}{\ln[(4k - 8)m - k]} + O(m^{-1}), \quad (54)$$

with a bond dimension $\chi = 2$ for the dimer model. Thus, we conclude that for tilings with high curvature (large n and k), our class of hyperbolic block-perfect codes based on Majorana dimers produce maximal entanglement for any connected boundary region A . This is equivalent to a statement that *residual bulk regions* become negligible in this limit, with a maximal flow of entanglement through the minimal cut γ_A .

VII. DISCRETE CONFORMAL TRANSFORMATIONS

In our analysis of central charges of discrete critical systems, we only considered the behavior of boundary states under *global* scaling transformations, corresponding to an application of inflation rules on all boundary sites at once. However, global scaling transformations only form a subset of the conformal algebra. To study the remaining symmetries, we can equivalently consider the bulk symmetries [25]; in our time-slice case, these are the symmetries of the Poincaré disk (5). Whereas the original AdS space-time (3) enjoys an

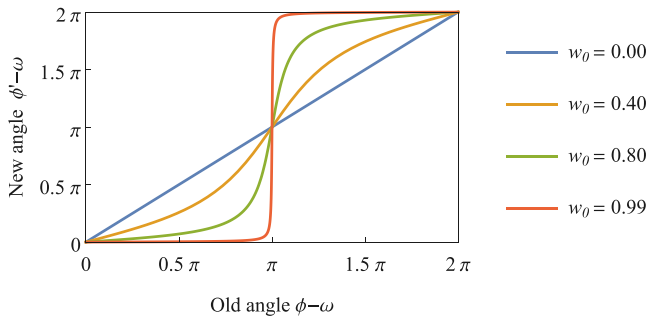


FIG. 8. Local scale transformation of Poincaré disk angle ϕ on the boundary under a translation in the bulk.

$SO(2, 2)$ symmetry [most apparent in its embedding as a hyperboloid in $(2+2)$ -dimensional flat space-time], the Poincaré disk is only invariant under $PSL(2, \mathbb{R})$ transformations, a subset of the *Möbius transformations*. If we represent a point in the disk as a complex number $z = \rho e^{i\phi}$, then these transformations $M_{\theta, v}$ are given by

$$z \mapsto z' = M_{\theta, v}(z) = e^{i\theta} \frac{w + z}{1 + w^* z}, \quad (55)$$

where $0 \leq \theta < 2\pi$ and $w = w_0 e^{i\omega}$ defines a point in the Poincaré disk, i.e., with $|w| < 1$. We can see how these transformations act on the AdS boundary by taking the $\rho = \rho_0 \rightarrow 1$ limit. We find the following:

(1) A *global scale transformation* determined by a change in cutoff $\rho_0 \rightarrow \rho'_0$: The total length L of the flat AdS boundary changes as

$$L \mapsto L' = \frac{1 - \rho_0}{1 - \rho'_0} L, \quad (56)$$

assuming that ρ_0 and ρ'_0 are close to one.

(2) A *translation* $T_\theta = M_{\theta, 0}$ produced by a rotation of the Poincaré disk. Introducing the boundary coordinate $x = \alpha\phi/(1 - \rho_0)$, this corresponds to a transformation

$$x \mapsto x' = x + \frac{\alpha\theta}{1 - \rho_0}. \quad (57)$$

(3) A *local scale transformation* $D_w = M_{0, w}$ by shifting the center of the Poincaré disk towards a point $w = w_0 e^{i\omega} \neq 0$. Without loss of generality, we now assume that $\omega = 0$. At $\rho \rightarrow 1$, we then find a transformation of the Poincaré angle ϕ of the form

$$\phi \mapsto \phi' = \arctan \frac{(1 - w_0^2) \sin \phi}{(1 + w_0^2) \cos \phi + 2w_0}. \quad (58)$$

This transformation is shown in Fig. 8 for different values of w_0 and general ω . Lengths around the boundary point $x = \alpha\omega/(1 - \rho_0)$ are stretched to

$$x \mapsto x' = \frac{1 + w_0}{1 - w_0} x, \quad (59)$$

while those around $y = \alpha(\pi + \omega)/(1 - \rho_0)$ are contracted to

$$y \mapsto y' = \frac{1 - w_0}{1 + w_0} y. \quad (60)$$

We can rewrite any combination of translations and local scale transformations as a single Möbius transformation $M_{\theta, v} = T_\theta \circ D_v$ by using the identities

$$T_\theta \circ T_\phi = T_{\theta+\phi}, \quad (61a)$$

$$D_v \circ D_w = T_{\arg \frac{1+wv^*}{1+v^*w}} \circ D_{\frac{v+w}{1+v^*w}}, \quad (61b)$$

$$D_v \circ T_\theta = T_\theta \circ D_{e^{-i\theta}v}. \quad (61c)$$

All transformations considered so far preserve orientation. If we drop this constraint, we also find the following:

(1) An *inversion* $I_{v, \theta}$ through a bulk reflection around a geodesic through a point v at normal angle θ , expressed with the complex conjugate $C(z) = z^*$ as

$$\begin{aligned} z \mapsto I_{v, \theta}(z) &= D_v \circ T_\theta \circ C \circ T_{-\theta} \circ D_{-v}(z) \\ &= D_{-v} \circ T_{-2\theta} \circ D_{v^*} \circ C(z). \end{aligned} \quad (62)$$

Note that $I_{v, \theta}^2 = \mathbb{1}$, and that any inversion is equivalent to complex conjugation and a Möbius transformation. For a boundary coordinate system centered around a boundary angle $\phi = 0$ and “infinity” identified as $\phi = \pi$, we choose $v = x$ with $x \in \mathbb{R}$ and $\theta = -\pi/2$, leading to a *canonical inversion*

$$\begin{aligned} z \mapsto I_x(z) &= D_{2x/(1+x^2)} \circ T_\pi \circ C(z) \\ &= C \circ T_\pi \circ D_{-2x/(1+x^2)}(z). \end{aligned} \quad (63)$$

(2) By combining inversion and translation, we can also construct the *special conformal transformation*

$$\begin{aligned} z \mapsto K_{\theta, x}(z) &= I_x \circ T_\theta \circ I_x(z) \\ &= D_{2x/(1+x^2)} T_{-\theta} D_{-2x/(1+x^2)}(z), \end{aligned} \quad (64)$$

which is just an (orientation-preserving) Möbius transformation.

Discretizing the Poincaré disk with a (regular) tiling breaks these continuous symmetries. First consider global and local scaling transformations. Rather than a continuous transformation (56), global inflation (Fig. 9, top) rescales the subsystem by an asymptotic constant λ , the eigenvalue of the substitution matrix for the given tiling. When a tensor network is embedded into a regular tiling, choosing identical tensors that are invariant under cyclic permutations of indices, thus preserving the tiling symmetries, leads to boundary states that can be fine- or coarse-grained by any power of λ under inflation or deflation.

Next, consider the local scale transformations: A regular tiling is invariant only under those bulk Möbius transformations that map tiles onto tiles. As shown in Fig. 9 (center), this requires a combination of bulk translation and rotation. At finite cutoff, i.e., finite number of tiles, this reduces the density of boundary edges in one region of the boundary while increasing it in the opposing region, just as for the continuous case shown in Fig. 8.

Finally, special conformal transformations are broken down into two parts, as they can be composed of inversions and translations: We previously constructed inversions through a bulk reflection around a geodesic, while in a $\{n, k\}$ tiling such transformations only leave the lattice invariant if we reflect around its (geodesic) *edges*. Furthermore, translations are broken down to \mathbb{Z}_n and \mathbb{Z}_k rotations when centering the lattice around tiles and vertices, respectively. The resulting

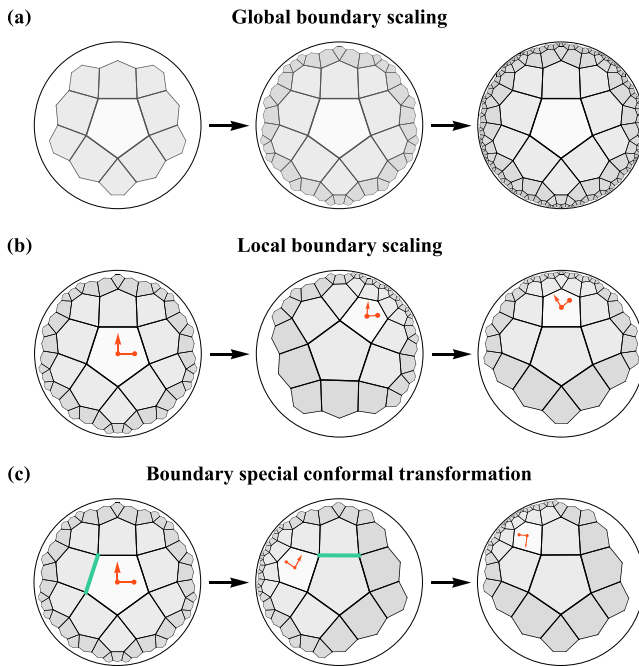


FIG. 9. (a) Global scale transformation by growing the hyperbolic bulk tiling through *vertex inflation*. (b) Local scale transformation by a Möbius transformation composed of a bulk translation (first step) and a rotation (second step). (c) Successive reflections around a bulk edge and its tiling-symmetric rotation (green lines), with the same effect as a Möbius transformation.

transformation, shown in Fig. 9 (bottom), is again equivalent to a bulk translation and rotation, yielding no new symmetries. Note that while exact translation invariance is broken, the quasiregular structure of the boundary still exhibits *self-similarity* between any sufficiently large subsystems [27].

To exemplify these invariance properties with actual states, consider the $\{5, 4\}$ HyPeC in Majorana dimers. By projecting the dimer endpoints on the Poincaré disk boundary, we can directly compare the states at different cutoffs, as shown in Fig. 10. A global scale transformation increases the resolution of the dimer pattern evenly on the boundary, while a local scale transformation changes it unevenly (Fig. 10, bottom). At the same time, the correlation structure of the boundary states is preserved. The local scale transformation produced by a bulk Möbius transformation can be seen as a special case of a local application of inflation and deflation rules. Suitable combinations of such local and global scalings are equivalent to an inflation rule applied only to a subsystem of the boundary, leaving the remainder unchanged. Note that these transformations are independent from the the actual choice of inflation rule, which fixes the boundary central charge.

VIII. DISCUSSION

In this work we have studied the entanglement entropy scaling of boundary states of generic hyperbolic tensor networks based on regular tilings. This has allowed us to derive a maximal central charge c^{\max} that such boundary states can possess, with a saturation of this bound corresponding to maximal entanglement through the bulk for any connected

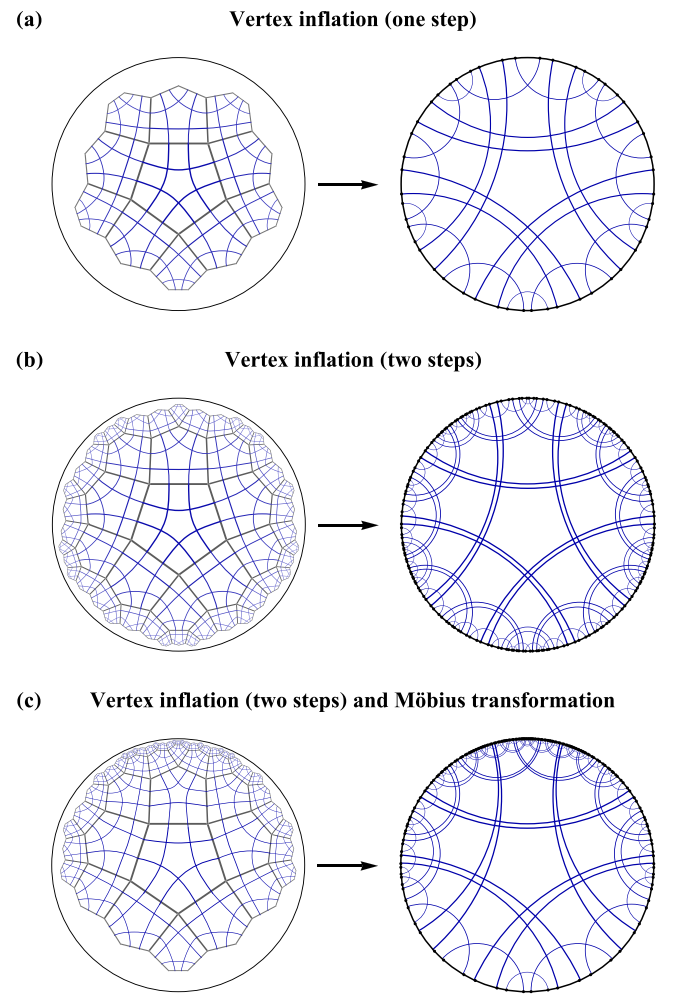


FIG. 10. (a) A contraction of a hyperbolic tensor network built from Majorana dimers (left) leads to a boundary Majorana dimer state (right). (b) An inflation step on the tiling (right) leads to a global scale transformation on the boundary state (right). (c) Certain combinations of Poincaré disk translations and rotations in the bulk (left) produce a local scaling transformation on the boundary state (right).

boundary region. We have then related c^{\max} to the radius of curvature α of the metric into which the tiling is embedded, leading to a discrete analog of the continuum BH formula, where we have identified the gravitational constant G via the RT prescription. We find that these bounds are always *above* the continuum value, i.e., that bulk entanglement through a regular hyperbolic tensor network can be as large as through a continuum AdS time slice. We have further identified two distinctly different regimes: At large AdS radius α and central charge c^{\max} , where the RT identification of G is expected to hold, we find an approximate relationship

$$c^{\max} \approx c_0 + 6 \frac{\alpha \ln \chi}{s}, \quad (65)$$

where s is the geodesic length of each edge in the tiling and χ the bond dimension of the tensor network embedded into the tiling. The constant c_0 , which produces an offset compared to the BH formula, depends on the n -gon tiling and increases

TABLE II. Relative depth of vertex neighbors to the left and right of a given vertex with depth d .

Type	a_1	a_2	a_3	a_4	a_5	$b = b_1$	b_2	b_3
d_L	$d - 1$	$d - 1$	$d + 1$	$d - 1$	d	$d + 1$	$d + 1$	d
d_R	$d - 1$	$d + 1$	$d - 1$	d	$d - 1$	$d + 1$	d	$d + 1$

with n . As the hyperbolic area of a single n -gon increases with n as well but remains finite at large k , we may interpret c_0 as counting the additional degrees in each n -gon in the coarse-grained lattice compared to the continuous Poincaré disk. In the opposite limit at small α and c , however, we identify a linear relationship without an offset,

$$c^{\max} \approx f_n \frac{\alpha \ln \chi}{s}, \quad (66)$$

where the tiling-dependent constant f_n increases with n , taking its lowest value $f_3 = 12$ for triangular tilings.

Furthermore, we find a specific holographic tensor network model that saturates these bounds: The HyPeC code, a toy model for quantum error correction in AdS/CFT. This model as well as its generalizations can be expressed in the fermionic language of Majorana dimers, which allows for an exact treatment of its entanglement structure in terms of paired Majorana modes. Using this picture, we showed how successively larger contractions of the tensor network produce a strong disorder renormalization group flow. This allowed us to endow a class of models of holographic quantum error correction with the notion of a discretized conformal field theory with aperiodic structure. The exact central charges resulting from this physical CFT interpretation were derived and shown to saturate to c^{\max} at large curvature.

Our approach advances the understanding of boundary states of holographic tensor network models, with bounds on central charges for any model based on a regular bulk geometry, which includes the HaPPY holographic codes [17], block-perfect CSS codes [21], holographic codes on ideal regular tilings [20], hyperinvariant tensor networks [18], random tensor networks on fixed backgrounds [40], and p -adic AdS/CFT models [41], whose Bruhat-Tits tree is identified with a regular tiling [42]. Note that our procedure reverses the approach of dynamically reconstructing a discrete bulk

geometry from the entanglement structure of a given boundary state, such as considered in Refs. [43,44]; instead, we started with a bulk geometry and derived constraints on the boundary entanglement. We have also shown that the formulation of quantum error correcting codes in terms of Majorana dimers is essential for understanding their boundary states and RG flow. The boundary states of these dimer models extend the properties of widely studied aperiodic singlet models to fractional fermionic modes with similar entanglement and RG properties, suggesting that both approaches are representations of a more general class of aperiodic critical theories. While the Majorana dimer states are *noninteracting*, their use as a code basis in a quantum error correction code such as the HyPeC generally leads to *interacting boundary states* whose correlations and entanglement structure follow those of the noninteracting basis states. Our results thus show that entanglement renormalization of CFTs can be performed with tensor network approaches other than the MERA, realizing geometries that can be more naturally embedded into an AdS time slice. Understanding their discrete symmetries will be crucial for the development of more powerful tensor network models of AdS/CFT.

ACKNOWLEDGMENTS

We thank Marek Gluza, Xiaoliang Qi, Sukhbinder Singh, Tadashi Takayanagi, and Charlotte Verhoeven for helpful comments and discussions. This work has been supported by the Studienstiftung des Deutschen Volkes, the John Templeton Foundation, the János Bolyai Scholarship, the DFG (CRC 183, EI 519/15-1), the NKFIH (Grants No. K124351, No. K124152, and No. K124176), the Hungarian Quantum Technology National Excellence Program (Project No. 2017-1.2.1-NKP-2017-00001), and the Foundational Questions Institute (FQXi).

APPENDIX A: GEODESIC INFLATION

In order to build inflation rules for regular tilings that inflate vertices on radial geodesics, we need to label vertices by their graph distance d to the center of the tiling, or *depth*. For an $\{n, k\}$ tiling with $n > 5$ and $k > 3$, we first distinguish between a vertices, which have two neighboring vertices (up to the given inflation layer), and b vertices, which have three. Within the sequence of vertices at a given layer, we consider the depths d_L and d_R of the neighbors to the left and right with respect to the depth d of a given vertex. For b vertices, $(d_L, d_R) = (d + 1, d + 1)$. However, we need to distinguish five types of a vertices, listed in Table II. For even $n = 2m$, only a_1 to a_3 appear, leading to an inflation rule

$$a_1 \mapsto a_3^{m-3} b (a_2^{m-2} a_1 a_3^{m-2} b)^{k-3} a_2^{m-3} a_1, \quad (A1)$$

$$a_2 \mapsto a_3^{m-3} b (a_2^{m-2} a_1 a_3^{m-2} b)^{k-3} a_2^{m-2} a_1, \quad (A2)$$

$$a_3 \mapsto a_3^{m-2} b (a_2^{m-2} a_1 a_3^{m-2} b)^{k-3} a_2^{m-3} a_1, \quad (A3)$$

$$b \mapsto a_3^{m-2} b (a_2^{m-2} a_1 a_3^{m-2} b)^{k-4} a_2^{m-2} a_1, \quad (A4)$$

and a corresponding substitution matrix

$$M_{\{2m,k\}} = \begin{pmatrix} k-2 & k(m-2)-2m+3 & k(m-2)-2m+3 & k-2 \\ k-2 & (k-2)(m-2) & k(m-2)-2m+3 & k-2 \\ k-2 & k(m-2)-2m+3 & (k-2)(m-2) & k-2 \\ k-3 & (k-3)(m-2) & (k-3)(m-2) & k-3 \end{pmatrix}. \quad (\text{A5})$$

The edge increase from inflation onto a b vertex is always 1, and increases with distance from the nearest b vertex. This is summarized in the entanglement matrix

$$E_{\{2m,k\}} = \begin{pmatrix} m + \frac{1}{2-k} & \frac{-2m^2+k(m-2)(m+1)+6}{2k(m-2)-4m+6} & \frac{-2m^2+k(m-2)(m+1)+6}{2k(m-2)-4m+6} & 1 \\ m & \frac{m+1}{2} & \frac{-2m^2+k(m-2)(m+1)+6}{2k(m-2)-4m+6} & 1 \\ m + \frac{1}{2-k} & \frac{-2m^2+k(m-2)(m+1)+6}{2k(m-2)-4m+6} & \frac{m+1}{2} & 1 \\ m & \frac{m+1}{2} & \frac{m+1}{2} & 1 \end{pmatrix}. \quad (\text{A6})$$

Applying (21) leads to the central charge bound

$$c_{\{2m,k\}} \leq c_{\{2m,k\}}^{\max} = \frac{3(m+1) \ln \chi}{\ln \{k(m-1) + \sqrt{(k-2)(m-1)[(k-2)m-k] - 2m+1}\}}, \quad (\text{A7})$$

where χ is the bond dimension of the underlying tensor network embedded into the $\{2m, k\}$ tiling. For odd $n = 2m+1$, the inflation rule is more complicated and includes all five types of a vertices,

$$a_1 \mapsto a_5 a_3^{m-3} b (a_2^{m-1} a_4 a_5 a_3^{m-1} b)^{k-3} a_2^{m-3} a_4, \quad (\text{A8})$$

$$a_2 \mapsto a_5 a_3^{m-3} b (a_2^{m-1} a_4 a_5 a_3^{m-1} b)^{k-3} a_2^{m-1} a_4, \quad (\text{A9})$$

$$a_3 \mapsto a_5 a_3^{m-1} b (a_2^{m-1} a_4 a_5 a_3^{m-1} b)^{k-3} a_2^{m-3} a_4, \quad (\text{A10})$$

$$a_4 \mapsto a_3^{m-3} b (a_2^{m-1} a_4 a_5 a_3^{m-1} b)^{k-3} a_2^{m-1} a_1, \quad (\text{A11})$$

$$a_5 \mapsto a_5 a_3^{m-1} b (a_2^{m-1} a_4 a_5 a_3^{m-1} b)^{k-3} a_2^{m-3} a_4, \quad (\text{A12})$$

$$b \mapsto a_3^{m-1} b (a_2^{m-1} a_4 a_5 a_3^{m-1} b)^{k-4} a_2^{m-1} a_4. \quad (\text{A13})$$

This leads to a substitution matrix

$$M_{\{2m+1,k\}} = \begin{pmatrix} 0 & k(m-2)-2m+3 & k(m-2)-2m+3 & k-2 & k-2 & k-2 \\ 0 & (k-2)(m-2) & k(m-2)-2m+3 & k-2 & k-2 & k-2 \\ 0 & k(m-2)-2m+3 & (k-2)(m-2) & k-2 & k-2 & k-2 \\ 1 & (k-2)(m-2) & k(m-2)-2m+3 & k-3 & k-2 & k-2 \\ 0 & k(m-2)-2m+3 & (k-2)(m-2) & k-2 & k-3 & k-2 \\ 0 & (k-3)(m-2) & (k-3)(m-2) & k-3 & k-3 & k-3 \end{pmatrix}. \quad (\text{A14})$$

The entanglement matrix is given by

$$E_{\{2m+1,k\}} = \begin{pmatrix} 0 & \frac{-2m^2+k(m-2)(m+1)+6}{2k(m-2)-4m+6} & \frac{-2m^2+k(m-2)(m+1)+6}{2k(m-2)-4m+6} & m + \frac{1}{2-k} & m + \frac{1}{2-k} & 1 \\ 0 & \frac{m+1}{2} & \frac{-2m^2+k(m-2)(m+1)+6}{2k(m-2)-4m+6} & m & m + \frac{1}{2-k} & 1 \\ 0 & \frac{-2m^2+k(m-2)(m+1)+6}{2k(m-2)-4m+6} & \frac{m+1}{2} & m + \frac{1}{2-k} & m & 1 \\ m & \frac{m+1}{2} & \frac{-2m^2+k(m-2)(m+1)+6}{2k(m-2)-4m+6} & m & m + \frac{1}{2-k} & 1 \\ 0 & \frac{-2m^2+k(m-2)(m+1)+6}{2k(m-2)-4m+6} & \frac{m+1}{2} & m + \frac{1}{2-k} & m & 1 \\ 0 & \frac{m+1}{2} & \frac{m+1}{2} & m & m & 1 \end{pmatrix}. \quad (\text{A15})$$

The resulting central charge bound is

$$c_{\{2m+1,k\}}^{\max} = \frac{3\left(m - \frac{1}{4m-2} + \frac{3}{2}\right) \ln \chi}{\ln \frac{2km + \sqrt{(-2km+k+4m)^2 - 4 - k - 4m}}{2}}. \quad (\text{A16})$$

Note that for large n , (A7) and (A16) lead to the same asymptotic behavior,

$$c_{\{n,k\}}^{\max} = \frac{(6+3n) \ln \chi}{2 \ln[2-2k+(k-2)n]} + O(n^{-1}). \quad (\text{A17})$$

For $\{n, 3\}$ tilings (hyperbolic for $n > 6$), we also need to distinguish between even and odd n . In the case $n = 2m$, we find the inflation rule

$$a_1 \mapsto a_3^{m-3} b a_2^{m-3} a_1, \quad (\text{A18})$$

$$a_2 \mapsto a_3^{m-3} b a_2^{m-2} a_1, \quad (\text{A19})$$

$$a_3 \mapsto a_3^{m-2} b a_2^{m-3} a_1, \quad (\text{A20})$$

$$b \mapsto \emptyset, \quad (\text{A21})$$

and the substitution and entanglement matrices

$$M_{\{2m,3\}} = \begin{pmatrix} 1 & m-3 & m-3 & 1 \\ 1 & m-2 & m-3 & 1 \\ 1 & m-3 & m-2 & 1 \\ 0 & 0 & 0 & 0 \end{pmatrix}, \quad E_{\{2m,3\}} = \begin{pmatrix} m-1 & \frac{m}{2} & \frac{m}{2} & 1 \\ m & \frac{m+1}{2} & \frac{m}{2} & 1 \\ m-1 & \frac{m}{2} & \frac{m+1}{2} & 1 \\ 0 & 0 & 0 & 0 \end{pmatrix}. \quad (\text{A22})$$

This yields a maximum central charge

$$c_{\{2m,3\}}^{\max} = \frac{3(m+1) \ln \chi}{\ln(\sqrt{m^2 - 4m + 3} + m - 2)}. \quad (\text{A23})$$

For odd $n = 2m + 1$, inflation again involves a_1 to a_5 :

$$a_1 \mapsto a_5 a_3^{m-3} b a_2^{m-3} a_4, \quad (\text{A24})$$

$$a_2 \mapsto a_5 a_3^{m-3} b a_2^{m-2} a_4, \quad (\text{A25})$$

$$a_3 \mapsto a_5 a_3^{m-2} b a_2^{m-3} a_4, \quad (\text{A26})$$

$$a_4 \mapsto a_5 a_3^{m-3} b a_2^{m-2} a_1, \quad (\text{A27})$$

$$a_5 \mapsto a_3^{m-2} b a_2^{m-3} a_4, \quad (\text{A28})$$

$$b \mapsto \emptyset. \quad (\text{A29})$$

This corresponds to

$$M_{\{2m+1,3\}} = \begin{pmatrix} 0 & m-3 & m-3 & 1 & 1 & 1 \\ 0 & m-2 & m-3 & 1 & 1 & 1 \\ 0 & m-3 & m-2 & 1 & 1 & 1 \\ 1 & m-2 & m-3 & 0 & 1 & 1 \\ 0 & m-3 & m-2 & 1 & 0 & 1 \\ 0 & 0 & 0 & 0 & 0 & 0 \end{pmatrix}, \quad (\text{A30})$$

$$E_{\{2m+1,3\}} = \begin{pmatrix} 0 & \frac{m}{2} & \frac{m}{2} & m-1 & m-1 & 1 \\ 0 & \frac{m+1}{2} & \frac{m}{2} & m & m-1 & 1 \\ 0 & \frac{m}{2} & \frac{m+1}{2} & m-1 & m & 1 \\ m & \frac{m+1}{2} & \frac{m}{2} & 0 & m-1 & 1 \\ 0 & \frac{m}{2} & \frac{m+1}{2} & m-1 & 0 & 1 \\ 0 & 0 & 0 & 0 & 0 & 0 \end{pmatrix}, \quad (\text{A31})$$

and gives a central charge bound of

$$c_{\{2m+1,3\}}^{\max} = \frac{3(m - \frac{1}{4m-2} + \frac{3}{2}) \ln \chi}{\ln \frac{\sqrt{4m^2 - 12m + 5} + 2m - 3}{2}}. \quad (\text{A32})$$

Note that even though the inflation rules are different, the bounds (A23) and (A32) agree with the generic $\{n, k\}$ bounds (A7) and (A16) derived earlier. Similarly, the $\{n, k\}$ inflation rules for $n = 4$ and $n = 5$ are special, as well, but lead to the same bounds. The $n = 4$ case was already covered in the main text. For $n = 5$, we need to split up b vertices into three categories b_1 , b_2 , and b_3 . For $n = 5$, we find the inflation rules

$$a_1 \mapsto b_3 (a_2 a_3 b_1)^{k-4} a_2 a_3 b_2, \quad (\text{A33})$$

$$a_2 \mapsto b_3(a_2a_3b_1)^{k-4}a_2a_3b_1a_1, \tag{A34}$$

$$a_3 \mapsto b_1(a_2a_3b_1)^{k-4}a_2a_3b_2, \tag{A35}$$

$$b_1 \mapsto a_3b_1(a_2a_3b_1)^{k-4}a_2, \tag{A36}$$

$$b_2 \mapsto a_3b_1(a_2a_3b_1)^{k-4}a_1, \tag{A37}$$

$$b_3 \mapsto b_1(a_2a_3b_1)^{k-4}a_2, \tag{A38}$$

leading to substitution and entanglement matrices

$$M_{\{5,k\}} = \begin{pmatrix} 0 & k-3 & k-3 & k-4 & 1 & 1 \\ 1 & k-3 & k-3 & k-3 & 0 & 1 \\ 0 & k-3 & k-3 & k-3 & 1 & 0 \\ 0 & k-3 & k-3 & k-3 & 0 & 0 \\ 1 & k-4 & k-3 & k-3 & 0 & 0 \\ 0 & k-3 & k-4 & k-3 & 0 & 0 \end{pmatrix}, \quad E_{\{5,k\}} = \begin{pmatrix} 0 & 2 & 2 & 1 & 1 & 1 \\ 2 & 2 & 2 & 1 & 0 & 1 \\ 0 & 2 & 2 & 1 & 1 & 0 \\ 0 & 2 & 2 & 1 & 0 & 0 \\ 2 & 2 & 2 & 1 & 0 & 0 \\ 0 & 2 & 2 & 1 & 0 & 0 \end{pmatrix}. \tag{A39}$$

This yields the expected maximum central charge

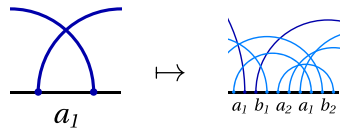
$$c_{\{5,k\}}^{\max} = \frac{10 \ln \chi}{\ln \frac{\sqrt{9k^2-48k+60}+3k-8}{2}}. \tag{A40}$$

APPENDIX B: MAJORANA DIMER POLYGON MODELS

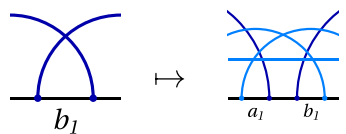
We can construct block-perfect Majorana dimer models for an $\{n, k\}$ tiling for $n = 4m+1, m \in \mathbb{N}$. The $n = 5$ case is simply the HyPeC model. In the main text, we already computed its central charge under edge inflation, which we now generalize to vertex inflation. From (24), we find the inflation rule

$$a \mapsto abaab, \quad b \mapsto ab. \tag{B1}$$

Without loss of generality, we identify each letter with the edge on the left (clockwise) to the vertex it stands for. To distinguish dimer content, we need to designate four subletters a_1, a_2, b_1, b_2 . In terms of dimer diagrams, using the convention of (41), the inflation rule is given by



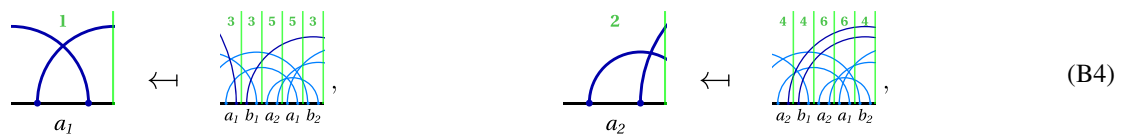
$$\tag{B2}$$



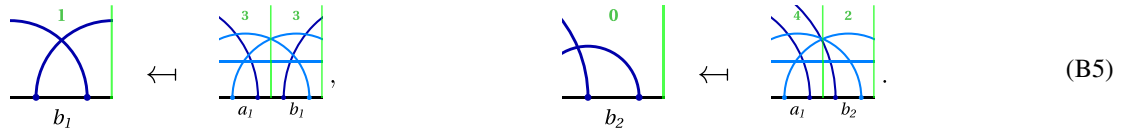
$$\tag{B3}$$

As in the main text, new dimers added at each step are drawn in a lighter color than those that are extended from the previous layer. Note that each inflated dimer configuration contains two open dimers on either end of the sequence that connect to the previous and following sequence within the layer added in a vertex inflation step. The full dimer configuration in the Poincaré disk is shown in Fig. 6 (top) along with the dimers at the first three inflation layers. When starting from the central pentagon, the initial sequence is given by $(a_1)^5$.

Again, we calculate the central charge by considering the loss of local entanglement through deflation. The corresponding cuts (green lines) and the number of dimers passing through it (green number) are given by



$$\tag{B4}$$



These diagrams lead us to the substitution and entanglement matrices M and E of the Markov process of the form

$$M = \begin{pmatrix} 2 & 1 & 1 & 1 \\ 1 & 2 & 1 & 1 \\ 1 & 0 & 1 & 0 \\ 1 & 0 & 0 & 1 \end{pmatrix}, \quad E = \begin{pmatrix} \frac{3}{2} & 2 & 1 & 1 \\ 2 & \frac{3}{2} & 1 & 1 \\ 1 & 0 & 1 & 0 \\ 2 & 0 & 0 & 1 \end{pmatrix}. \quad (B6)$$

Turning (21) into an equality, we find the effective central charge

$$c_{\{5,4\}}^d = \frac{9 \ln 2}{\ln(\sqrt{3} + 2)} \approx 4.74. \quad (B7)$$

Note that this result is *larger* than $c_{\{5,4\}_e}^d$ from (53), our result for edge inflation. Instead of a $\{5, 4\}$ tiling, we can also consider a general $\{5, k\}$ tiling with $k > 3$, using the same perfect tensors on each tile. This corresponds to a vertex inflation rule

$$a_1 \mapsto a_1 b_1 (a_2 a_1 b_2)^{k-3}, \quad b_1 \mapsto a_1 b_1 (a_2 a_1 b_2)^{k-4}, \quad (B8)$$

$$a_2 \mapsto a_2 b_1 (a_2 a_1 b_2)^{k-3}, \quad b_2 \mapsto a_1 b_2 (a_2 a_1 b_2)^{k-4}. \quad (B9)$$

The substitution and entanglement matrices then take the more general form

$$M = \begin{pmatrix} k-2 & k-3 & 1 & k-3 \\ k-3 & k-2 & 1 & k-3 \\ k-3 & k-4 & 1 & k-4 \\ k-3 & k-4 & 0 & k-3 \end{pmatrix}, \quad (B10)$$

and

$$E = \begin{pmatrix} \frac{1+2(k-3)}{1+k-3} & 2 & 1 & 1 \\ 2 & \frac{1+2(k-3)}{1+k-3} & 1 & 1 \\ \frac{1+2(k-4)}{1+k-4} & 2 & 1 & 1 \\ 2 & 2 & 0 & 1 \end{pmatrix}. \quad (B11)$$

This leads us to the central charge

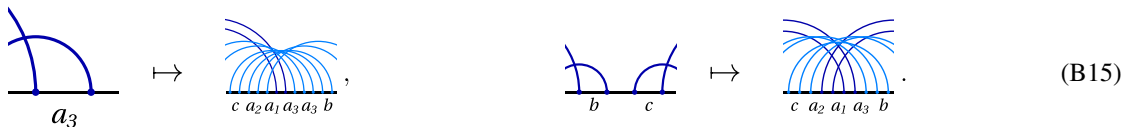
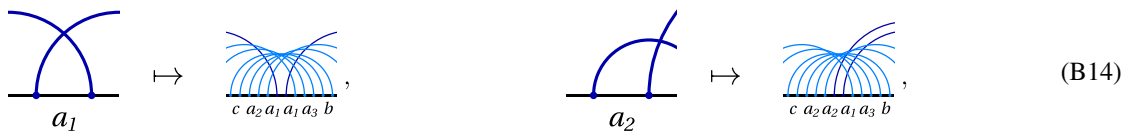
$$c_{\{5,k\}}^d = \frac{(\frac{2}{10-3k} + 10) \ln 2}{\ln \left[\frac{1}{2} (\sqrt{9k^2 - 48k + 60} + 3k - 8) \right]}. \quad (B12)$$

Note that this model corresponds to a bond dimension $\chi = 2$, hence the $\ln 2$ term in the numerator. Considering the large k limit, we find

$$c_{\{5,k\}}^d = \frac{10 \ln 2}{\ln(3k - 8)} + O(k^{-1}), \quad (B13)$$

which is exactly the same limit as the geodesic bound on central charges (Table I). As shown in Fig. 7, this saturation occurs quickly as k is increased.

For $n = 9$ and more complex polygons, we have to distinguish two cases: If $k = 3$, the inflation rule requires five different types of letters, while only four are needed in the $k > 3$ case. The inflation rule for the $\{9, 3\}$ tiling with dimer states (43) follows from (25) and is given by the following dimer substitutions:



The inflation rule for the letters b and c has been combined for the sake of simplicity. The entanglement change under deflation depends on the cut and is given by

$$\begin{array}{ccc} \begin{array}{c} 1 \\ \text{---} \\ a_1 \end{array} & \leftarrow & \begin{array}{c} 5 \ 7 \ 7 \ 7 \ 5 \ 3 \\ \text{---} \\ c \ a_2 \ a_1 \ a_3 \ b \end{array}, \\ \begin{array}{c} 2 \\ \text{---} \\ a_2 \end{array} & \leftarrow & \begin{array}{c} 4 \ 6 \ 8 \ 8 \ 6 \ 4 \\ \text{---} \\ c \ a_2 \ a_2 \ a_1 \ a_3 \ b \end{array}, \end{array} \quad (\text{B16})$$

$$\begin{array}{ccc} \begin{array}{c} 0 \\ \text{---} \\ a_3 \end{array} & \leftarrow & \begin{array}{c} 6 \ 8 \ 8 \ 6 \ 4 \ 2 \\ \text{---} \\ c \ a_2 \ a_1 \ a_3 \ a_3 \ b \end{array}, \\ \begin{array}{c} 0 \\ \text{---} \\ b \quad c \end{array} & \leftarrow & \begin{array}{c} 6 \ 8 \ 8 \ 6 \ 4 \\ \text{---} \\ c \ a_2 \ a_1 \ a_3 \ b \end{array}. \end{array} \quad (\text{B17})$$

The substitution and entanglement matrices follow accordingly,

$$M = \begin{pmatrix} 2 & 1 & 1 & 1 & 1 \\ 1 & 2 & 1 & 1 & 1 \\ 1 & 1 & 2 & 1 & 1 \\ 1 & 1 & 1 & 1 & 1 \\ 0 & 0 & 0 & 0 & 0 \end{pmatrix}, \quad E = \begin{pmatrix} 3 & 3 & 2 & 1 & 2 \\ 3 & \frac{5}{2} & 2 & 1 & 1 \\ 4 & 4 & \frac{5}{2} & 1 & 3 \\ 4 & 4 & 3 & 2 & 3 \\ 0 & 0 & 0 & 0 & 0 \end{pmatrix}, \quad (\text{B18})$$

which leads to a central charge

$$c_{\{9,3\}}^d = \frac{16 \ln 2}{\ln \frac{\sqrt{21}+5}{2}} \approx 7.08. \quad (\text{B19})$$

We can generalize this result to tilings at higher $n = 4m+1$, which correspond to an inflation rule

$$a_1 \mapsto ca_2^{2m-3}a_1a_3^{2m-3}b, \quad b \mapsto ca_2^{2m-3}a_1a_3^{2m-3}b, \quad (\text{B20})$$

$$a_2 \mapsto ca_2^{2m-2}a_1a_3^{2m-3}b, \quad c \mapsto \emptyset, \quad (\text{B21})$$

$$a_3 \mapsto ca_2^{2m-3}a_1a_3^{2m-2}b. \quad (\text{B22})$$

The matrices M and E then take the form

$$M = \begin{pmatrix} 2 & 2m-3 & 2m-3 & 1 & 1 \\ 1 & 2m-2 & 2m-3 & 1 & 1 \\ 1 & 2m-3 & 2m-2 & 1 & 1 \\ 1 & 2m-3 & 2m-3 & 1 & 1 \\ 0 & 0 & 0 & 0 & 0 \end{pmatrix}, \quad E = \begin{pmatrix} 2m-1 & m+1 & m & 1 & 2 \\ 2m-1 & m+\frac{1}{2} & m & 1 & 1 \\ 2m & m+\frac{1}{2} & m+\frac{1}{2} & 1 & 3 \\ 2m & m+2 & m+\frac{1}{2} & 2 & 3 \\ 0 & 0 & 0 & 0 & 0 \end{pmatrix}. \quad (\text{B23})$$

From this we find the central charge

$$c_{\{4m+1,3\}}^d = \frac{(6m + \frac{3}{10-8m} + \frac{9}{2}) \ln 2}{\ln \frac{\sqrt{16m^2-24m+5}+4m-3}{2}}. \quad (\text{B24})$$

Now consider the cases $n = 4m+1, k > 3$, which correspond to the inflation rules

$$a_1 \mapsto a_2^{2m-2}a_1a_3^{2m-3}b(a_2^{2m-1}a_1a_3^{2m-2}b)^{k-3}, \quad (\text{B25})$$

$$a_2 \mapsto a_2^{2m-1}a_1a_3^{2m-3}b(a_2^{2m-1}a_1a_3^{2m-2}b)^{k-3}, \quad (\text{B26})$$

$$a_3 \mapsto a_2^{2m-2}a_1a_3^{2m-2}b(a_2^{2m-1}a_1a_3^{2m-2}b)^{k-3}, \quad (\text{B27})$$

$$b \mapsto a_2^{2m-2}a_1a_3^{2m-2}b(a_2^{2m-1}a_1a_3^{2m-2}b)^{k-4}. \quad (\text{B28})$$

We explicitly compute the $\{9, 4\}$ tiling, which can be expressed by the dimer inflation rules

$$\begin{array}{ccc} \begin{array}{c} \text{---} \\ a_1 \end{array} & \mapsto & \begin{array}{c} \text{---} \\ a_2 \ a_2 \ a_1 \ a_3 \ b \ a_2 \ a_2 \ a_1 \ a_3 \ a_3 \ b \end{array}, \\ \begin{array}{c} \text{---} \\ a_2 \end{array} & \mapsto & \begin{array}{c} \text{---} \\ a_2 \ a_2 \ a_2 \ a_1 \ a_3 \ b \ a_2 \ a_2 \ a_2 \ a_1 \ a_3 \ a_3 \ b \end{array}, \end{array} \quad (\text{B29})$$

(B30)

Under deflation, the letters correspond to the following cuts:

(B31)

(B32)

From this we construct the entanglement and substitution matrices

$$M = \begin{pmatrix} 3 & 5 & 3 & 2 \\ 2 & 6 & 3 & 2 \\ 2 & 5 & 4 & 2 \\ 1 & 2 & 2 & 1 \end{pmatrix}, \quad E = \begin{pmatrix} \frac{10}{3} & \frac{14}{5} & \frac{7}{3} & 1 \\ \frac{7}{2} & \frac{5}{2} & \frac{7}{3} & 1 \\ 4 & \frac{16}{5} & \frac{5}{2} & 1 \\ 4 & \frac{7}{2} & \frac{5}{2} & 1 \end{pmatrix}. \quad (B33)$$

We then find the central charge

$$c_{[9,4]}^d = \frac{81 \ln 2}{5 \ln(\sqrt{35} + 6)} \approx 4.53. \quad (B34)$$

For arbitrary k , we find

$$M = \begin{pmatrix} k-1 & 3k-7 & 2k-5 & k-2 \\ k-2 & 3(k-2) & 2k-5 & k-2 \\ k-2 & 3k-7 & 2(k-2) & k-2 \\ k-3 & 3k-10 & 2(k-3) & k-3 \end{pmatrix}, \quad E = \begin{pmatrix} \frac{4k-6}{k-1} & \frac{22-9k}{7-3k} & \frac{13-5k}{5-2k} & 1 \\ \frac{4k-9}{k-2} & \frac{3k-7}{k-2} & \frac{13-5k}{5-2k} & 1 \\ 4 & \frac{20-9k}{7-3k} & \frac{5}{2} & 1 \\ 4 & \frac{29-9k}{10-3k} & \frac{5}{2} & 1 \end{pmatrix}, \quad (B35)$$

leading to

$$c_{[9,k]}^d = \frac{6 \frac{19k-49}{7k-18} \ln 2}{\ln \frac{\sqrt{49k^2-224k+252}+7k-16}{2}}. \quad (B36)$$

Generalizing even further to arbitrary $n = 4m+1$ yields the matrices

$$M = \begin{pmatrix} k-1 & -4m+k(2m-1)+1 & 2k(m-1)-4m+3 & k-2 \\ k-2 & (k-2)(2m-1) & 2k(m-1)-4m+3 & k-2 \\ k-2 & -4m+k(2m-1)+1 & 2(k-2)(m-1) & k-2 \\ k-3 & -6m+k(2m-1)+2 & 2(k-3)(m-1) & k-3 \end{pmatrix}, \quad (B37)$$

$$E = \begin{pmatrix} 2m - \frac{2}{k-1} & \frac{-4m(m+1)+k(2m^2+m-1)+2}{-k+2(k-2)m+1} & \frac{-4m^2+k(m-1)(2m+1)+3}{2k(m-1)-4m+3} & 1 \\ 2m + \frac{1}{2-k} & \frac{k-3}{k-2} + m & \frac{-4m^2+k(m-1)(2m+1)+3}{2k(m-1)-4m+3} & 1 \\ 2m & \frac{2(k-2)m^2+(k-2)m-k}{-k+2(k-2)m+1} & m + \frac{1}{2} & 1 \\ 2m & \frac{2(k-3)m^2+(k-3)m-k+1}{-k+2(k-3)m+2} & m + \frac{1}{2} & 1 \end{pmatrix}. \quad (B38)$$

Finally, the central charge for the $\{4m+1, k\}$ (block) perfect Majorana dimer model for $m \geq 1, k \geq 4$ follows as

$$c_{\{4m+1, k\}}^d = \frac{6 \left(\frac{-3km+k+6m+1}{-4km+k+8m+2} + m \right) \ln 2}{\ln \frac{4km + \sqrt{(-4km+k+8m)^2 - 4 - k - 8m}}{2}}. \quad (\text{B39})$$

In the large k limit the central charge behaves as

$$c_{\{4m+1, k\}}^d = \frac{6 \frac{(4m^2+2m-1)}{4m-1} \ln 2}{\ln[(4m-1)k - 8m]} + O(k^{-1}). \quad (\text{B40})$$

-
- [1] J. M. Maldacena, *Int. J. Theor. Phys.* **38**, 1113 (1999); *Adv. Theor. Math. Phys.* **2**, 231 (1997).
- [2] E. Witten, *Adv. Theor. Math. Phys.* **2**, 253 (1998).
- [3] J. D. Bekenstein, *Phys. Rev. D* **7**, 2333 (1973).
- [4] S. W. Hawking, *Commun. Math. Phys.* **43**, 199 (1975).
- [5] J. Eisert, M. Cramer, and M. B. Plenio, *Rev. Mod. Phys.* **82**, 277 (2010).
- [6] S. Ryu and T. Takayanagi, *Phys. Rev. Lett.* **96**, 181602 (2006).
- [7] R. Orús, *Ann. Phys.* **349**, 117 (2014).
- [8] F. Verstraete, J. I. Cirac, and V. Murg, *Adv. Phys.* **57**, 143 (2008).
- [9] N. Schuch, *Quantum Information Processing: Lecture Notes of the 44th IFF Spring School 2013* (Forschungszentrum, Jülich, 2013).
- [10] J. C. Bridgeman and C. T. Chubb, *J. Phys. A* **50**, 223001 (2017).
- [11] G. Vidal, *Phys. Rev. Lett.* **101**, 110501 (2008).
- [12] B. Swingle, *Phys. Rev. D* **86**, 065007 (2012).
- [13] S. Singh, *Phys. Rev. D* **97**, 026012 (2018).
- [14] C. Beny, *New J. Phys.* **15**, 023020 (2013).
- [15] N. Bao, C. J. Cao, S. M. Carroll, A. Chatwin-Davies, N. Hunter-Jones, J. Pollack, and G. N. Remmen, *Phys. Rev. D* **91**, 125036 (2015).
- [16] A. Milsted and G. Vidal, [arXiv:1812.00529](https://arxiv.org/abs/1812.00529).
- [17] F. Pastawski, B. Yoshida, D. Harlow, and J. Preskill, *J. High Energy Phys.* **06** (2015) 149.
- [18] G. Evenbly, *Phys. Rev. Lett.* **119**, 141602 (2017).
- [19] A. Jahn, M. Gluza, F. Pastawski, and J. Eisert, *Sci. Adv.* **5**, eaaw0092 (2019).
- [20] T. J. Osborne and D. E. Stiegemann, *J. High Energy Phys.* **04** (2020) 154.
- [21] R. J. Harris, N. A. McMahon, G. K. Brennen, and T. M. Stace, *Phys. Rev. A* **98**, 052301 (2018).
- [22] T. Kohler and T. Cubitt, *J. High Energy Phys.* **08** (2019) 017.
- [23] A. Jahn, M. Gluza, F. Pastawski, and J. Eisert, *Phys. Rev. Res.* **1**, 033079 (2019).
- [24] A. Almheiri, X. Dong, and D. Harlow, *J. High Energy Phys.* **04** (2015) 163.
- [25] J. D. Brown and M. Henneaux, *Commun. Math. Phys.* **104**, 207 (1986).
- [26] P. Calabrese and J. L. Cardy, *J. Stat. Mech.* (2004) P06002.
- [27] L. Boyle, M. Dickens, and F. Flicker, *Phys. Rev. X* **10**, 011009 (2020).
- [28] S.-K. Ma, C. Dasgupta, and C.-K. Hu, *Phys. Rev. Lett.* **43**, 1434 (1979).
- [29] D. S. Fisher, *Phys. Rev. Lett.* **69**, 534 (1992).
- [30] G. Refael and E. Altman, *C. R. Phys.* **14**, 725 (2013).
- [31] D. Pekker, G. Refael, E. Altman, E. Demler, and V. Oganesyan, *Phys. Rev. X* **4**, 011052 (2014).
- [32] W. Berdanier, M. Kolodrubetz, S. A. Parameswaran, and R. Vasseur, *Proc. Natl. Acad. Sci. U. S. A.* **115**, 9491 (2018).
- [33] V. Alba, S. N. Santalla, P. Ruggiero, J. Rodriguez-Laguna, P. Calabrese, and G. Sierra, *J. Stat. Mech.* **2019**, 023105 (2019).
- [34] F. Iglói and C. Monthus, *Eur. Phys. J. B* **91**, 290 (2018).
- [35] R. Juhász and Z. Zimborás, *J. Stat. Mech.* **04** (2007) P04004.
- [36] F. Iglói, R. Juhász, and Z. Zimborás, *Europhys. Lett.* **79**, 37001 (2007).
- [37] G. Vidal, *Phys. Rev. Lett.* **99**, 220405 (2007).
- [38] C. H. Bennett, D. P. DiVincenzo, J. A. Smolin, and W. K. Wootters, *Phys. Rev. A* **54**, 3824 (1996).
- [39] R. Laflamme, C. Miquel, J. P. Paz, and W. H. Zurek, *Phys. Rev. Lett.* **77**, 198 (1996).
- [40] P. Hayden, S. Nezami, X.-L. Qi, N. Thomas, M. Walter, and Z. Yang, *J. High Energy Phys.* **11** (2016) 009.
- [41] S. S. Gubser, J. Knaute, S. Parikh, A. Samberg, and P. Witaszczyk, *Commun. Math. Phys.* **352**, 1019 (2017).
- [42] M. Heydeman, M. Marcolli, I. Saberi, and B. Stoica, *Adv. Theor. Math. Phys.* **22**, 93 (2018).
- [43] N. Bao, G. Penington, J. Sorce, and A. C. Wall, *J. High Energy Phys.* **11** (2020) 69.
- [44] N. Bao, G. Penington, J. Sorce, and A. C. Wall, [arXiv:1902.10157](https://arxiv.org/abs/1902.10157).

Chapter 5

Concluding remarks

The confluence of quantum information and high-energy theory has led to exciting new research directions and will likely stimulate theoretical physics for years to come. Progress in these directions is still exploratory and many steps are taken in uncertainty of the eventual destination. Will the foray of quantum information into fundamental physics simply develop into another branch of methods to study quantum field theory, similar to how canonical quantization and Feynman diagram techniques already offer distinct approaches to the same underlying theoretical object? Or will quantum information itself form the foundation on which progress towards the fundamental questions of physics is made? Whatever the future holds, it appears that many boundaries between traditional subfields will need to be eroded to advance our understanding of nature beyond its current bounds.

During my doctoral research, I was fortunate to be exposed to ideas from many of these fields — even including subjects such as condensed matter physics and computer science — and to be given the chance to use them to build something new. The results may not amount to any grand discoveries, but they should illustrate how many avenues there are yet to be explored, and how much richness can come out of simple ingredients, such as contracted tensors and fermionic pairs. Indeed, compared to the mathematical finesse of string theory many new approaches from quantum information seem conceptually humble at first glance, though deep mathematical ideas are often hidden behind them. These new approaches, rather than its experimental applications in the shape of quantum computers, may well turn out to be quantum information's greatest contribution to modern physics, similar to how the invention of thermodynamics endowed physics with more than just an efficient description of steam engines.

The future of tensor networks, a topic which many of the preceding pages relate to, is certainly a bright one: They are already used for purposes far beyond the original one-dimensional quantum chains for which they were initially conceived, and will likely shape considerable portions of physics and computer science in the years to come. Some of the applications to holography, alluded to in the discussion sections of the

publications contained in this thesis, will likely enrich our understanding of conformal field theory and perhaps even shed light on the fundamental principles that give rise to AdS/CFT.

There are many people whose indispensable support of the work that led to this thesis ought to be acknowledged. Having been given the opportunity to work in a research group full of vibrant exchange between people with exciting ideas was tremendously helpful in taking my first steps as a scientist. In following my own interests and ideas, I am grateful to having been given great leeway and enormous support from my advisor, Prof. Jens Eisert, who taught me to turn my occasional strange ideas into publishable papers and share my results with others around the globe. I am also greatly thankful to Dr. Fernando Pastawski, who inspired many of the directions my research has taken and helped me keep the aforementioned strange ideas grounded. Marek Gluza, who taught me many tricks to tame fermions, greatly supported my HEP \rightarrow QI transition and pushed our projects ahead with countless ideas and suggestions. I greatly benefited from my many unexpected encounters with Prof. Zoltán Zimborás, which always led to fascinating discussions and sometimes to joint papers. During my 2018 stay in Japan, I was kindly hosted by Prof. Tadashi Takayanagi, who had already supervised my Master's thesis and later helped me develop its ideas into my first scientific paper. He and his group in Kyoto are a constant source of inspiration on quantum information and holography, and I am particularly obliged to Koji Umemoto and Dr. Arpan Bhattacharyya for their fruitful collaboration. I am also thankful to Prof. Robert Myers and Prof. Beni Yoshida, who hosted my visit at the Perimeter Institute for Theoretical Physics in spring 2020, a thoroughly enriching experience despite the restrictions imposed by a certain pandemic. During my three-year *Studienstiftung* fellowship, I was also part of the mentoring group of Prof. Irene Albers, who organized many opportunities for us to expand our knowledge beyond our field of specialization. Of the many inspiring discussions that have shaped my time as a doctoral student, I particularly wish to thank Andreas Bauer, Hugo Camargo, Prof. Pawel Caputa, Dr. Lucas Hackl, Prof. Michal Heller, Dr. Aleksander Kubica, Alexander Nietner, Prof. Xiaoliang Qi, Dr. Sukhbinder Singh, Matthew Steinberg, Dr. Nicholas Tarantino, Charlotte Verheoven, Prof. Michael Walter, Dr. Carolin Wille, Bennet Windt, and Han Yan for their contributions. Despite its public appearance, physics is very much a science of community rather than isolated individuals, and it is with their exchange that its ideas prosper and develop into something meaningful.

Bibliography

- [1] J. D. Bekenstein, “Black holes and entropy,” *Phys. Rev. D*, vol. 7, pp. 2333–2346, 1973. doi:10.1103/PhysRevD.7.2333.
- [2] S. W. Hawking, “Particle Creation by Black Holes,” *Commun. Math. Phys.*, vol. 43, pp. 199–220, 1975. doi:10.1007/BF02345020.
- [3] L. Susskind, “The World as a hologram,” *J. Math. Phys.*, vol. 36, pp. 6377–6396, 1995, arXiv:hep-th/9409089. doi:10.1063/1.531249.
- [4] G. 't Hooft, “Dimensional reduction in quantum gravity,” *Conf. Proc.*, vol. C930308, pp. 284–296, 1993, arXiv:gr-qc/9310026.
- [5] R. Bousso, “A Covariant entropy conjecture,” *JHEP*, vol. 07, p. 004, 1999, arXiv:hep-th/9905177. doi:10.1088/1126-6708/1999/07/004.
- [6] J. M. Maldacena, “The Large N limit of superconformal field theories and supergravity,” *Int. J. Theor. Phys.*, vol. 38, pp. 1113–1133, 1999, arXiv:hep-th/9711200. doi:10.1023/A:1026654312961.
- [7] A. Polyakov, “Quantum geometry of bosonic strings,” *Physics Letters B*, vol. 103, no. 3, pp. 207 – 210, 1981. doi:10.1016/0370-2693(81)90743-7.
- [8] F. Gliozzi, J. Scherk, and D. Olive, “Supersymmetry, supergravity theories and the dual spinor model,” *Nuclear Physics B*, vol. 122, no. 2, pp. 253 – 290, 1977. doi:10.1016/0550-3213(77)90206-1.
- [9] E. Witten, “String theory dynamics in various dimensions,” *Nucl. Phys. B*, vol. 443, pp. 85–126, 1995, arXiv:hep-th/9503124. doi:10.1016/0550-3213(95)00158-O.
- [10] J. Dai, R. Leigh, and J. Polchinski, “New Connections Between String Theories,” *Mod. Phys. Lett. A*, vol. 4, pp. 2073–2083, 1989. doi:10.1142/S0217732389002331.
- [11] B. Zwiebach, *A First Course in String Theory*. Cambridge University Press, 2004. doi:10.1017/CBO9780511841682.
- [12] D. Lüst and S. Theisen, “Lectures on string theory,” in *Lecture Notes in Physics*, vol. 346, Springer-Verlag Berlin Heidelberg, 1 ed., 1989. doi:10.1007/BFb0113507.
- [13] M. B. Green, J. H. Schwarz, and E. Witten, *Superstring Theory: 25th Anniversary Edition*, vol. 1 of *Cambridge Monographs on Mathematical Physics*. Cambridge University Press, 2012. doi:10.1017/CBO9781139248563.
- [14] J. Polchinski, *String Theory*, vol. 1 of *Cambridge Monographs on Mathematical Physics*. Cambridge University Press, 1998. doi:10.1017/CBO9780511816079.

- [15] G. T. Horowitz and A. Strominger, “Black strings and P-branes,” *Nucl. Phys. B*, vol. 360, pp. 197–209, 1991. doi:10.1016/0550-3213(91)90440-9.
- [16] E. Witten, “AdS / CFT correspondence and topological field theory,” *JHEP*, vol. 12, p. 012, 1998, arXiv:hep-th/9812012. doi:10.1088/1126-6708/1998/12/012.
- [17] G. Hooft, “A planar diagram theory for strong interactions,” *Nuclear Physics B*, vol. 72, no. 3, pp. 461 – 473, 1974. doi:10.1016/0550-3213(74)90154-0.
- [18] S. Coleman and J. Mandula, “All possible symmetries of the s matrix,” *Phys. Rev.*, vol. 159, pp. 1251–1256, Jul 1967. doi:10.1103/PhysRev.159.1251.
- [19] R. Haag, J. T. Lopuszanski, and M. Sohnius, “All Possible Generators of Supersymmetries of the s Matrix,” *Nucl. Phys. B*, vol. 88, p. 257, 1975. doi:10.1016/0550-3213(75)90279-5.
- [20] E. Ising, “Beitrag zur Theorie des Ferromagnetismus,” *Zeitschrift für Physik*, vol. 31, pp. 253–258, Feb. 1925. doi:10.1007/BF02980577.
- [21] J. D. Brown and M. Henneaux, “Central Charges in the Canonical Realization of Asymptotic Symmetries: An Example from Three-Dimensional Gravity,” *Commun. Math. Phys.*, vol. 104, pp. 207–226, 1986. doi:10.1007/BF01211590.
- [22] E. Witten, “Anti-de Sitter space and holography,” *Adv. Theor. Math. Phys.*, vol. 2, pp. 253–291, 1998, arXiv:hep-th/9802150. doi:10.4310/ATMP.1998.v2.n2.a2.
- [23] M. Natsuume, “AdS/cft duality user guide,” in *Lecture Notes in Physics*, vol. 903, Springer Japan, 1 ed., 2015. doi:10.1007/978-4-431-55441-7.
- [24] H. Năstase, *Introduction*, pp. xvii–xviii. Cambridge University Press, 2015. doi:10.1017/CBO9781316090954.002.
- [25] M. Ammon and J. Erdmenger, *Gauge/Gravity Duality: Foundations and Applications*. Cambridge University Press, 2015. doi:10.1017/CBO9780511846373.
- [26] O. Aharony, S. S. Gubser, J. M. Maldacena, H. Ooguri, and Y. Oz, “Large N field theories, string theory and gravity,” *Phys. Rept.*, vol. 323, pp. 183–386, 2000, arXiv:hep-th/9905111. doi:10.1016/S0370-1573(99)00083-6.
- [27] H. Nastase, “Introduction to AdS-CFT,” 12 2007, arXiv:0712.0689.
- [28] A. V. Ramallo, “Introduction to the AdS/CFT correspondence,” *Springer Proc. Phys.*, vol. 161, pp. 411–474, 2015, arXiv:1310.4319. doi:10.1007/978-3-319-12238-0_10.
- [29] M. Natsuume, *AdS/CFT Duality User Guide*, vol. 903. 2015, arXiv:1409.3575. doi:10.1007/978-4-431-55441-7.
- [30] D. Harlow, “TASI Lectures on the Emergence of Bulk Physics in AdS/CFT,” *PoS*, vol. TASI2017, p. 002, 2018, arXiv:1802.01040. doi:10.22323/1.305.0002.
- [31] J. Eisert, M. Cramer, and M. B. Plenio, “Area laws for the entanglement entropy - a review,” *Rev. Mod. Phys.*, vol. 82, pp. 277–306, 2010, arXiv:0808.3773. doi:10.1103/RevModPhys.82.277.
- [32] F. Verstraete and J. I. Cirac, “Matrix product states represent ground states faithfully,” *Physical Review B*, vol. 73, p. 094423, Mar. 2006, arXiv:cond-mat/0505140. doi:10.1103/PhysRevB.73.094423.
- [33] D. Perez-Garcia, F. Verstraete, M. M. Wolf, and J. I. Cirac, “Matrix Product State Representations,” *arXiv e-prints*, pp. quant-ph/0608197, Aug. 2006, arXiv:quant-ph/0608197.

- [34] M. B. Hastings, “An area law for one-dimensional quantum systems,” *Journal of Statistical Mechanics: Theory and Experiment*, vol. 2007, p. 08024, Aug. 2007, arXiv:0705.2024. doi:10.1088/1742-5468/2007/08/P08024.
- [35] F. G. Brandao and M. Horodecki, “Exponential Decay of Correlations Implies Area Law,” *Commun. Math. Phys.*, vol. 333, no. 2, pp. 761–798, 2015, arXiv:1206.2947. doi:10.1007/s00220-014-2213-8.
- [36] A. Rényi, “On Measures of Information and Entropy,” *Proceedings of the 4th Berkeley Symposium on Mathematics, Statistics and Probability*, vol. 1, pp. 547–561, 1960.
- [37] J. L. Cardy and I. Peschel, “Finite Size Dependence of the Free Energy in Two-dimensional Critical Systems,” *Nucl. Phys. B*, vol. 300, pp. 377–392, 1988. doi:10.1016/0550-3213(88)90604-9.
- [38] C. Holzhey, F. Larsen, and F. Wilczek, “Geometric and renormalized entropy in conformal field theory,” *Nucl. Phys. B*, vol. 424, pp. 443–467, 1994, arXiv:hep-th/9403108. doi:10.1016/0550-3213(94)90402-2.
- [39] P. Calabrese and J. L. Cardy, “Entanglement entropy and quantum field theory,” *J. Stat. Mech.*, vol. 0406, p. P06002, 2004, arXiv:hep-th/0405152. doi:10.1088/1742-5468/2004/06/P06002.
- [40] G. Vidal, “Class of Quantum Many-Body States That Can Be Efficiently Simulated,” *Phys. Rev. Lett.*, vol. 101, p. 110501, 2008, arXiv:quant-ph/0610099. doi:10.1103/PhysRevLett.101.110501.
- [41] G. Vidal, “Entanglement Renormalization,” *Phys. Rev. Lett.*, vol. 99, no. 22, p. 220405, 2007, arXiv:cond-mat/0512165. doi:10.1103/PhysRevLett.99.220405.
- [42] B. Swingle, “Entanglement renormalization and holography,” *Phys. Rev. D*, vol. 86, p. 065007, 2012. doi:10.1103/PhysRevD.86.065007.
- [43] J. Eisert, “Entanglement and tensor network states,” in *Autumn School on Correlated Electrons: Emergent Phenomena in Correlated Matter Jülich, Germany, 23-27. September 2013*, 2013, arXiv:1308.3318.
- [44] R. Orús, “A practical introduction to tensor networks: Matrix product states and projected entangled pair states,” *Annals of Physics*, vol. 349, pp. 117–158, Oct. 2014, arXiv:1306.2164. doi:10.1016/j.aop.2014.06.013.
- [45] J. C. Bridgeman and C. T. Chubb, “Hand-waving and interpretive dance: an introductory course on tensor networks,” *Journal of Physics A Mathematical General*, vol. 50, p. 223001, June 2017, arXiv:1603.03039. doi:10.1088/1751-8121/aa6dc3.
- [46] I. S. Reed and G. Solomon, “Polynomial codes over certain finite fields,” *Journal of the Society for Industrial and Applied Mathematics*, vol. 8, no. 2, pp. 300–304, 1960, arXiv:10.1137/0108018. doi:10.1137/0108018.
- [47] D. Gross, S. T. Flammia, and J. Eisert, “Most quantum states are too entangled to be useful as computational resources,” *Phys. Rev. Lett.*, vol. 102, p. 190501, May 2009. doi:10.1103/PhysRevLett.102.190501.
- [48] W. K. Wootters and W. H. Zurek, “A single quantum cannot be cloned,” *Nature*, vol. 299, pp. 802–803, 1982. doi:10.1038/299802a0.

- [49] D. Dieks, "Communication by epr devices," *Physics Letters A*, vol. 92, no. 6, pp. 271 – 272, 1982. doi:10.1016/0375-9601(82)90084-6.
- [50] D. Gottesman, "Stabilizer codes and quantum error correction," 1997, arXiv:quant-ph/9705052.
- [51] P. W. Shor, "Scheme for reducing decoherence in quantum computer memory," *Phys. Rev. A*, vol. 52, pp. R2493–R2496, Oct 1995. doi:10.1103/PhysRevA.52.R2493.
- [52] A. Steane, "Multiple particle interference and quantum error correction," *Proc. Roy. Soc. Lond. A*, vol. A452, p. 2551, 1996, arXiv:quant-ph/9601029. doi:10.1098/rspa.1996.0136.
- [53] A. Ekert and C. Macchiavello, "Quantum error correction for communication," 2 1996, arXiv:quant-ph/9602022.
- [54] C. H. Bennett, D. P. DiVincenzo, J. A. Smolin, and W. K. Wootters, "Mixed state entanglement and quantum error correction," *Phys. Rev.*, vol. A54, pp. 3824–3851, 1996, arXiv:quant-ph/9604024. doi:10.1103/PhysRevA.54.3824.
- [55] R. Laflamme, C. Miquel, J. P. Paz, and W. H. Zurek, "Perfect quantum error correcting code," *Phys. Rev. Lett.*, vol. 77, pp. 198–201, Jul 1996. doi:10.1103/PhysRevLett.77.198.
- [56] D. Gottesman, "Class of quantum error-correcting codes saturating the quantum hamming bound," *Phys. Rev. A*, vol. 54, pp. 1862–1868, 1996. doi:10.1103/PhysRevA.54.1862.
- [57] E. Knill and R. Laflamme, "A Theory of quantum error correcting codes," *Phys. Rev. Lett.*, vol. 84, pp. 2525–2528, 2000, arXiv:quant-ph/9604034. doi:10.1103/PhysRevLett.84.2525.
- [58] A. Calderbank and P. W. Shor, "Good quantum error correcting codes exist," *Phys. Rev. A*, vol. 54, p. 1098, 1996, arXiv:quant-ph/9512032. doi:10.1103/PhysRevA.54.1098.
- [59] D. G. Cory, M. D. Price, W. Maas, E. Knill, R. Laflamme, W. H. Zurek, T. F. Havel, and S. S. Somaroo, "Experimental quantum error correction," *Phys. Rev. Lett.*, vol. 81, pp. 2152–2155, Sep 1998. doi:10.1103/PhysRevLett.81.2152.
- [60] A. Y. Kitaev, "Quantum computations: algorithms and error correction," *Russian Mathematical Surveys*, vol. 52, pp. 1191–1249, dec 1997. doi:10.1070/rm1997v052n06abeh002155.
- [61] E. Dennis, A. Kitaev, A. Landahl, and J. Preskill, "Topological quantum memory," *J. Math. Phys.*, vol. 43, pp. 4452–4505, 2002, arXiv:quant-ph/0110143. doi:10.1063/1.1499754.
- [62] H. Bombin and M. A. Martin-Delgado, "Topological quantum distillation," *Phys. Rev. Lett.*, vol. 97, p. 180501, Oct 2006. doi:10.1103/PhysRevLett.97.180501.
- [63] D. Litinski, "A game of surface codes: Large-scale quantum computing with lattice surgery," *Quantum*, vol. 3, p. 128, Mar 2019. doi:10.22331/q-2019-03-05-128.
- [64] D. Poulin, "Stabilizer formalism for operator quantum error correction," *Phys. Rev. Lett.*, vol. 95, p. 230504, Dec 2005. doi:10.1103/PhysRevLett.95.230504.
- [65] L. Egan, D. M. Debroy, C. Noel, A. Risinger, D. Zhu, D. Biswas, M. Newman, M. Li, K. R. Brown, M. Cetina, and C. Monroe, "Fault-tolerant operation of a quantum error-correction code," 2020, arXiv:2009.11482.
- [66] M. A. Nielsen and I. L. Chuang, *Quantum Computation and Quantum Information: 10th Anniversary Edition*. Cambridge University Press, 2010. doi:10.1017/CBO9780511976667.

- [67] J. P. Preskill, "Lecture notes for physics 229: Quantum information and computation." California Institute of Technology, 1998.
- [68] B. M. Terhal, "Quantum error correction for quantum memories," *Rev. Mod. Phys.*, vol. 87, pp. 307–346, 2015. doi:10.1103/RevModPhys.87.307.
- [69] S. J. Devitt, W. J. Munro, and K. Nemoto, "Quantum error correction for beginners," *Reports on Progress in Physics*, vol. 76, p. 076001, Jun 2013. doi:10.1088/0034-4885/76/7/076001.
- [70] S. Ryu and T. Takayanagi, "Holographic derivation of entanglement entropy from the anti-de Sitter space/conformal field theory correspondence," *Phys. Rev. Lett.*, vol. 96, p. 181602, 2006. doi:10.1103/PhysRevLett.96.181602.
- [71] V. E. Hubeny, M. Rangamani, and T. Takayanagi, "A Covariant holographic entanglement entropy proposal," *JHEP*, vol. 07, p. 062, 2007, arXiv:0705.0016. doi:10.1088/1126-6708/2007/07/062.
- [72] T. Faulkner, "The Entanglement Renyi Entropies of Disjoint Intervals in AdS/CFT," 3 2013, arXiv:1303.7221.
- [73] T. Hartman, "Entanglement Entropy at Large Central Charge," 3 2013, arXiv:1303.6955.
- [74] A. Lewkowycz and J. Maldacena, "Generalized gravitational entropy," *JHEP*, vol. 08, p. 090, 2013, arXiv:1304.4926. doi:10.1007/JHEP08(2013)090.
- [75] T. Faulkner, A. Lewkowycz, and J. Maldacena, "Quantum corrections to holographic entanglement entropy," *JHEP*, vol. 11, p. 074, 2013, arXiv:1307.2892. doi:10.1007/JHEP11(2013)074.
- [76] S. Ryu and T. Takayanagi, "Aspects of Holographic Entanglement Entropy," *JHEP*, vol. 08, p. 045, 2006, arXiv:hep-th/0605073. doi:10.1088/1126-6708/2006/08/045.
- [77] M. Rangamani and T. Takayanagi, *Holographic Entanglement Entropy*, vol. 931 of *Lecture Notes in Physics*. Springer International Publishing, 2017. doi:10.1007/978-3-319-52573-0.
- [78] M. Rangamani and T. Takayanagi, *Holographic Entanglement Entropy*, vol. 931. Springer, 2017, arXiv:1609.01287. doi:10.1007/978-3-319-52573-0.
- [79] N. Bao, C. Cao, S. M. Carroll, A. Chatwin-Davies, N. Hunter-Jones, J. Pollack, and G. N. Remmen, "Consistency conditions for an AdS multiscale entanglement renormalization ansatz correspondence," *Phys. Rev.*, vol. D91, no. 12, p. 125036, 2015, arXiv:1504.06632. doi:10.1103/PhysRevD.91.125036.
- [80] C. Beny, "Causal structure of the entanglement renormalization ansatz," *New J. Phys.*, vol. 15, p. 023020, 2013, arXiv:1110.4872. doi:10.1088/1367-2630/15/2/023020.
- [81] A. Milsted and G. Vidal, "Geometric interpretation of the multi-scale entanglement renormalization ansatz," 2018, arXiv:1812.00529.
- [82] P. Hayden, S. Nezami, X.-L. Qi, N. Thomas, M. Walter, and Z. Yang, "Holographic duality from random tensor networks," *JHEP*, vol. 11, p. 009, 2016, arXiv:1601.01694. doi:10.1007/JHEP11(2016)009.
- [83] X.-L. Qi and Z. Yang, "Space-time random tensor networks and holographic duality," 1 2018, arXiv:1801.05289.
- [84] A. Hamilton, D. N. Kabat, G. Lifschytz, and D. A. Lowe, "Holographic representation of local bulk operators," *Phys. Rev. D*, vol. 74, p. 066009, 2006, arXiv:hep-th/0606141. doi:10.1103/PhysRevD.74.066009.

- [85] B. Czech, J. L. Karczmarek, F. Nogueira, and M. Van Raamsdonk, “The Gravity Dual of a Density Matrix,” *Class. Quant. Grav.*, vol. 29, p. 155009, 2012, arXiv:1204.1330. doi:10.1088/0264-9381/29/15/155009.
- [86] R. Bousso, S. Leichenauer, and V. Rosenhaus, “Light-sheets and AdS/CFT,” *Phys. Rev. D*, vol. 86, p. 046009, 2012, arXiv:1203.6619. doi:10.1103/PhysRevD.86.046009.
- [87] V. E. Hubeny and M. Rangamani, “Causal Holographic Information,” *JHEP*, vol. 06, p. 114, 2012, arXiv:1204.1698. doi:10.1007/JHEP06(2012)114.
- [88] I. A. Morrison, “Boundary-to-bulk maps for AdS causal wedges and the Reeh-Schlieder property in holography,” *JHEP*, vol. 05, p. 053, 2014, arXiv:1403.3426. doi:10.1007/JHEP05(2014)053.
- [89] A. Almheiri, X. Dong, and D. Harlow, “Bulk locality and quantum error correction in ads/cft,” *JHEP*, vol. 1504, p. 163, 2015.
- [90] F. Pastawski, B. Yoshida, D. Harlow, and J. Preskill, “Holographic quantum error-correcting codes: Toy models for the bulk/boundary correspondence,” *JHEP*, vol. 2015, p. 149, 2015. doi:10.1007/JHEP06(2015)149.
- [91] W. Helwig, W. Cui, A. Riera, J. I. Latorre, and H.-K. Lo, “Absolute Maximal Entanglement and Quantum Secret Sharing,” *Phys. Rev. A*, vol. 86, p. 052335, 2012, arXiv:1204.2289. doi:10.1103/PhysRevA.86.052335.
- [92] R. J. Harris, N. A. McMahon, G. K. Brennen, and T. M. Stace, “Calderbank-shor-steane holographic quantum error-correcting codes,” *Phys. Rev. A*, vol. 98, p. 052301, Nov 2018. doi:10.1103/PhysRevA.98.052301.
- [93] B. Yoshida, “Quantum gravity from quantum error-correcting codes,” *Quantum Frontiers blog, California Institute of Technology*, 3 2015.
- [94] M. Van Raamsdonk, “Building up spacetime with quantum entanglement,” *Gen. Rel. Grav.*, vol. 42, pp. 2323–2329, 2010, arXiv:1005.3035. doi:10.1142/S0218271810018529.
- [95] J. M. Maldacena, “Eternal black holes in anti-de Sitter,” *JHEP*, vol. 04, p. 021, 2003, arXiv:hep-th/0106112. doi:10.1088/1126-6708/2003/04/021.
- [96] M. M. Wolf, F. Verstraete, M. B. Hastings, and J. I. Cirac, “Area Laws in Quantum Systems: Mutual Information and Correlations,” *Phys. Rev. Lett.*, vol. 100, no. 7, p. 070502, 2008, arXiv:0704.3906. doi:10.1103/PhysRevLett.100.070502.
- [97] T. Takayanagi and K. Umemoto, “Entanglement of purification through holographic duality,” *Nature Phys.*, vol. 14, no. 6, pp. 573–577, 2018, arXiv:1708.09393. doi:10.1038/s41567-018-0075-2.
- [98] P. Caputa, M. Miyaji, T. Takayanagi, and K. Umemoto, “Holographic Entanglement of Purification from Conformal Field Theories,” *Phys. Rev. Lett.*, vol. 122, no. 11, p. 111601, 2019, arXiv:1812.05268. doi:10.1103/PhysRevLett.122.111601.
- [99] D. Stanford and L. Susskind, “Complexity and Shock Wave Geometries,” *Phys. Rev. D*, vol. 90, no. 12, p. 126007, 2014, arXiv:1406.2678. doi:10.1103/PhysRevD.90.126007.
- [100] A. R. Brown, D. A. Roberts, L. Susskind, B. Swingle, and Y. Zhao, “Holographic Complexity Equals Bulk Action?,” *Phys. Rev. Lett.*, vol. 116, no. 19, p. 191301, 2016, arXiv:1509.07876. doi:10.1103/PhysRevLett.116.191301.

- [101] A. R. Brown, H. Gharibyan, S. Leichenauer, H. W. Lin, S. Nezami, G. Salton, L. Susskind, B. Swingle, and M. Walter, “Quantum Gravity in the Lab: Teleportation by Size and Traversable Wormholes,” 11 2019, arXiv:1911.06314.
- [102] M. Van Raamsdonk, “Lectures on Gravity and Entanglement,” in *Theoretical Advanced Study Institute in Elementary Particle Physics: New Frontiers in Fields and Strings*, pp. 297–351, 2017, arXiv:1609.00026. doi:10.1142/9789813149441_0005.
- [103] G. Penington, “Entanglement Wedge Reconstruction and the Information Paradox,” 5 2019, arXiv:1905.08255.
- [104] A. Almheiri, N. Engelhardt, D. Marolf, and H. Maxfield, “The entropy of bulk quantum fields and the entanglement wedge of an evaporating black hole,” *JHEP*, vol. 12, p. 063, 2019, arXiv:1905.08762. doi:10.1007/JHEP12(2019)063.
- [105] G. C. Wick, “The evaluation of the collision matrix,” *Phys. Rev.*, vol. 80, pp. 268–272, Oct 1950. doi:10.1103/PhysRev.80.268.
- [106] A. Hamilton, D. Kabat, G. Lifschytz, and D. A. Lowe, “Local bulk operators in ads/cft correspondence: A boundary view of horizons and locality,” *Phys. Rev. D*, vol. 73, p. 086003, Apr 2006. doi:10.1103/PhysRevD.73.086003.
- [107] S. Lee, S. Minwalla, M. Rangamani, and N. Seiberg, “Three point functions of chiral operators in $D = 4$, $N=4$ SYM at large N ,” *Adv. Theor. Math. Phys.*, vol. 2, pp. 697–718, 1998, arXiv:hep-th/9806074. doi:10.4310/ATMP.1998.v2.n4.a1.
- [108] D. Z. Freedman, S. D. Mathur, A. Matusis, and L. Rastelli, “Correlation functions in the CFT(d) / AdS(d+1) correspondence,” *Nucl. Phys. B*, vol. 546, pp. 96–118, 1999, arXiv:hep-th/9804058. doi:10.1016/S0550-3213(99)00053-X.
- [109] X.-L. Qi, “Exact holographic mapping and emergent space-time geometry,” 9 2013, arXiv:1309.6282.
- [110] C. H. Lee and X.-L. Qi, “Exact holographic mapping in free fermion systems,” *Phys. Rev. B*, vol. 93, p. 035112, Jan 2016. doi:10.1103/PhysRevB.93.035112.
- [111] G. Evenbly and S. R. White, “Entanglement renormalization and wavelets,” *Phys. Rev. Lett.*, vol. 116, p. 140403, 2016. doi:10.1103/PhysRevLett.116.140403.
- [112] G. Evenbly, “Hyperinvariant tensor networks and holography,” *Phys. Rev. Lett.*, vol. 119, p. 141602, Oct 2017. doi:10.1103/PhysRevLett.119.141602.